

DISSERTATION

INVESTIGATION OF THE SUMMER CLIMATE OF NORTH AMERICA:
A REGIONAL ATMOSPHERIC MODELING STUDY

Submitted by

Christopher Lawrence Castro

Department of Atmospheric Science

In partial fulfillment of the requirements

For the Degree of Doctor of Philosophy

Colorado State University

Fort Collins, Colorado

Fall 2005

COLORADO STATE UNIVERSITY

June 22, 2005

WE HEREBY RECOMMEND THAT THE DISSERTATION PREPARED UNDER OUR SUPERVISION BY CHRISTOPHER LAWRENCE CASTRO ENTITLED **INVESTIGATION OF THE SUMMER CLIMATE OF NORTH AMERICA: A REGIONAL ATMOSPHERIC MODELING STUDY** BE ACCEPTED AS FULFILLING IN PART REQUIREMENTS FOR THE DEGREE OF DOCTOR OF PHILOSOPHY.

Committee on Graduate Work

[Redacted Signature]

Dr. William R. Cotton

[Redacted Signature]

Dr. David W.J. Thompson

[Redacted Signature]

Dr. Jorge A. Ramirez

[Redacted Signature]

Dr. Roger A. Pielke Sr., Adviser

[Redacted Signature]

Dr. Steven A. Rutledge, Department Head

ABSTRACT OF DISSERTATION

INVESTIGATION OF THE SUMMER CLIMATE OF NORTH AMERICA:

A REGIONAL ATMOSPHERIC MODELING STUDY

The Regional Atmospheric Modeling System (RAMS) is used to investigate model sensitivity and the summer climate of North America. The value restored and added by dynamical downscaling is first evaluated. At large scales, RAMS underestimates atmospheric variability and this worsens as the grid spacing increases or domain size increases. The model simulated evolution of kinetic energy relative to the driving reanalysis kinetic energy exhibits a decrease with time which is more pronounced with larger grid spacing. The surface boundary forcing is the dominant factor in generating atmospheric variability and exerts greater control on the model as the influence of lateral boundary conditions diminish. The sensitivity to surface forcing is also influenced by the model parameterizations. Dynamical downscaling with RAMS does not retain value of the large scale of that which exists in the driving global reanalysis. The value added is to resolve smaller-scale features which have a greater dependence on the surface boundary.

The NCEP Reanalysis is then dynamically downscaled with RAMS to generate a regional model climatology of the contiguous U.S. and Mexico (1950-2002). The simulations capture climatic features and seasonal transitions associated with the North

American monsoon system. The diurnal cycle is the dominant time-varying mode of convective activity and is modulated by the large-scale circulation. Lower frequency modes account for the variability of convection at a remote distance from elevated terrain. The climatology is evaluated with respect to the dominant modes of global sea surface temperature. An additional series of simulations dynamically downscales data from a general circulation model executed with idealized sea surface temperature corresponding to the modes with greatest variability in the Pacific, to establish a casual link to remote sea surface temperature forcing. Time-evolving teleconnections related to tropical Pacific sea surface temperature modulate the evolution of North American summer climate, in particular the low-level moisture transport into the continental interior and convective activity. The most significant response occurs in early summer and affects the distribution of rainfall at that time. A global increase in tropical sea surface temperature over the period has also significantly affected North American summer climate.

Christopher Lawrence Castro
Department of Atmospheric Science
Colorado State University
Fort Collins, CO 80523
Fall 2005

ACKNOWLEDGEMENTS

I thank my graduate adviser these past years, Dr. Roger A. Pielke, Sr., for his unwavering support of my research endeavors and personal encouragement. I also appreciate the efforts of my graduate committee members, Drs. William R. Cotton, David W.J. Thompson, and Jorge A. Ramírez, for their advice and support. Dr. Jimmy O. Adegoke provided computing resources at the University of Missouri, Kansas City, which were used for RAMS simulations in this study. The general circulation model data and SST EOF analyses were provided by Dr. Siegfried Schubert, Michael Kistler, and Phillip Pegion from NASA Goddard Space Flight Center.

I am indebted to past and present students and staff of the Pielke and Cotton groups for their assistance during my time at CSU. This dissertation would not have come to fruition without them. I thank all my friends and family for their love and support, especially my parents, Anthony and Marlene Castro.

Funding for this research was provided by NOAA Grant NA17RJ1228, Amendment 6, NOAA Grant NA67RJ0152, Amendment 6, a NASA Earth System Science Fellowship (NASA Grant NGT5-30344), and DOD cooperative agreement DAAD19-02-2-0005.

TABLE OF CONTENTS

Abstract	iii
Acknowledgements	v
List of Tables	vii
List of Figures	ix
1. Introduction	1
1.1 Dynamical Downscaling with a Regional Climate Model (RCM)	1
1.2 Application of RCMs to Investigate North American Summer Climate	6
1.3 Relationship of North American Summer Climate to Pacific SSTs	10
1.4 Dissertation Overview	14
2. The Regional Climate Model and Kain-Fritsch Scheme	15
2.1 The Regional Atmospheric Modeling System (RAMS)	15
2.2 The Kain-Fritsch Cumulus Parameterization Scheme in RAMS	17
2.2.1 RAMS-Kain-Fritsch Interface	18
2.2.2 Updraft Source Layer and Convective Trigger	22
2.2.3 Kain-Fritsch Updraft Model	25
2.2.4 Kain-Fritsch Downdraft Model	30
2.2.5 Compensational Subsidence and Final Outputs	33
3. Dynamical Downscaling: Assessment of Value Retained and Added Using RAMS	37
3.1 Description of Basic Dynamical Downscaling Sensitivity Experiments	37
3.2 Two-dimensional Spectral Analysis of Model Variables	41
3.3 Model Variables Analyzed	44
3.4 Results for Basic Experiments	47
3.5 Results for Follow-on Experiments	60
3.6 Discussion	75
3.7 Summary	82
4. A Summer RCM Climatology of the Contiguous U.S. and Mexico	85
4.1 Description of RAMS Simulations	85
4.2 Validation Datasets	89
4.3 Validation of RCM Results	90

4.4 Behavior of Atmospheric Circulation and Surface Heat Fluxes	109
4.5 Integrated Moisture Flux and 500-mb Vorticity	114
4.6 Discussion	125
4.7 Summary	130
5. Diagnosing the Effect of Pacific SST Associated Teleconnections on North American Summer Climate	132
5.1 Methodology for Compositing Years According to Dominant SST REOFs	132
5.2 Observed Time-Evolving SST Associated Teleconnection Patterns	144
5.3 Response of Teleconnections in RCM-Simulated Fields	151
5.4 Dynamical Downscaling of Idealized GCM Experiments	169
5.5 Summary and Discussion	181
6. General Summary, Conclusions, and Suggestions for Future Work	188
References	194

LIST OF TABLES

Table 1.1: Dependence of regional model on indicated constraints.

Table 1.2: Examples of predictability.

Table 2.1: Physical variables used in the description of the Kain-Fritsch cumulus parameterization scheme.

Table 2.2: Significant levels and identifiers used in the description of the Kain-Fritsch cumulus parameterization scheme.

Table 2.3: Physical constants used in the description of the Kain-Fritsch cumulus parameterization scheme

Table 3.1: Commonly used symbols in this chapter.

Table 3.2: Model domain specifications and computational increase for the six basic experiments. The computational increase is computed as the time to complete one model timestep for the given domain divided by that for the basic experiment #1.

Table 5.1: Correlation coefficients between Pacific SST indices in Castro et al. (2001) and PCs of global SST for the period 1950-2000. Highlighted values indicate the highest explained variance of the PC.

Table 5.2: Positive and negative composites for PC 1 of global SST for the period 1950-2002.

Table 5.3: Positive and negative composites for PC 2 of global SST for the period 1950-2002.

Table 5.4: Positive and negative composites for PC 3 of global SST for the period 1950-2002.

LIST OF FIGURES

Figure 3.1: RAMS domains for model sensitivity experiments in this chapter for $\Delta x = 200$ km.

Figure 3.2: Observed 500-mb height (m) on 0Z UTC, 12 May 1993, for a) basic experiment 1, b) basic experiment 3, c) basic experiment 4, and d) NCEP Reanalysis.

Figure 3.3: Average error in RAMS-simulated 500-mb height (m) for the given model domain constraints (last fifteen days of simulation). Contour interval is 10 m.

Figure 3.4: Fractional change in spectral power ($\Delta S(k)_{frac}$) versus $\log_{10}(k)$ and wavelength, small domain experiments for a) column-average total kinetic energy and b) column integrated moisture flux convergence (MFC). The dashed black line indicates k_{max}^* and the solid black line $k_{Nyquist}^*$. k in units of m^{-1} . Wavelength in units of m.

Figure 3.5: Fractional change in spectral power ($\Delta S(k)_{frac}$) versus $\log_{10}(k)$ for column average total kinetic energy, small and large domain experiments: a) $\Delta x = 200$ km, b) $\Delta x = 100$ km, and c) $\Delta x = 50$ km. Small domain experiments color coded as in Fig. 3.4 and large domain experiments shown as corresponding solid black curve. The dashed black line indicates k_{max}^* and the solid black line $k_{Nyquist}^*$. k in units of m^{-1} . Wavelength in units of m.

Figure 3.6: Time evolution of the fraction of model simulated to reanalysis regridded domain-averaged total kinetic energy for the six basic experiments on equivalent grids. The small domain is indicated by a solid curve, and the large domain is indicated by a dashed curve.

Figure 3.7: Same as Fig. 3.6 for model domain-averaged kinetic energy variance.

Figure 3.8: Same as Fig. 3.3 for Follow-on 1 (internal nudging). Contour interval is 5 m. wavelength for a) column average kinetic energy and b) column integrated moisture flux convergence (MFC), Follow-on 1 (internal nudging). The dashed black line indicates k_{max}^* and the solid black line $k_{Nyquist}^*$. k in units of m^{-1} . Wavelength in units of m.

Figure 3.10: RAMS-simulated convective precipitation with the Kuo scheme for model constraints indicated. Period considered is last 15 days of simulation. Precipitation in mm.

Figure 3.11: Same as Fig. 3.9 for Follow-on 2 (larger grid).

Figure 3.12: RAMS-simulated convective precipitation (mm) with the Kain-Fritsch scheme for model constraints indicated and observed precipitation from NCEP. Period considered is last 15 days of simulation.

Figure 3.13: Same as Fig. 3.9 for Follow-on experiment 3 (Kain-Fritsch convection).

Figure 3.14: Difference of between RAMS-simulated precipitation and NCEP observed precipitation (mm) over the contiguous U.S. for the model conditions specified. Domain-averaged bias and explained variance (r^2) included. Period considered is last 15 days of simulation.

Figure 3.15: Fractional change in spectral power ($\Delta S(k)_{frac}$) versus $\log_{10}(k)$ and wavelength for different RAMS-generated model precipitation solutions on the 50 km small domain grid. k in units of m^{-1} . Wavelength in units of m.

Figure 3.16: Fractional change in spectral power ($\Delta S(k)_{frac}$) versus $\log_{10}(k)$ and wavelength, experiments with the Kuo scheme compared to Follow-on 4. The quantity considered is the MFC multiplied by the topographic gradient in the model. k in units of m^{-1} . Wavelength in units of m.

Figure 3.17: Same as Fig. 3.16 for experiments with the KF scheme.

Figure 3.18: Fractional change in spectral power ($\Delta S(k)_{frac}$) versus $\log_{10}(k)$ and wavelength, for column-average total kinetic energy. The red curve is the basic experiment 3 simulation (convection scheme only) and the black curve is the same simulation with convection and explicit microphysics. The dashed black line indicates k_{max}^* and the solid black line $k_{Nyquist}^*$. k in units of m^{-1} . Wavelength in units of m.

Figure 4.1: RAMS model domain for North American summer climatology.

Figure 4.2: Climatological May soil moisture (as a fraction of saturation) from data used as input to RAMS simulations. Shading indicated by color bar.

Figure 4.3: Observed CPC gauge-derived (1950-2002) average precipitation (mm) for the summer months and the difference between the monsoon peak and premonsoon periods. Shading indicated by color bars.

Figure 4.4: Same as Fig. 4.3 for the GPI (1998-2004) average satellite-derived precipitation.

Figure 4.5: Same as Fig. 4.3 for (1950-2002) RAMS average precipitation.

Figure 4.6: Same as Fig. 4.3 for (1950-2002) NCEP Reanalysis precipitation.

Figure 4.7: Selected regions used in considering the time evolution of temperature and precipitation.

Figure 4.8: Evolution of average observed precipitation (mm day^{-1}) by gauge and satellite data for the regions identified in Fig. 4.7. Premonsoon, monsoon onset, and monsoon peak periods identified.

Figure 4.9: Same as Fig. 4.8 for NCEP Reanalysis and RAMS precipitation.

Figure 4.10: Summary of the day (1973-1996) averaged observed surface temperature (K) for the summer months and the difference between the monsoon peak and monsoon onset periods. Shading indicated by the color bar. Data missing in unshaded areas.

Figure 4.11: Same as Fig. 4.10 for RAMS (1950-2002) average temperature at the first model level.

Figure 4.12: Evolution of average observed surface temperature (K) from summary of the day data and RAMS temperature at the first model level for the regions identified in Fig. 4.7. Premonsoon, monsoon onset, and monsoon peak periods identified.

Figure 4.13: Observed average (1973-1996) surface moisture flux ($\text{m s}^{-1} \text{ g kg}^{-1}$) from summary of the day data for the summer months and the difference between the monsoon peak and monsoon onset periods. Shading indicated by color bars. Data missing in unshaded areas.

Figure 4.14: Same as Fig. 4.13 for (1950-2002) RAMS average moisture flux at the first model level.

Figure 4.15: Monthly RAMS average 500-mb geopotential height (m) and 700-mb wind vectors for the summer months. Contour interval for geopotential height is 20 m. The average zero mean zonal wind line is indicated by a solid line on the streamline plots. Vector length is 10 m s^{-1} .

Figure 4.16: RAMS average monthly sensible heat flux (W m^{-2}) for the summer months and the difference between the monsoon peak and premonsoon periods. Shading indicated by the color bar.

Figure 4.17: Same as Fig. 4.16 for average RAMS latent heat flux.

Figure 4.18: Weighted spectral power of RAMS integrated moisture flux convergence ($\text{mm}^2 \text{day}^{-2}$) in the diurnal band for the summer months and the difference between the monsoon peak and premonsoon periods. Shading indicated by the color bar.

Figure 4.19: Same as Fig. 4.18 for the sub-synoptic (1.5 – 3 day) band.

Figure 4.20: Same as Fig. 4.18 for the synoptic (4 – 15 day) band

Figure 4.21: Ratio of weighted spectral power of the synoptic MFC to the diurnal MFC for the summer months and the difference between the monsoon peak and premonsoon periods. Shading indicated by the color bar.

Figure 4.22: Hovmöller diagram of weighted spectral power of the synoptic component of 500-mb vorticity ($\times 10^{-13} \text{s}^{-2}$) longitudinally averaged over $95 - 115^\circ \text{W}$ for the period 1 June through 16 August. The solid line indicates the zero mean zonal wind line. Dashed lines indicate one standard deviation of the zero mean zonal wind line.

Figure 5.1: The first three rotated EOFs of global SST and composite SST anomalies in boreal summer with percent explained variance. Period considered is 1950-2000. For REOF patterns units are arbitrary and contour interval is one unit. SST anomalies in K and contour interval is 0.4 K.

Figure 5.2: Normalized principal component time series (1950-2000) for boreal summer SST modes in Fig. 5.1.

Figure 5.3: Summer PDO index based on the first PC of Pacific SST poleward of 20°N .

Figure 5.4: The Pacific SST variability mode, computed as the average of ENSO and PDO-like global SST modes for the period 1950-2000. Contouring as in Fig. 5.1.

Figure 5.5: Time evolution of 30-day average 500-mb height anomalies (m) through the summer season for the PC 1 composites in Table 5.2. Contour interval is 5 m. Shading indicates statistical significance at the 90 and 95% levels.

Figure 5.6: Same as Fig. 5.5 for PC 2 composites in Table 5.3.

Figure 5.7: Same as Fig. 5.5 for PC 3 composites in Table 5.4.

Figure 5.8: Same as Fig. 5.5 for composites constructed with the summer PDO index of Mantua et al. (1997).

Figure 5.9: Time evolution of 30-day average RAMS precipitation anomalies (mm) through the summer season for PC 1 composite in Table 5.2. Contour interval is 10 mm. Shading indicates statistical significance at the 90 and 95% levels.

Figure 5.10: Same as Fig. 5.9 for PC 2 composite in Table 5.3.

Figure 5.11: Same as Fig. 5.9 for PC 3 composite in Table 5.4.

Figure 5.12: Same as Fig. 5.9 for average of PC 1 and PC 3 (Pacific SST variability mode) composite in Table 5.5.

Figure 5.13: 30-day average surface temperature (K) and moisture flux ($\text{m s}^{-1} \text{ g kg}^{-1}$) anomalies for Pacific SST variability mode composites and SST regime shift composites at the time of maximum teleconnectivity (see text for details). Shading indicates statistical significance at the 90 and 95% levels. Contour interval for temperature is 0.2 K and contour interval for moisture flux is $1 \text{ m s}^{-1} \text{ g kg}^{-1}$.

Figure 5.14: Fractional difference in weighted spectral power of integrated moisture flux convergence for Pacific SST variability mode and SST regime shift mode at the time of maximum teleconnectivity (see text for details). Shown are the diurnal (1 day), sub-synoptic (1.5-3 day) and synoptic (4-15 day) bands. Shading indicated by color bars.

Figure 5.15: Time evolution of 30-day average 500-mb height anomalies (m) for NSIPP SST REOF 1 (ENSO mode) modeled summers. Contour interval is 5 m. Shading indicates statistical significance at the 90 and 95% levels.

Figure 5.16: Same as Fig. 5.15 for NSIPP SST REOF 2 (PDO-like mode) modeled summers.

Figure 5.17: 30-day average RAMS precipitation anomalies (mm) of NSIPP REOF 1 and REOF 2 SST forced simulations at the time of maximum teleconnectivity (see text for details). Shading indicates statistical significance at the 90 and 95% levels. Contour interval is 5 mm up to 10 mm and 10 mm thereafter.

Figure 5.18: Same as Fig. 5.17 for RAMS surface temperature (K). Contour interval is 0.5 K.

Figure 5.19: Same as Fig. 5.17 for surface moisture flux ($\text{m s}^{-1} \text{ g kg}^{-1}$). Contour interval is $2 \text{ m s}^{-1} \text{ g kg}^{-1}$.

Figure 5.20: Same as Fig. 5.17 for the fractional difference in weighted spectral power of integrated moisture flux convergence. Only the diurnal band shown. Shading indicated by color bars.

Chapter 1

INTRODUCTION

1.1 Dynamical Downscaling with a Regional Climate Model (RCM)

The term “downscaling” refers to the use of either fine spatial scale numerical atmospheric models (dynamical downscaling), or statistical relationship (statistical downscaling) in order to achieve detailed regional and local atmospheric data. The starting point for downscaling is typically a larger-scale atmosphere or coupled ocean-atmosphere model run globally (GCM). The downscaled high resolution data can then be inserted into other types of numerical simulation tools such as hydrological, agricultural, and ecological models. This dissertation focuses on dynamical downscaling with a regional climate model (RCM). By RCM we mean a limited area (weather prediction) model (LAM) run for an integration time greater than approximately two weeks, so that the sensitivity to initial atmospheric conditions is lost (Jacob and Podzun 1997). A summary of dynamical downscaling is reported in Chapter 10 of the 2001 Intergovernmental Panel on Climate Change (IPCC) science report. LAM dynamical downscaling can be classified into four distinct types:

- Type 1: LAM forced by lateral boundary conditions from a numerical weather prediction GCM or global data reanalysis at regular time intervals (typically 6 or 12 h), by bottom boundary conditions (e.g., terrain), and specified initial

conditions. A numerical weather prediction GCM is a GCM in which the global initial atmospheric conditions are not yet forgotten.

- Type 2: LAM initial atmospheric conditions have been forgotten, but results are still dependent on the lateral boundary conditions from an NWP GCM or global data reanalysis and on the bottom boundary conditions.
- Type 3: Lateral boundary conditions are provided from a GCM which is forced with specified surface boundary conditions.
- Type 4: Lateral boundary conditions from a completely coupled earth system global climate model in which the atmosphere-ocean-biosphere and cryosphere are interactive.

Tables 1.1 and 1.2 illustrate examples of each type of downscaled model. Table 1.1 overviews RCM dependence on the indicated constraints for the four types. Table 1.2 shows that these constraints and the predictive skill of LAMs becomes less as an attempt is made to forecast further into the future. Types 2 through 4 can be considered RCM modes.

With short-term numerical weather prediction (Type 1), the observations used in the analysis to initialize a model retain a component of realism even when degraded to the coarser model resolution of a global model (i.e., the data is sampled from a continuous field). This realism persists for a period of time (up to a week or so), when used as lateral boundary conditions for a weather prediction LAM. This is not true with Type 4 simulations, where observed data does not exist to influence the predictions (Pielke 2001a). LAMs cannot significantly increase predictability if the solution is

	TYPE I	TYPE II	TYPE III	TYPE IV
Bottom Boundary Conditions	Terrain; LDAS ^a ; Observed SSTs	Terrain; Climatological Vegetation; Observed SSTs; Deep Soil Moisture	Terrain; Climatological Vegetation; Observed SSTs; Deep Soil Moisture	Terrain; Soils
Initial Conditions	ETA Analysis Field	NONE	NONE	NONE
Lateral Boundary Conditions	Global Forecast System Atmospheric Model ^b	NCEP Reanalysis ^c	Global Model Forced by Observed SSTs	IPCC ^d ; US National Assessment ^e
Regional	ETA ^f MM5 ^g RAMS ^h ARPS ⁱ	PIRCS ^j	COLA ^k /ETA ^l	RegCM ^m

^a <http://ldas.gsfc.nasa.gov/>

^b <http://wwwt.emc.ncep.noaa.gov/gmb/moorthi/gam.html>

^c Kalnay et al. (1996)

^d Houghton et al. (2001)

^e <http://www.gcrio.org/NationalAssessment/>

^f Black (1994)

^g Grell et al. (1994)

^h Pielke et al. (1992)

ⁱ Xue et al. (2000, 2001)

^j Takle et al. (1999)

^k <http://www-pcmdi.llnl.gov/modldoc/amip/14cola.html>

^l Mesinger et al. (1997)

^m Giorgi (1993a, b)

Table 1.1: Dependence of regional model on indicated constraints.

More Constraints	Greater Predictive Skill
---------------------	--------------------------------

Constraints

Day-to-Day Weather Prediction	Type 1	Initial Conditions Lateral Boundary Conditions Topography Other Bottom Land Boundary Conditions Solar Irradiance Well-Mixed Greenhouse Gases
Seasonal Weather Simulation	Type 2	Lateral Boundary Conditions Topography Other Bottom Land Boundary Conditions Solar Irradiance Well-Mixed Greenhouse Gases
Season Weather Prediction	Type 3	Topography Other Bottom Land Boundary Conditions Sea Surface Temperatures Solar Irradiance Well-Mixed Greenhouse Gases
Multiyear Climate Prediction	Type 4	Topography Solar Irradiance Well-Mixed Greenhouse Gases

Fewer Constraints	Less Predictive Skill
----------------------	-----------------------------

Table 1.2: Examples of predictability

highly dependent on the large-scale forcing supplied by the lateral boundaries. Even when the model solution is strongly influenced by the surface boundary, improved skill still cannot be achieved without accurate lateral boundary conditions.

What is the value retained and value added by dynamical downscaling with a RCM? By “value retained” it is meant how well the RCM maintains fidelity with the large-scale behavior of the global model forcing data. By “value added” it is meant how much additional information the RCM can provide beyond the highest resolved wavelength of the global model. “Perfect” bottom and lateral boundary conditions can be assumed, as defined respectively by observed SSTs and atmospheric reanalyses (e.g. Type 2). Examples of Type 2 simulations include the Project to Intercompare Regional Climate Simulations (PIRCS) as reported in Takle et al. (1999). In such a framework the following questions can be posed: 1) what is the dependence on the evolution of synoptic features to the lateral boundary conditions and 2) what is the most appropriate domain size and grid spacing for RCM downscaling?

These questions have been previously investigated to some extent by RCM experiments which change the specification of the lateral boundaries. This may be done using a so-called “Big Brother” approach (e.g., de Elía et al. 2002, Denis et al. 2002, Denis et al. 2003). In these types of experiments, forcing data to a nested RCM grid (Little Brother) are spectrally degraded to eliminate small-scale variability. The results are then compared to a reference simulation (Big Brother) with no spectral degradation of the forcing. Another approach is to change the specification of the primary RCM grid itself. Denis et al. (2002) provide a good summary of studies of this type, including Jones et al. (1995, 1997), Jacob and Podzun (1997), and Seth and Giorgi (1998). All of

these studies note significant sensitivities to the specification of the RCM grid, as shown, for example, in precipitation and strength of mesoscale features. This work is extended here to show that, absent a means of updating the interior of the domain, the RCM cannot retain value of the large scale. It is then shown the value added, or skill of the RCM, is dependent on how the large scale is represented, how the surface boundary is prescribed, and the model physics. Exploring these issues is a necessary prerequisite step before application of the RCM to the investigation of North American summer climate, the main theme of this dissertation.

1.2 Application of RCMs to Investigate North American Summer Climate

Summer climate in North America, and its variability, is strongly influenced by the North American Monsoon System (NAMS). The large-scale changes in climate resulting from NAMS development are well understood. In brief, dry mid-latitude westerly flow persists over western North America until the middle of June. Monsoon onset is associated with a shift in the lower- and upper-level circulation over the continent in late June or early July. An extension of the Bermuda high retreats west, initiating light easterly flow over the Southwest U.S. and northwest Mexico (Bryson and Lowry 1955; Adams and Comrie 1997; Douglas et al. 1993; Higgins et al. 1997). A diurnal surface heat low forms over the Colorado River valley. Two low level jets (LLJ), the Great Plains LLJ and the Baja LLJ, are active at night and early morning to midday, respectively (Douglas 1995; Higgins et al. 1997b). As precipitation increases in the Southwest U.S. and Mexico, there is a corresponding decrease in the strength of the Great

Plains LLJ and precipitation in the central U.S. (Douglas 1995; Adams and Comrie 1997; Higgins et al. 1997b; Barlow 1998).

A great deal of present understanding of the NAMS has come about because of the advent of long-term atmospheric reanalyses. The reanalysis which will be used here is the NCEP-NCAR Reanalysis (Kalnay et al. 1996). Reanalyses are advantageous because they have long records (on the order of 50 years) and are based on atmospheric general circulations models (GCMs) with a fixed dynamical core and physics package. However, because of their coarse resolution and physical parameterizations, they cannot resolve fundamental aspects of mesoscale summer climate in North America. The problem is particularly acute in the western U.S. and Mexico because of the large influence of the topography. Atmospheric reanalyses have difficulty capturing the diurnal cycle of convection, the Baja LLJ, and the seasonal maximum in precipitation associated with the northwestward advance of monsoon rainfall into northwest Mexico and the Southwest U.S. A more detailed regional reanalysis over North America (Mesinger et al. 2004) will greatly aid in future diagnostic studies that use its record (on the order of twenty years).

An alternative is to use a RCM in a Type 2 or 3 dynamical downscaling mode. For such simulations, RCMs typically have a grid spacing of 10 – 50 km and a horizontal domain dimension on the order of several thousand kilometers. The area of interest may be the primary domain or a nested domain. RCM studies of summer climate in North America thus far fall into two categories: diagnostic evaluations and sensitivity studies. We focus our review of the literature to recent studies which focus on the core NAMS region (which we define as western Mexico and the Southwest U.S.) and the central U.S.

In diagnostic evaluations, the emphasis is to produce mesoscale features of the NAMS missing in the reanalysis and/or improve the correspondence with available observations beyond a reanalysis. Typically these studies have focused on one particular season or a few seasons in sequence. Using the ETA model, Berbery (2001) investigated three summer seasons in the core monsoon region. The simulations revealed the importance of the diurnal cycle in generating the precipitation maximum along the Sierra Madre Occidental (SMO) in Mexico and the influence of transient moisture flux (or Gulf surges) for precipitation in the southwest U.S. Berbery and Fox Rabinovitz (2003) used a stretched grid GCM to simulate the monsoon for the 1993 summer season. The resolution of their stretched grid in North America basically corresponds with the typical resolution of a RCM. Inclusion of smaller-scale features of the core monsoon region helped represent the continental out-of-phase relationship between the monsoon and southern Great Plains region. A spectral analysis of the Baja LLJ showed significant peaks for both the diurnal cycle and synoptic modes. Saleeby and Cotton (2004) concentrated on simulating NAMS onset for the 1993 season using the Regional Atmospheric Modeling System (RAMS). They identified coherent changes in the mesoscale atmospheric circulation associated with Gulf surge events and also demonstrated a connection of surge events to a decrease in strength and more easterly component of the Great Plains LLJ. Using the NCEP Regional Spectral Model, Anderson et al. investigated the nature of the atmospheric moisture budget in the core monsoon region (Anderson et al. 2004), characterized the hydrologic cycle associated with two spatio-temporal regimes in the Southwest U.S. (Anderson et al. 2002), and simulated the Baja LLJ (Anderson et al. 2000). Li et al. (2004) demonstrated with the

MM5 model that model accumulated rainfall for the 2002 season generally matched a satellite derived product and correctly matched the timing of rainfall as shown by gauge observations. However, they also noted substantial differences in observed precipitation derived from satellite and rain gauge measurements.

The creation of a long-term RCM climatology of North America has not been widely attempted. Xu et al. (2004) examined the seasonal development of the NAMS onset period during a 22 year simulation (1980-2001) with a climate version of the MM5 model over Mexico and part of the southern U.S. This work was the first of its kind to compute long-term averages using RCM data in the NAMS region and demonstrate correspondence with observations. Their principal result was that the model could produce a correct climatological timing of monsoon rains coincident with the changes in the large-scale circulation. The Xu et al. (2004) study will serve as an important point of reference in evaluating the simulations to be described in this dissertation.

Sensitivity studies of the NAMS fall into two categories. The surface boundary is changed (soil moisture, vegetation, or sea surface temperature), or the configuration of the RCM (model physical parameterization, grid spacing, domain size, and/or nudging options) is varied. The sensitivity studies in which RCM configurations are varied have revealed important caveats about RCMs themselves. As previously mentioned, there is a large sensitivity to the specification of model domain size and grid spacing. Miguez-Macho et al. (2005) demonstrate the utility of spectral nudging using the Regional Atmospheric Modeling System (RAMS) on a continental scale domain, particularly in improving precipitation estimates over the central U.S. There are also large sensitivities to model physical parameterization schemes. Gochis et al. (2002) and Gochis et al.

(2003) showed in simulations with the MM5 model over Mexico that changing the convection scheme may affect the model solution as much as feedback processes from the land surface. Also using MM5 over a larger domain which included the contiguous U.S., Liang et al (2004) note that the ability of the model to simulate precipitation in the core monsoon region is almost exclusively dependent on the choice of convection scheme. Xu and Small (2002) showed the combined importance of the convection and radiation schemes. By comparing different land surface treatments in the same RCM, Kanamitsu and Mo (2003) found a change soil moisture in Arizona and New Mexico significant enough to alter the large-scale flow, and precipitation, in the Southwest U.S. Given such problems, it is not surprising that various RCM solutions for the same NAMS season can be very different, as seen for example in results from the North American Monsoon Model Assessment Project (Gutzler et al. 2004).

1.3 Relationship of North American Summer Climate to Pacific SSTs

There are numerous observational analyses that suggest a strong connection between North American summer climate and Pacific SSTs. However, there is currently no RCM or regional reanalysis for North America that has a long enough record (longer than twenty years) to diagnose interannual and interdecadal variability on the mesoscale. The main motivation for constructing such a long-term RCM climatology is the earlier study by Castro et al. (2001). Using 50 years of NCEP Reanalysis data, that study showed statistically significant relationships between tropical and north Pacific SSTs, reflecting El Niño Southern Oscillation and the Pacific Decadal Oscillation (PDO; Mantua et al. 1997; Zhang et al. 1997), and the evolution of the monsoon ridge over

North America. This affects the timing of summer rainfall. The strongest relationship to Pacific SSTs occurs at monsoon onset (late June, early July). A positive (negative) phase of ENSO and a positive (negative) PDO phase tend to favor a late (early) onset of the monsoon in the Southwest U.S. and a delayed (accelerated) end to the late spring wet period in the central U.S. The positioning of the monsoon ridge for wet and dry monsoons in the Southwest U.S. is in agreement with Carleton et al. (1990) and Cavazos et al. (2002). These relationships with Pacific SST decay in the latter part of the summer.

Though other observational analyses have typically considered the core monsoon region and central U.S. separately, their conclusions are generally in agreement with Castro et al. (2001). Ting and Wang (1997) showed Great Plains precipitation has two modes of covariation related to ENSO and PDO-associated SST. Hu and Feng (2001) suggest ENSO teleconnections with rainfall in the central U.S. have been modulated by multidecadal variation in north Pacific SST over the last century. With similar century-long datasets, Englehart and Douglas (2002; 2003) demonstrate a link between central U.S. drought and the PDO and show there is a time-dependent nature of large-scale climate modes as the summer evolves. Higgins et al. (1999) found a statistically significant positive (negative) correlation between La Niña (El Niño) and total summer precipitation in southwest Mexico. This is mainly related to a shift in the summer ITCZ (e.g. Hu and Feng 2002). Mo and Paegle (2000) concluded rainfall evolution from winter to summer in the Southwest U.S. is modulated by tropical and north Pacific SSTs and that SSTs in the tropical Pacific are not sufficient to explain observed summer rainfall variability. Higgins and Shi (2001) have related NAMS onset and precipitation in the southwest United States to decade-scale fluctuations in north Pacific SSTs.

The most likely explanation for the connection of North American summer climate to Pacific SST is via a midlatitude atmospheric teleconnection response. The physical mechanism for such a response is discussed, for example, in the idealized modeling experiments by Sardeshmukh and Hoskins (1988), though this specific paper focuses on the boreal winter. Upper level divergence due to anomalous atmospheric heating occurs in the tropics in easterly flow. The anomalous heating would be related to a change in tropical convection forced by changes in SST. The Rossby wave source term (S) in the non-linear vorticity equation may be written as:

$$S = -v_{\chi} \bullet \nabla \zeta - D\zeta . \quad (1.1)$$

In this equation, v_{χ} is the divergent part of the wind, ζ is the vorticity, and D is the divergence. Inclusion of the first term on the right hand side in considering S is key. Advection of the vorticity gradient by the divergent part of the flow creates the effective Rossby wave source in the midlatitudes. The strength of the source, then, depends principally on the strength and sharpness of the westerly jet and not the precise location of the heating anomaly itself.

Idealized modeling studies suggest that the distribution of tropical and midlatitude Pacific SST, and associated diabatic heating patterns, can produce a boreal summer atmospheric teleconnection response as well. Some of these are summarized in Castro et al. (2001), and the most relevant are highlighted. In their study of the 1988 drought, Trenberth and Branstator (1992) demonstrated a connection of height anomalies over North America to a latitudinal variation in the eastern Pacific ITCZ. Lau and Peng (1992) achieved a similar result and concluded the teleconnection response is strongest in June. In addition, they found a single teleconnection response associated with forcing in

the central and west Pacific over a wide range of longitudes, in agreement with the idea that the teleconnection response is relatively insensitive to the longitudinal positioning of the anomalous tropical convection. This latter response is largely responsible for the positioning of the monsoon ridge over North America. Newman and Sardeshmukh (1998) demonstrated height anomalies over western North America have a time-varying sensitivity to Rossby wave forcing in the west Pacific, which is maximized in late spring.

Atmospheric general circulation models (GCMs) have also been employed to investigate boreal summer climate and its relationship to sea surface temperature. Hoerling and Kumar (2003) reproduced the atmospheric circulation conditions associated with the recent 1998-2002 drought in North America by varying SSTs in the tropical Pacific. The combination of warm SSTs in the western tropical Pacific and cold SSTs in the eastern tropical Pacific acted synergistically to produce a robust drought signal in their GCM ensemble. Schubert et al. (2002) specifically tested the hypothesis that variations in the dominant modes of global SST variability produce global teleconnections in boreal summer. They executed boreal summer ensemble simulations with the NASA Seasonal-to-Interannual Prediction Project (NSIPP) GCM forced with the projections of the first and second rotated EOFs of global SST superimposed on climatology for the 1980-99 SST record. These modes are related to two global teleconnection patterns which are symmetric with respect to the equator in both observations and GCM simulations. The first mode, which reflects ENSO, has maximum variance in the tropics, while the second mode has a greater amount of variance in the mid-latitudes of both hemispheres. In a similar and more recent GCM study with the same model, Schubert et al. (2004) have related long-term (greater than 6 year) rainfall

variability in the Great Plains to a pan-Pacific mode in SST and concluded it is the tropical part of the SST anomalies that has the most influence on the extratropical teleconnection.

1.4 Dissertation Overview

The outline for the dissertation is as follows. In Chapter 2 a description of the RCM that is used in these investigations, the Regional Atmospheric Modeling System (RAMS) is presented. This description will include how a new convection scheme (Kain-Fritsch) was implemented into the RCM. In Chapter 3 the value retained and added by dynamical downscaling with RAMS via a series of sensitivity experiments is quantitatively evaluated. In Chapter 4 a summer RCM climatology (1950-2002) using RAMS over the contiguous U.S. and Mexico is evaluated. In Chapter 5 this RCM climatology is used to diagnose the effect of Pacific SST associated teleconnections on North American summer climate. Results are followed by a discussion and summary in each chapter. A general summary, conclusions, and suggestions for future work are given in Chapter 6.

Chapter 2

THE REGIONAL CLIMATE MODEL AND KAIN-FRITSCH SCHEME

2.1 The Regional Atmospheric Modeling System (RAMS)

The LAM used in the experiments to be described in the proceeding chapters is the Regional Atmospheric Modeling System (RAMS), Version 4.3. RAMS was originally developed at Colorado State University to facilitate research into predominately mesoscale and cloud-scale atmospheric phenomena, but has been extended to larger scales over the last decade or so (Cotton et al. 2003). The model is fully three-dimensional, non-hydrostatic; includes telescoping, interactive nested grid capabilities, supports various turbulence closure, short and long wave radiation, initialization, and boundary condition schemes (Pielke 1992). RAMS has demonstrated its utility as a RCM in diagnostic studies for the contiguous U.S., for example, in Eastman et al. (2001), Adegoke et al. (2003), and Liston et al. (2001). Here the RAMS characteristics common to all experiments are described. More specific information particular to each of the experiments, such as model domain size, grid spacing, and soil moisture initialization, will be given the proceeding chapters.

The user-specified model options are chosen appropriate for the use of RAMS as a RCM. The model time step ranges from 30 to 60 s. The turbulent mixing parameterization of Mellor and Yamada (1974) is used to compute the vertical mixing

coefficients. A modified Smagorinsky (1963) deformation-based scheme is used to compute the horizontal mixing coefficient (or diffusion), per grid point defined as:

$$K_i = \rho_o \max \left[K_{mh}, (C_x \Delta x)^2 S_2^{0.5} \right] \quad (2.1)$$

where ρ_o is the basic state air density, Δx is the model grid spacing, C_x is a user-specified dimensionless coefficient to obtain a characteristic horizontal mixing length scale, and S_2 is the horizontal strain rate (a function of the horizontal winds). K_{mh} is a lower limit on the horizontal diffusion according to the empirical formula:

$$K_{mh} = 0.075 K_A \left(\Delta x^{4/3} \right) \quad (2.2)$$

where K_A is a user-defined parameter.

Surface fluxes of heat and moisture are represented through the LEAF-2 (Land Ecosystem Feedback) land-surface model (Walko et al. 2000). For the dynamical downscaling sensitivity experiments in Chapter 3, either the Kuo scheme (Kuo 1974; Molinari 1985) or Kain-Fritsch scheme (Kain 2004) are used to simulate convective rainfall and there is no representation of non-convective rainfall. The radiation scheme in Chapter 3 experiments is that of Mahrer and Pielke (1977). For the North American summer RCM climatology (Chapters 4 and 5), the Kain-Fritsch scheme is used to simulate convective rainfall and non-convective rainfall is simulated by a simple dumpbucket scheme which considers the supersaturation of an air parcel. The Kain-Fritsch scheme has demonstrated superior performance in representation of North American warm season precipitation in RCM sensitivity experiments with other models (Gochis et al. 2002; Gochis et al. 2003; Liang et al. 2004). The radiation scheme for the RCM climatology is that of Chen and Cotton (1983, 1987).

Unless otherwise specified, the surface boundary is prescribed with RAMS products available on-line from the Atmet Corporation (<http://www.atmet.com>). This includes USGS topography at 30 minute resolution, variable soil type according to U.N. Food and Agriculture (FAO) data, and Olson Global Ecosystem (OGE) vegetation datasets. Sea surface temperatures are from Reynolds and Smith (1994) and are updated monthly. The model is initialized and updated at the lateral boundaries by the NCEP-NCAR Reanalysis (Kalnay et al. 1996) at 6h intervals at regular analysis times. There are three nudging points at the lateral boundaries. Lateral boundary nudging is according to the form of Davies (1976). This common technique in LAMs is summarized by Laprise (2003). The model variables are nudged to the large-scale forcing data over a sponge zone of grid points, and the e-folding time varies from a short time scale near the boundary to an infinite value beyond the sponge zone. The version of RAMS used here also has a simple four-dimensional data assimilation option to nudge the interior prognostic variables of wind, temperature, pressure (Exner function), and water vapor at a user-specified timescale. Weak interior nudging at a one-day timescale is used for the North American summer RCM climatology, as it is exactly what is done in operational numerical weather forecasts with RAMS in South America (P. Silva Dias, personal communication). Additional justification for its use will be discussed in Chapter 3.

2.2. The Kain-Fritsch Cumulus Parameterization Scheme in RAMS

The original version of RAMS 4.3 did not incorporate the Kain-Fritsch cumulus parameterization code (Kain 2004). The following description thoroughly describes code as implemented in the RAMS model. The physical variables, significant levels and

identifiers, and physical constants relevant to the following description are given in Tables 2.1, 2.2, and 2.3, respectively.

2.2.1 RAMS-Kain Fritsch Interface

3-D grid point variables are converted to 1-D column variables to exchange with the Kain-Fritsch column module. As part of this conversion, the Exner function must be converted to pressure.

$$p = p_0 \left(\frac{\Pi + \Pi'}{c_p} \right)^{\frac{c_p}{R_d}} \quad (2.3)$$

The dry and moist static energy terms are computed for the column.

$$s = c_p T + gz \quad (2.4)$$

$$h = c_p T + gz + L_v q \quad (2.5)$$

Convection is initiated for the following conditions:

- If there is sinking motion in the lowest 200-mb, a superadiabatic layer is required in the lowest 400-mb
- If there is upward motion, conditional instability is required in the lowest 400-mb

If convection is initiated, then the scheme returns temperature and moisture tendency terms. The temperature tendency must be converted to a θ_{il} tendency. Since explicit treatment of microphysics is not activated, the scheme evaporates or sublimates all liquid and solid water. Only the water vapor tendency term is fed back to RAMS. The θ_{il} tendency is:

Variable	Description	Units
p	Pressure	Pa
θ_{il}	Ice-liquid potential temperature	K
θ	Potential temperature	K
θ_e	Equivalent Potential Temperature	K
T	Temperature	K
T_v	Virtual Temperature	K
q	Water vapor mixing ratio	kg kg ⁻¹
q_{liq}	Liquid water mixing ratio	kg kg ⁻¹
q_{sol}	Solid water mixing ratio	kg kg ⁻¹
q_{liqnew}	Liquid water mixing ratio of new liquid condensate generated in convective updraft	kg kg ⁻¹
q_{solnew}	Solid water mixing ratio of new ice condensate generated in convective updraft	kg kg ⁻¹
$q_{out_{liq}}$	Mixing ratio of liquid precipitation generated in updraft	kg kg ⁻¹
$q_{out_{sol}}$	Mixing ratio of solid precipitation generated in updraft	kg kg ⁻¹
w	Vertical motion	m s ⁻¹
w_{slope}	Vertical motion reduction parameter which incorporates the horizontal components of the contravariant velocity	m s ⁻¹
z	Model height	m
z_g	Terrain height	m
B	Buoyancy	m ² s ⁻²
UMF	Updraft mass flux	kg s ⁻¹
DMF	Downdraft mass flux	kg s ⁻¹
E	Entrainment	kg s ⁻¹
D	Detrainment	kg s ⁻¹
ρ	Density of air	kg m ⁻³
r	Updraft/downdraft radius	m
P_{drag}	Coefficient which represents the effect of precipitation drag on updraft vertical velocity	
R_{in}	Rate of environmental inflow used to determine updraft entrainment and detrainment rates	kg s ⁻¹
$Efrac_{up}$	Environmental updraft entrainment fraction	
$Dfrac_{up}$	Environmental updraft detrainment fraction	
P	Precipitation generated at given model level	kg s ⁻¹
$EVAP$	Evaporation at given model level in downdraft	kg s ⁻¹

Table 2.1: Physical variables used in the description of the Kain-Fritsch cumulus parameterization scheme.

D_{liq}	Detrainment rate of liquid water mixing ratio	kg m
D_{sol}	Detrainment rate of solid water mixing ratio	kg m
u	Zonal velocity	$m s^{-1}$
v	Meridional velocity	$m s^{-1}$
$Timec$	Convective time scale	s
V	Total horizontal velocity	$m s^{-1}$
$Peff$	Precipitation efficiency	
RH	Relative humidity	
TKE	Turbulent kinetic energy	$m^2 s^{-2}$
Fxm	Compensating mass flux	kg m
$fxin$	Compensating mass flux of a given variable x into a layer	$kg s^{-1}$ (dim x)
$fxout$	Compensating mass flux of a given variable x out of a layer	$kg s^{-1}$ (dim x)
$DDinc$	Downdraft adjustment parameter	
$Ainc$	Mass flux increase parameter	
$CAPE$	Convective available potential energy	$m^2 s^{-2}$ ($J kg^{-1}$)
$CAPE_{mod}$	Convective available potential energy after parameterized convective process completed	$m^2 s^{-2}$ ($J kg^{-1}$)
Rt_3	Fraction of liquid water in “fresh” condensate	
Rt_4	Fraction of liquid water in the total amount of condensate involved in the precipitation process.	
s	Dry static energy	$m^2 s^{-2}$
h	Moist static energy	$m^2 s^{-2}$
NCA	Integer counter for number of model time steps convection is activated	
Π	Exner function	$J kg^{-1} K^{-1}$

Table 2.1: continued.

Identifier	Significance
<i>USL</i>	Updraft source layer
<i>LCL</i>	Lifting condensation level
<i>ENV</i>	Environmental variable not associated with updraft or downdraft properties
<i>k</i>	Model level
<i>up</i>	Updraft property
<i>down</i>	Downdraft property
<i>LFS</i>	Level of free sink
<i>CT</i>	Cloud top
<i>CB</i>	Cloud base
<i>EL</i>	Equilibrium level
<i>s</i>	Surface
<i>T</i>	Model top

Table 2.2: Significant levels and identifiers used in the description of the Kain-Fritsch cumulus parameterization scheme.

Constant	Description	Value
<i>g</i>	Gravitational acceleration	9.8 m s^{-2}
<i>R_d</i>	Dry gas constant	$287 \text{ J K}^{-1} \text{ kg}^{-1}$
<i>p₀</i>	Reference pressure	1000 mb
<i>c_p</i>	Specific heat at constant pressure	$1004 \text{ J K}^{-1} \text{ kg}^{-1}$
<i>L_v</i>	Latent heat of vaporization for water	$\sim 2.5 \times 10^6$ (varies with <i>T</i>)
<i>L_f</i>	Latent heat of fusion for water	$\sim 3.3 \times 10^5$ (varies with <i>T</i>)

Table 2.3: Physical constants used in the description of the Kain-Fritsch cumulus parameterization scheme.

$$\frac{d\theta_{il}}{dt} = \left(\frac{p_o}{p}\right)^{R_d/c_p} \left(\frac{-TR_d}{c_p p} \frac{dp}{dt} + \frac{dT}{dt} \right) \quad (2.6)$$

Convection is maintained for a given number of model time steps as computed by the Kain-Fritsch scheme (see *NCA* variable computed later in the scheme). If convection is still active on a grid cell the next time the convection scheme is called, the preceding steps are skipped. The value of *NCA* (see equation 2.36) is reduced by one per model time step. The complete tendency terms for heating and moisture terms are updated and the convective precipitation is accumulated.

2.2.2 Updraft Source Layer and Convective Trigger

To start the Kain-Fritsch scheme, a vertical sounding is input to the column module. A pressure interval (15-mb) is specified to move up in sequential check of different 50-mb deep groups of adjacent model layers in the process of identifying an updraft source layer (*USL*). The search is terminated as soon as a buoyant parcel is found and this parcel can produce a cloud greater than a specified minimum depth (between 2000 and 4000 m, positively dependent on temperature). The temperature and moisture characteristics of each layer are mass weighted. The height of the lifting condensation level (*LCL*) is determined from the thermodynamic characteristics of the parcel lifted from the *USL*. Environmental temperature and moisture at the *LCL* are estimated.

An empirical expression for a temperature perturbation at the *LCL* is required as part of the convective trigger function. In the original Kain-Fristch scheme:

$$\Delta T_{LCL} = 4.64 w_{ENV}^{1/3} \quad (2.7)$$

where w_{ENV} is a positive (upward) vertical velocity from RAMS at the grid point. For RAMS, this formulation gave very large values of precipitation in areas of steep and elevated terrain. If the formulation for w_{LCL} includes an additional (reduction) factor, this problem can be alleviated. The following criteria were used to define and test the performance of the reduction factor in RAMS:

- Includes physical parameters related the problem, in this case the terrain slope.
- The expression should be physically intuitive and mathematically simple as possible.
- The expression should be made continuous as possible, to prevent “steps” in the trigger function.
- The solution should be tuned and tested for actual model use for a wide variety of grid spacing and locations.

The reduction factor (w_{slope}) is a modification of the horizontal component of the contravariant vertical velocity (e.g. Pielke 2002). A good first guess would be:

$$w_{slope} \propto u \left(\frac{\frac{dz_g}{dx} \left(1 - \frac{z - z_g}{z_T} \right)}{1 - \frac{z_g}{z_T}} \right) + v \left(\frac{\frac{dz_g}{dx} \left(1 - \frac{z - z_g}{z_T} \right)}{1 - \frac{z_g}{z_T}} \right). \quad (2.8)$$

However, because the cube root of vertical velocity is used in the actual trigger function formulation, the terrain associated terms should be cubed.

$$w_{slope} \propto u \left(\frac{\frac{dz_g}{dx} \left(1 - \frac{z - z_g}{z_T} \right)}{1 - \frac{z_g}{z_T}} \right)^3 + v \left(\frac{\frac{dz_g}{dx} \left(1 - \frac{z - z_g}{z_T} \right)}{1 - \frac{z_g}{z_T}} \right)^3. \quad (2.9)$$

For surface pressure greater than 900-mb, w_{slope} is reduced to zero over the range of 900 to 950-mb. w_{slope} is set to zero if negative, so it can never increase the value of the temperature perturbation at the *LCL*. The expression for the temperature perturbation at the *LCL* for a positive vertical motion is:

$$\Delta T_{LCL} = 4.64(w_{ENV} - w_{slope})^{1/3}. \quad (2.10)$$

And for negative vertical motion:

$$\Delta T_{LCL} = 4.64(-w_{slope})^{1/3}. \quad (2.11)$$

Note that a negative value of ΔT_{LCL} can exist if w_{slope} is sufficiently large enough or if w_{ENV} is less than zero. A tuning coefficient is necessary for w_{slope} and it may be changed by the model user if so desired or entirely shut off.

Convection is triggered if the following condition is satisfied:

$$\Delta T_{LCL} + T_{LCL} > T_{ENV}. \quad (2.12)$$

An updraft equivalent potential temperature is computed from the thermodynamic properties of the *USL*. This will be used later by subroutine TPMIX2 in the updraft model. The buoyancy of the updraft at the *LCL* is:

$$B_{LCL} = g\Delta T_{LCL} \frac{z_{LCL} - z_{USL}}{Tv_{USL} - Tv_{ENV}}. \quad (2.13)$$

The original formulation for updraft vertical motion at the *LCL* is (for positive B_{LCL}):

$$w_{up(LCL)} = 1 + 0.5B_{LCL}^{1/2}. \quad (2.14)$$

For RAMS, if the elevation is greater than 1500 m, then

$$w_{up(LCL)} = 0.5B_{LCL}^{1/2}. \quad (2.15)$$

If B_{LCL} is negative, then $w_{up(LCL)}$ is set to either 1 or 0, depending on the elevation.

Dependent on the strength of the net vertical motion term in ΔT_{LCL} , an updraft radius (r)

is specified, ranging from 1000 to 2000 m. This represents the horizontal extent of the updraft area in a (parameterized) cloud.

2.2.3 Kain-Fritsch Updraft Model

The initial strength of the updraft is given by $w_{up(LCL)}$ and its associated updraft mass flux (UMF) is:

$$UMF_{LCL} \propto \pi \rho_{LCL} r^2 . \quad (2.16)$$

The updraft model scheme loops from the LCL to the top of the model, computing the updraft mass flux, updraft entrainment and detrainment rates, liquid and ice phases of water, and precipitation generated at each level.

Within the updraft loop, subroutine TPMIX2 determines if there is enough liquid or ice to saturate the parcel. If the parcel is supersaturated, then the vapor is condensed to form “new” liquid water or ice (q_{newliq} or q_{newsol}). Otherwise, if there is enough liquid or ice to saturate the parcel, the temperature stays at its wet bulb value, the vapor mixing ratio is at saturation, and the mixing ratios of liquid and ice are adjusted to make up the original saturation deficit. If there is not enough liquid/ice to saturate the parcel, any available liquid or ice vaporizes and appropriate adjustments to the parcel temperature, water vapor, and liquid and ice mixing ratios are made. A check is made to see if the updraft temperature is above the temperature at which glaciation is assumed to initiate (268.16 K). If so, a fraction of liquid water to freeze is calculated. If the temperature is less than 248.16 K, then all liquid water is frozen. The new thermodynamic properties of the column due to the effects of freezing are calculated in subroutine DTFRZNEW. The virtual temperature of the updraft is computed:

$$Tv_{up} = T_{up} (1 + 0.608q_{up}). \quad (2.17)$$

A buoyancy (B) term is calculated at a given model level k :

$$B = 2g\Delta z \frac{Tv_{up}}{Tv_{ENV}}. \quad (2.18)$$

Precipitation generated in the updraft is determined in subroutine CONDLOAD.

Two ratios are defined:

- Rt_3 : Fraction of liquid water in “fresh” condensate, generated by subroutine TPMIX2.
- Rt_4 : Fraction of liquid water in the total amount of condensate involved in the precipitation process. Only 60% of the fresh condensate is allowed to participate in the conversion process. Note that this assumed value will affect the updraft calculations and grid generated precipitation.

The mixing ratio of liquid precipitation generated at the given model level is:

$$qout_{liq} = Rt_4 \left((q_{liq} + q_{sol}) - (q_{liq} + q_{sol}) \exp \left(-0.03 \frac{\Delta z}{w_{up}} \right) \right) \quad (2.19)$$

The mixing ratio of solid precipitation generated at the given model level is:

$$qout_{sol} = (1 - Rt_4) \left((q_{liq} + q_{sol}) - (q_{liq} + q_{sol}) \exp \left(-0.03 \frac{\Delta z}{w_{up}} \right) \right) \quad (2.20)$$

The effect of drag from the liquid and solid water phases on the vertical motion of the updraft is:

$$P_{drag} = 0.5 \left((q_{liq} + q_{sol}) + (q_{liq} + q_{sol}) \exp \left(-0.03 \frac{\Delta z}{w_{up}} \right) - 0.2(q_{newliq} + q_{newsol}) \right) \quad (2.21)$$

The updated vertical motion of the updraft parcel is then calculated, modified by the effects of buoyancy, updraft entrainment (see equation 2.28), and total condensate:

$$w_{up}^2 = w_{up}^2 + B - 2E_{up} \frac{w_{up}^2}{UMF} - 1.33g\Delta z(P_{drag}) \quad (2.22)$$

The updated values of liquid and ice water mixing ratios are:

$$q_{liq} = Rt_4(q_{liq} + q_{sol}) \exp\left(-0.03 \frac{\Delta z}{w_{up}}\right) + Rt_3(q_{newliq} + q_{newsol}) \quad (2.23)$$

$$q_{sol} = (1 - Rt_4)(q_{liq} + q_{sol}) \exp\left(-0.03 \frac{\Delta z}{w_{up}}\right) + 0.4(1 - Rt_3)(q_{newliq} + q_{newsol}) \quad (2.24)$$

The updated values in equations 2.22-2.24 are passed from CONDLOAD back to the updraft loop. If w_{up} is less than zero, cloud top (*CT*) is defined at this point and the updraft calculations are finalized.

A value of equivalent potential temperature to entrain in the updraft is calculated from the thermodynamic properties of the environment. The rate of environmental inflow (R_{in}) is given by

$$R_{in} \propto \frac{UMF_{LCL}\Delta p}{r}. \quad (2.25)$$

A new updraft virtual temperature is defined which takes into account liquid and ice phases:

$$Tv_{up} = T_{up} (1 + 0.608q_{up} - q_{liq} - q_{sol}). \quad (2.26)$$

The convective available potential energy (CAPE) at each model level k is:

$$CAPE = \left(\frac{T_{v_{up}}}{T_{v_{ENV}}} - 1 \right) g \Delta z. \quad (2.27)$$

The total CAPE is computed by summing the CAPE from each model level during the updraft calculations. If $T_{v_{up}} < T_{ENV}$, then cloud parcels are virtually colder than the environment and minimal entrainment is imposed. This point defines the equilibrium level (*EL*) of the cloud. The fractions of entrained ($Efrac_{up}$) and detrained ($Dfrac_{up}$) air are set to 0.5 and 1.0, respectively. Otherwise, a critical mixed fraction of updraft and environmental air is determined by the thermodynamic characteristics of the updraft parcel and environment. Based on the value of the critical mixed fraction, $Efrac_{up}$ and $Dfrac_{up}$ are determined. The particular thresholds and equations in the code are omitted here. The updraft entrainment and detrainment rates at the given model level are:

$$E_{up} = R_{in} Efrac_{up} \quad (2.28)$$

$$D_{up} = R_{in} Dfrac_{up}. \quad (2.29)$$

If the detrainment rate is greater than the updraft mass flux at the given model level, then all cloud mass detrains and updraft calculations are completed.

The updraft mass flux at the given model level (k) is a function of the updraft mass flux at the previous model level ($k-1$) and detrainment and entrainment:

$$UMF_k = UMF_{k-1} - D_{up} + E_{up}. \quad (2.30)$$

The detrainment rates of liquid and ice are:

$$D_{liq} = q_{liq} D_{up}. \quad (2.31)$$

$$D_{sol} = q_{sol} D_{up} \quad (2.32)$$

The updated water vapor mixing ratio, liquid water mixing ratio, and ice mixing ratios are:

$$q_{up} = \frac{UMF_{k-1}q_{up} - D_{up}q_{up} + E_{up}q_{ENV}}{UMF_k} \quad (2.33)$$

$$q_{liq} = q_{liq} \frac{UMF_{k-1} - D_{up}}{UMF_k} \quad (2.34)$$

$$q_{sol} = q_{sol} \frac{UMF_{k-1} - D_{up}}{UMF_k}. \quad (2.35)$$

The precipitation generated at the given model level is:

$$P = q_{out_{liq}}UMF + q_{out_{sol}}UMF. \quad (2.36)$$

The total updraft-generated precipitation is calculated as the sum of precipitation generated at each model level. This ends the updraft loop calculations.

After the updraft calculations are finished, the updraft mass flux above the equilibrium level must still be accounted for. If the equilibrium level and the cloud top are the same, then all mass detrains and the updraft mass flux and entrainment rates are equal to zero. Otherwise the updraft mass flux decreases linearly as a function of the pressure difference between the equilibrium level and cloud top. Below cloud base, the updraft mass flux and updraft entrainment are a function of UMF_{LCL} divided by the pressure depth of the USL . All updraft variables above cloud top are set to zero.

The convective timescale (Δt_c), which determines how long convective precipitation persists at a grid point, is a function of the horizontal wind at the LCL and 500-mb and the model grid spacing (Δx).

$$\Delta t_c = \frac{\Delta x}{V_{LCL} + V_{500}} \quad (2.37)$$

The convective timescale is permitted to range between 1800 and 3600 s (30 minutes to an hour). The number of model time steps that convection persists at a grid point (NCA) is:

$$NCA = \frac{\Delta t_c}{\Delta t}. \quad (2.38)$$

2.2.4 Kain-Fritsch Downdraft Model

Precipitation efficiency ($Peff$) is defined to be a function of wind shear and height of cloud base. The wind shear velocity is computed as

$$V_{shear} = \pm \frac{\sqrt{(u_T - u_{LCL})^2 - (v_T - v_{LCL})^2}}{z_T - z_{LCL}} \quad (2.39)$$

V_{shear} is positive (negative) if the wind at the model top is greater (less) than the wind at the LCL . The precipitation efficiency due to wind shear is based on Fritsch-Chappell's efficiency equation:

$$Peff_{shear} = 1.591 + V_{shear} \left(-0.639 + V_{shear} (0.0953 - 0.00496 V_{shear}) \right) \quad (2.40)$$

The same equation also appears in the Kuo scheme in RAMS. $Peff_{shear}$ is allowed to vary between 0.2 and 0.9.

The cloud base height (z_{CB}) is difference between the height of the LCL and surface. If z_{CB} is between approximately 1000 m and 7500 m the precipitation efficiency due to cloud base height is given by a similar empirical equation with fifth order dependence on z_{CB} (omitted here). The precipitation efficiency due to cloud base height ($Peff_{CBH}$) ranges from 0.9 to 1. $Peff_{shear}$ and $Peff_{CBH}$ are averaged to compute $Peff$. It should be noted in actual fact the precipitation efficiency additionally varies with mid-tropospheric humidity and presence of solid water species.

Within the downdraft loop, the level of free sink (*LFS*) at which the downdraft starts is assumed to be at least 150-mb above cloud base. At the *LFS* subroutine TPMIX2DD is called to determine wet bulb temperature and water vapor mixing ratio at the *LFS*. Downdraft thermodynamic properties at the *LFS* are computed. The initial downdraft mass flux at the *LFS*:

$$DMF_{LFS} \propto -(1 - Peff)\pi\rho_{LFS}r^2. \quad (2.41)$$

The downdraft entrainment rate (E_{down}) is a function of DMF_{LFS} . There is no downdraft detrainment while still in the cloud. Integrating downward to cloud base, at each model level:

$$E_{down} = DMF_{LFS} \frac{\Delta p}{\Delta p_{LFS}} \quad (2.42)$$

and

$$DMF = E_{down} + DMF_{k+1}. \quad (2.43)$$

Downdraft θ_e and downdraft q are adjusted to account for entrainment of environmental air. For example:

$$q_{down(k)} = \frac{q_{down(k+1)}DMF_{k+1} + q_{ENV(k)}E_{down(k)}}{DMF_k}. \quad (2.44)$$

A pressure weighted average relative humidity (\overline{RH}) is calculated through the downdraft layer from the *LFS* to the *LCL*.

If the source level of the updraft parcel is below the melting level, then all solid phase precipitation (P_{sol}) in the column is melted.

$$P_{melt} = \frac{L_f P_{sol}}{c_p UMF_{LCL}}. \quad (2.45)$$

New thermodynamic properties of the downdraft at the *LCL* are computed accounting for the conversion from ice to liquid phase.

Integrating from the *LCL* to the surface θ_{edown} and q_{down} are set to their values at the *LCL*. The wet-bulb temperature and saturation vapor mixing ratio ($q_{satdown}$) are defined for each model level in the downdraft. For these calculations, the relative humidity is assumed to decrease 20% per km in the downdraft from the *LCL*. If the downdraft virtual temperature exceeds that of the environment, the parcel is neutrally buoyant and that level is where the downdraft stops sinking. From the *LCL* to the level of downdraft neutral buoyancy, no downdraft entrainment is assumed, so at each model level:

$$D_{down} = -DMF_{LCL} \frac{\Delta p}{\Delta p_{LFS}} \quad (2.46)$$

$$DMF = D_{down} + DMF_{k+1}. \quad (2.47)$$

The parcel evaporates water on its decent from the *LCL* to the level of neutral buoyancy. At each model level this evaporated water is equal to the difference between the downdraft saturation water vapor mixing ratio and the downdraft water vapor mixing ratio multiplied by the downdraft detrainment rate:

$$EVAP = (q_{satdown} - q_{down})D_{down}. \quad (2.48)$$

If no evaporation occurs, a downdraft is not allowed and the downdraft properties for the entire column are set to zero. Otherwise a downdraft adjustment factor is calculated which incorporates the average relative humidity:

$$DDinc \propto -\left(1 - \overline{RH}\right) \frac{UMF_{LCL}}{DMF_{LCL}}. \quad (2.49)$$

The downdraft mass flux, entrainment, and detrainment rates are multiplied by $DDinc$ from the LFS to the level of downdraft neutral buoyancy. The precipitation calculated in the updraft model is reduced by the amount of evaporation that occurs in the downdraft, so:

$$P = P - EVAP. \quad (2.50)$$

This ends the downdraft loop calculations.

RAMS includes the shallow convection option for Kain-Fritsch, which modifies the updraft and downdraft properties, evaporation, and precipitation as a function of the turbulent kinetic energy (TKE) at the grid point. Shallow convection occurs when the integrated CAPE (equation 2.27) does not exceed a value of $1 \text{ m}^2 \text{ s}^{-2}$ (J kg^{-1}). The shallow convection modification factor is:

$$Ainc_{shallow} \propto \frac{TKE(\Delta p_{USL} \Delta x^2)}{\pi g \rho_{LCL} r^2 \Delta t_c}. \quad (2.51)$$

2.2.5 Compensational Subsidence and Final Outputs

Compensating vertical motion must exist to satisfy mass continuity. At each model level through the depth of the column this compensating mass flux is:

$$Fxm = E_{up} - E_{down} - D_{up} - D_{down}. \quad (2.52)$$

Compensating terms for q and θ are computed at a given model level, from the surface to the model top. If the compensating mass flux is negative, there is flux into the layer and flux out of the preceding layer:

$$\begin{aligned}\theta_{fxin_k} &= -Fxm_k \theta_{ENV(k-1)} \\ q_{fxin_k} &= -Fxm_k q_{ENV(k-1)}\end{aligned}\tag{2.53}$$

$$\begin{aligned}\theta_{fxout_{k-1}} &= \theta_{fxout_{k-1}} + \theta_{fxin_k} \\ q_{fxout_{k-1}} &= q_{fxout_{k-1}} + q_{fxin_k}\end{aligned}$$

And for positive compensating mass flux, there is flux out of the layer and flux into the preceding layer:

$$\begin{aligned}\theta_{fxout_k} &= Fxm_k \theta_{ENV(k)} \\ q_{fxout_k} &= Fxm_k q_{ENV(k)}\end{aligned}\tag{2.54}$$

$$\begin{aligned}\theta_{fxin_{k-1}} &= \theta_{fxin_{k-1}} + \theta_{fxout_k} \\ q_{fxin_{k-1}} &= q_{fxin_{k-1}} + q_{fxout_k}.\end{aligned}$$

The final θ and q values in each layer incorporate the mass flux correction terms in equations 2.53 and 2.54. For example, for θ :

$$\theta = \theta_{ENV} + \left(\theta_{fxin_k} + D_{up} \theta_{up} + D_{down} \theta_{down} - \theta_{fxout_k} - E_{up} \theta_{ENV} + E_{down} \theta_{ENV} \right) \frac{g \Delta t_c^*}{\Delta p \Delta x^2}.\tag{2.55}$$

where Δt_c^* is the convective timescale modified by the magnitude of compensating mass flux. There are checks to see if the final mixing ratio dips below zero at any model layer, and if so moisture is borrowed from adjacent layers to bring it back up above zero. θ is then converted back to a virtual temperature.

Using the updated thermodynamic profile which accounts for effects of parameterized convection, a new lifting condensation level and convective available potential energy ($CAPE_{mod}$) are computed in an identical manner to that in equation 2.27. If $CAPE_{mod}$ is greater than 10% of the original $CAPE$ computed in the updraft model,

then the mass flux variables, downdraft evaporation, and precipitation are increased by a factor:

$$Ainc = \frac{CAPE(\Delta p \Delta x^2)}{g(E_{up} - E_{down})(CAPE - CAPE_{mod})}. \quad (2.56)$$

Hydrometeors are redistributed in the same manner as q and θ in equation 2.55 based on the sign of Fxm . These feed back the detrained values of liquid and solid water to RAMS, updating their original values (q_{liqENV} and q_{solENV}) if microphysics are activated.

$$q_{liq} = q_{liqENV} + (q_{liqENV} fxin_k + D_{liq} - q_{liqENV} fxout_k) \frac{g\Delta t_c^*}{\Delta p \Delta x^2} \quad (2.57)$$

$$q_{sol} = q_{solENV} + (q_{solENV} fxin_k + D_{sol} - q_{solENV} fxout_k) \frac{g\Delta t_c^*}{\Delta p \Delta x^2}. \quad (2.58)$$

There are also options to feed back a (user-specified) percentage of convectively generated liquid and solid precipitation to back to the large-scale precipitation. However, this option is not used for the simulations described in subsequent chapters because no explicit treatment of microphysics is considered.

There is an error check to verify that the final total water amount in the column that remains unprecipitated is less than the initial total water amount. If this condition fails the entire model stops. For RAMS, if microphysics options are not activated, then all of the detrained liquid and ice water is evaporated or sublimated, so the temperature and water vapor mixing ratio at each model level are:

$$T = T - \frac{L_c q_{liq} + L_f q_{sol}}{c_p} \quad (2.59)$$

$$q = q + q_{liq} + q_{ice}. \quad (2.60)$$

And the temperature and moisture tendencies that are fed back to RAMS are:

$$\frac{dT}{dt} = \frac{T - T_{ENV}}{\Delta t_c} \quad (2.61)$$

$$\frac{dq}{dt} = \frac{q - q_{ENV}}{\Delta t_c}. \quad (2.62)$$

The final rainfall rate fed back to RAMS is P divided by the area of a grid cell (Δx^2).

Chapter 3

DYNAMICAL DOWNSCALING: ASSESSEMENT OF VALUE RETAINED AND ADDED USING RAMS

3.1 Description of Basic Dynamical Downscaling Sensitivity Experiments

The objective in this chapter is to quantitatively evaluate the value retained and value added in dynamical downscaling with RAMS by considering the spectral behavior of the model solution in relation to its domain size and grid spacing. The results of these sensitivity experiments will prove helpful in the RCM design for the North American summer climatology in the next chapter. Two domain sizes are used in the model sensitivity experiments (Fig. 3.1). The month of May 1993 is simulated because it is a time of vigorous synoptic wave activity associated with large scale flooding over the central U.S. (e.g. Bell and Janowiak 1995). The first domain covers all of the contiguous U.S. and is similar to a typical numerical weather forecast domain used operationally for the WRF and ETA models at the National Center for Environmental Prediction and National Severe Storms Laboratory. The second domains covers almost the entire western half of the Northern Hemisphere. A summary of the domain information and relative computational expense is shown in Table 3.2.

Each domain is run for a horizontal grid spacing corresponding to 200, 100, and 50 km for a total of six runs which comprise the basic set of experiments. Aside of the grid spacing and domain size, all the other conditions in RAMS are uniform. Thirty vertical

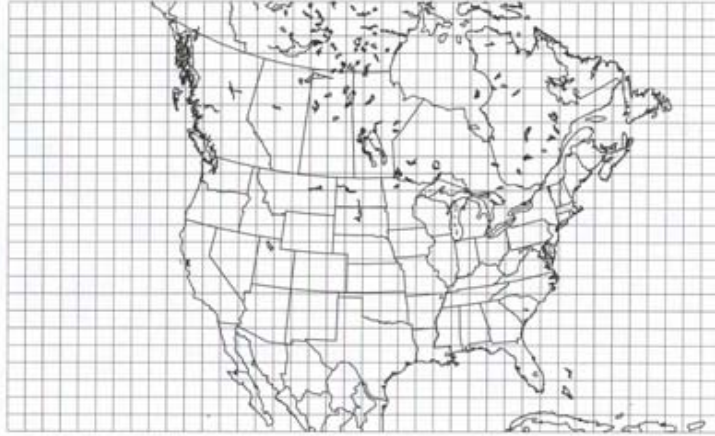


Figure 3.1: RAMS domains for model sensitivity experiments in this chapter for $\Delta x = 200$ km.

<u>Symbol</u>	<u>Meaning</u>
$a_{i,j}$	RCM variable
$a_{i,j}^N$	Detrended RCM variable
$c_{p,q}$	Spectral coefficient of given detrended atmospheric model variable as function of zonal and meridional wavenumber
C_x	User-specified coefficient to obtain a characteristic horizontal mixing length scale
$Ek_{i,j}$	Column average total kinetic energy
\overline{Ek}	Domain-averaged total kinetic energy
I	Subscript for x-dimension of reduced RCM grid
J	Subscript for y-dimension of reduced RCM grid
K	Wavenumber
k_{\max}^*	Maximum physically resolved wavenumber of NCEP reanalysis
$k_{Nyquist}$	Nyquist wavenumber of RCM
$k_{Nyquist}^*$	Nyquist wavenumber of NCEP reanalysis
Δk	Minimum wavenumber for a given RCM grid spacing
K_A	User-specified parameter used in computing lower limit of horizontal mixing coefficient
K_i	Horizontal mixing (diffusion) coefficient
N_I	Maximum x-dimension of reduced RCM grid
N_J	Maximum y-dimension of reduced RCM grid
P	Subscript for zonal wavenumber
Q	Subscript for meridional wavenumber
S_2	Horizontal strain rate
$S(k)_{obs}$	Spectral power per wavenumber of regridded reanalysis
$S(k)_{mod}$	Spectral power per wavenumber of RCM simulation
$\Delta S(k)_{frac}$	Fractional change in spectral power per wavenumber
Δx	RCM grid spacing
λ	Wavelength
ρ_o	Basic state air density
$\overline{\sigma}_{EK}^2$	Domain-averaged kinetic energy variance

Table 3.1: Commonly used symbols in this chapter.

Basic Experiment	Δx (km)	Domain	RCM Grid Dimensions	Computational Increase
1	200	Small	40 × 25	1
2	100	Small	80 × 50	3.5
3	50	Small	160 × 100	15.2
4	200	Large	80 × 50	3.5
5	100	Large	160 × 100	15.2
6	50	Large	320 × 200	62.8

Table 3.2: Model domain specifications and computational increase for the six basic experiments. The computational increase is computed as the time to complete one model timestep for the given domain divided by that for the basic experiment #1.

levels are used with a maximum vertical grid spacing of 1000 m and a minimum vertical grid spacing of 100 m with a vertical stretch ratio of 1.2. The soil type (sandy clay loam) is uniform for all land areas and the model is initialized with homogeneous soil moisture at 50% field capacity. No internal nudging issued for the first set of basic experiments in Section 3.4. The nudging timescale and other user-specified parameters are held constant according to suggested values in the RAMS Users Guide (<http://www.atmet.com/html/documentation.shtml>). The choice of user-defined parameters and parameterization options could be varied to see if the results from the present investigation would possibly change. However, the intent here is to demonstrate the characteristics of the basic RAMS model “off the shelf” without any adjustment to suggested user specifications. Additional experiments which investigate the influence of surface boundary and interior nudging are described in Section 3.5.

Data were saved twice per day at 0 UTC and 12 UTC. To determine how model variables differ from the “perfect” reanalysis model as time proceeds, the reanalysis data were vertically and horizontally interpolated to RAMS grid each day at 0 UTC and 12 UTC for all the model simulations. The RAMS regridded reanalysis are treated as the “observed” NCEP reanalysis on the given LAM grid. While this procedure may introduce errors into what is considered “perfect observations” (R. Walko, personal communication), the regridded reanalysis is very consistent with the reanalysis itself, particularly for larger-scale features. Any difference between the model output and regridded reanalysis less than the smallest wavelength resolved by the reanalysis, then, is due to the physics of the RAMS model. The “physics” refers to the dynamical core of the model and the model parameterization schemes. As in de Elía et al. (2002), to eliminate possible spurious values at the model lateral boundaries, the three outermost grid points were first removed from the raw model grid. The reduced grid of $N_I \times N_J$ defines the grid used henceforth in the analyses.

3.2 Two-Dimensional Spectral Analysis of Model Variables

There are various methods to determine the power spectra of an atmospheric variable ($a_{i,j}$) within a LAM domain. As summarized by Laprise (2003), the earliest and most straightforward method is that of Errico (1985) which uses a double Fourier series after removing a linear trend in each direction. Other approaches which also remove a trend in the RCM domain include those of Tatsumi (1986) and Chen and Kuo (1992). Denis et al. (2002) recently used double cosine transforms to spectrally analyze LAM fields without subtracting any component. Errico’s (1985) method is chosen here for its

simplicity. The caveats of this method are discussed for example in Denis et al. (2002). Detrending removes the large-scale gradient across the LAM domain, which may affect the large-scale components of the spectrum. A spurious pattern of lines may appear in the detrended data, as shown, for example, in Figure 3 from Denis et al. (2002). Finally, the technique should not be used for fields which are noisier at the boundaries than in the LAM interior.

Errico's (1985) method to determine the power spectra of $(a_{i,j})$ within the LAM domain with constant grid spacing and dimension $N_I \times N_J$ is described. To remove the partially resolved spatial variability of waves beyond the scale of the domain, the data are linearly detrended along constant i,j . For example, for each j , the slope is determined:

$$s_j = \frac{a_{N_I,j} - a_{1,j}}{N_I - 1}. \quad (3.1)$$

For each i,j the linear trend in the I direction is removed:

$$a'_{i,j} = a_{i,j} - \frac{1}{2}(2i - N_I - 1)s_j. \quad (3.2)$$

An identical procedure is completed with i and j reversed in (1) and (2) and with $a'_{i,j}$ replacing $a_{i,j}$ in (2). The result is a detrended field $a_{i,j}^N$. The spectral coefficients $(c_{p,q})$ of $a_{i,j}^N$ are determined by the discrete two-dimensional Fourier transform:

$$c_{p,q} = \frac{1}{(N_I - 1)(N_J - 1)} \sum_{j=1}^{N_J - 1} \sum_{i=1}^{N_I - 1} a_{i,j}^N e^{\sqrt{-1}\Delta x \varpi} \quad (3.3)$$

$$\varpi = p(i - 1) + q(j - 1). \quad (3.4)$$

where p and q represent zonal and meridional wavenumbers with discrete values:

$$p = \frac{2\pi l}{\Delta x} \frac{1}{N_I - 1} \quad l = 0, \pm 1, \dots, \pm \frac{N_I}{2} \quad (3.5)$$

$$q = \frac{2\pi l}{\Delta x} \frac{1}{N_J - 1} \quad l = 0, \pm 1, \dots, \pm \frac{N_J}{2} \quad (3.6)$$

The one-dimensional power spectrum (in k space) is given by:

$$S(k) = \sum c_{p,q} c_{p,q}^* \quad (3.7)$$

where $c_{p,q}^*$ is the complex conjugate of $c_{p,q}$. The one-dimensional wave number (k) is:

$$k = (p^2 + q^2)^{1/2}. \quad (3.8)$$

Successive values of k are evenly spaced in wavenumber space by the minimum wavenumber (Δk), which is defined by the minimum fundamental wavenumber of p and q :

$$k - \frac{1}{2} \Delta k < (p^2 + q^2)^{1/2} < k + \frac{1}{2} \Delta k. \quad (3.9)$$

The maximum wavenumber is defined by the Nyquist wavenumber of the grid:

$$k_{Nyquist} = \frac{\pi}{\Delta x}. \quad (3.10)$$

When the reanalysis data are interpolated to the RAMS oblique polar stereographic (rectangular) grid, the maximum resolved wavenumber in Cartesian space will slightly decrease with decreasing latitude. For reference, the Nyquist wavenumber of the reanalysis here is nominally defined as its minimum possible value on the globe, which occurs at the equator:

$$k_{Nyquist}^* = 1.13 \times 10^{-5} \text{ m}^{-1}.$$

This corresponds to a minimum resolved wavelength (λ) of approximately 550 km. Some atmospheric modeling texts, though, suggest that the minimum wavelength that has meaningful representation in a discrete model is not $2\Delta x$, but at least $4\Delta x$ (Pielke 2002). Using this definition, the wavenumber of physically resolved waves in the reanalysis is likely:

$$k_{\max}^* = 5.65 \times 10^{-6} \text{ m}^{-1}$$

corresponding to a maximum wavelength of approximately 1100 km. This differentiation between $k_{Nyquist}^*$ and k_{\max}^* will prove helpful in explaining the behavior of model spectra in the proceeding sections. Henceforth, k_{\max}^* will also be used as the separation point between what is referred to as “large” ($k < k_{\max}^*$) and “small” scale ($k > k_{\max}^*$).

3.3 Model Variables Analyzed

Two atmospheric model variables ($a_{i,j}$) are analyzed using the methodology of just described: 1) the column average total kinetic energy ($Ek_{i,j}$), and 2) the column integrated moisture flux convergence ($MFC_{i,j}$). There are two a priori reasons for selecting these particular atmospheric variables. First, they are good diagnostic measures of the energy and moisture budgets, respectively, within the model. Second, each variable reflects different scales of atmospheric behavior. The integrated kinetic energy is principally a function of large-scale winds at upper-levels (less than 500-mb) and so should be relatively insensitive to surface forcing. MFC, on the other hand, should be more sensitive to surface boundary forcing since water vapor rapidly decreases upward. MFC

is a good proxy for rainfall and low-level vertical motion. Additionally, in spring and summer MFC on a continental scale in North America is related to a topographically-forced diurnal cycle (see Chapter 4). This a priori physical understanding of the two atmospheric fields being analyzed is critical in explaining their spectral behavior in the RAMS simulations. The model generated precipitation is also analyzed and compared to observations. As a surface field, precipitation is considered because it is one of the best observed quantities to validate RCM performance and a principle diagnostic variable used in RCM studies.

The column-average total kinetic energy is computed using a stepwise integration downward through the column, divided by the pressure depth of the (model) atmosphere.

For each i,j point:

$$Ek_{i,j} = \frac{1}{g(p_s - p_{Top})} \int_{p_{Top}}^{p_s} \frac{1}{2} (u^2 + v^2 + w^2) dp \quad (3.11)$$

Where p_s is surface pressure, p_{Top} is the pressure at the highest vertical level, and u,v , and w correspond to the zonal, meridional, and vertical wind, respectively. The domain-averaged total kinetic energy is then:

$$\overline{Ek} = \frac{\sum_{j=1}^{N_j} \sum_{i=1}^{N_I} Ek_{i,j}}{N_I N_j} . \quad (3.12)$$

Similarly, the column integrated moisture flux convergence for each i,j point is:

$$MFC_{i,j} = -\frac{1}{g} \int_{p_{Top}}^{p_s} \nabla \cdot (q\bar{v}) dp . \quad (3.13)$$

It is important to note that these fields are computed as a post-processing step after the model simulations are completed. None of the model variables used in the

computation of kinetic energy or MFC exhibits variability at the boundary that is significantly different from the interior, so the two dimensional 2-D spectral analysis procedure is justified. While the same cannot perhaps be said of precipitation, the spectral analysis for that field is also justified because the area analyzed (the contiguous U.S.) for this variable is well within the RCM interior. The results for precipitation spectra, as will be shown later, are also physically reasonable.

Once the spectrum of a given variable is computed for a particular analysis time, it is smoothed using a three-point weighted filter. This smoothing is necessary to reduce noise before comparison with different spectra. To compare the spectral power per wavenumber of the reanalysis assimilation $S(k)_{obs}$ to the model simulation $S(k)_{mod}$, the fractional change in spectral power per wavenumber is computed at each analysis time as:

$$\Delta S(k)_{frac} = \frac{S(k)_{mod}}{S(k)_{obs}} - 1. \quad (3.14)$$

Results are presented in terms of this ratio averaged over the thirty (twice-daily) analysis times for the last fifteen days of simulation, rather than the actual spectra themselves. It is important to note that only the latter part of the simulation is analyzed, to avoid any spin-up issues and ensure the model is in a RCM mode. If the model simulation has, on average, more variability than the regridded reanalysis for a given wavenumber, the ratio will be positive, and vice versa. If $\Delta S(k)_{frac}$ is less than zero for a given value of k , then RAMS does not add any variability to $a_{i,j}$ beyond the NCEP reanalysis. For experiments described in Section 3.5, in which one model simulation (mod_1) is compared to a second model simulation (mod_2) the formulation for $\Delta S(k)_{frac}$ is:

$$\Delta S(k)_{frac} = \frac{S(k)_{mod_1}}{S(k)_{mod_2}} - 1. \quad (3.15)$$

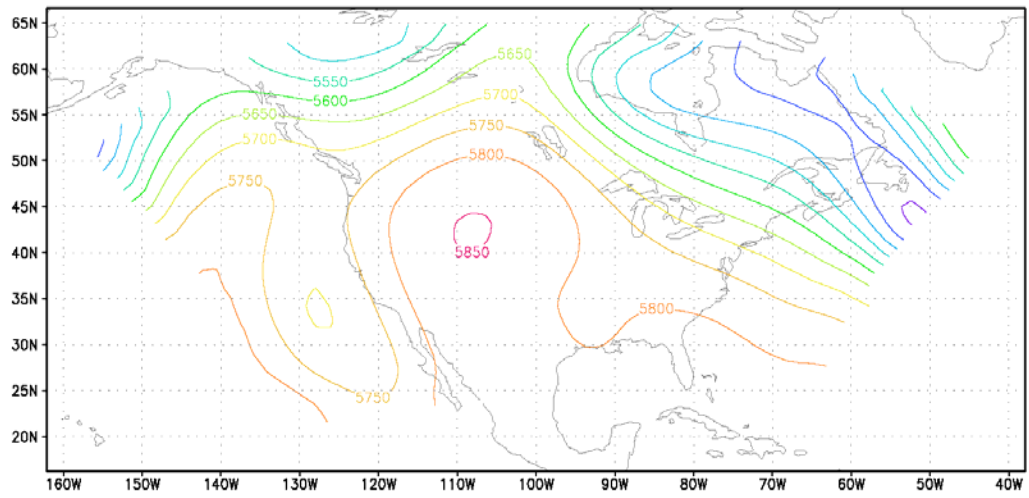
This second formulation is useful to determine if surface information is adding value for $k > k_{max}^*$, in the absence of observed mesoscale data to validate the model against. The model spectra of precipitation are also compared directly to the corresponding NCEP observations (regridded to the RAMS model grid) in Section 3.5, in which case:

$$\Delta S(k)_{frac} = \frac{S(k)_{precip_{RAMS}}}{S(k)_{precip_{NCEP}}} - 1. \quad (3.16)$$

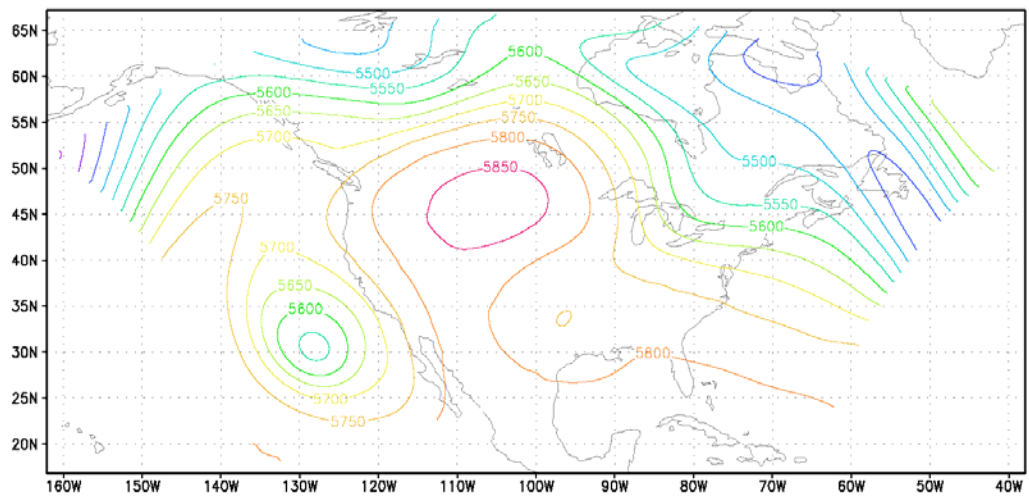
The results for $\Delta S(k)_{frac}$ are presented in the proceeding sections on a logarithmic (base 10) scale with the corresponding wavelength scale (in m) also displayed on the plots. $\Delta S(k)_{frac}$ may appear more noisy at smaller scales, and this is expected because 1) the spectrum is more highly resolved in physical space and 2) the ratio is emphasizing very small differences between two spectra at high wavenumbers and very large differences at low wavenumbers.

3.4 Results for Basic Experiments

A sample model-simulated day with a highly amplified 500-mb height field (Fig. 3.2) is selected. This particular day is twelve days from model initialization, and it is generally illustrative of what the RAMS model produces in a Type 2 downscaling mode absent internal nudging. Significant synoptic features apparent in reanalysis observations

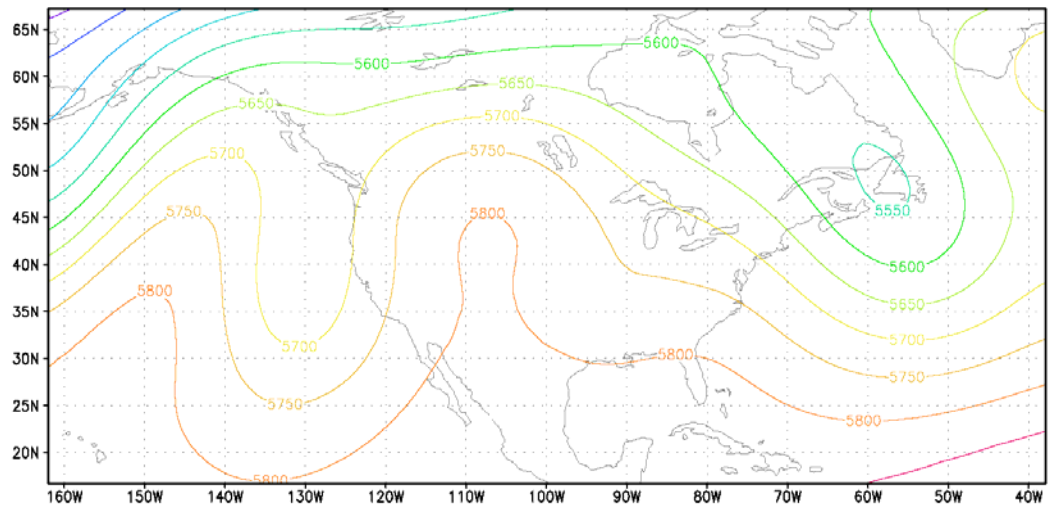


(a)

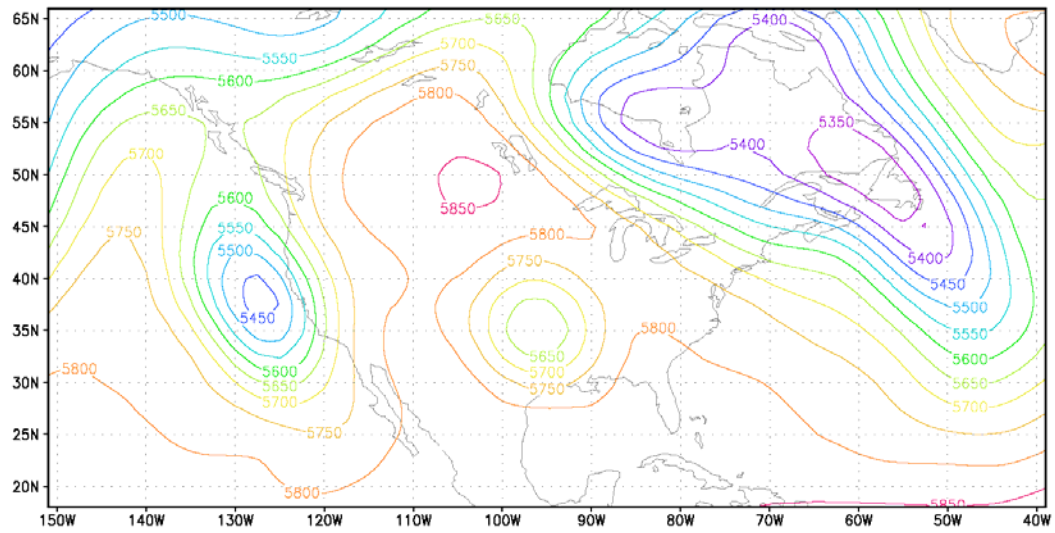


(b)

Figure 3.2: Observed 500-mb height (m) on 0Z UTC, 12 May 1993, for a) basic experiment 1, b) basic experiment 3, c) basic experiment 4, and d) NCEP Reanalysis.



(c)



(d)

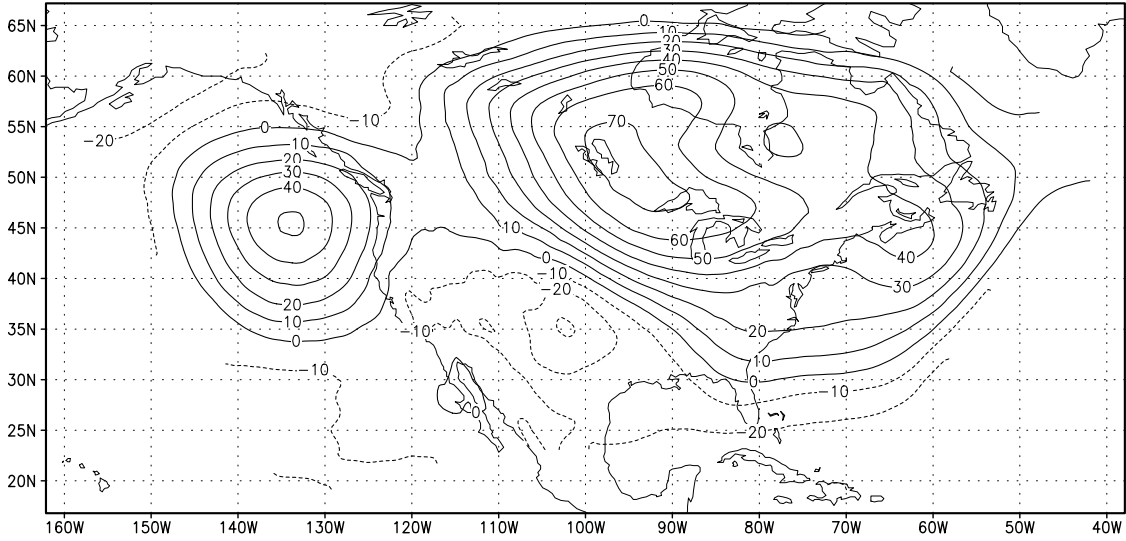
Figure 3.2: Continued

are not present in the model simulations. For example, the ridge in the central U.S. is too far south and west, and the cutoff lows off the California coast and in the central U.S. are not as strong or appear as open waves. The height field degrades with increased domain size. Such errors leads to significant differences in representation of surface fields, such as precipitation (see next section). Even with the smallest domain and 50 km grid spacing, the highly amplified features are not as defined as they are in the reanalysis.

To illustrate this loss of variability in 500-mb height further, Fig. 3.3 shows the average error in 500-mb height for the last fifteen days of simulation for the three model domain sizes corresponding to Fig. 3.2. The errors progressively worsen as both grid spacing increase and domain size increase, exceeding 120 m in the central North Pacific for the large 200 km domain. The greatest underestimation of mean 500-mb height occurs in regions of low pressure troughs, such as off the west coast of North America and Europe, and the semi-permanent trough near Hudson Bay. These observations indicate that RAMS is not correctly retaining value of the large-scale as given by the NCEP reanalysis. A very similar result was found by Jones et al. (1995) downscaling GCM data over Europe, particularly for a large RCM domain.

$\Delta S(k)_{frac}$ averaged over the last fifteen days of simulation is shown for kinetic energy and MFC for the small domain (basic experiments 1-3) in Fig. 3.4. As previously mentioned, k in Fig. 3.4 is presented on a logarithmic scale. k_{max}^* and $k_{Nyquist}^*$ are indicated with dashed and solid lines, respectively, for reference. There are two a priori expectations for behavior of $\Delta S(k)_{frac}$ with respect to k . First, the regional model should correctly retain value of the variability of kinetic energy and MFC present in the reanalysis data. Thus, in the region $k < k_{max}^*$ $\Delta S(k)_{frac}$ should be near zero. Second,

Small Domain: 50 km



Small Domain: 200km

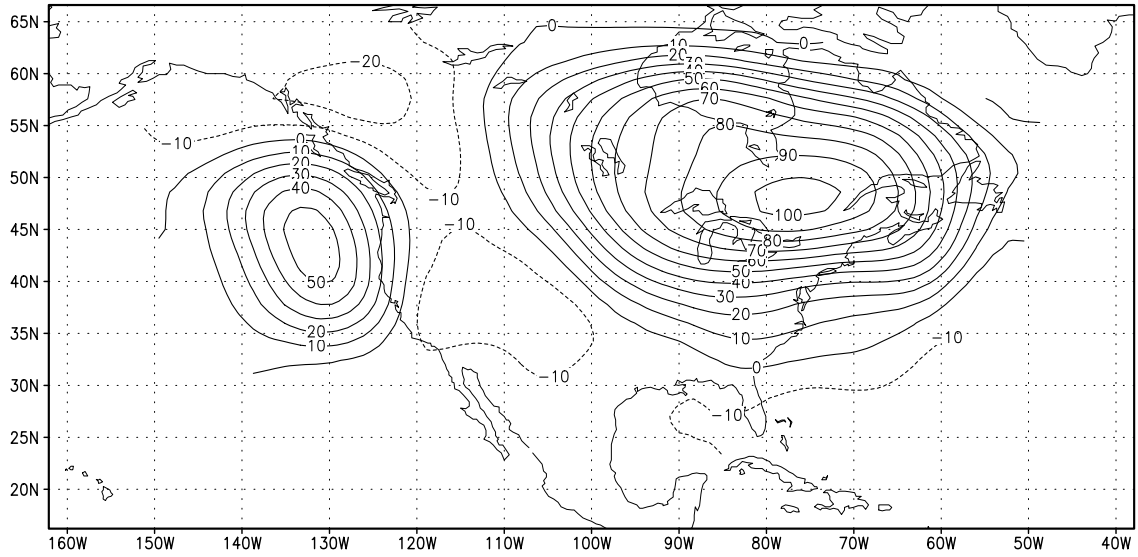


Figure 3.3: Average error in RAMS-simulated 500-mb height (m) for the given model domain constraints (last fifteen days of simulation). Contour interval is 10 m.

Large Domain: 200 km

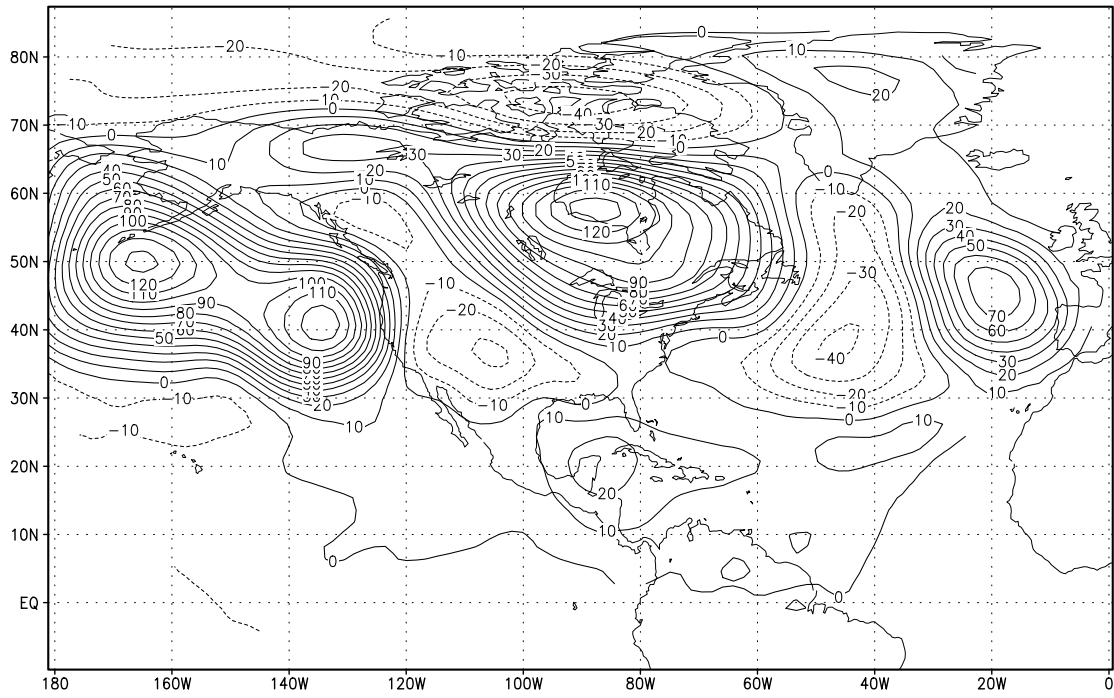


Figure 3.3: continued

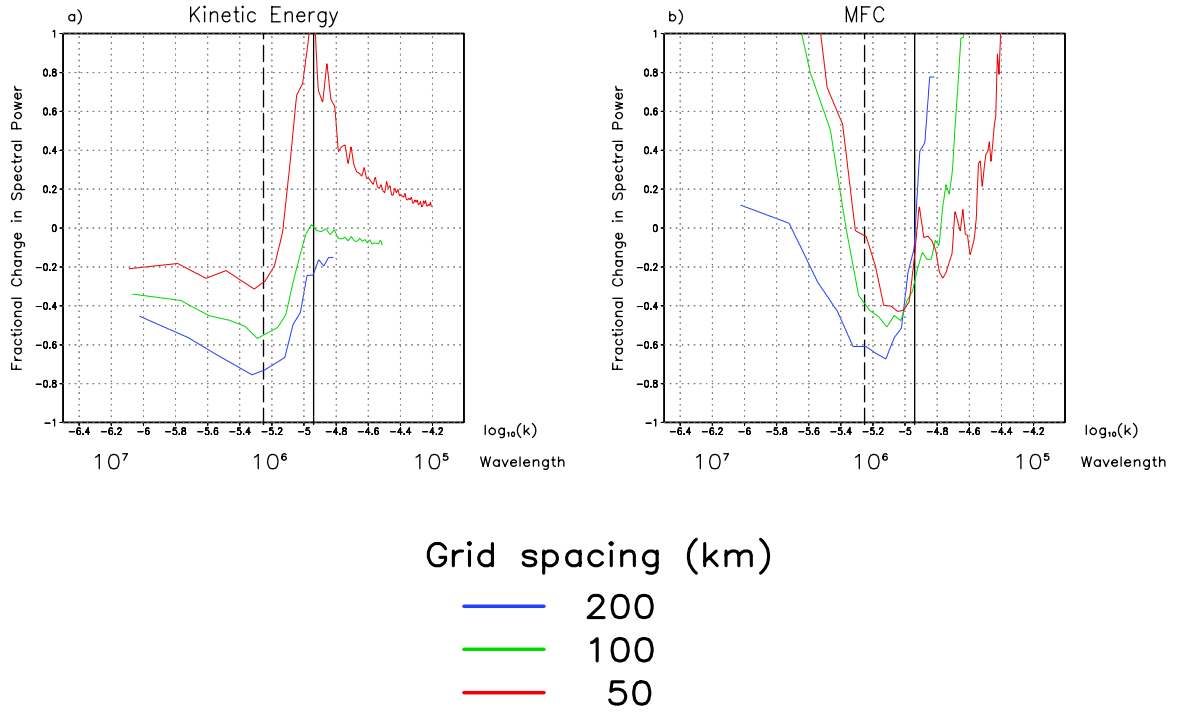


Figure 3.4: Fractional change in spectral power ($\Delta S(k)_{frac}$) versus $\log_{10}(k)$ and wavelength, small domain experiments for a) column-average total kinetic energy and b) column integrated moisture flux convergence (MFC). The dashed black line indicates k_{max}^* and the solid black line $k_{Nyquist}^*$. k in units of m^{-1} . Wavelength in units of m.

though there is likely some aliasing of the reanalysis data to larger wavenumbers, the regridded reanalysis ($S(k)_{obs}$) should have rapidly decreasing spectral power from k_{max}^* to $k_{Nyquist}^*$ and little or no spectral power for $k > k_{Nyquist}^*$. It should then be expected that $\Delta S(k)_{frac}$ should always be greater than zero in the region $k > k_{Nyquist}^*$. It is in the region $k < k_{max}^*$ where $\Delta S(k)_{frac}$ is more physically meaningful. Dissipation of kinetic energy in nature occurs at wavenumbers greater than $k_{Nyquist}^*$ and so the value of $\Delta S(k)_{frac}$ at the large scale (low wavenumbers) is due entirely to the physics of the RCM.

For kinetic energy (Fig. 3.4a), several characteristic behaviors of $\Delta S(k)_{frac}$ are independent of grid spacing. For wavenumbers below k_{max}^* ($\lambda > 1100$ km), the model underestimates the spectral power and does not retain value of the large scale. The greatest underestimation appears to be at k_{max}^* itself. This affects the development of baroclinic waves in the model, which was apparent from Fig. 3.2. Then, as k increases towards $k_{Nyquist}^*$ and beyond, there is an increase in spectral power of the RCM compared to the regridded reanalysis. This makes sense given the a priori assumption for behavior of regridded reanalysis spectra. The increase could be due to either forcing from the surface boundary or local hydrodynamic instabilities. For the 50 km simulation, as k increases RAMS begins to add value to kinetic energy ($\Delta S(k)_{frac} > 0$) at a point between k_{max}^* and $k_{Nyquist}^*$ and continues to add value thereafter. Similar behavior is also observed for MFC as k increases (Fig. 3.4b), with a low value of $\Delta S(k)_{frac}$ near k_{max}^* and an increase near $k_{Nyquist}^*$ and beyond.

Changes in the grid spacing and domain size also have characteristic responses in $\Delta S(k)_{frac}$. As grid spacing increases, $\Delta S(k)_{frac}$ decreases for $k < k_{max}^*$. For the 200 km or 100 km grid spacing small domain run (basic experiments 1 and 2), $\Delta S(k)_{frac}$ for kinetic energy does not exceed zero for any value of k . Though it should be expected that $\Delta S(k)_{frac}$ to be greater than zero beyond $k_{Nyquist}^*$, it is not for the larger domains. In these cases RAMS is not adding any information beyond the noise present in the regridded reanalysis. The same general behavior is also observed for MFC (Fig. 3.4b). $\Delta S(k)_{frac}$ does exceed zero for the very largest of scales, though much of the variability of MFC and rainfall occurs at smaller scales. The larger domain (kinetic energy shown in Fig. 3.5) exhibits identical behavior as the small domain, except that the loss in $\Delta S(k)_{frac}$ at large scales, with the exception of the 200 km grid spacing simulation, is worse than for the corresponding small domain experiments at the same grid spacing. The underestimation of variability at larger scales dramatically affects how the RCM adds value at the smaller scale ($k > k_{max}^*$), and this will be shown for RCM-generated precipitation in the next section.

The time evolution of the fraction of model simulated to regridded reanalysis domain averaged total kinetic energy (\overline{Ek}) is shown in Fig. 3.6 for the six basic experiments. \overline{Ek} should be very well reflected by the regridded reanalysis since, as mentioned, it mostly reflects the upper-level horizontal winds at scales large scales. Regardless of grid spacing or grid size, the ratio of model simulated to regridded reanalysis \overline{Ek} in all of the simulations decreases in time, on average. It is closer to the model kinetic energy at certain times when the flow is more zonal. This decrease is

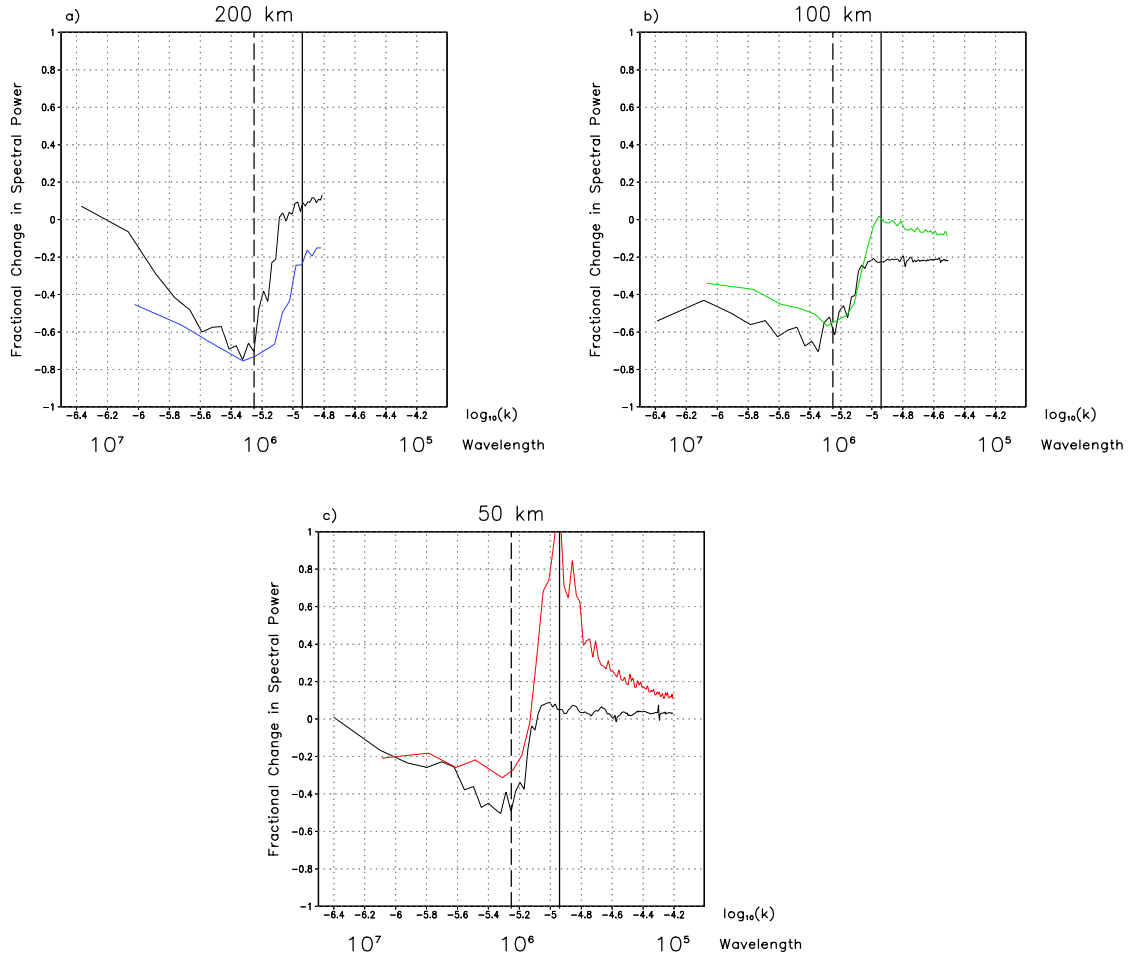


Figure 3.5: Fractional change in spectral power ($\Delta S(k)_{frac}$) versus $\log_{10}(k)$ for column average total kinetic energy, small and large domain experiments: a) $\Delta x = 200$ km, b) $\Delta x = 100$ km, and c) $\Delta x = 50$ km. Small domain experiments color coded as in Fig. 3.4 and large domain experiments shown as corresponding solid black curve. The dashed black line indicates k_{max}^* and the solid black line $k_{Nyquist}^*$. k in units of m^{-1} . Wavelength in units of m.

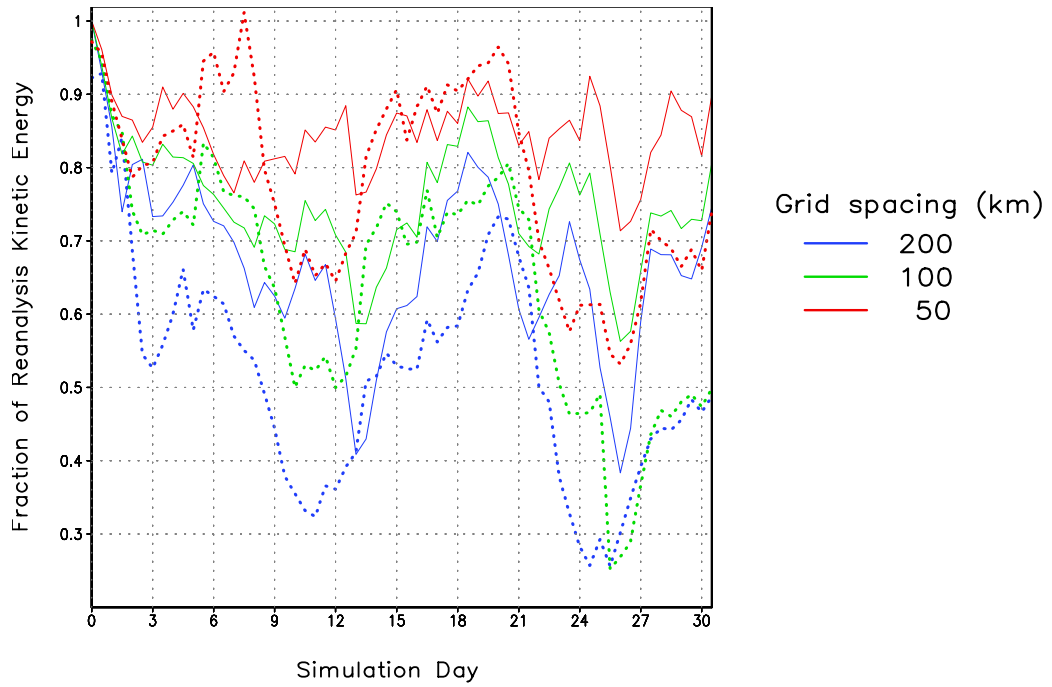


Figure 3.6: Time evolution of the fraction of model simulated to reanalysis regridded domain-averaged total kinetic energy for the six basic experiments on equivalent grids. The small domain is indicated by a solid curve, and the large domain is indicated by a dashed curve.

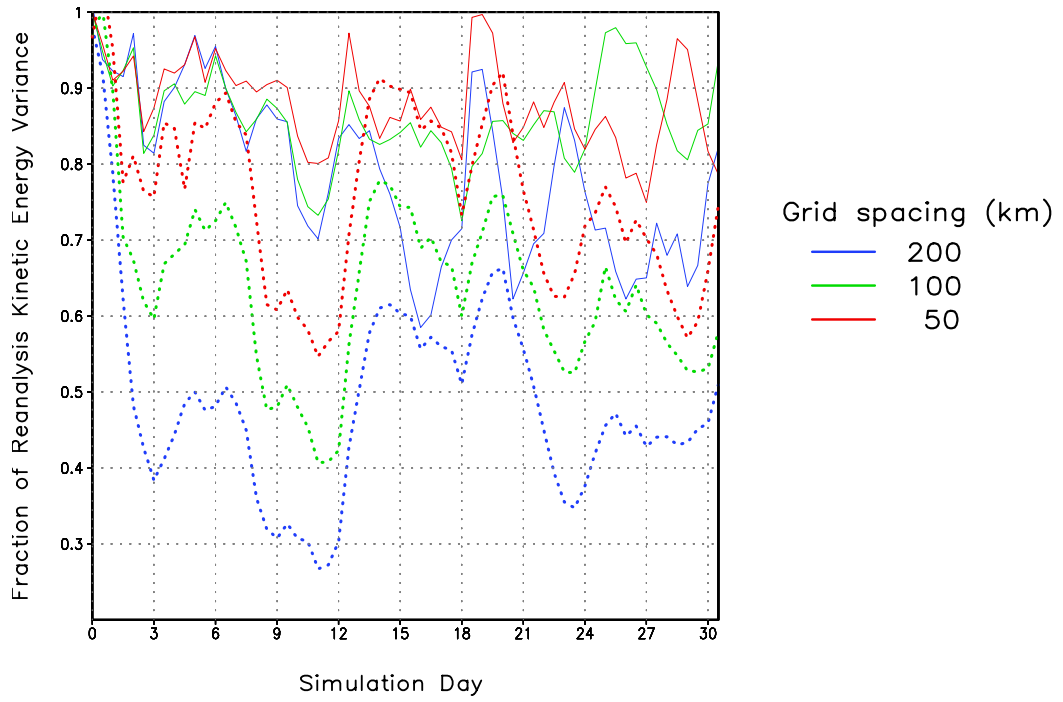


Figure 3.7: Same as Fig. 3.6 for model domain-averaged kinetic energy variance.

particularly pronounced during approximately the first few days of RCM simulation, then gradually levels off. For the small grid, 50 km grid spacing simulation (basic experiment 3), approximately 85% of the regridded reanalysis \overline{Ek} is preserved after 30 days of simulation, but over 30% is lost for the 200 km grid spacing simulation (basic experiment 1) . As the grid spacing for the small domain increases, the loss of kinetic energy worsens more so than for the larger domain. Shown also in Fig. 3.6 are the same results for the area of the large domain within the small domain (dotted curves). Considering the same area in all the simulations, the loss in kinetic energy also worsens with increased domain size. For the 200 km grid spacing large domain, the model underestimates the observed kinetic energy by nearly 50% after thirty days of simulation. The reasons for this loss in kinetic energy, and solutions to alleviate it, will be discussed in Section 3.6.

Additionally, Fig. 3.7 shows the time evolution of the fraction of model simulated to reanalysis regridded domain-average kinetic energy variance ($\overline{\sigma}_{EK}^2$). It is very similar to Fig. 3.6. The model underestimates $\overline{\sigma}_{EK}^2$ for all grid spacings. In general, as the domain size gets larger and the grid spacing increases, the underestimation of $\overline{\sigma}_{EK}^2$ worsens, though there are specific days that are exceptions. In a mean sense, this underestimation also worsens as time proceeds, irrespective of grid spacing or domain size. The periods where $\overline{\sigma}_{EK}^2$ is most underestimated are times where the synoptic pattern is highly amplified; it is better estimated at times of more zonal flow. At the end of the simulation period, $\overline{\sigma}_{EK}^2$ is underestimated by the model in the range of approximately 10-30% for the small domain. A similar result is shown by von Storch et al. (2000) considering the meridional winds simulated by the regional climate model REMO with only lateral boundary forcing (their Fig. 5).

3.5 Results for Follow-on Experiments

Four additional follow-on experiments were performed to investigate the effect of internal nudging (Follow-on 1); a larger grid (Follow-on 2); a change in the convective parameterization (Follow-on 3); and a homogeneous surface boundary (Follow-on 4). These were performed using the grid of basic experiment 3 (50 km, small domain) because that maintained the best fidelity with the reanalysis. In Follow-on 1, weak internal nudging on a one-day timescale was activated. To put this in perspective, according to the *RAMS Users Guide*, internal nudging at an hourly timescale corresponds to “very strong nudging.” The *RAMS Users Guide* recommends an internal nudging timescale of two to four hours for the typical RAMS simulation with a short-term model integration (less than a day), multiple nested grids, and explicit treatment of microphysics. In Follow-on 2, the model domain of the smaller grid is extracted from the larger one in basic experiment 6. Follow-on 3 uses the Kain-Fritsch (KF) convection scheme (with an unadjusted convective trigger), in lieu of the Kuo scheme, with and without internal nudging. In Follow-on 4, the model was run using flat topography, a constant sea surface temperature (295 K), a single vegetation type (mixed cropland), and a single soil type (sandy clay loam). This experiment serves as a control run to see how the characteristic behavior of $\Delta S(k)_{frac}$ is influenced by the variable surface boundary, principally the topography. These additional experiments are designed to assess the value added by RAMS for small scales ($k > k_{max}^*$).

For Follow-on experiments 1-3 we use equation 3.15 for computation of $\Delta S(k)_{frac}$, where mod_1 is the follow-on experiment and mod_2 corresponds with basic experiment 3. Since we are now comparing model to model results for, $\Delta S(k)_{frac}$ is

physically meaningful for all k , even greater than k_{\max}^* . A positive value of $\Delta S(k)_{frac}$ in this case means the model generated variability is greater than the basic experiment, and vice versa.

The monthly average difference in 500-mb height from observations for Follow-on 1 (internal nudging) is shown in Fig. 3.8. Compared to basic experiment 3 shown in Fig. 3.3 earlier, the same pattern of error appears, but the magnitudes are less. This shows internal nudging, as would be expected, is improving the model representation of the large scale. $\Delta S(k)_{frac}$ for kinetic energy and MFC are shown for Follow-on 1 in Fig. 3.9. With internal nudging activated, variability of kinetic energy wavenumbers less than k_{\max}^* does improve, and, therefore, lessens the loss in kinetic energy with time as observed in Fig. 3.6. There is still some loss of kinetic energy compared to the reanalysis, but it is not as large as that for the no-nudge case shown in Fig. 3.4. However, by imposing a strong constraint on the interior of the domain, the variability of kinetic energy is decreased for wavenumbers greater than k_{\max}^* . For MFC, $\Delta S(k)_{frac}$ is negative for all k . The decrease in variability at high wavenumbers means that the small-scale features are diminished in strength when internal nudging is activated. In their work with RAMS, Weaver et al. (2002) similarly found internal nudging weakened mesoscale motions and lead to stronger turbulence in a shallower boundary layer. For example, Fig. 3.10 shows the comparison values of monthly precipitation for the small domains using lateral boundary nudging only and with interior nudging on the small domain. In the nudged run, precipitation throughout the domain is reduced, particularly in the central and eastern U.S. Fig. 3.10 also shows the precipitation for Follow-on 2 and Follow on 4,

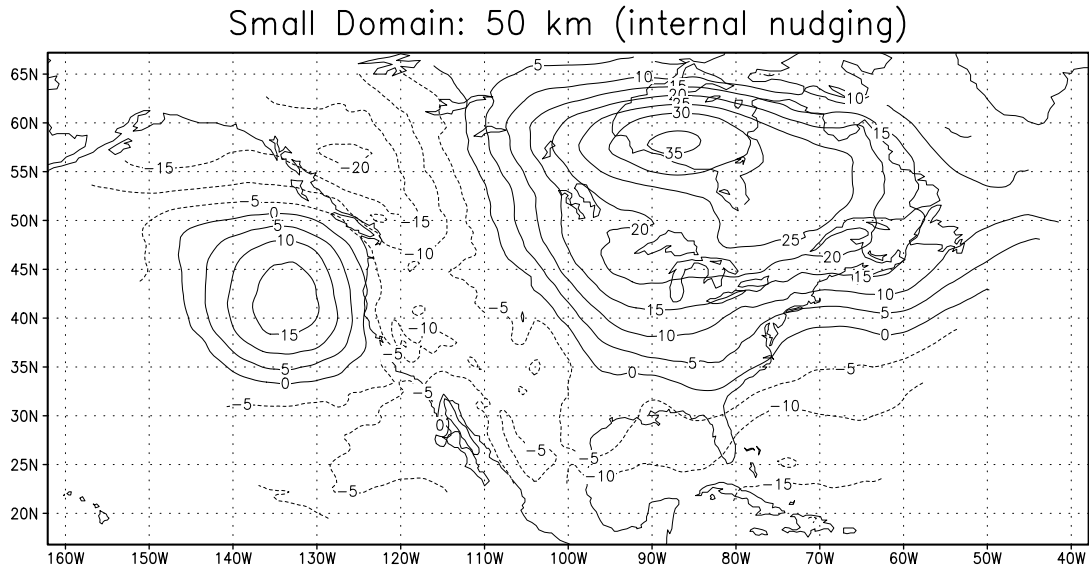


Figure 3.8: Same as Fig. 3.3 for Follow-on 1 (internal nudging). Contour interval is 5 m.

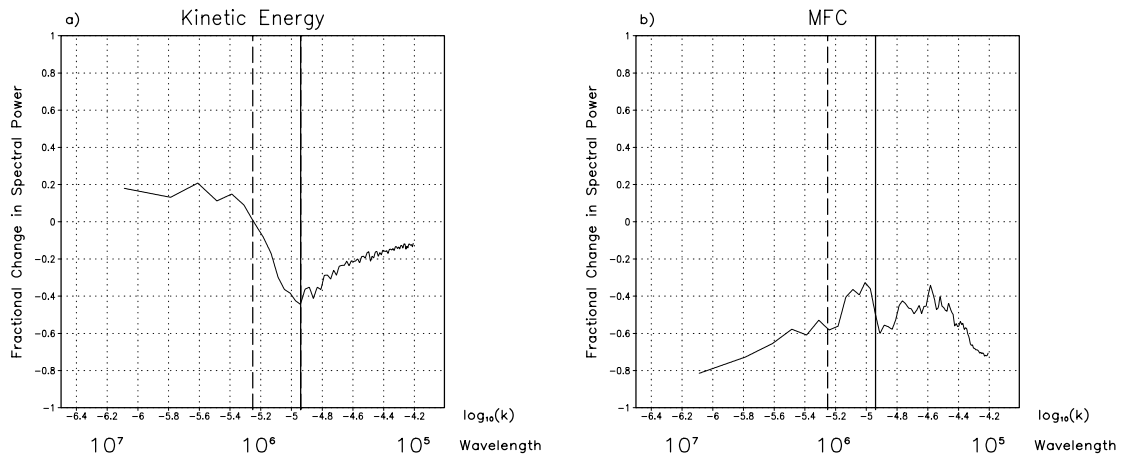


Figure 3.9: Average fractional change in spectral power ($\Delta S(k)_{frac}$) versus $\log_{10}(k)$ and wavelength for a) column average kinetic energy and b) column integrated moisture flux convergence (MFC), Follow-on 1 (internal nudging). The dashed black line indicates k_{max}^* and the solid black line $k_{Nyquist}^*$. k in units of m^{-1} . Wavelength in units of m.

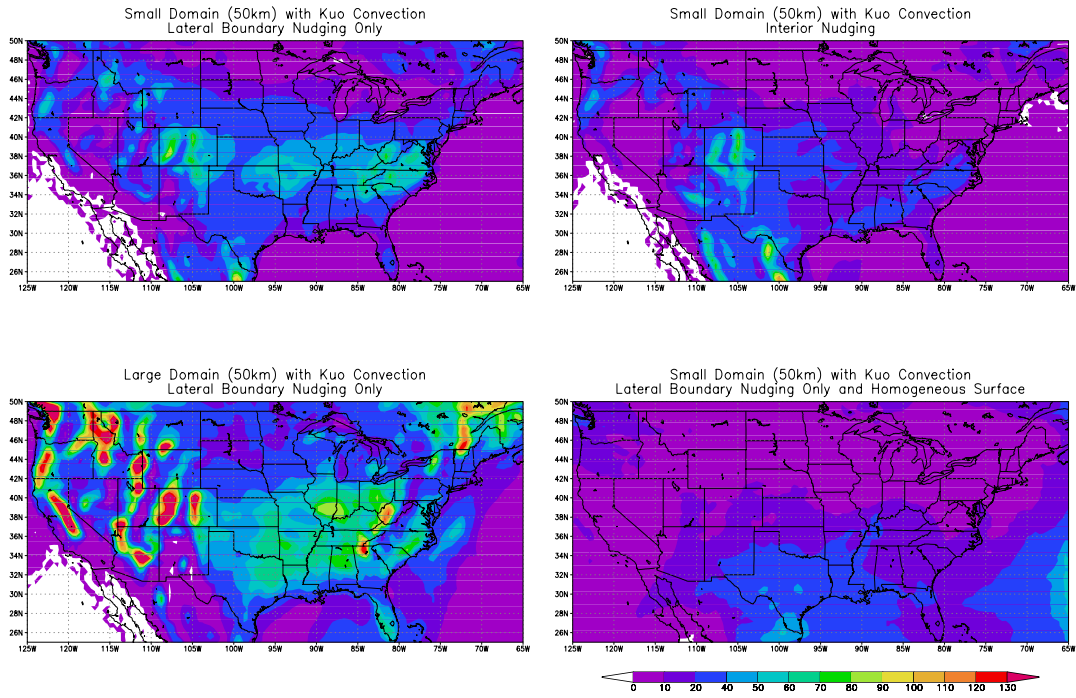


Figure 3.10: RAMS-simulated convective precipitation with the Kuo scheme for model constraints indicated. Period considered is last 15 days of simulation. Precipitation in mm.

which will be discussed later. For Follow-on 2, precipitation is substantially increased in regions of significant topography.

The precipitation results for Follow-on 2 (large-domain) in Fig. 3.10 would imply that the weaker the influence of the larger-scale forcing of the reanalysis, the greater control the surface boundary conditions exert on the vertical motion and distribution of precipitation. The behavior of RAMS in this respect would be identical to other mesoscale models (e.g. Jones et al. 1995, 1997; Jacob and Podzun 1997; Seth and Giorgi 1998). For Follow-on 2, the ratio of the spectra of the large (extracted) domain (mod_1) to the small domain (mod_2) was computed using equation 3.15, and these are shown in Fig. 3.11. Increasing the domain size reduces the variability of kinetic energy for all k , and this should be expected given the results already seen. However, $\Delta S(k)_{frac}$ for MFC is greater than zero for $k > k_{max}^*$. It will be shown later in Follow-on 4 that the mechanism which is enhancing variability of MFC at that scale is the topography.

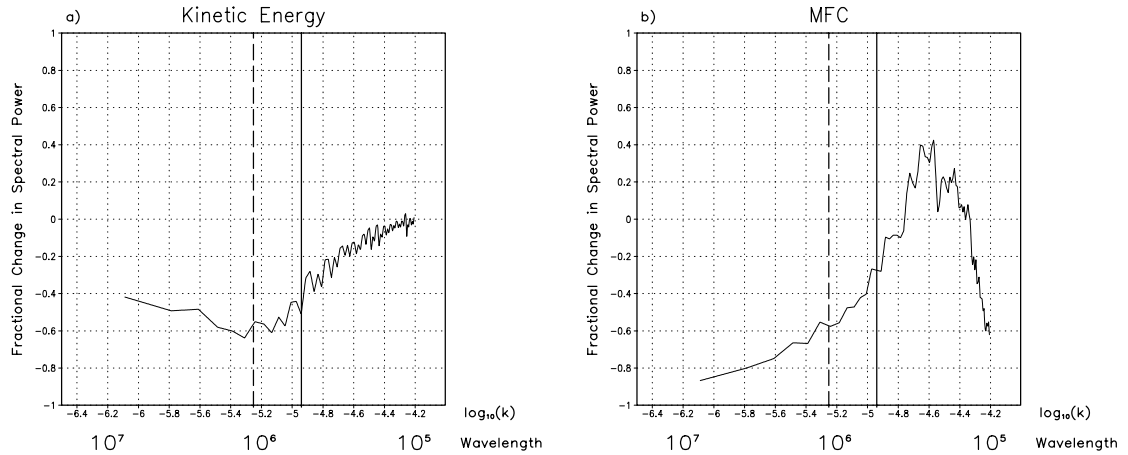


Figure 3.11: Same as Fig. 3.9 for Follow-on 2 (larger grid).

Use of the KF convective parameterization scheme (Follow-on 3) markedly changes the model-generated precipitation, as shown in Fig. 3.12 along with the corresponding NCEP 0.25° gauge observations (Higgins et al. 1996). The KF scheme produces more precipitation in the simulation domain than the Kuo scheme, whether internal nudging is activated or not. The KF scheme in RAMS generally overestimates precipitation in areas of steep, elevated terrain. As mentioned in the previous section, the terrain-adjusted trigger function (not used for these experiments) can alleviate this problem. In Fig. 3.13, changing the convection scheme does not change the kinetic energy for $k < k_{\max}^*$. It does modestly increase the kinetic energy (by about 20%) beyond k_{\max}^* . The variability in MFC is much larger, particularly for $k > k_{\max}^*$. In this range, the KF scheme is more than doubling the variability of MFC. In the KF simulations, the stronger MFC variability is explained by the enhanced rainfall. Over the length of a RCM simulation, the use of a different convection scheme may dramatically effect the surface energy and moisture budget of the model and, hence, surface feedback to the atmosphere.

The question, however, is to determine, with respect to precipitation, which particular model setup yields the best result in terms of the NCEP observations shown in Fig. 3.12. Given that these are Type 2 dynamical downscaling simulations, it is reasonable to expect that the RCM should reproduce (in a gross sense) the day-to-day climate variability on weekly and longer timescales. An evaluation of model performance against observations defines the model skill. Precipitation results are considered for four different RAMS experiments: Kuo with no interior nudging (basic experiment 3), Kuo with interior nudging (Follow-on 1), KF with no interior nudging,

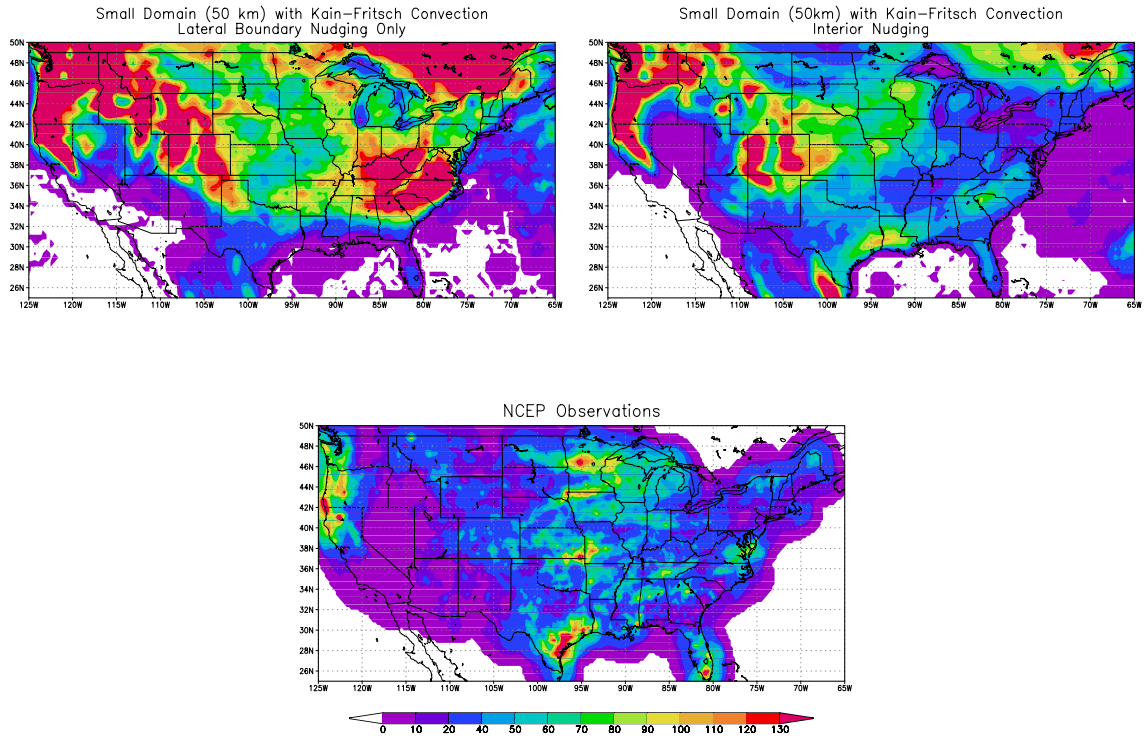


Figure 3.12: RAMS-simulated convective precipitation (mm) with the Kain-Fritsch scheme for model constraints indicated and observed precipitation from NCEP. Period considered is last 15 days of simulation.

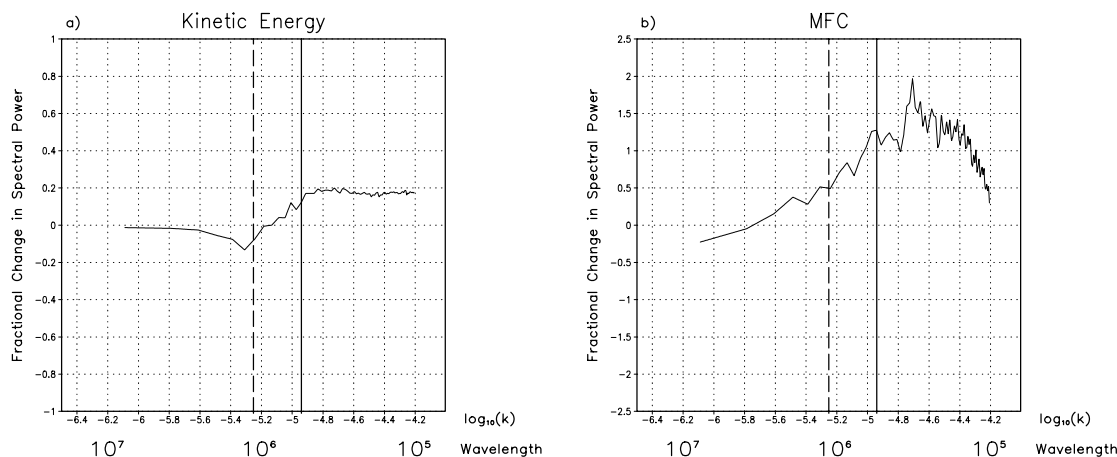


Figure 3.13: Same as Fig. 3.9 for Follow-on experiment 3 (Kain-Fritsch convection).

and KF with interior nudging (Follow on 3). Considering the last fifteen days of simulation, a spatially varying correlation coefficient was determined using daily precipitation totals. The square of the correlation coefficient yields the spatially-averaged explained variance of model precipitation to observations. The difference in monthly precipitation from the NCEP observations along with the domain-averaged bias and explained variance are shown in Fig 3.14. Though fifteen days of data are insufficient to generate a statistically significant signal, they are nonetheless good enough to show the biases associated with each convection scheme and how interior nudging changes the explained variance of precipitation in the model domain.

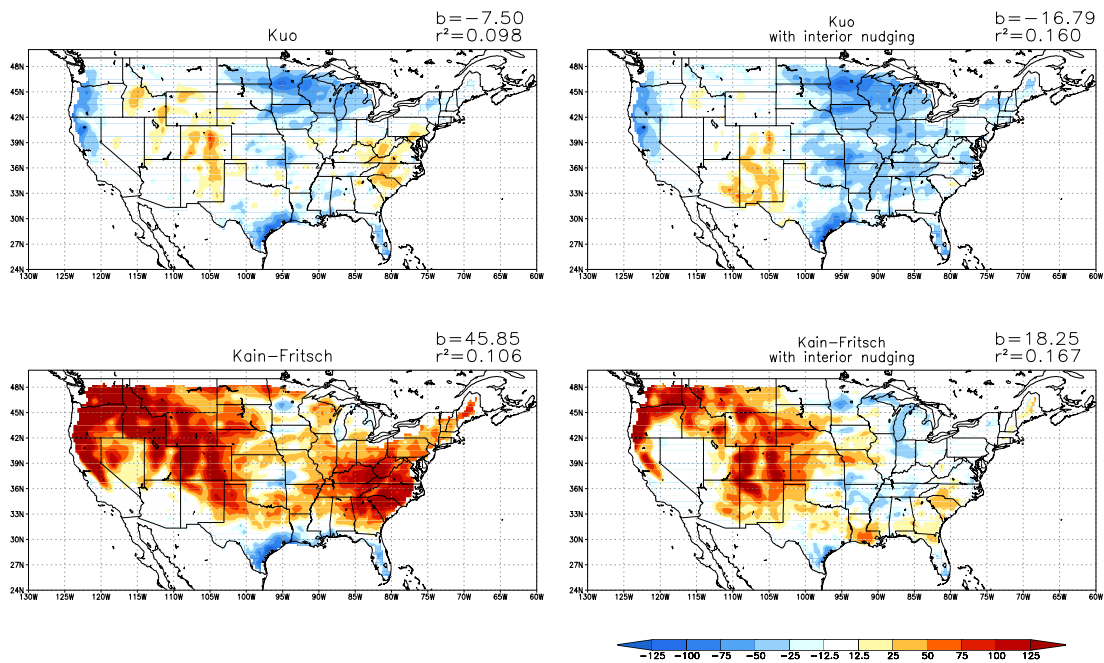


Figure 3.14: Difference of between RAMS-simulated precipitation and NCEP observed precipitation (mm) over the contiguous U.S. for the model conditions specified. Domain-averaged bias and explained variance (r^2) included. Period considered is last 15 days of simulation.

The Kuo scheme underestimates the precipitation in the central U.S. and overestimates in regions of steep terrain gradients, such as occurs in the Rocky Mountains or Appalachians. Though the bias in the no interior nudging case is the smallest of the simulations considered (-7.50 mm), the domain-averaged explained variance of precipitation is the lowest of the simulations considered in Fig. 3.14 (9.7%). The domain-average explained variance is about the same for Follow-on 2 (large domain), but precipitation biases associated with terrain are enhanced (not shown). When the entire month is considered, the explained variance for the large-domain experiment is lower than that of the small domain. This suggests that better representation of the large scale in the smaller domain experiment improves the RAMS model-generated precipitation. When interior nudging is applied, the underestimation of the Kuo scheme worsens in the central U.S. (a domain-average bias of -16.79 mm). The explained variance of daily precipitation increases (to 16.7%). Even though precipitation is more underestimated when interior nudging is applied, its spatial distribution is closer to observations.

Considering the KF simulation without internal nudging, precipitation is generally overestimated everywhere with a large positive domain-averaged bias (45.85 mm). The problem with excessive precipitation in steep terrain gradients is magnified. The KF simulation with interior nudging greatly improves the precipitation error in the central and eastern U.S. However, the problem with high precipitation in the mountains still exists, and therefore there is a high bias in precipitation (18.75 mm). As with the Kuo scheme, the simulation with interior nudging yields a better domain-averaged explained variance.

How does the spectral behavior of model-generated precipitation correspond to observations for these four simulations in Fig. 3.14? Fig. 3.15 shows $\Delta S(k)_{frac}$ of the RAMS precipitation compared to the NCEP observations following equation 3.16. The Kuo scheme, whether internal nudging is applied or not, underestimates the observed spatial variability at all scales. For the KF runs, variability is enhanced, particularly at the larger scales, because of the pattern of precipitation bias associated with the terrain in the western U.S. The best representation of the spatial variability of NCEP observations is captured by the KF scheme with internal nudging. At the small scale, the spatial variance of the KF generated precipitation from the nudged run and the NCEP observed precipitation is roughly identical. Therefore, though the Kuo scheme has a lower-domain averaged bias, the Kain-Fritsch scheme with internal nudging does the superior job of representing the spatial distribution and variability of precipitation in RAMS for this particular month of May 1993.

Finally, Follow-on 4 (homogeneous surface boundary experiment) serves as a control to evaluate the impact of topographic forcing. The precipitation for this experiment is included in Fig. 3.10. Compared to the other experiments with the Kuo scheme, there is little precipitation in the western U.S. associated with the topography, as would be expected. There is also less precipitation in the central and eastern U.S., in areas of relatively homogeneous terrain. Because spring and summer precipitation is tied to a diurnal cycle of convection forced by the topography, eliminating the topography alters the precipitation distribution across the entire continent. In the evaluation of $\Delta S(k)_{frac}$, since the integrated kinetic energy has little relationship to surface forcing, it is omitted analysis here and the focus is exclusively on MFC. Also, instead of evaluating

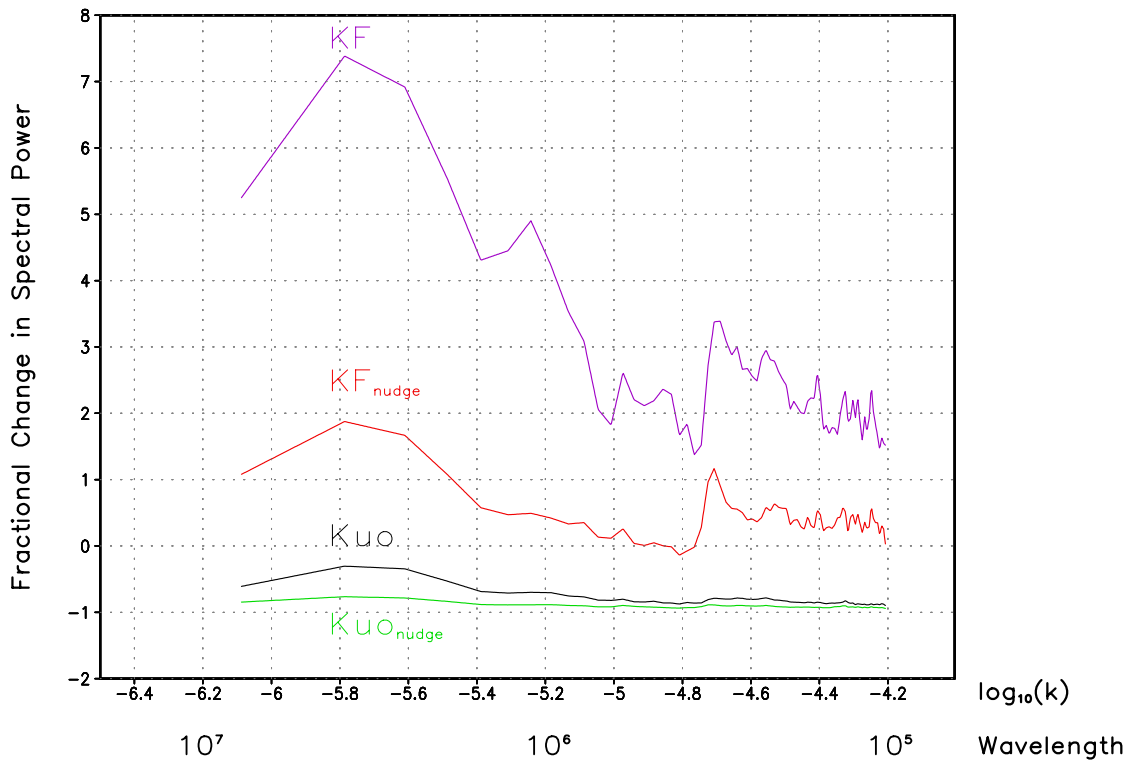


Figure 3.15: Fractional change in spectral power ($\Delta S(k)_{frac}$) versus $\log_{10}(k)$ and wavelength for different RAMS-generated model precipitation solutions on the 50 km small domain grid. k in units of m^{-1} . Wavelength in units of m.

the MFC on its own, it is first multiplied by the topographic gradient in the model and then the two-dimensional spectral analysis is performed. In this way, the relationship between the topography and MFC can be evaluated. This analysis is performed on Follow-on 4 (*mod 2*) as the control experiment against which all other previous experiments with the 50 km small domain are evaluated (*mod 1*) using equation 3.15. For these experiments, $\Delta S(k)_{frac}$ is interpreted as follows: if greater than zero, the topography contributes to the variability in MFC at a given value of k beyond what its variability would be with no topography; if less than zero, it does not.

Fig. 3.16 shows $\Delta S(k)_{frac}$ for the experiments with the Kuo scheme (experiments labeled in the plot). For these experiments, the largest positive value for $\Delta S(k)_{frac}$ occurs at approximately $\lambda \sim 250$ km for the large domain experiment. A similar, though weaker, peak appears for the smaller domain, confirming that the increase in MFC variability in Fig. 3.11 is indeed due to increased sensitivity to the topography when the domain is enlarged. In the run with internal nudging, though, $\Delta S(k)_{frac}$ is always below zero, so the topography does not contribute to the variability of MFC beyond the model simulation with no topography. This does not necessarily imply, though, that the topography is not contributing to the variability of MFC in this particular simulation. Its influence is just weaker. Recalling the pattern of precipitation bias in Fig 3.14, this likely explains why the precipitation in the Kuo simulation, with internal nudging especially, underestimates the precipitation in the central and eastern U.S. This convective precipitation is due to a topographically-forced diurnal cycle of MFC which is underestimated by the model in that particular configuration.

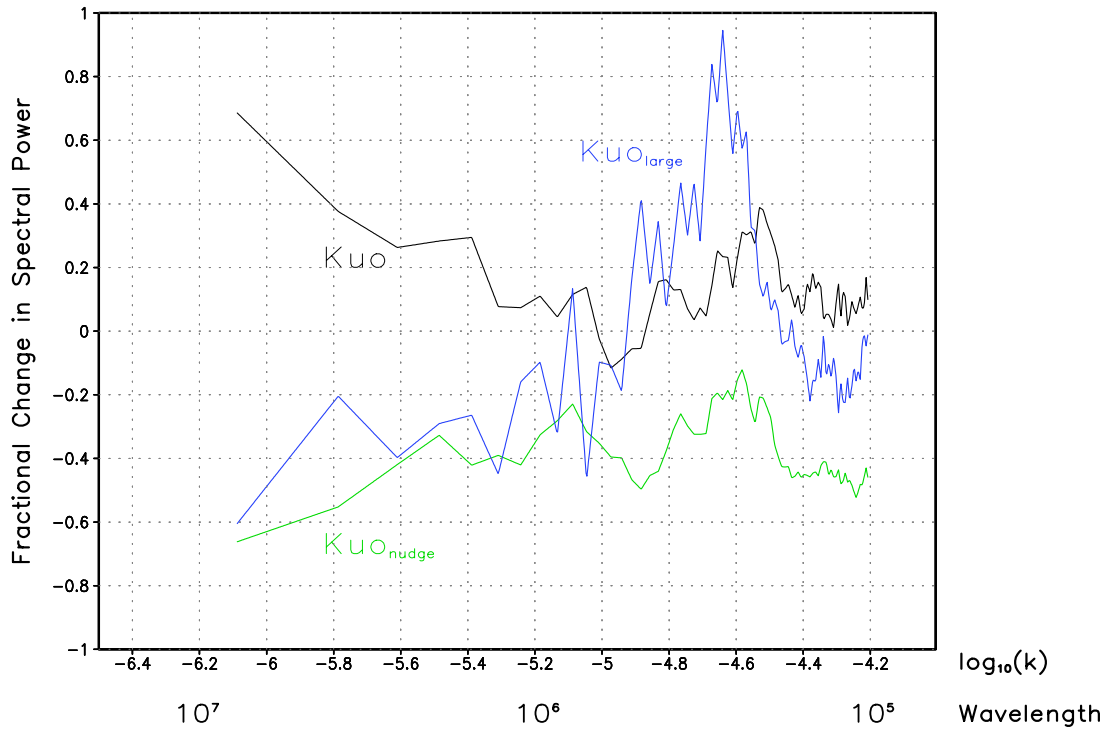


Figure 3.16: Fractional change in spectral power ($\Delta S(k)_{frac}$) versus $\log_{10}(k)$ and wavelength, experiments with the Kuo scheme compared to Follow-on 4. The quantity considered is the MFC multiplied by the topographic gradient in the model. k in units of m^{-1} . Wavelength in units of m.

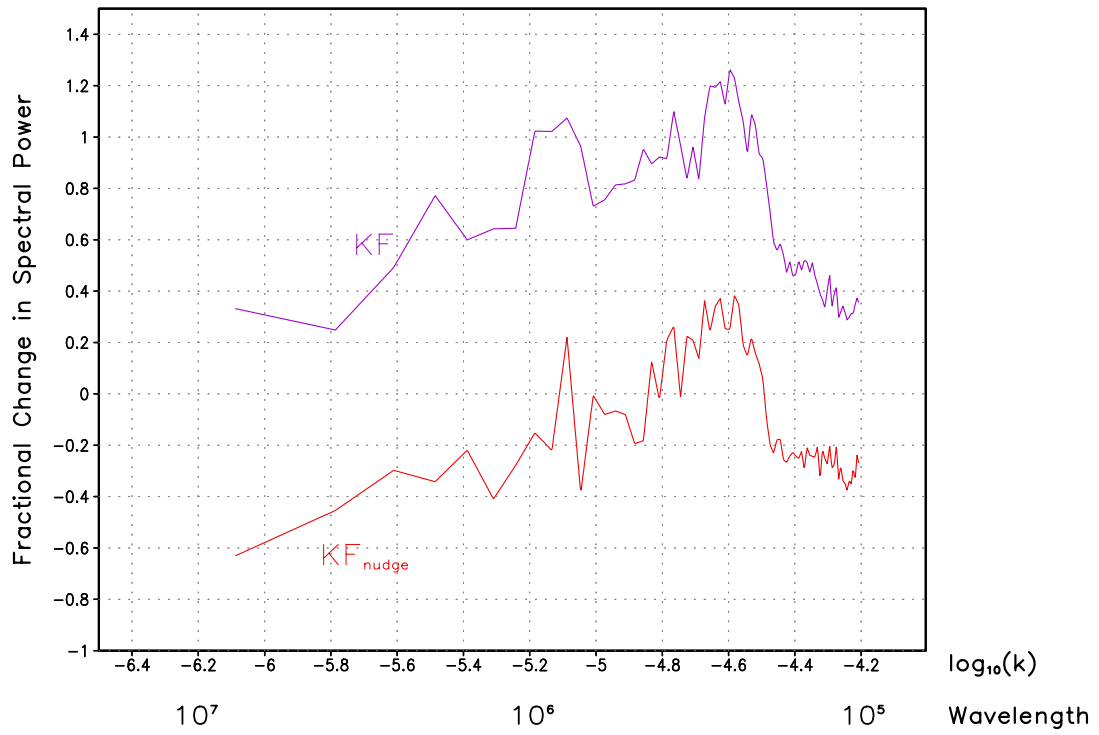


Figure 3.17: Same as Fig. 3.16 for experiments with the KF scheme.

For the experiments with the KF scheme (Fig. 3.17), similar behavior to the Kuo experiments is seen. Topography enhances MFC at the same preferential scale, and the peak in $\Delta S(k)_{frac}$ exceeds zero for the simulations in which nudging is and is not applied. In spite of the internal nudging for the KF case, the topography is able to add information to the RCM and influence the diurnal cycle of MFC. Hence, the improvement in the spatial variability of precipitation in the KF internally nudged simulation described earlier is observed. This provides further evidence that the choice of (convective) parameterization schemes seriously affects how the surface boundary adds information to the RCM.

3.6 Discussion

Without interior nudging, the RAMS model in RCM mode will have greater error at larger scales as both horizontal grid spacing and domain size increase. This error is due to the failure of the RCM to correctly retain value of the large scale, which is particularly acute at the limit of physically resolved waves in the larger global model (k_{max}^*). For the typical RCM setup in which a continental-scale domain is used, with a grid spacing less than 50 km, the underestimation of kinetic energy over a month of simulation may be tolerable and barely noticeable (less than 5%). However, when the RAMS model was applied to a very large domain or a coarse grid spacing ($\Delta x > 50$ km) on a continental-scale domain is used, kinetic energy was underestimated for all k . RAMS does add value for k greater than k_{max}^* especially if there is sufficient surface boundary forcing, such as variations in topography, and that forcing can be resolved by the model. The sensitivity to the surface forcing increased when the model domain size

increased, as shown by analysis of the integrated moisture flux convergence. Though the focus here was on topography, presumably similar effects may occur for any variable surface field, like vegetation, soil moisture, or snow cover. It was also observed that changing the model convective parameterization scheme increased the sensitivity to the surface boundary.

The first important question raised in this chapter is what causes the loss of large scale kinetic energy with time, without interior nudging in a the RCM? The most obvious answer would seem to be the parameterized horizontal diffusion. Because of the dependence on grid spacing, the lower limit of the diffusion coefficient will increase by about an order of magnitude from a 50 km to 200 km simulation. This increase in diffusion is necessary for numerical stability. The loss of kinetic energy is well known problem of global models, and can be directly linked to diffusion. A reduction in the user-specified parameters (C_x and K_A) used in diffusion computation to their minimum values as suggested by the *RAMS Users Guide* was attempted, but this did not mitigate the kinetic energy loss. There is also the likely possibility that, in addition to horizontal diffusion some or all of the other one dimensional column parameterizations are insufficient to retain value of the large scale. These would include the parameterizations for convection and/or cloud microphysics, radiation, and sub-grid scale mixing.

As an example, let us consider the simulation of large-scale precipitation in addition to a convective parameterization scheme. Accounting for large-scale precipitation allows for supersaturation through explicit uplift of moisture. The resulting heating increases the buoyancy of uplifted air and enhances its upward vertical motion, providing a mechanism for conversion of potential to kinetic energy. Reliance entirely

on the convection scheme can also suppress large-scale vertical motions by increasing static stability and further reduce the energy conversion. An additional simulation (50 km , small grid) was executed with a full cloud microphysical representation of large-scale precipitation. $\Delta S(k)_{frac}$ was computed according to equation 3.15 and the results are shown in Fig. 3.18. For comparison, $\Delta S(k)_{frac}$ from Fig. 3.4 (the simulation with only the convection scheme) is included for reference. Accounting for the large-scale precipitation decreases the loss of kinetic energy at the large scale, but does not eliminate it. At k_{max}^* the loss decreases from approximately 30% to 10%. Beyond k_{max}^* the variability of kinetic energy is substantially increased over using the convection scheme alone. In spite of the better representation of large-scale energy, though, the domain average precipitation for this simulation is overestimated and its spatial pattern is poor compared to observations (not shown).

The second important question is why there seems to be a change in trend in $\Delta S(k)_{frac}$ at k_{max}^* . For $k < k_{max}^*$ there is always a kinetic energy loss compared to the reanalysis, irrespective of grid size or grid spacing. For $k > k_{max}^*$, this loss either decreases in magnitude or the RCM begins to add value. Would there be a similar dependence of k_{max}^* on $\Delta S(k)_{frac}$ irrespective of the resolution of the GCM or reanalysis? If so, then it would possible to determine a priori which wavelengths the RCM would tend to degrade, absent some interior nudging technique.

Is there a way to alleviate the large-scale kinetic energy loss shown in Fig. 3.6 and yet preserve the value added by the RCM at the small scale? Simply increasing the

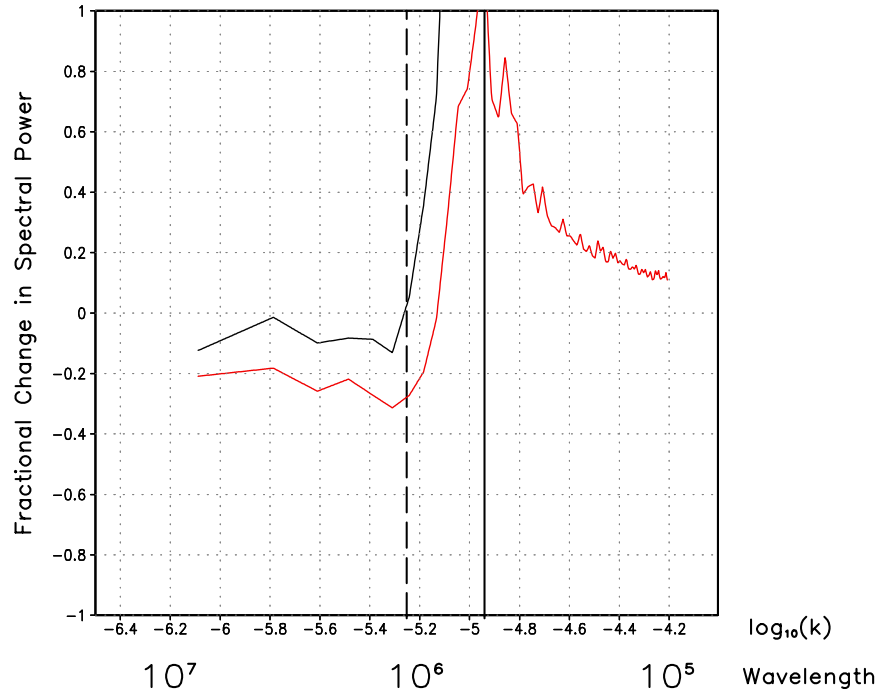


Figure 3.18: Fractional change in spectral power ($\Delta S(k)_{frac}$) versus $\log_{10}(k)$ and wavelength, for column-average total kinetic energy. The red curve is the basic experiment 3 simulation (convection scheme only) and the black curve is the same simulation with convection and explicit microphysics. The dashed black line indicates k_{max}^* and the solid black line $k_{Nyquist}^*$. k in units of m^{-1} . Wavelength in units of m.

number of nudging points would seem to be a solution, but exactly the same loss of kinetic energy was found when the number of nudging points was increased to ten. The albeit crude, four dimensional data assimilation technique of internal nudging may be applied, as demonstrated in Fig. 3.9. The results in Fig. 3.9 are really nothing new and should not be surprising in light of the results from studies using a variety of other RCMs over the past decade (e.g. von Storch 2000, Sasaki et al. 1995, Giorgi et al. 1993b, Kida et al. 1991). These studies conclude that improvement in RCM simulation can be achieved by selective nudging of the large-scale, or a spectral nudging technique. This is probably the best solution. Miguez-Macho et al. (2005) recently demonstrated the utility of a spectral nudging technique for RAMS (not yet incorporated in the standard release of the model). Using a domain very similar to the small domain used here, they found a large improvement in the June 2000 precipitation over the central U.S. solely due to spectral nudging of the large-scale (defined as $\lambda > 2500$ km) throughout the entire depth of the troposphere.

Internal nudging such as has been used here, in which all wavelengths are relaxed to the reanalysis solution, it is acknowledged, is far less desirable. In agreement with Weaver et al. (2002), it was found interior nudging tends to weaken small scale variability. This small scale variability may not only arise from the presence of topography, but purely via local hydrodynamic variability. Examples include frontogenesis, development of convective cloud bands, and hurricane intensification. None of these examples requires surface inhomogeneities for their development and none is resolvable on the reanalysis grid. Without detailed mesoscale data or regional reanalyses, there is no way to quantify what the value added may be. Weak internal

nudging at a long timescale may still preserve some of the small scale variability because most it occurs at a diurnal timescale or less. For example, with the KF scheme in RAMS, the internally nudged solution yields the better model representation of precipitation, in terms of spatial distribution and variability. Aside of areas of significant topography in western North America, some areas of relatively homogeneous topography, such as in the central and eastern U.S., also exhibited a low precipitation bias in the KF simulation in which internal nudging was applied.

What is really advocated with the use of spectral nudging, or interior nudging for that matter, is the introduction of some method of large-scale closure needed by the LAM when run as a RCM. The use of spectral nudging would retain the kinetic energy of the large-scale and let the large-scale forcing reinitialize the fine-scale domain during the model integration period. In the absence of four dimensional data assimilation, however, in order to retain the kinetic energy requires that the model dynamics and physics, as have been previously defined, generate the energy. As has been demonstrated, the one-dimensional forms of the parameterized model physics are unable to generate enough kinetic energy to retain that of the reanalysis. This issue is likely endemic to all RCMs, since each use similar dynamic and physical representations.

To test this hypothesis, it is suggested that this experiment (or similar) be repeated with other RCMs to demonstrate whether this behavior exists. If this is the case, it implies that only applying lateral boundary nudging only using Davies (1976) nudging or similar technique is insufficient for RCMs. A universal alternative needs to be implemented. Previous work, with RAMS and other models, shows the best alternative is a spectral nudging technique. The evidence presented here suggests the domain should

be nudged for $k < k_{\max}^*$, where k_{\max}^* is dependent on the resolution of the forcing data. Because there is such a large sensitivity to the RCM experimental design, when comparing results from different models it is necessary to ensure they use the same grid size, grid spacing, and nudging options in order to accurately assess the RCM-generated small scale variability.

The results here also challenge the traditional notion of a grid setup for RCM dynamical downscaling. RAMS was originally designed for simulation of short-term weather events on a cloud-resolving scale. Recall that “short term” is defined as a time scale of days to a couple of weeks. For these Type 1 experiments, a multiple nesting paradigm is typically followed. The coarsest grid has the same approximate horizontal scale as the reanalysis or global model ($\Delta x = 100\text{-}250$ km). Within the coarsest grid, there is an intermediate nested (mesoscale) grid ($\Delta x = 10\text{-}50$ km). Finer nested grid(s) ($\Delta x < 10$ km) may be added to capture specific weather events, if so desired. There are two reasons for such a model setup. First, it has been assumed inappropriate to assimilate the reanalysis or global model data at a scale much smaller than $k_{Nyquist}^*$. Second, it is typically computationally prohibitive to run a cloud-resolving simulation for a very large grid. There have been recent advances in computing power so that this may be come widely feasible in the near future, though. The multiple grid nesting approach works because the model retains a large sensitivity to the initial conditions. For example, even after a week of simulation the 200 km grid spacing small domain still preserves approximately 90% of the reanalysis assimilated kinetic energy.

The results here, though, suggest the multiple grid nesting paradigm may not yield the most desirable results when RAMS (or other RCM) is run in a RCM mode. A coarse

grid of $\Delta x = 100\text{-}200$ km may introduce undesirable weakening of large-scale atmospheric variability for a model integration exceeding two weeks or so. A better strategy may be to assimilate the reanalysis directly to the mesoscale grid (a single grid paradigm). The global model or reanalysis data are then driving the RCM for the scale in which it retains value of the large scale. Bypassing the coarser grid may also 1) save computing resources, and 2) avoid the problem of using different parameterization schemes, such as for convection, on different grids which may introduce additional uncertainties in model simulation results (e.g. Gochis et al. 2002). However, caution must be taken not to have too large a ratio of GCM grid spacing to LAM grid spacing. The *RAMS Users Guide* suggests that if this ratio exceeds a value of six, reflections may occur at the lateral boundaries due to grid disparities.

3.7 Summary

In this chapter, the value retained and added by dynamical downscaling has been quantitatively evaluated by considering the spectral behavior of RAMS in relation to its domain size and grid spacing. To do this, a RAMS-RCM simulation was compared with a regridded reanalysis at each model analysis time for a set of six basic experiments. At large scales RAMS cannot restore the variability present in the global model forcing data, and this loss is particularly acute at the limit of the global model physically resolved waves. As the grid spacing increases or domain size increases, the underestimation of variability at large scales worsens. The model simulated to regridded reanalysis kinetic energy exhibits a decrease with time, which is more pronounced with larger grid spacing. This underestimation of kinetic energy is not only linked to the parameterized horizontal

diffusion, but all the other one dimensional column parameterizations in the model. The results here and past studies suggest the only solution to alleviate this problem is to constrain the RCM with the large scale model (or reanalysis) values.

Additional follow-on experiments investigated the effect of internal nudging, enlarging the domain, the use of a different convective parameterization, and a homogeneous surface boundary. These were designed mainly to investigate the value added by RAMS at the small scale. Weak internal nudging, as currently implemented in RAMS, did improve the representation of the large-scale features, but weakened the variability at small scales. The surface boundary forcing appeared to be the dominant factor in generating variability for small-scale features and exerts greater control on the RCM solution as the influence of lateral boundary conditions diminish. Changing the convection scheme increased the variability on the small scale and improved the model generated precipitation. The influence of the surface boundary forcing, then, is highly dependent on the model experimental design, such as domain size, nudging options, specification of the surface boundary itself, and model parameterization schemes. Further studies are, of course, necessary to confirm whether these behaviors apply in general to all RCMs, but previous work suggests they do. It would be a very worthwhile exercise to repeat these experiments with an assortment of different RCMs, especially those which use a spectral nudging technique.

These RAMS simulations are of a Type 2 framework, assuming a perfect model, so the same conclusions will apply to RAMS-RCM applications with greater degrees of freedom (Types 3 and 4). A good example for these latter types is that of Jones (1995) that demonstrated similar results and conclusions for RCM simulations over Europe. It

was found for this particular case, dynamical downscaling with RAMS does not retain value of the large scale over and above that which exists in the larger global model or reanalysis. If the variability of synoptic features is underestimated or there is a consistent bias in the larger model, no increased skill would be gained by dynamical downscaling with RAMS. The utility of the RAMS-RCM, then, is not to add increased skill to the large scale, rather the value added is to resolve the smaller-scale features which have a greater dependence on the surface boundary.

Chapter 4

A SUMMER RCM CLIMATOLOGY OF THE CONTIGUOUS UNITED STATES AND MEXICO

4.1 Description of RAMS Simulations

So far, the sensitivities of RAMS as a RCM have been investigated and the most ideal RAMS experimental design for Type 2 and greater simulations has been described. The optimal experimental design (like the case for all RCMs) is one that uses no larger than a continental scale domain, a single grid, and some sort of interior nudging within the domain. Additionally, for RAMS it was found that the Kain-Fritsch cumulus parameterization scheme yielded better precipitation results than the existing Kuo scheme. Using these conclusions as a guide, in this chapter a set of dynamical downscaling simulations is completed with RAMS. The goal is to create a summer RCM climatology over the contiguous U.S. and Mexico using nearly the entirely NCEP Reanalysis record (1950-2002). This will go beyond the previous diagnostic or sensitivity studies in which only one or a few years are the focus. As mentioned in Section 1.2, the climatology is similar, in principle, to that of Xu et al. (2004).

The RAMS domain (Fig. 4.1) for these simulations has horizontal dimensions of 160 x 120 grid points with a grid spacing of 35 km. As in Chapter 3, the model uses a vertically stretched grid with a maximum vertical grid spacing of 1000 m. The minimum

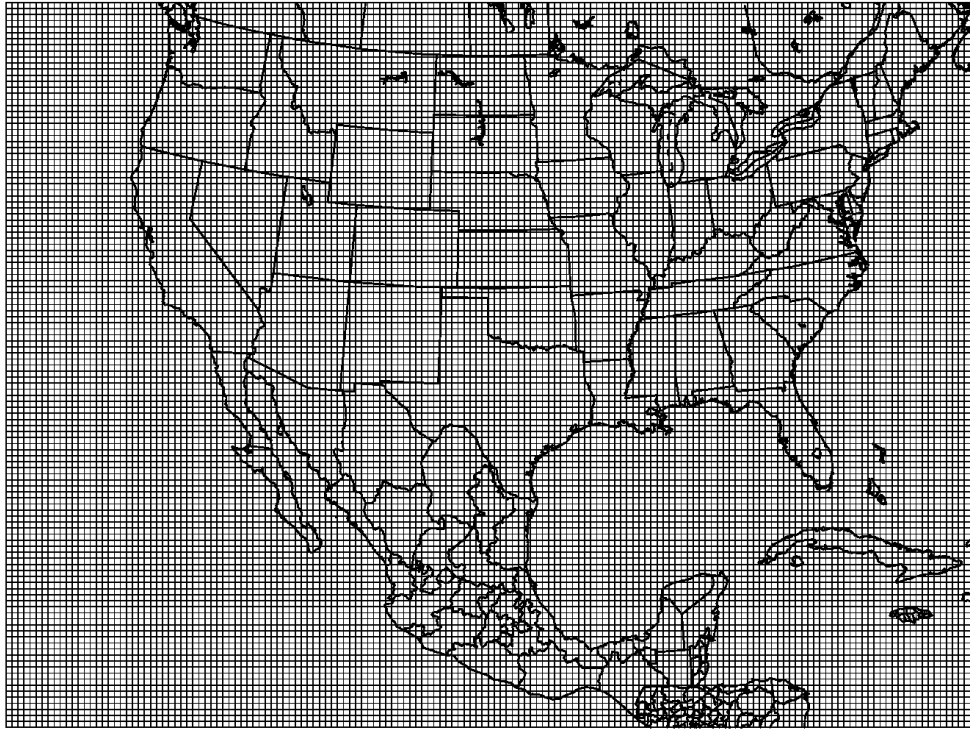


Figure 4.1: RAMS model domain for North American summer climatology.

vertical grid spacing is 100 m with a vertical stretch ratio of 1.2. There are 30 grid points in the vertical. Initial volumetric soil moisture data is prescribed by two datasets. In the part of the domain which corresponds to the North American Land Data Assimilation (NLDAS) domain monthly soil moisture from the Variable Infiltration Capacity (VIC) model is used. VIC is a large-scale hydrologic model run retrospectively over the NLDAS domain for the years 1950-2000 at one-eighth degree resolution (Maurer et al. 2002). The monthly data are available on-line from the Department of Hydrology at the University of Washington. For the years 2001 and 2002 a similar NLDAS product is used. Outside the NLDAS domain, year specific soil moisture is prescribed by a NCEP global soil moisture dataset which uses a one-layer hydrologic model described in Huang et al. (1996). The May climatology of the combined product is shown in Fig. 4.2. At model initialization, soil moisture is assumed constant through the model depth of 2.5 m. It is important to acknowledge here that the most optimal way to derive an initial soil moisture condition would be a “spin-up” of the model before the period of interest, so the soil moisture would be specific to the LEAF-2 model. However, this is very computationally expensive for multiple years of simulation. The specification of initial soil moisture by the NLDAS product provides an alternative to the “spin-up” approach. It is probably also better than prescribing the soil moisture from the NCEP Reanalysis itself. The RAMS summer simulations begin 15 May and end 31 August. This interval is sufficient to capture premonsoon conditions (late May and early June), the onset of the North American Monsoon (late June, early July), and the peak of the monsoon (late July, early August). Henceforth these definitions will be used to contrast the climate as it evolves during the summer.

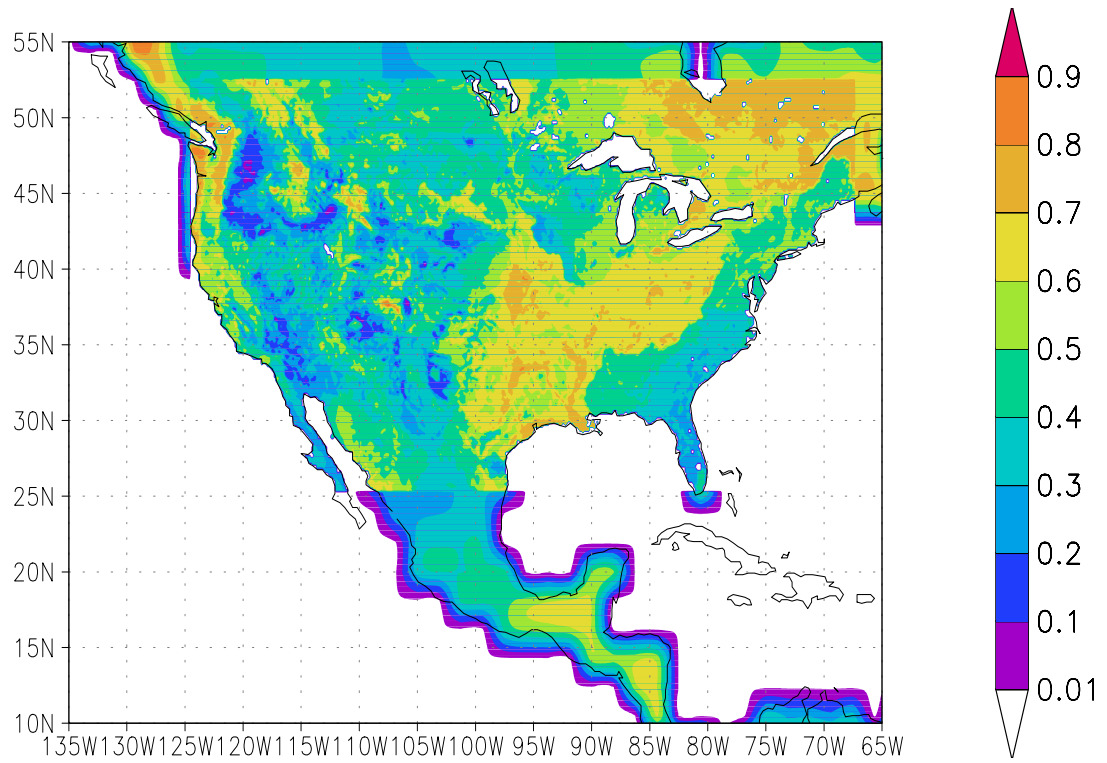


Figure 4.2: Climatological May soil moisture (as a fraction of saturation) from data used as input to RAMS simulations. Shading indicated by color bar.

4.2 Validation Datasets

As in Xu et al. (2004), the observed daily precipitation gauge data are from the U.S. Climate Prediction Center (CPC) real-time and retrospective dataset (Higgins et al. 1996), derived from the U.S. Cooperative observing network. These data span the period 1950-present and encompass all of the contiguous U.S. and Mexico. These data are available on-line via the Climate Prediction Center.

Satellite derived precipitation is from the Arkin and Janowiak GOES Precipitation Index (GPI), a Global Precipitation Climatology Project produced distributed by the National Center for Environmental Prediction (NCEP). This dataset contains daily 1° x 1° gridded rainfall estimates from 40° S to 40° N based on infrared radiometer measurements. Estimates are generated using a simple cloud-top temperature-thresholding algorithm (Arkin 1979) and are valid for the tropics and warm season extratropics. These data span the period 1998-present, and the data from 1998-2004 are used. This product is used primarily to demonstrate the large difference between satellite and gauge-derived precipitation.

Surface temperature, dewpoint, and mean wind speed over land are taken from U.S. and global summary of the day data from stations in the contiguous U.S. and Mexico. These data were gridded to the model domain using an algorithm developed by Lixin Lu at Colorado State University. These data are available for the period 1973-1996.

4.3 Validation of RCM Results

There are several a priori expectations as to where the enhanced surface boundary of a RCM should add value to the climatology of precipitation and atmospheric moisture beyond an atmospheric reanalysis. First, it should be expected that the RCM should yield a better representation of rainfall as the summer season progresses. Analysis of radar data shows rainfall becomes less dependent on large-scale synoptic weather systems and more dependent on diurnally-forced convection or propagating mesoscale convective systems as the summer proceeds (Carbone et al. 2002). Second, rainfall should be more realistically represented in locations where the diurnal cycle of convection is dominant, arising from complex topography and/or land sea contrast. These are also areas where periodic surges of moisture occur due to low level jets. Finally, it should be expected that precipitation should improve in areas where land surface feedback may be important. For these reasons, the focus of the discussion here will be the core monsoon region and the central U.S. In analyzing the precipitation data, the monthly accumulated precipitation is shown for the months of June, July, and August. Then the difference between the premonsoon period (defined as the thirty-day period about 1 June) and the monsoon peak period (defined as the thirty-day period about 1 August) is shown. The onset period is defined as the thirty-day period about 1 July.

The observed CPC precipitation gauge data are shown in Fig. 4.3. The features in the observed precipitation are well known and have been described in previous studies (e.g. Higgins et al. 1999). In June, there is a maximum of precipitation in the central U.S. greater than 125 mm. The moisture source for this precipitation is the Great Plains LLJ, which is strongest at this time relative to the latter part of the summer. In Mexico, the

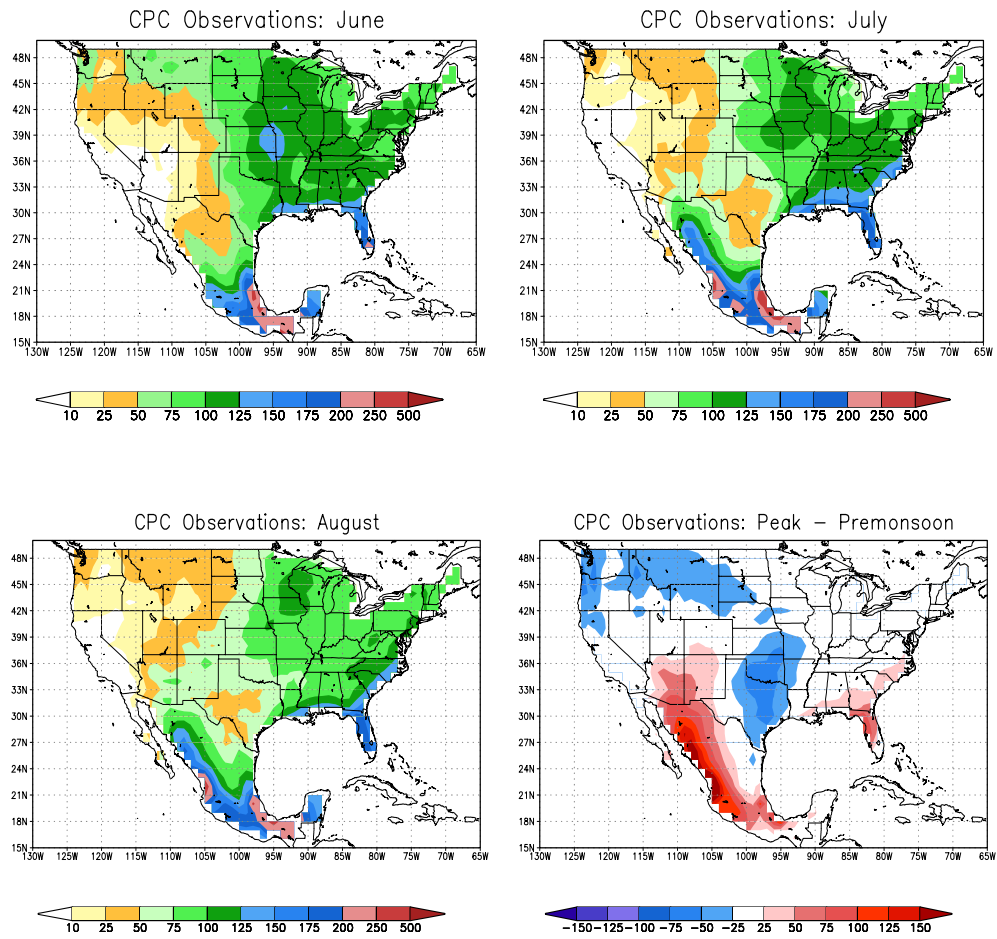


Figure 4.3: Observed CPC gauge-derived (1950-2002) average precipitation (mm) for the summer months and the difference between the monsoon peak and premonsoon periods. Shading indicated by color bars.

North American Monsoon is beginning to advance northwestward along the Sierra Madre Occidental (SMO) into the core monsoon region. In the Southwest U.S. during the premonsoon period there is little, if any, rainfall and hot, dry conditions. By July, the typical monsoon pattern has developed across the continent. According to Higgins et al. (1999), monsoon onset in the core monsoon region occurs sometime between late June and early July with a sudden increase in rainfall. This change in rainfall is on the order of 50 mm per month in the Southwest U.S. and more than 100 mm per month along the SMO. The maximum rainfall amounts occur on the crests of the mountain ranges, like the SMO and the Mogollon Rim in Arizona. Such features are more resolved in the 0.25° data available over the contiguous U.S. (not shown). Correspondingly in July, there is a decrease in rainfall in the central U.S., particularly in the southern Great Plains where rainfall decreases 50 to 75 mm per month from June. In the Southeast U.S., there is a slight increase in rainfall following monsoon onset in the Southwest. This monsoon pattern of precipitation is maintained through August.

The GPI satellite-derived precipitation climatology is shown in Fig. 4.4. Compared to the gauge observations, the satellite-derived product overestimates precipitation. This is particularly true along the SMO, where the difference in July rainfall is in the range of 100 mm. Similar discrepancies in satellite versus gauge data were found by Li et al. (2004) in their evaluation of the 2002 monsoon. The difference may be due to two possible factors. First, the algorithm used to derive rain rate may tend to overestimate. The algorithm tends to perform more poorly in areas with a high coverage of cirrus clouds. That may explain why the rainfall maximum in western Mexico is shifted a bit farther west than observations. Second, the stations which are

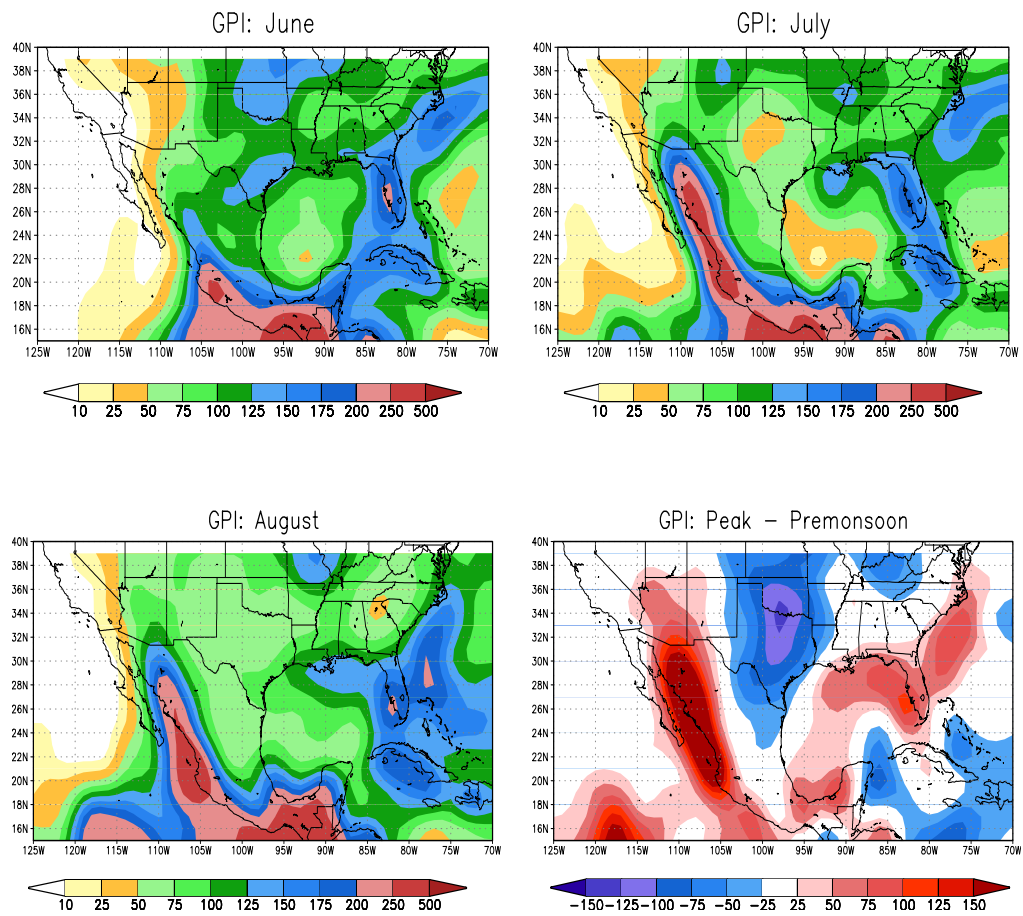


Figure 4.4: Same as Fig. 4.3 for the GPI (1998-2004) average satellite-derived precipitation.

used to collect the gauge data in areas of complex terrain are typically located in valleys where rainfall amounts may be lower than the surrounding higher elevations. In spite of the difference in rainfall amount, the GPI product does capture the evolution of summer rainfall from premonsoon to monsoon peak conditions.

The RAMS-Reanalysis downscaled precipitation (Fig. 4.5) shows a similar pattern of precipitation, though there are important differences. As in observations, RAMS captures the springtime maximum in precipitation in the central U.S. and the onset of the North American monsoon in northwest Mexico and the Southwest U.S. In western North America, the precipitation is clearly tied to the topography, with a greater amount of precipitation occurring with higher elevation. In general, in this particular model configuration with the Kain-Fritsch scheme, RAMS tends to overestimate total precipitation throughout the entire domain when compared to the gauge data. It overestimates most in the Southeast U.S. and Mexico with rainfall errors approaching 100 mm in a month. An exception to this is the western part of the NAMS region (western Sonora and western Arizona), where precipitation is slightly underestimated. This may be a result of the model underestimating the strength of moisture flux from the Gulf of California into this region. As in Li et al. (2004), the RCM data tend to agree better with the satellite-derived rainfall overall.

The corresponding NCEP reanalysis precipitation (Fig. 4.6), in contrast to the RAMS data and observational data, does not capture the seasonal evolution of precipitation well. The NAMS, as represented in the reanalysis, does not properly advance northwestward along the SMO and into the Southwest U.S. in July and August. The core of maximum rainfall (greater than 100 mm per month) does not even reach

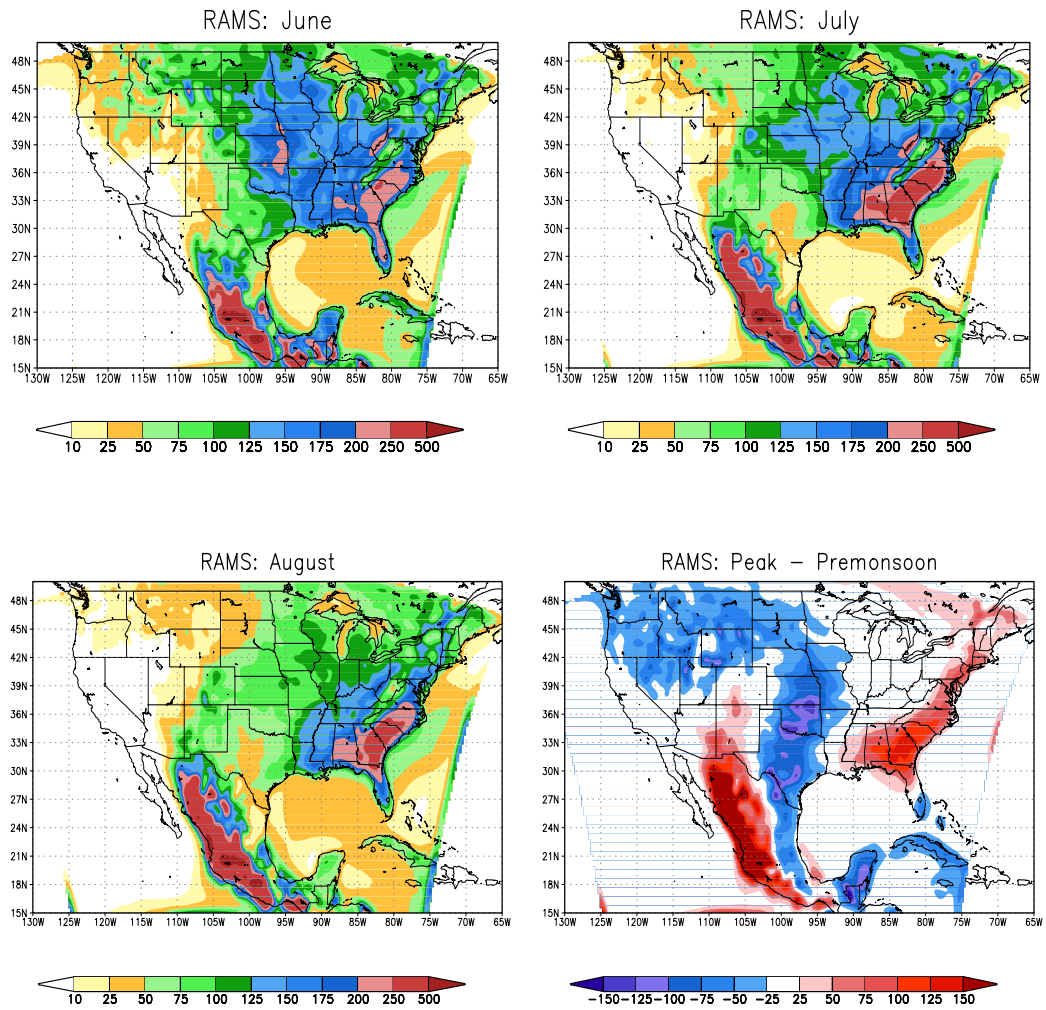


Figure 4.5: Same as Fig. 4.3 for (1950-2002) RAMS average precipitation.

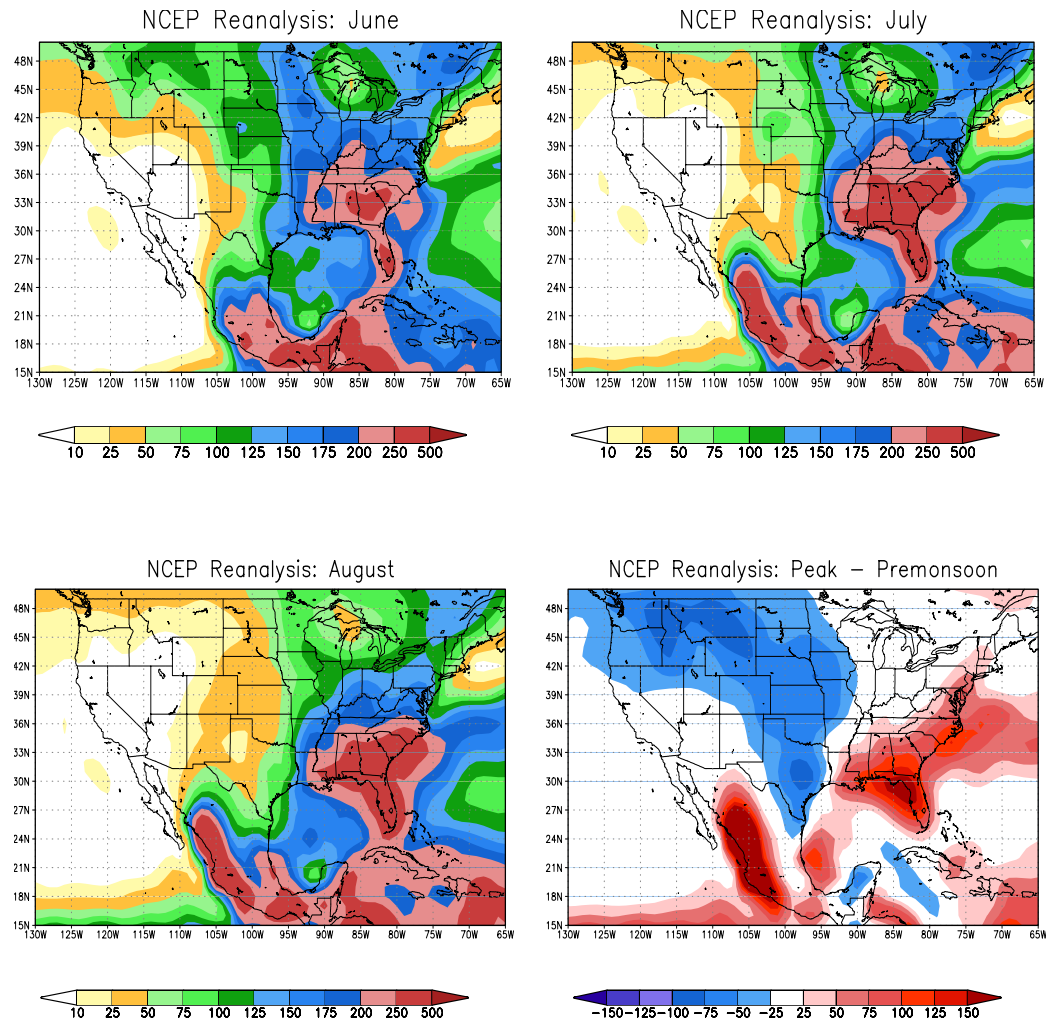


Figure 4.6: Same as Fig. 4.3 for (1950-2002) NCEP Reanalysis precipitation.

Sonora. August rainfall in Arizona barely exceeds 10 mm. In the eastern U.S., beyond the Great Plains, rainfall is overestimated through the entire summer compared to gauge data, particularly in July. In the Great Plains itself, however, the precipitation is slightly underestimated in July and August. Overall, the reanalysis tends to have difficulties in under-representing the precipitation in the areas where NAMS has the greatest influence on the precipitation; the core monsoon region and the central U.S. It will later be shown that the most likely cause is the underestimation of the diurnal cycle.

To further investigate the timing and amount of precipitation in the core monsoon region and central U.S., the time evolution of daily average precipitation for the Great Plains (GP), Southwest U.S. (SW), northern Sierra Madre Occidental (NSMO), and southern Sierra Madre Occidental (SSMO) is considered. The locations of these regions are shown in Fig. 4.7. The Great Plains and Southwest regions are nearly identical to those in Castro et al. (2001). First, the observational products of NCEP gauge precipitation and the GPI product are considered. Note that only the part of the Great Plains south of 40° N is included in the GPI data. Both observational products (Fig. 4.8) show a dry premonsoon period in the core monsoon region with a sudden jump in the precipitation during the onset period. Again, this onset period agrees with Higgins et al. (1999). The differences between the gauge precipitation and the GPI product become most apparent during this time. In the NSMO, in particular, the precipitation amount estimated by the satellite product is about double that of the gauge observations (6 mm day⁻¹ versus 3 mm day⁻¹). Meanwhile, precipitation in the Great Plains gradually decreases following onset by about 1 mm day⁻¹ in the gauge data and 2 mm day⁻¹ in the GPI data.

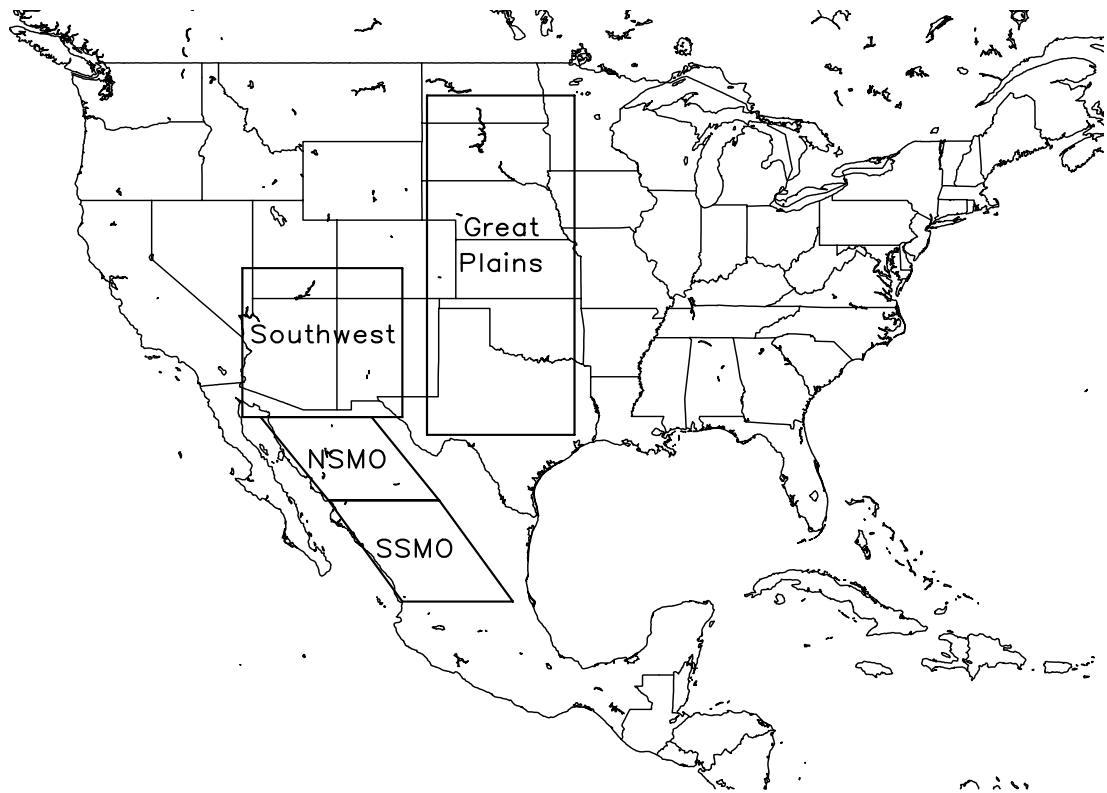


Figure 4.7: Selected regions used in considering the time evolution of temperature and precipitation.

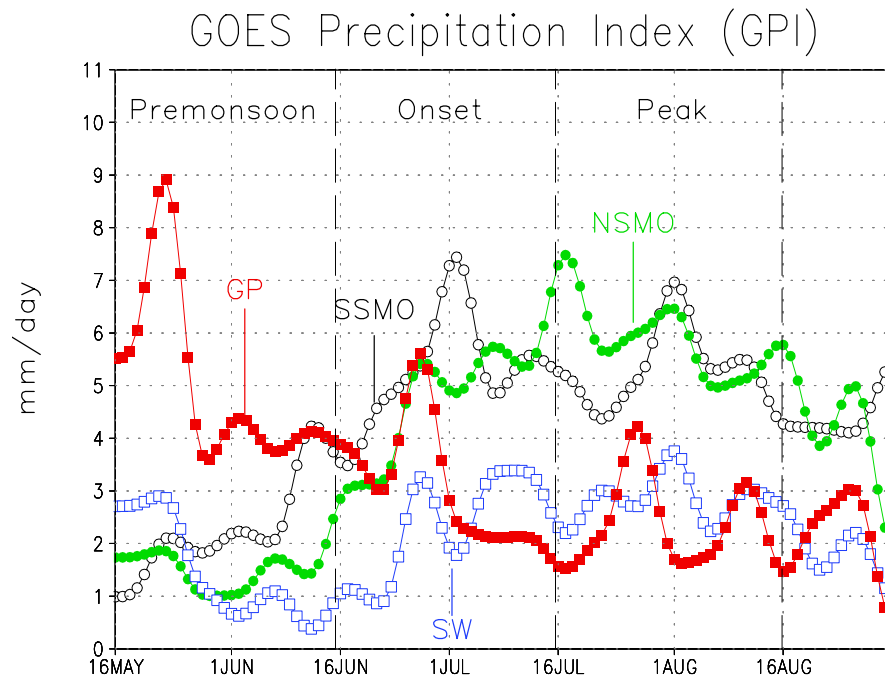
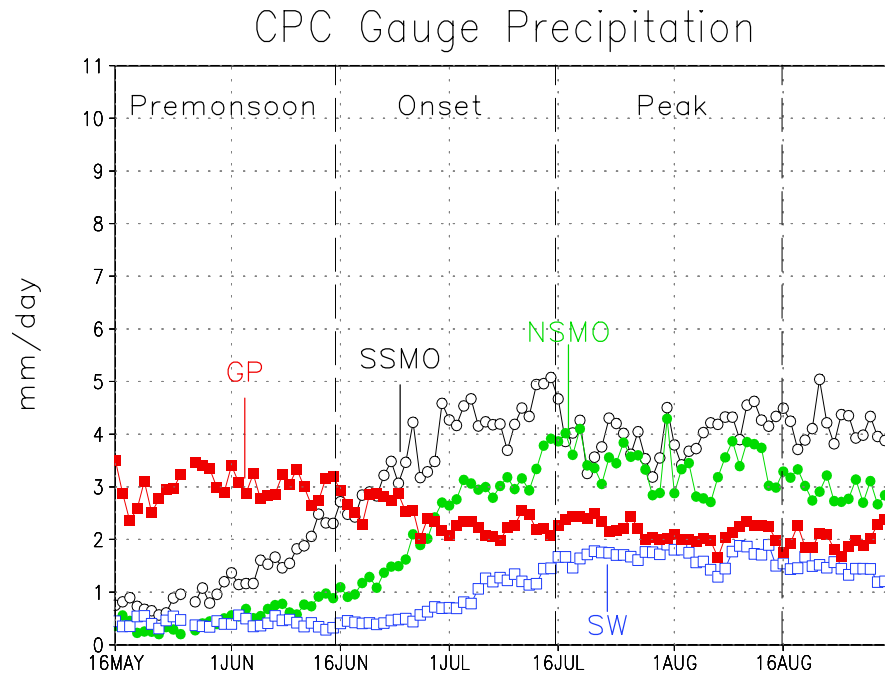


Figure 4.8: Evolution of average observed precipitation (mm day^{-1}) by gauge and satellite data for the regions identified in Fig. 4.7. Premonsoon, monsoon onset, and monsoon peak periods identified.

The corresponding NCEP reanalysis and RAMS precipitation are shown in Fig. 4.9. Recall the original hypothesis that the reanalysis precipitation should worsen as the summer proceeds, and that is the case. While the reanalysis overestimates precipitation in the SSMO by several mm day^{-1} , in the other monsoon regions precipitation amounts are underestimated throughout the summer season. The sudden increase in precipitation during the monsoon onset period does not occur. In the Southwest U.S., precipitation remains virtually unchanged through the entire summer and there is no monsoon at all. Though the Great Plains does exhibit a decrease in precipitation through the summer, August precipitation is underestimated. RAMS increases the precipitation in all regions and shows an RCM can improve upon the reanalysis in some regions. Most important, RAMS captures the sudden jump in precipitation in the NSMO and Southwest U.S. regions at monsoon onset. As mentioned earlier, the evolution of precipitation in the GP, NSMO, and SW are close to that depicted by the GPI product. The one region in which RAMS appears to degrade the precipitation estimate is the SSMO, where the NCEP reanalysis already overestimates precipitation. This comparison of precipitation between the observational and model products demonstrates that the higher resolution of the RCM is necessary to capture the abrupt transitions in North American climate associated with NAMS development.

June-August averaged observed surface temperature from summary of the day data along with the difference between the monsoon peak and onset periods are shown in Fig. 4.10. Note here only the core monsoon region and the central U.S. are shown, as

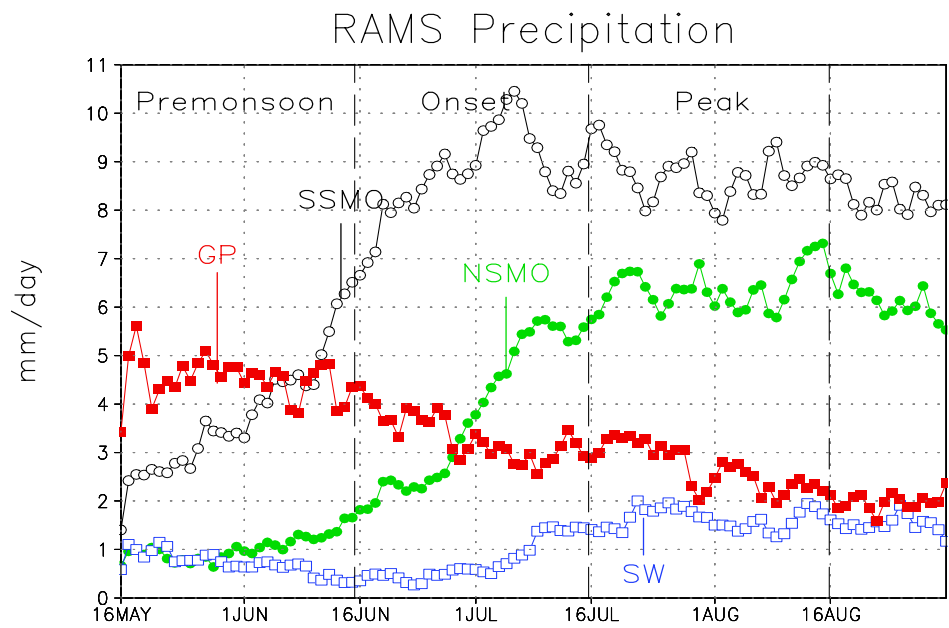
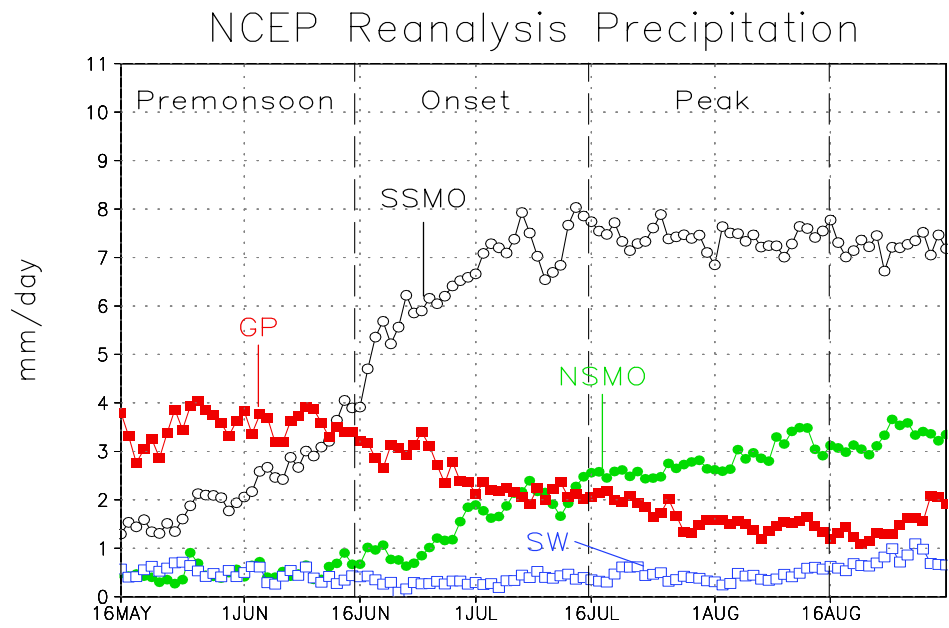


Figure 4.9: Same as Fig. 4.8 for NCEP Reanalysis and RAMS precipitation.

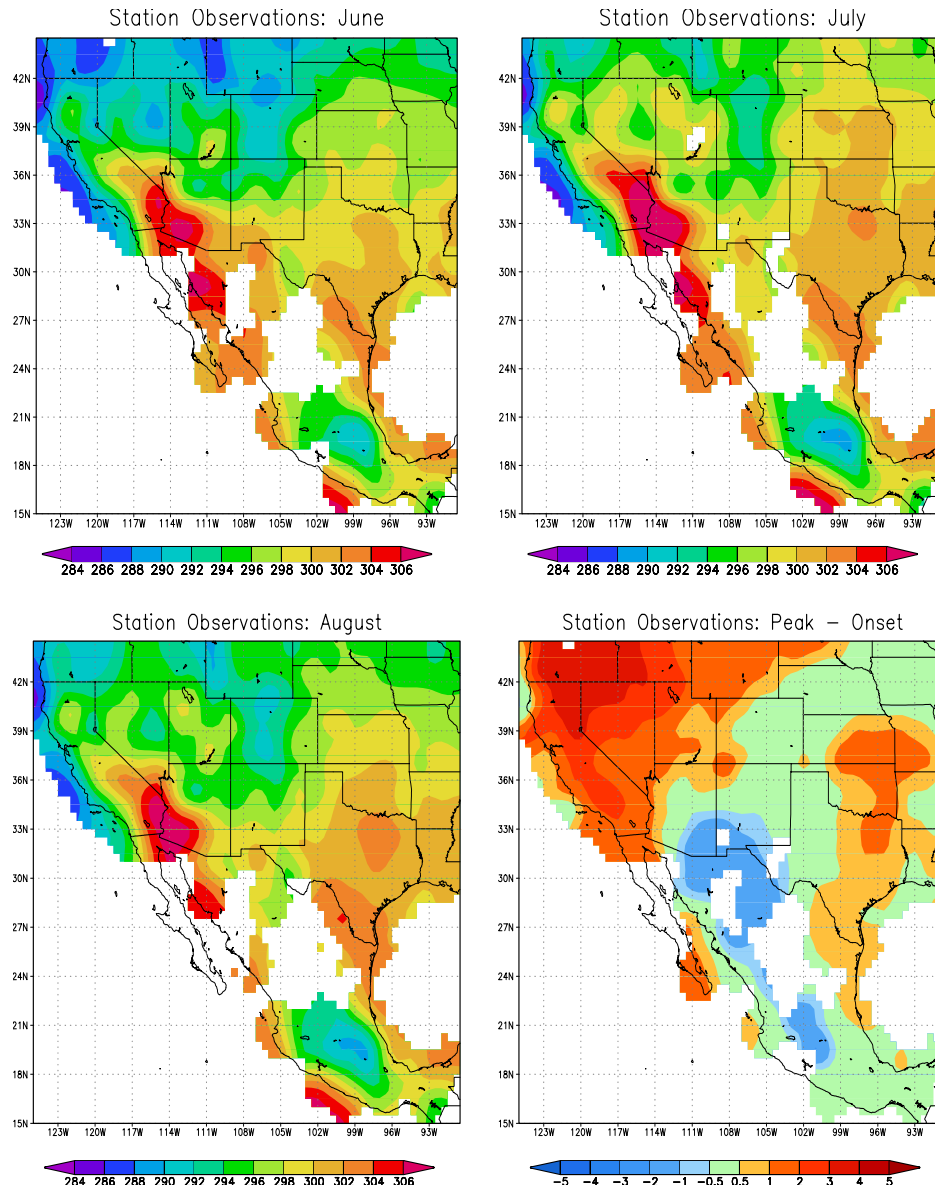


Figure 4.10: Summary of the day (1973-1996) averaged observed surface temperature (K) for the summer months and the difference between the monsoon peak and monsoon onset periods. Shading indicated by the color bar. Data missing in unshaded areas.

those are the regions of greatest interest. In general, the station observations seen here agree well with satellite-derived skin temperature documented in the Xu et al. (2004) climatology. The most striking feature is the temperature maximum in the Colorado River Valley matching the climatological position of a surface heat low that forms in this location. This local maximum in average surface temperature is greater than 306 K. The difference plot shows that in the region of heaviest monsoon rainfall surface temperature decreases after monsoon onset by 1 to 2 K. This region includes northwest Mexico and the southern parts of Arizona and New Mexico. While this occurs, temperatures in the surrounding areas increase, including the central U.S. Shown in Fig. 4.11 is the corresponding RAMS temperature at the first model level. As in the MM5 simulations of Xu et al. (2004), RAMS captures these climatological transitions in surface temperature well. The area of temperature decrease from monsoon peak to onset nearly matches observations in terms of strength and magnitude, though the corresponding temperature increase in other areas is slightly overestimated.

The time evolution of average surface temperature through the summer season for the regions in Fig. 4.7 is shown in Fig 4.12. In all the monsoon regions, temperatures increase until monsoon onset, then temperatures begin a more gradual decrease. Xu et al. (2004) show their MM5 modeled surface temperature in northwest Mexico and the Southwest U.S. to continue to increase after onset, but that result does not agree with the station observations. The temperature decreases are more dramatic in Mexico, especially in the SMO (3-4 K) due to the higher amount of monsoon rainfall. The average surface temperature in the Great Plains tends to increase to a maximum of 300 K in mid-July, then decrease into August. In the RAMS simulations, there is a small cold bias for all of

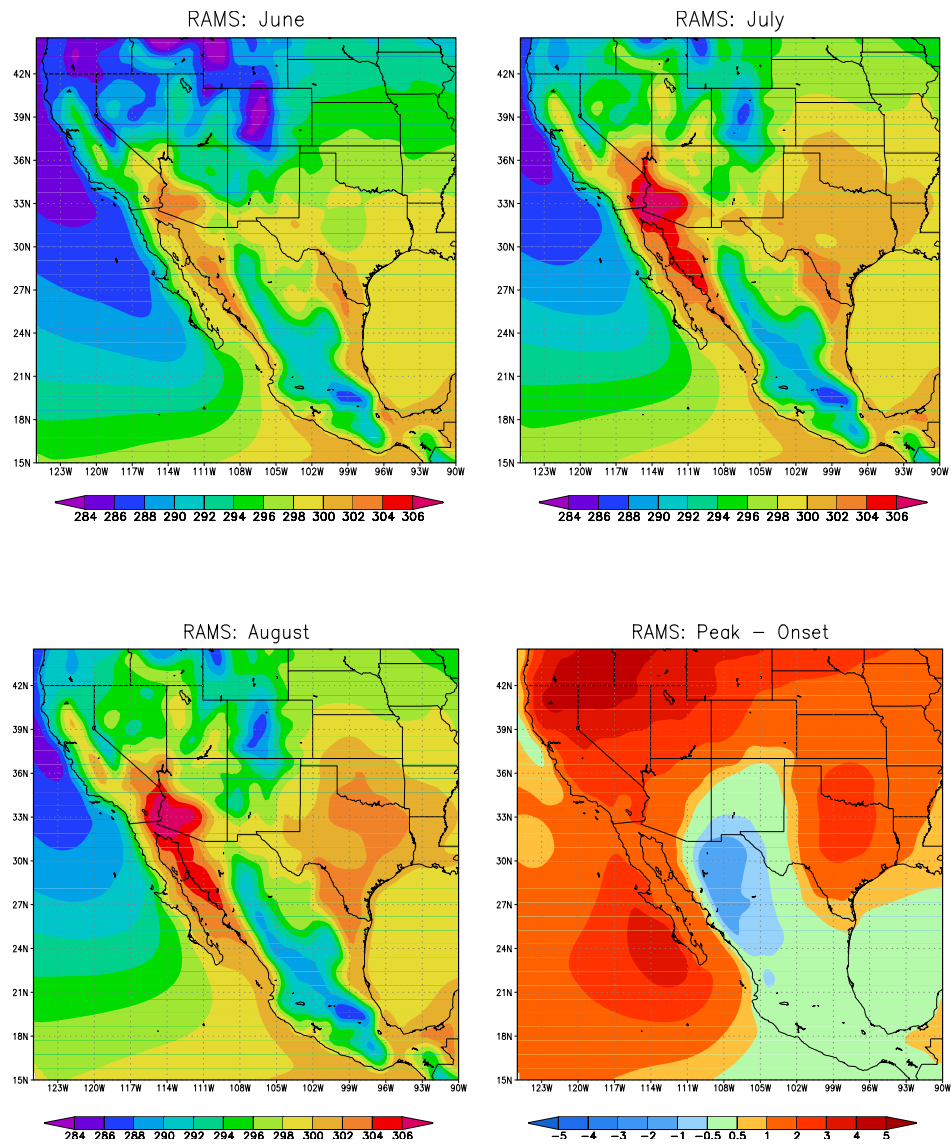


Figure 4.11: Same as Fig. 4.10 for RAMS (1950-2002) average temperature at the first model level.

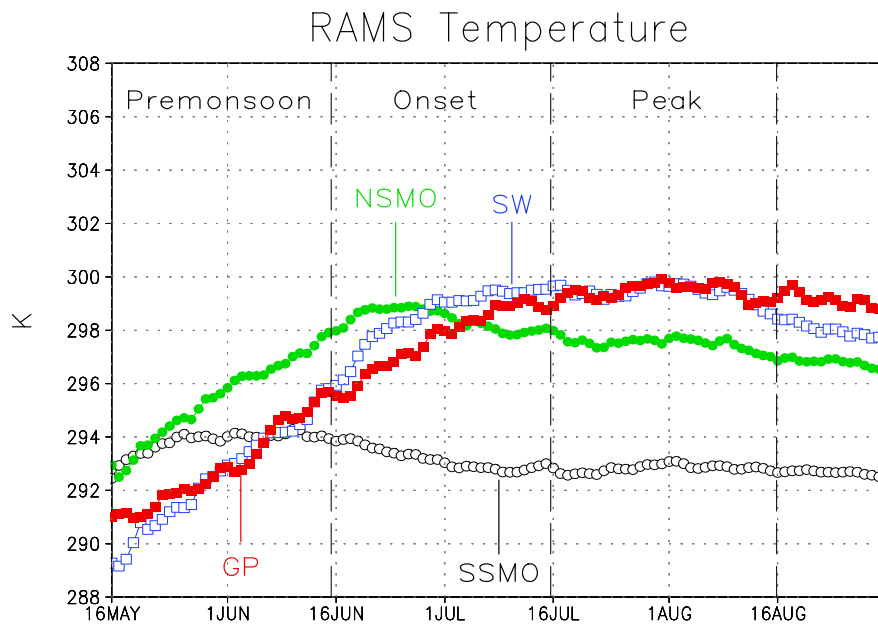
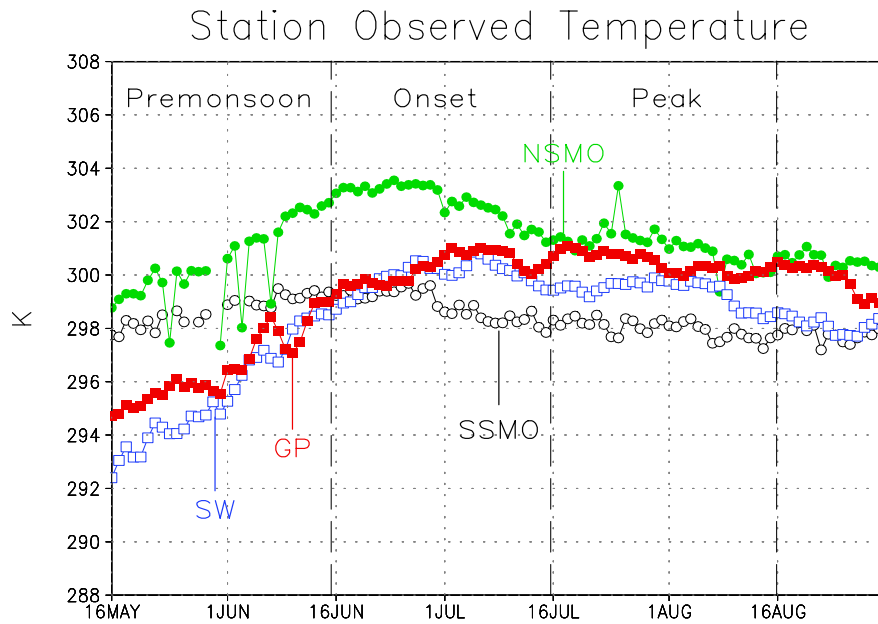


Figure 4.12: Evolution of average observed surface temperature (K) from summary of the day data and RAMS temperature at the first model level for the regions identified in Fig. 4.7. Premonsoon, monsoon onset, and monsoon peak periods identified.

the regions. The cold bias in the monsoon regions may be due to the fact that rainfall is overestimated or that observing stations are located at lower elevations. As in observations, all regions, except the SSMO, exhibit an increase in surface temperature through June. Modeled surface temperatures in the NSMO show a decrease following monsoon onset. However, modeled surface temperatures do not decrease in the Southwest U.S. The reason for the discrepancy between the two regions relates to their surface energy budgets, which will be discussed later in this section.

In lieu of showing the evolution of the surface winds, the surface moisture flux is shown because the two LLJ are more apparent. The Great Plains LLJ maximum is actually above the surface, but the model data are viewed at the surface because it is directly comparable with station observations. Fig. 4.13 shows the surface moisture flux calculated from the station observations. The Great Plains LLJ is strongest over the central U.S. in June (near $80 \text{ m s}^{-1} \text{ g kg}^{-1}$), then gradually decreases in strength over the Southern Great Plains (Texas) into July and August. As this occurs, the Gulf of California LLJ increases in strength, as seen by the increased moisture flux in the Colorado River Valley and southern Arizona. Moisture flux also increases east of the continental divide as the summer proceeds, from an enhanced easterly component of the Great Plains LLJ. The magnitude of loss in strength of the Great Plains LLJ is about equal to the gain the Baja LLJ (around $15 \text{ m s}^{-1} \text{ g kg}^{-1}$). Together, these LLJ appear to provide moisture for monsoon rainfall, with the GP LLJ to the east of the continental divide and the Baja LLJ to the west of the continental divide. This would agree with Saleeby and Cotton (2004). The RAMS surface moisture flux at the first model level

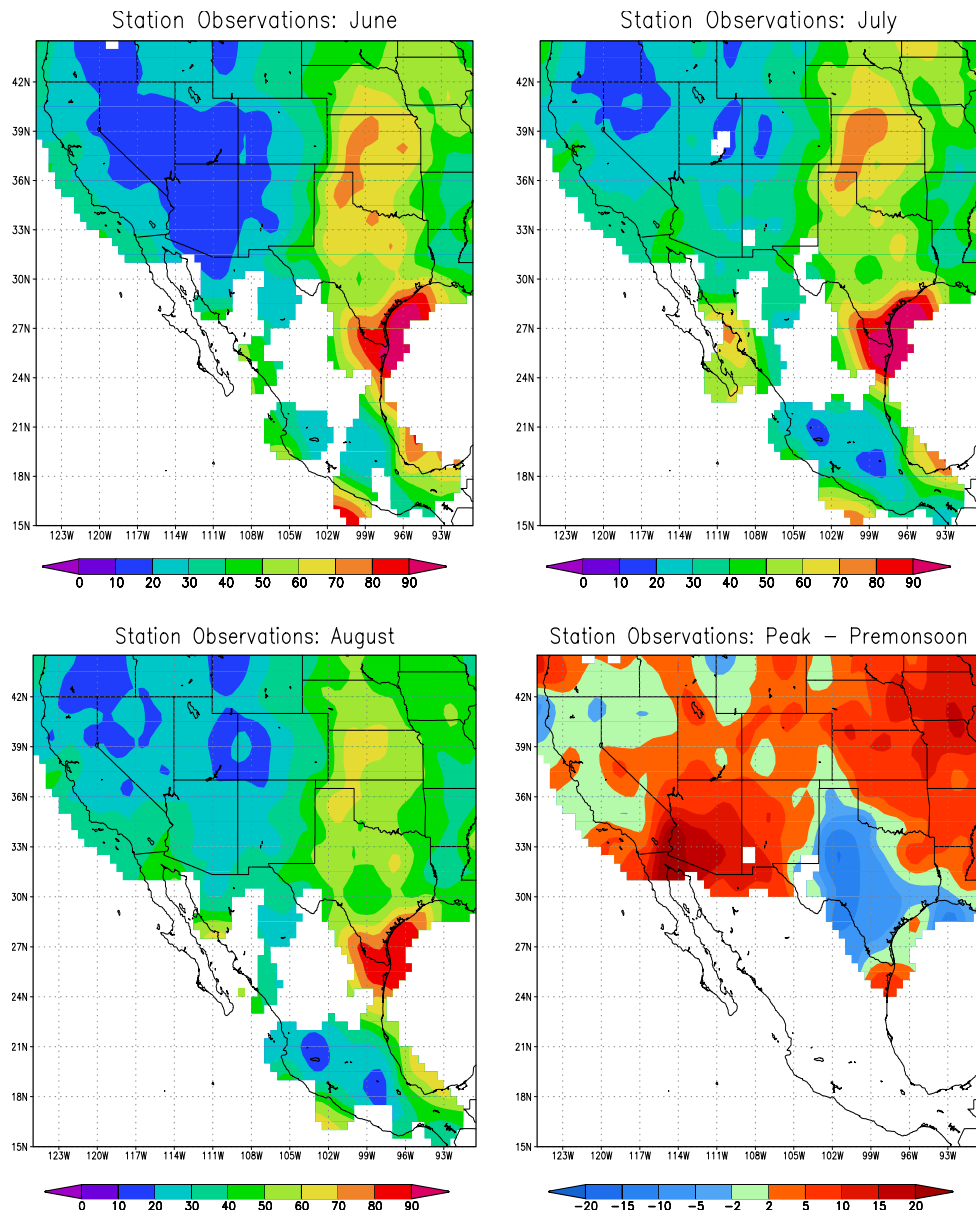


Figure 4.13: Observed average (1973-1996) surface moisture flux ($\text{m s}^{-1} \text{g kg}^{-1}$) from summary of the day data for the summer months and the difference between the monsoon peak and monsoon onset periods. Shading indicated by color bars. Data missing in unshaded areas.

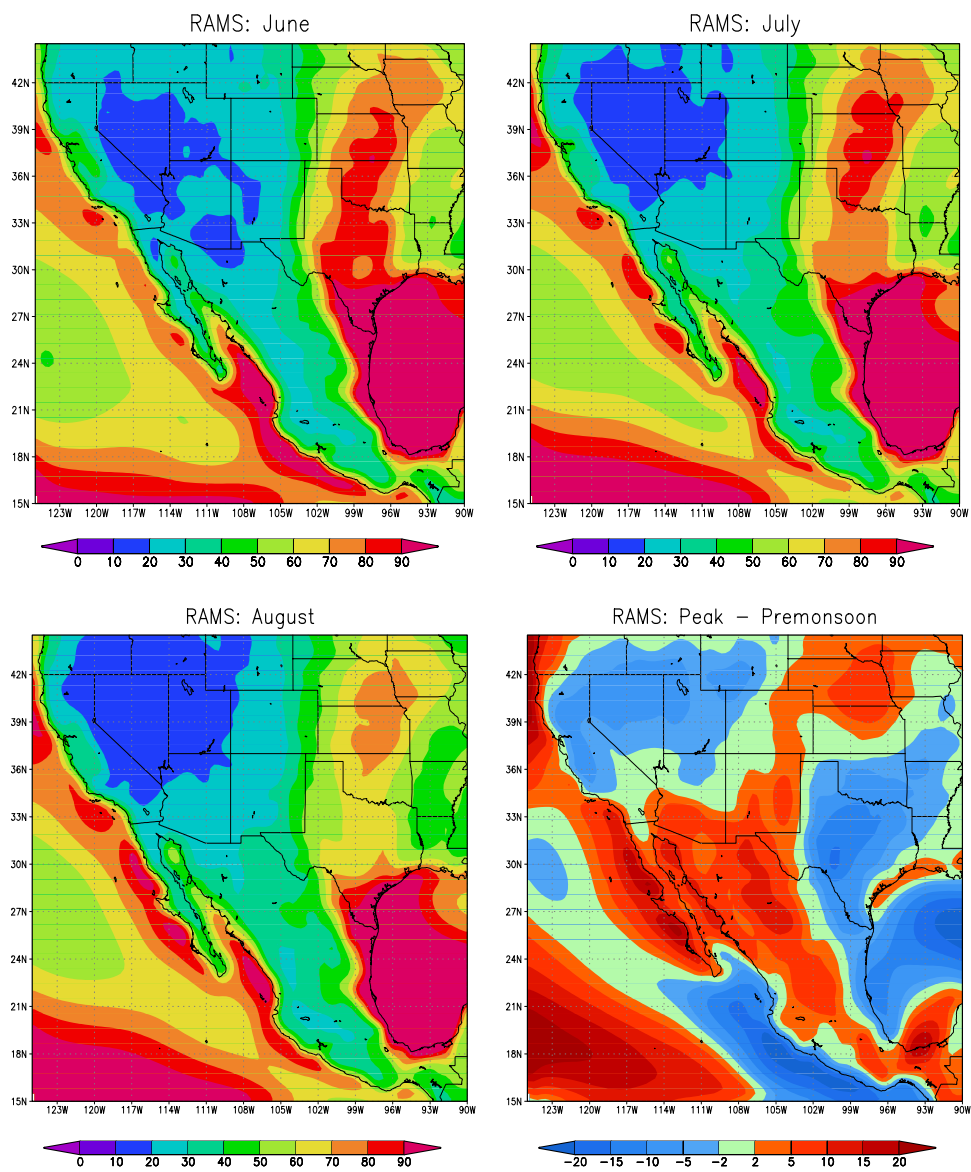


Figure 4.14: Same as Fig. 4.13 for (1950-2002) RAMS average moisture flux at the first model level.

(Fig. 4.14) show these key features, with some subtle differences. The Great Plains LLJ maximum is located slightly eastward of where it occurs in observations and is slightly stronger, but still exhibits a decrease over the southern Great Plains as the summer proceeds. The corresponding increase in moisture flux from the Gulf of California, however, is not as dramatic as the station observations.

A significant portion of the variability of the Baja LLJ occurs due to periodic Gulf surge events, such as demonstrated by Berbery et al. (2001) and Berbery et al. (2003). Surges are characterized by southeasterly winds through the Gulf of California, so the total wind vector is parallel to the coast. To investigate whether RAMS in this particular configuration captures this behavior, RAMS winds were compared with winds derived from the QuikSCAT satellite along axis of the Gulf of California for the summer 2000 season (not shown). The QuikSCAT data clearly showed such surge events. However, the corresponding RAMS model simulation showed southerly winds confined to the far northern end of the Gulf of California during the surges. The zonal component of the wind was always westerly (not easterly), but did slacken when a surge event occurred. Possible reasons for RAMS to incorrectly represent the surge events will be discussed in Section 4.5.

4.4 Behavior of Atmospheric Circulation and Surface Heat Fluxes

The monthly average 500-mb height and 700-mb winds (Fig. 4.15) shows results nearly identical to the Xu et al. (2004) climatology and the NCEP reanalysis (not shown). Such a result should not be surprising since in this case the regional model is being nudged in its interior. The salient features of the climatology of the 500-mb height field

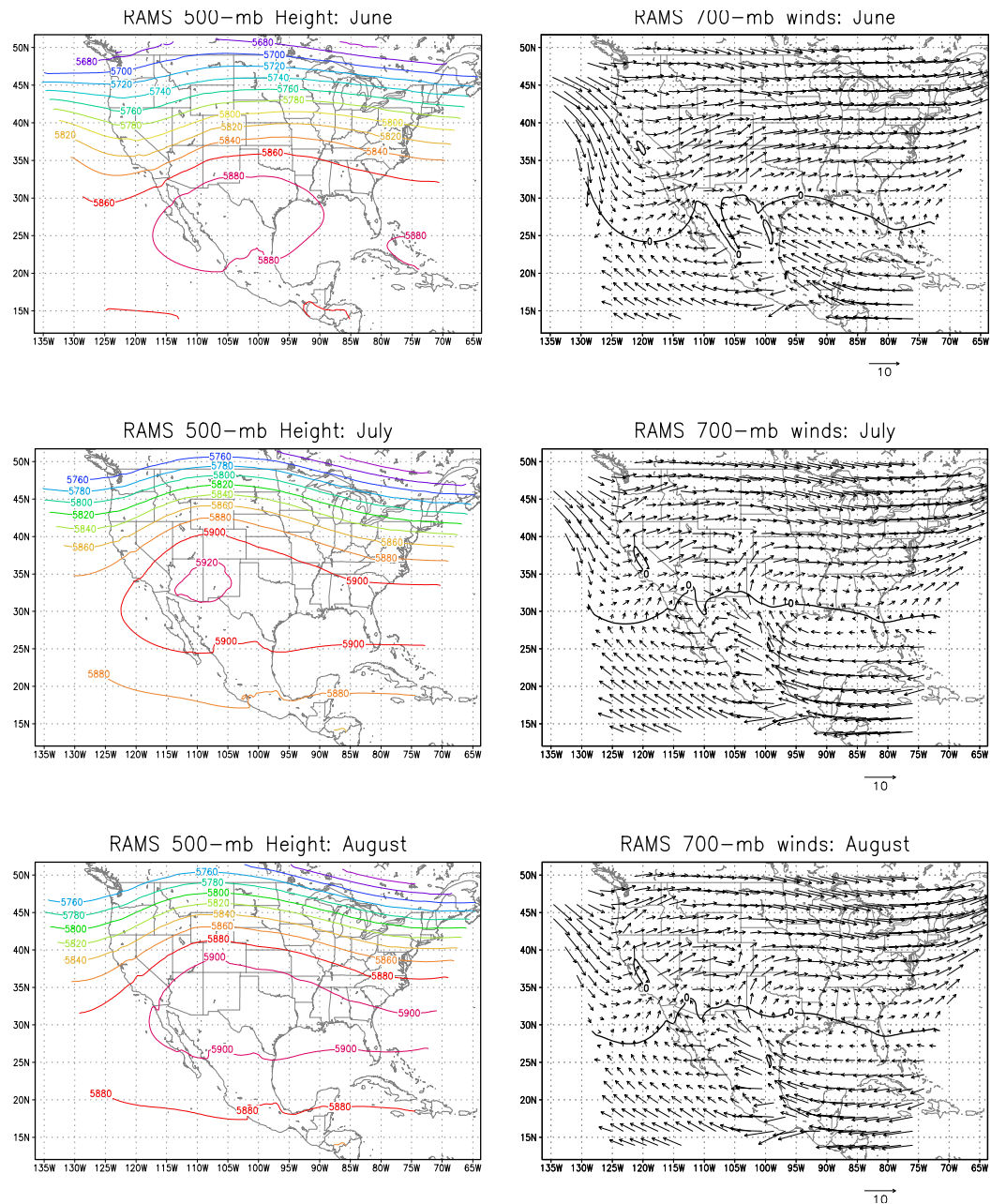


Figure 4.15: Monthly RAMS average 500-mb geopotential height (m) and 700-mb wind vectors for the summer months. Contour interval for geopotential height is 20 m. The average zero mean zonal wind line is indicated by a solid line on the streamline plots. Vector length is 10 m s^{-1} .

evolution have been documented, for example, in Castro et al. (2001). An upper-level monsoon ridge begins to move northwestward from the Mexican plateau in June. The ridge attains its maximum strength and northward position over the four corners region in late July and August. The 700-mb winds also show a northwestward advancing anticyclonic circulation which centers itself over the Colorado River Valley during July and August. To the south of this anticyclonic center, winds are easterly. At this time, the zero mean zonal wind line reaches into Arizona and New Mexico, but easterlies can periodically penetrate further northward with the passage of disturbances around the southern periphery of the ridge. In the monsoon regions identified earlier, the switch to easterly flow at 700-mb generally corresponds to monsoon onset. This suggests that most of the upper level moisture for the monsoon is originating from the Gulf of Mexico after onset, in agreement with previous reanalysis studies (e.g. Schmitz and Mullen 1996).

The average monthly sensible and latent heat fluxes, and the difference between the monsoon peak minus premonsoon period are shown in Figs. 4.16 and 4.17. The surface heat fluxes reflect the evolution of the surface temperature shown earlier, and the largest changes over the summer are found in the south-central U.S. and core monsoon region. Before the onset of the monsoon in June there is a maximum in sensible heat flux located over the Sonoran desert and east coast of Mexico. In the south-central U.S., most of the surface energy is being partitioned to latent heat (greater than 200 W m^{-2}), which confirms that this region is an important moisture source for precipitation (Brubaker 2001). In the monsoon months of July and August, the latent heat flux decreases and the sensible heat flux increases as the soil dries out. The core monsoon region can be divided into two parts with distinct behavior with respect to surface heat fluxes. In areas with the

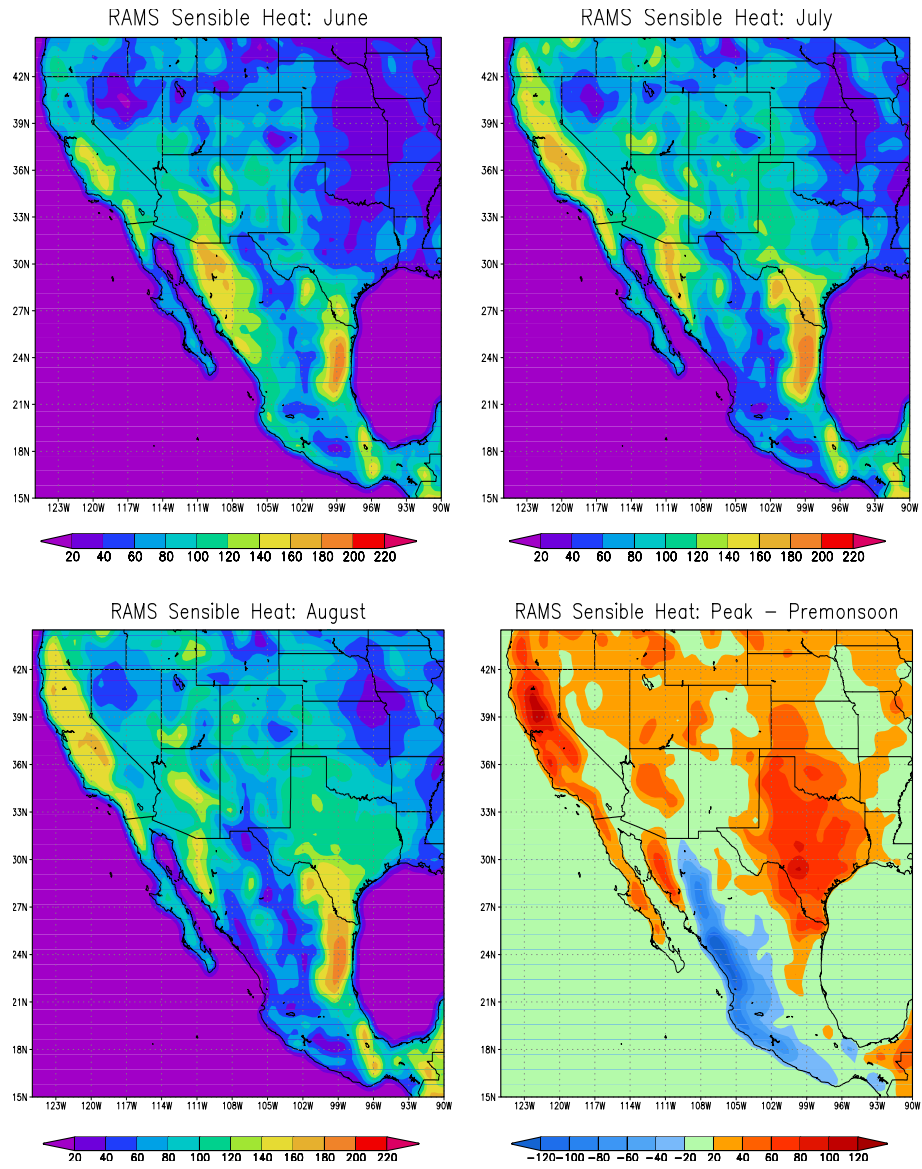


Figure 4.16: RAMS average monthly sensible heat flux ($W m^{-2}$) for the summer months and the difference between the monsoon peak and premonsoon periods. Shading indicated by the color bar.

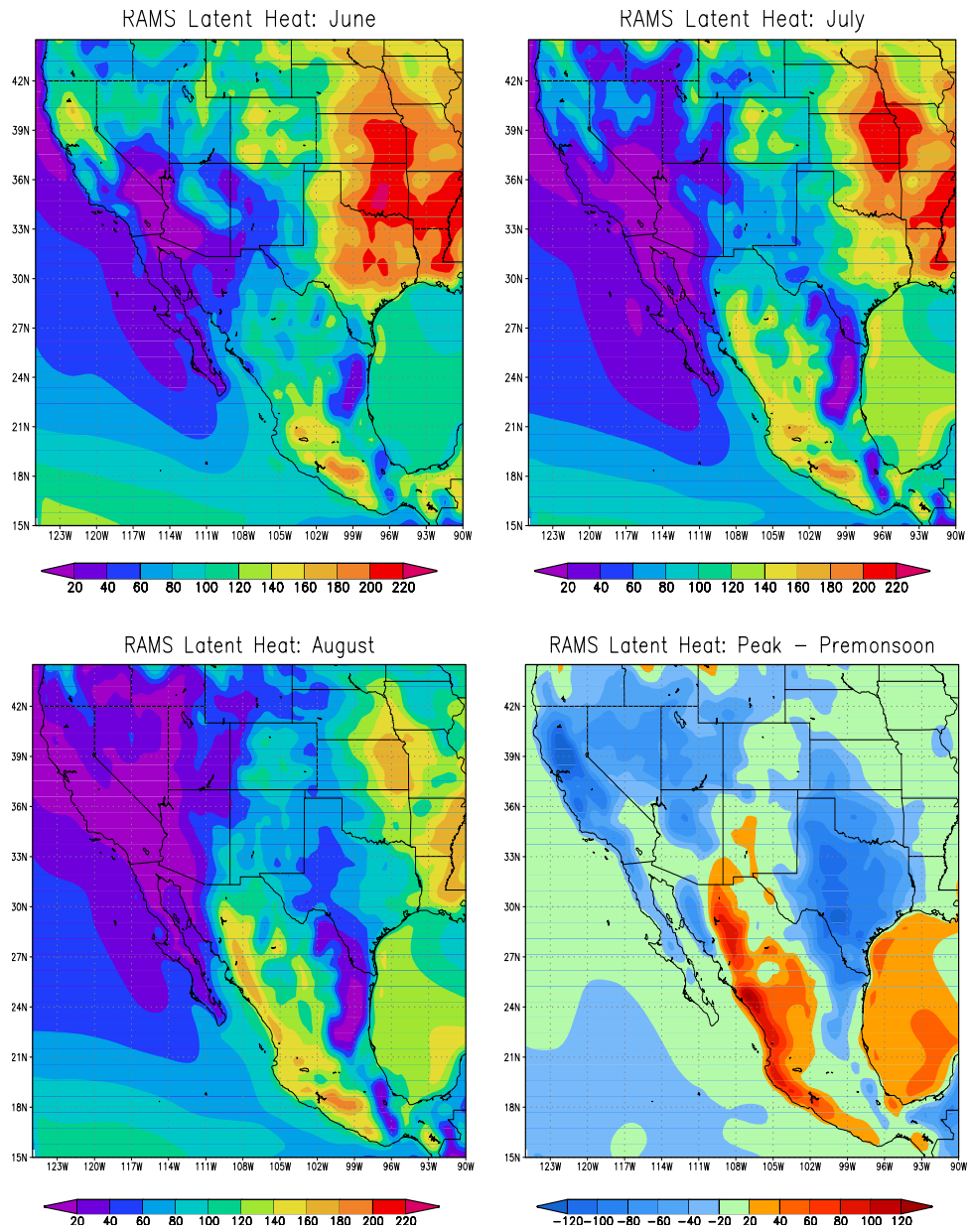


Figure 4.17: Same as Fig. 4.16 for average RAMS latent heat flux.

heaviest rainfall, namely the SMO in Mexico, the sensible heat flux decreases and latent heat increases after monsoon onset. To the north and west, in the Southwest U.S. and most of Sonora, even though rainfall increases in the monsoon season it is less and more intraseasonally variable. So the sensible heat flux increases and the latent heat decreases after monsoon onset. The changes in the surface energy budget are comparable to the central U.S. This would explain why modeled surface temperatures do not decrease following monsoon onset in the Southwest U.S. (Fig. 4.12). What precipitation that does fall is evaporated quickly enough so surface temperatures recover.

4.5 Integrated Moisture Flux Convergence and 500-mb Vorticity

Since the integrated moisture flux and 500-mb vorticity reflect time-varying modes of atmospheric variability, they are evaluated using a conventional Fourier analysis technique (e.g. von Storch and Zwiers 1999). Similar spectral decomposition approaches have been done in other studies using RCM data (Berbery et al. 2003) and radar observations (Carbone et al. 2002). First, the given model variable (x) is defined for a thirty day period about a given date. Since the model output is four times per day, N is equal to 120. The data are tapered using a Hanning, or cosine bell, window. For each time t .

$$x_t = \frac{1}{2} \left(1 - \cos \left(\frac{2\pi t}{N} \right) \right) x_t \quad (4.1)$$

for $1 \leq t \leq N$.

The Fourier coefficients of x_t are

$$A_k = \frac{2}{N} \sum_{t=1}^N x_t \cos\left(\frac{2\pi kt}{N}\right) \quad (4.2)$$

$$B_k = \frac{2}{N} \sum_{t=1}^N x_t \sin\left(\frac{2\pi kt}{N}\right) \quad (4.3)$$

for $k = 1, 2, \dots, N/2$.

The spectral power for each k is:

$$\frac{C_k^2}{2} = \frac{A_k^2 + B_k^2}{2}. \quad (4.4)$$

To compute the red noise spectrum, the formulation of Gilman (1963) is used. The normalized red noise spectrum as a function of k is

$$\phi_k = \frac{(1 - \rho^2)}{\left(1 - 2\rho \cos\left(\frac{2\pi k}{N}\right) + \rho^2\right)}. \quad (4.5)$$

The autocorrelation (ρ) is computed as the average of the lag one autocorrelation and the square root of the lag 2 autocorrelation. ϕ_k is then recalculated so the integrated red noise spectrum is equal to the integrated spectral power. The spectral power in a given band k_1 to k_2 is:

$$\frac{C^2}{2} = \sum_{k_1}^{k_2} \left(\frac{C_k^2}{2}\right) \left(\frac{2\pi}{N}\right). \quad (4.6)$$

This is multiplied by a weighting factor (W) that accounts for the area that is above a red noise spectrum. The weighting factor is determined in the following way. First, the integrated spectral power in the band exceeding red noise (A_+) is calculated.

If $\frac{C_k}{2} > \phi_k$ for k in the band k_1 to k_2 then:

$$\sum_{k_1}^{k_2} \left(\frac{C_k^2}{2} - \phi_k \right) \left(\frac{2\pi}{N} \right) = A_+ . \quad (4.7)$$

Next, the total area above and below the red noise spectrum (A_{tot}) is:

$$\sum_{k_1}^{k_2} \left| \frac{C_k^2}{2} - \phi_k \right| \frac{2\pi}{N} = A_{tot} . \quad (4.8)$$

The weighting factor (W) is:

$$W = \frac{A_+}{A_{tot}} . \quad (4.9)$$

A value of $W = 1$ means that all the spectral power in the band exceed red noise and a value of $W = 0$ means that all the spectral power in the band is below red noise.

For each day in the simulation, averaged integrated climatological spectra for the 53 year period ($\frac{C^2}{2}$) are weighted by the fraction of spectral power above the climatological red noise spectrum in a given frequency band (W). The weighting ensures that the most physically relevant features are emphasized. We henceforth refer to the quantity $W \frac{C^2}{2}$ as the weighted spectral power. Three distinct frequency bands are specified: a synoptic mode (4-15 days), a sub-synoptic mode (1.5-3 days) and a diurnal mode (1 day).

Since the integrated moisture flux convergence (MFC) is a proxy for convection, the diurnal band should be expected to have the strongest weighted spectral power, and this is indeed the case. Fig. 4.18 shows the weighted spectral power of the diurnal band

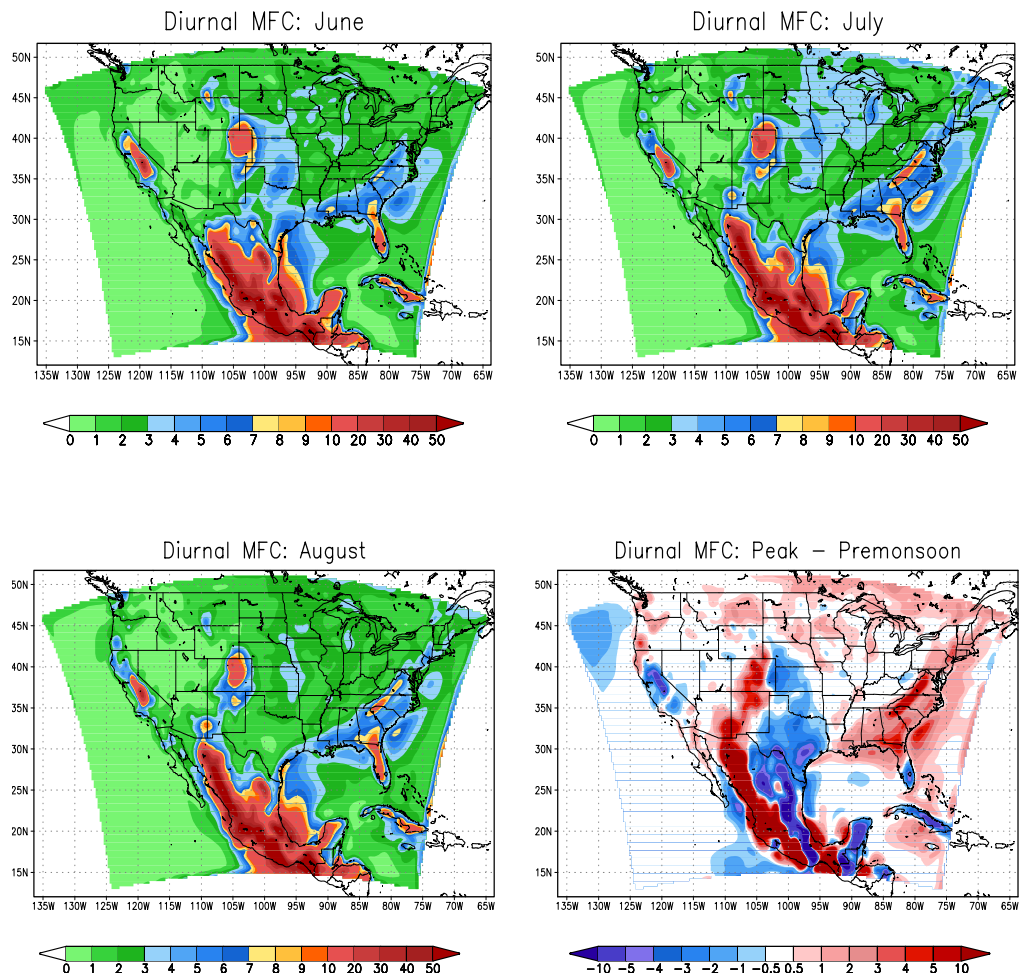


Figure 4.18: Weighted spectral power of RAMS integrated moisture flux convergence ($\text{mm}^2 \text{day}^{-2}$) in the diurnal band for the summer months and the difference between the monsoon peak and premonsoon periods. Shading indicated by the color bar.

for the summer months and the monsoon minus premonsoon period. The weighted spectral power is positive throughout the entire domain. The strongest diurnal signal (greater than $50 \text{ mm}^2 \text{ day}^{-2}$), as would be expected, occurs in central and southern Mexico associated with the tropical convection. This maximum in weighted spectral power advances northwestward along the SMO with the advance of the North American Monsoon, with weighted spectral power exceeding $5 \text{ mm}^2 \text{ day}^{-2}$ in parts of Arizona and New Mexico by August. Another maximum in the diurnal cycle occurs on the eastern side of the Rocky Mountains in Colorado (weighted spectral power greater than $10 \text{ mm}^2 \text{ day}^{-2}$) and extends into the Great Plains, reflecting the nocturnal peak in convection there. In the Southeast U.S., there is a diurnal cycle tied to a sea breeze circulation, particularly in Florida, and diurnal convection along the Appalachians. The difference in diurnal MFC between the monsoon and premonsoon periods mirrors the large-scale changes in rainfall in RAMS and observations shown earlier. There is an increase in the strength of the diurnal cycle in western Mexico and the Southwest U.S., and a decrease over the southern Great Plains and northeast Mexico. Though the diurnal convection is locally forced, its strength is modulated the large-scale circulation. If a similar spectral analysis is performed on the NCEP reanalysis, the magnitude of the diurnal cycle of MFC is about 10 times weaker (not shown). The reanalysis rainfall is most profoundly impacted in areas where the diurnal cycle is the dominant mechanism for summer rainfall, namely the core monsoon region and the central U.S. This provides further evidence that increased resolution of the complex terrain in western North America is very important to an accurate representation of summer climate.

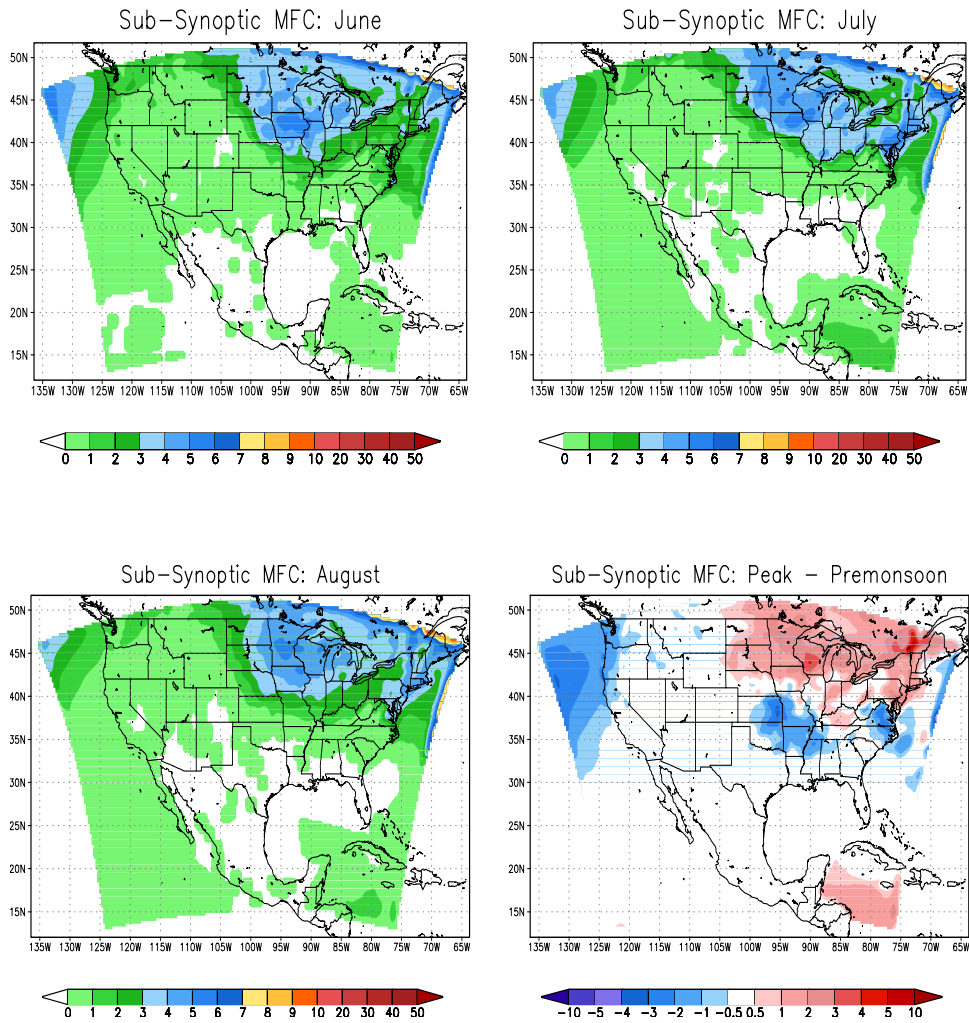


Figure 4.19: Same as Fig. 4.18 for the sub-synoptic (1.5 – 3 day) band.

The other modes of variability in MFC are much weaker in strength than the diurnal cycle, but are still physically important and display different spatial patterns. The sub-synoptic component (Fig. 4.19), unlike the diurnal cycle, has virtually no weighted spectral power in the western U.S., Southeast U.S., or Mexico. Virtually all the variability in this band occurs east of the Rocky Mountains, where it is approximately equal to or slightly more than the magnitude of the diurnal cycle. This band is reflecting convection which is occurring beyond the diurnal timescale, from fast moving synoptic weather systems or propagating mesoscale convective systems (MCSs) around the northeastern periphery of the monsoon ridge. These MCSs typically originate as diurnal convection over the Rocky Mountains that propagate through the Great Plains and into the Midwest (Wetzel et al. 1983; Carbone et al. 2002). As the monsoon ridge evolves through the summer, the peak minus premonsoon difference shows that this mode decreases in strength in the south central U.S. and increases in strength in the upper Midwest. This mode is partially responsible for the rainfall maximum in the central U.S. in the late spring to early summer.

The synoptic mode of MFC is shown in Fig. 4.20. In addition, the ratio of the weighted spectral power of synoptic MFC to diurnal MFC is also shown in Fig. 4.21 for the central U.S. and core monsoon region. Like the diurnal cycle, this mode has the largest weighted spectral power in the southeast U.S., Mexico, and western U.S. This mode reflects the passage of slower moving, eastward propagating disturbances or tropical easterly waves (TEWs) around the southern periphery of the monsoon ridge. The monsoon minus premonsoon difference in the synoptic MFC clearly shows that the TEWs advance northward as the summer proceeds, affecting convection in central and

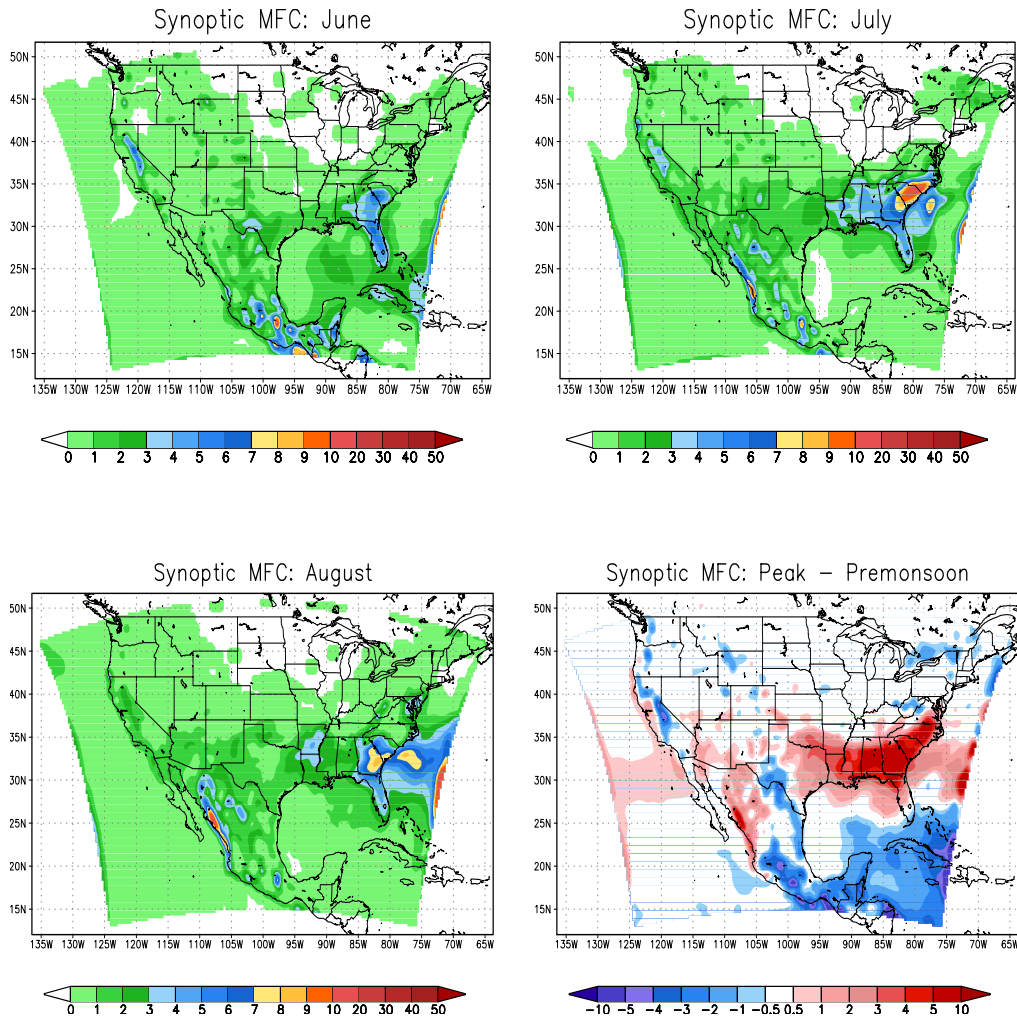


Figure 4.20: Same as Fig. 4.18 for the synoptic (4 – 15 day) band

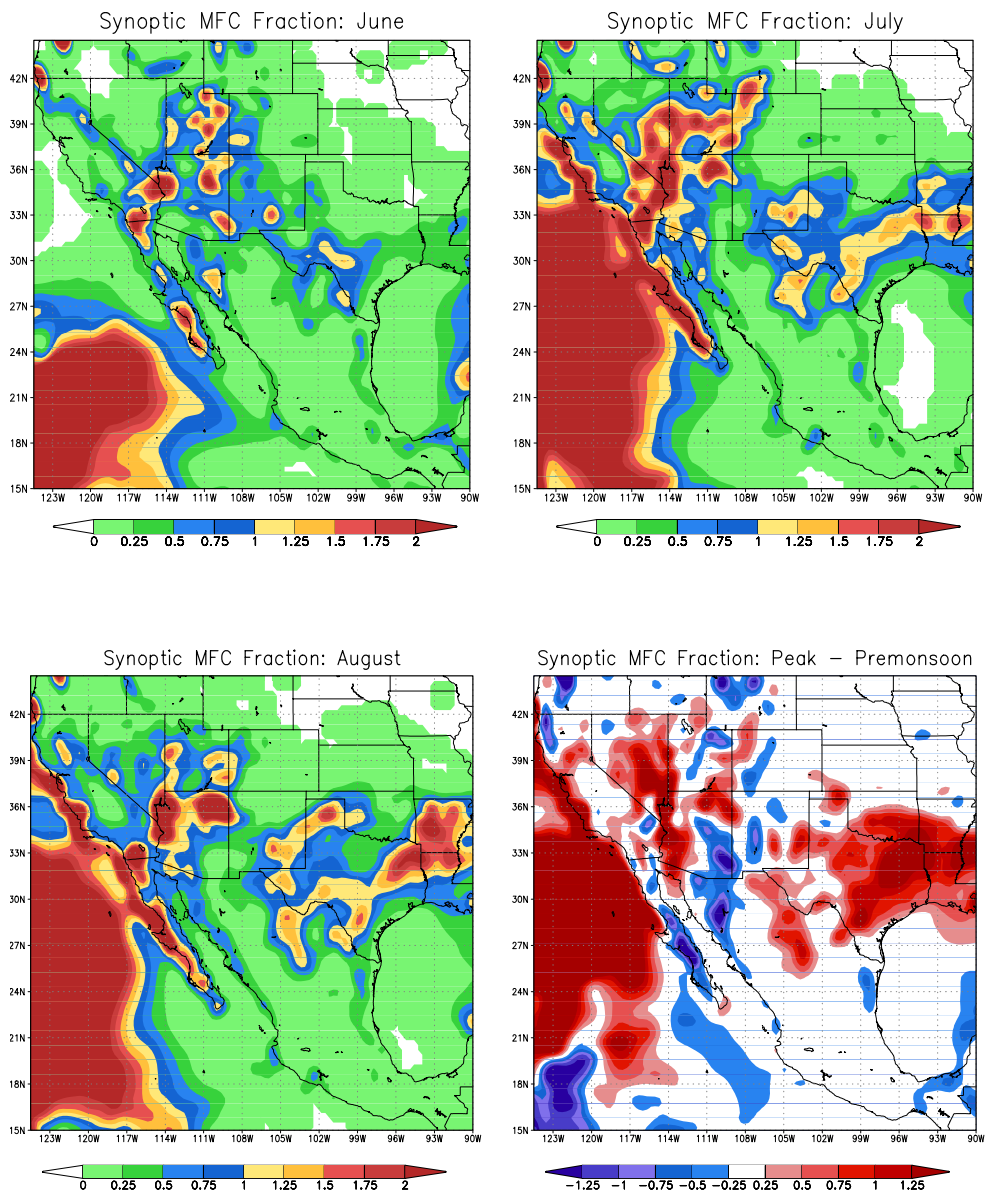


Figure 4.21: Ratio of weighted spectral power of the synoptic MFC to the diurnal MFC for the summer months and the difference between the monsoon peak and premonsoon periods. Shading indicated by the color bar.

southern Mexico in the premonsoon period and then the Southeast U.S. and core monsoon region during the peak of the monsoon. These TEWs cause periodic bursts of convection which enhance the diurnal convection and allow it to more readily propagate off the elevated terrain and organize into MCSs. These bursts are reflected in a significant spectral peak in rainfall in the 12-18 day band in Arizona, for example see Cavazos et al. (2002). If they are propagating westward off the SMO, the MCSs may trigger gulf surges in the Gulf of California. A major surge may be triggered if these events are preceded by the passage of a westerly trough (Adams and Comrie 1997; Stensrud et al. 1997). From Fig. 4.21 it is clear that the synoptic mode has more weighted spectral power than the diurnal mode over lower elevations. In particular, note the Colorado River valley in July and August. In this area the variability of synoptic MFC is about double that of the diurnal cycle, reflecting convection which periodically propagates westward off the Mogollon Rim in Arizona during a gulf surge. Such a westward propagation of convection has been observed in radar observations (Carbone et al. 2002). Though RAMS underestimates the magnitude of the precipitation in central and western Arizona, previous RCM studies have shown that Gulf surge related precipitation accounts for the majority of summer precipitation in that region (Berbery et al. 2003).

The same spectral analysis technique was also applied to the 500-mb vorticity. To get a clearer idea of when the spectral power of the TEWs is greatest, Fig. 4.22 shows a Hovmöller diagram of weighted spectral power of the synoptic component of 500-mb vorticity longitudinally averaged over 95-115° W along with the zero mean zonal wind line. Only the synoptic component is considered because the weighted spectral power in

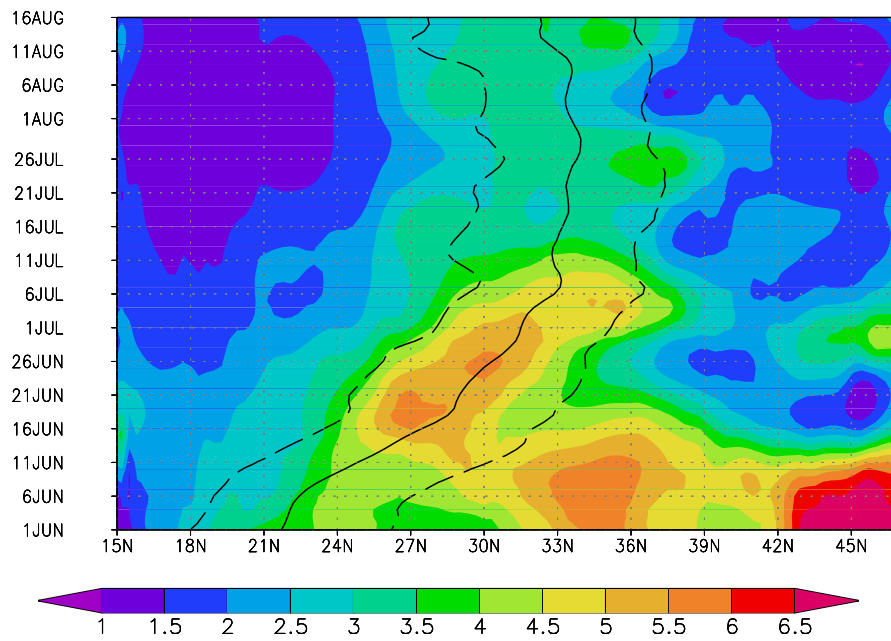


Figure 4.22: Hovmöller diagram of weighted spectral power of the synoptic component of 500-mb vorticity ($\times 10^{-13} \text{ s}^{-2}$) longitudinally averaged over $95 - 115^\circ \text{ W}$ for the period 1 June through 16 August. The solid line indicates the zero mean zonal wind line. Dashed lines indicate one standard deviation of the zero mean zonal wind line.

the other bands is much weaker. There are two distinct maxima in the weighted spectral power. The first occurs in early June to the north of 30° N associated with the passage of synoptic weather systems in westerly flow. The second occurs in late June to early July in a band from approximately 24° N to 36° N. The placement of the zero zonal mean wind suggests that this variability in the 500-mb vorticity is due to the propagation of TEWs around the southern periphery of the monsoon ridge. Though TEWs occur throughout the summer, these data suggest they are more frequent in early summer (monsoon onset), and not the peak of the monsoon in August. However, the RAMS data are not conclusive enough to say whether a greater frequency of Gulf surge events occurs climatologically during the monsoon onset period.

4.6 Discussion

In considering this North American RCM monsoon climatology, three questions are posed. First, given the conclusions of Chapter 3, how well does the model retain value at the large-scale? Recall the large-scale is defined as wavelengths larger or equal to four times the reanalysis grid spacing. Second, how does the RCM enhance physical understanding of the processes on the smaller-scale which an atmospheric reanalysis cannot resolve and have a greater dependence on the surface boundary? Third, what are the deficiencies in the current experimental design and how might it be improved?

The RCM must necessarily maintain fidelity with the large-scale reanalysis, otherwise how the higher resolution surface information adds value to the simulation will be affected. Since the model is being weakly nudged in its interior, the fields we should expect to be nearly identical to the reanalysis are those which are mostly dependent on

the lateral boundary forcing and have little dependence on the surface forcing. These would be the upper-level height fields and winds. As stated Chapter 1, the evolution of these features has been documented by numerous studies, so the results obtained here should be of no surprise. The RCM fields show the development of a monsoon ridge that advances northwestward from central Mexico beginning in June and attains its maximum strength over the Four Corners region of the U.S. in July and August. On the northeast side of the ridge, the flow is northwesterly and subsidence increases in the central U.S. following monsoon onset. On the south and east sides of the ridge, the flow is easterly, transporting moisture into the core monsoon region mainly from the Gulf of Mexico. The present work and the previous study of Xu et al. (2004) show with a sufficiently constrained domain, the RCM maintains these large-scale features.

In general, the reanalysis demonstrates a continental shift in precipitation through the summer, but some important details are missing. The reanalysis fails to capture the rainfall along the northern SMO in Mexico and the Southwest U.S. The majority of this summer rainfall is due to the diurnal cycle of convection in this region, as revealed by analysis of the RAMS integrated moisture flux convergence. Though the diurnal cycle is physically relevant at all land locations in the model domain, it has its greatest spectral power where there are gradients in the surface heating caused by terrain and/or land sea contrast. Where both of these factors are maximized, the strongest amplitude of the diurnal cycle is observed. Specifically, this occurs on the slopes of the SMO in western Mexico during the monsoon.

What the RAMS simulations show, not surprisingly, is that the addition of high resolution surface information is necessary to simulate the terrain-induced mesoscale

circulations which lead to rainfall. In particular, a correct representation of the diurnal cycle is critical to modeling the abrupt precipitation transitions which occur at monsoon onset. Of course, this means the rapid increase in rainfall in the core monsoon region. It is also important, to a lesser extent, in the central U.S., where most of the variability in precipitation is from the diurnal cycle as well. It follows that the transitions in rainfall change the surface energy budget and mean surface air temperatures. For example, the RAMS simulations reveal that if monsoon rainfall is sufficient to lower the ratio of sensible to latent heat flux (Bowen ratio), the mean surface air temperature will decrease. This is the case along the SMO in Mexico and part of southeast Arizona and southern New Mexico, but not the case in the rest of the Southwest U.S. and western Sonora. Only a RCM can provide such a level of detail.

The diurnal cycle necessarily affects the other longer-term modes of atmospheric variability greater than one day. Though these modes may be much weaker than the diurnal cycle, they are nonetheless important for rainfall at a remote distance from the areas of terrain-induced convection. Summer precipitation in the central and eastern U.S. originates from diurnal convection in the Rocky Mountains. With addition of moisture from the Great Plains LLJ this convection organizes into MCSs which have lifetimes greater than one day (e.g. Tripoli and Cotton 1989; Cotton et al. 1983; Wetzel et al. 1983). The RAMS model data show that the MCSs are just as important for rainfall in the Midwest as diurnal convection, as the magnitude of weighted spectral power of MFC is nearly the same for both modes. Fritsch et al. (1986) suggest that MCSs may account for 30-70% of the rainfall in the central U.S. during a summer with average precipitation.

Similarly, in the core monsoon region, there may be periodic enhancements to the diurnal cycle of convection caused by the passage of tropical easterly waves on the southern periphery of the monsoon ridge. These occur on a timescale of 4-15 days, or possibly longer, and tend to occur more frequently in July. The enhanced convection may then propagate westward off the terrain and into the Gulf of California, possibly triggering a Gulf surge. The Gulf surge, in turn, carries moisture northwestward into the Southwest U.S., and enhances convection propagating off the Rocky Mountains or Mogollon Rim in Arizona. Even though RAMS simulated weaker than observed gulf surges, it was nonetheless able to capture this behavior. Analysis of the spectral power of MFC in the synoptic band shows that this mode is more important in lowland regions off the maxima in terrain, like the coastal plain along the Gulf of California or the Colorado River Valley. In these locations, the intraseasonal variability caused by TEWs and gulf surges is more important than the diurnal cycle in producing summer rainfall.

In spite of the ability of RAMS to successfully represent aspects of the summer climate of North America, there were some deficiencies in the simulations. The Baja LLJ was not well resolved in terms of the southeasterly winds through the length of the Gulf of California. The failure to reproduce features of the Baja LLJ may be due to a combination of factors in the experimental design. Though other models have achieved a reasonable representation of the Baja LLJ at comparable grid spacing, a grid spacing of 35 km may not be sufficient for RAMS. The Gulf of California is being resolved by a width of only four grid points at its narrowest point, near the minimum physically resolved wavelength of the model (Pielke 2002). The simplifications in the representation of precipitation may also be a factor. Specifically the model did not

include an explicit microphysical representation of the precipitation nor any parameterization of mesoscale slantwise motion that may account for 40-50% of MCS precipitation. We executed a similar run for the summer 2000 season was executed with a 5 km nested grid over the Gulf of California with explicit microphysics and found RAMS could represent winds in the Gulf of California much better (not shown). It is suspected the fact that the Baja LLJ is not correctly represented may result in the underestimation of precipitation in the western part of the NAMS region, where Gulf surges account for the majority of summer rainfall.

RAMS represented aspects of the summer precipitation well in some regions but not in others. Summer precipitation is notoriously difficult to simulate in a RCM, particularly in the core monsoon region. As discussed in Chapters 1 and 3, the specific choice of model domain size, grid spacing, surface boundary conditions, interior nudging options, the convection scheme, and the choice of reanalysis or GCM forcing data can all significantly affect the model-generated precipitation. It is difficult to define the “correct” RCM configuration which will validate well against observations over all regions in a continental-scale simulation. As seen from the results here, RAMS improved the representation of precipitation, as compared to the NCEP reanalysis, in regions most significantly impacted by NAMS evolution. These were generally regions where the NCEP Reanalysis underestimated precipitation in the first place. RAMS, however, did not significantly improve precipitation in regions where the NCEP Reanalysis already overestimated precipitation, such as the SSMO or Southeast U.S. In addition, what is the “correct” observed precipitation to validate model results against? There can be large discrepancies in the observed precipitation as seen from comparison of gauge versus

satellite observations. The greatest discrepancy in this particular case occurs in the data-sparse region of the SMO in western Mexico. Improving the estimation of precipitation in this region in observations and regional models was one of the major goals of the recent North American Monsoon Experiment (NAME) and is an area of ongoing research.

4.7 Summary

In this chapter, 53 years of the NCEP-NCAR reanalysis have been dynamically downscaled using RAMS to generate a RCM summer climatology of the contiguous U.S. and Mexico. Data from the RAMS simulations were validated against observed precipitation, temperature, and surface moisture flux data. RAMS captures the seasonal transitions in precipitation and temperature associated with the development of the NAMS, particularly the abrupt increase in precipitation in the core monsoon region. As in previous studies, the model-generated precipitation is overestimated compared to gauge data and agrees better with satellite-derived estimates. The Baja and Great Plains LLJ and their evolution through the summer were represented, though the Baja LLJ and associated Gulf surge events were not as strong as observations. The RCM also showed the development of a monsoon ridge at 500-mb over western North America and a transition to easterlies at 700-mb to the south of the ridge.

The integrated moisture flux convergence, a proxy for convective activity, and 500-mb vorticity were spectrally decomposed to investigate the time-varying modes of atmospheric variability. The diurnal cycle is the dominant mode of variability, especially in the core monsoon region and central U.S., and is modulated by the large-scale

circulation. The longer modes of variability, though weaker, are still physically important and have distinct spatial patterns of variability. These longer modes account for the variability of convective rainfall at a remote distance from elevated terrain.

Chapter 5

DIAGNOSING THE EFFECT OF PACIFIC SST ASSOCIATED TELECONNECTIONS ON NORTH AMERICAN SUMMER CLIMATE

5.1 Methodology for Compositing Years According to Dominant Global SST REOFs

Having established that the RAMS RCM 53 year summer climatology of North America adds value above and beyond the corresponding NCEP Reanalysis, the objective of the present chapter is to investigate the important issue of summer climate variability in North America. Specifically, what is the relationship to remote sea surface temperature (SST)? To answer this question with respect to the RCM simulations, it is first necessary to determine and physically characterize the dominant modes of global SST variability. It is convenient to use the existing EOF analysis described in Schubert et al. (2002). In this analysis, the five leading rotated EOFs (REOFs) of global SST were computed using the VARIMAX rotation algorithm (e.g. Richman 1986). The rotation of EOFs reduces the orthogonality constraints and allows more localized structures to emerge, while the EOFs remain uncorrelated in time. The first two leading REOFs for the period 1980-99 are shown in their Fig. 6. Using the same methodology, the SST REOFs were recomputed using SST data from Reynolds and Smith (1994) for the period 1950-2000.

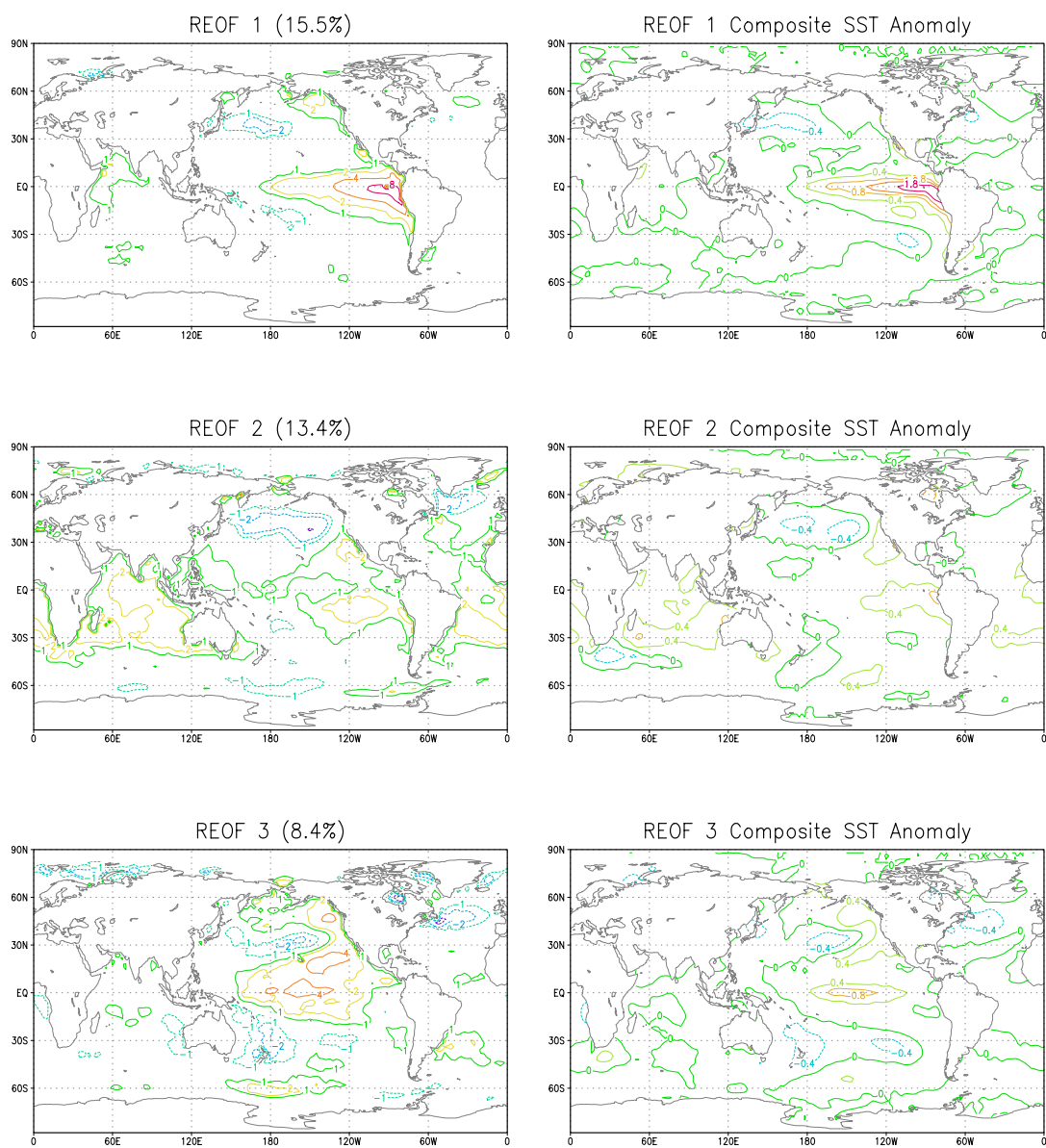


Figure 5.1: The first three rotated EOFs of global SST and composite SST anomalies in boreal summer with percent explained variance. Period considered is 1950-2000. For REOF patterns units are arbitrary and contour interval is one unit. SST anomalies in K and contour interval is 0.4 K.

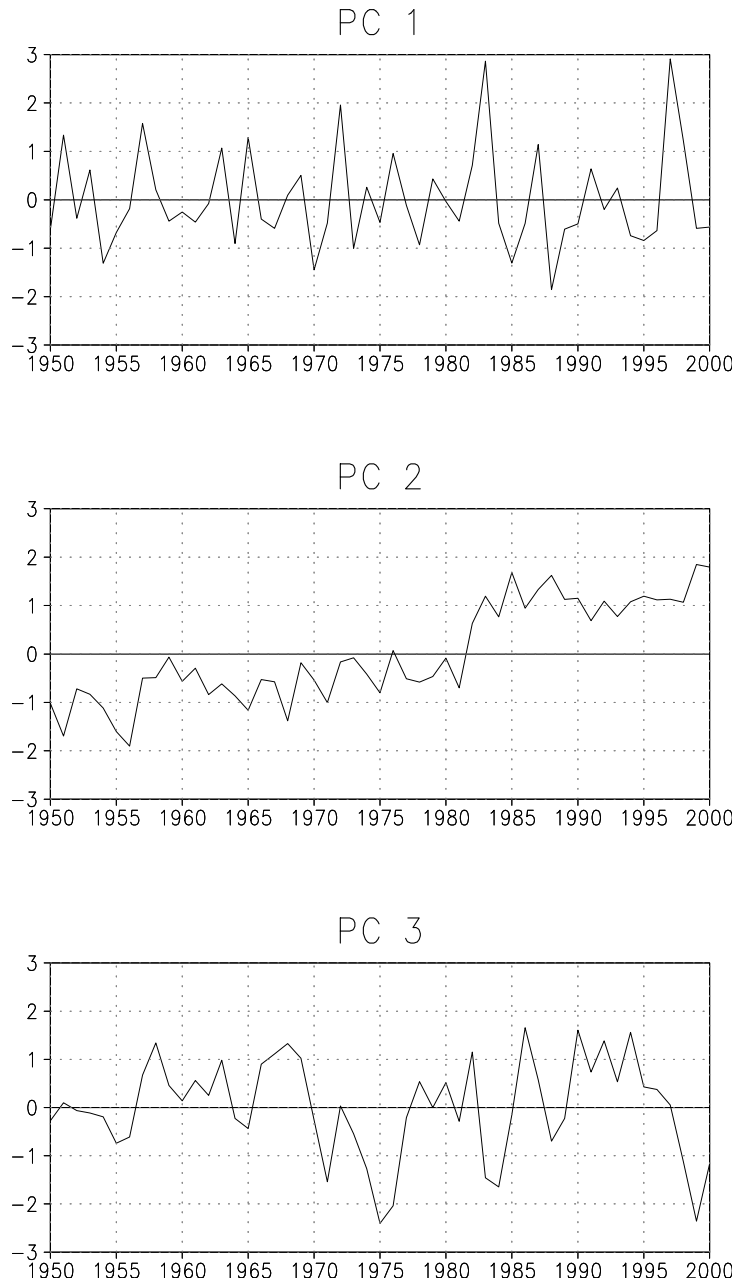


Figure 5.2: Normalized principal component time series (1950-2000) for boreal summer SST modes in Fig. 5.1.

Shown in Figs. 5.1 and 5.2 are the first three REOFs of the 1950-2000 period and the normalized principal component (PC) time series. Fig. 5.1 also shows the SST anomalies associated with each REOF as determined by a composite analysis technique which considers years exceeding half a standard deviation of a given PC, to be discussed in more detail later in this section. The first and third REOFs most closely resemble the first and second REOFs of the 1980-99 period, in terms of their spatial pattern and correspondence of their PC time series for the years of overlap, so these are discussed first. Though these REOFs do not explain as much variance as they do for the 1980-99 period, it is clear from their PC time series they are nonetheless physically meaningful. PC 1 reflects ENSO variability, with large positive values during the El Niños of 1951, 1957, 1965, 1972, 1983, and 1997, and large negative values during the La Niñas of 1954, 1964, 1970, 1973, 1985, and 1988. The maximum composite SST anomaly is about 2 K in the eastern tropical Pacific. The longer SST record is more revealing for REOF 3, which has more variability in the North Pacific. The composite SST anomalies in the North Pacific are on the order of 0.4 K and in the eastern tropical Pacific on the order of 0.8 to 1 K. The spatial pattern of SST associated with this mode resembles that of the Pacific Decadal Oscillation (PDO), as defined by Zhang et al. (1997) and Mantua et al. (1997). However, the time series for PC 3 looks different from the traditional PDO index of Mantua et al. (1997) based on the first PC of Pacific SSTs poleward of 20° N, as shown in Fig. 5.3. The PDO index is available on-line at <http://jisao.washington.edu/pdo/PDO.latest>. PC 3 is only weakly correlated with the summer PDO index (0.20).

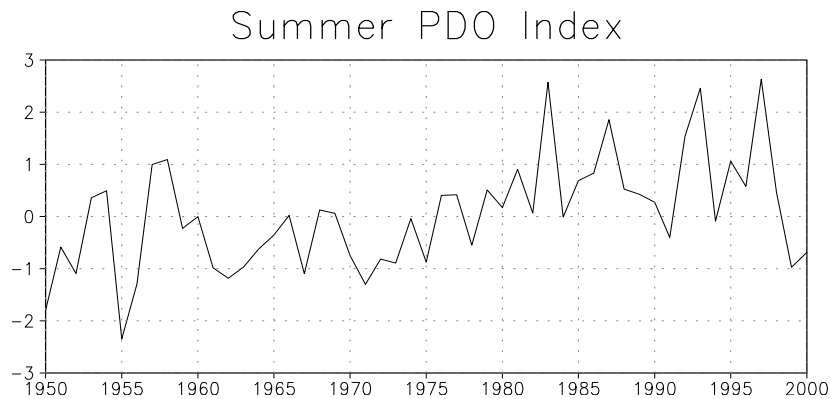


Figure 5.3: Summer PDO index based on the first PC of Pacific SST poleward of 20° N.

The most distinguishing characteristic of the traditional PDO index over the latter half of the twentieth century is a shift from mostly negative values to mostly positive values which occurred in the late 1970s. A recent shift to negative values occurred from about the late 1990s on and continued to about 2002 (not shown in Fig. 5.3). While PC 3 perhaps cannot be strictly referred to as the PDO by the standard definition, its behavior is certainly PDO-like and it will be referred to as such here. The differences between PC 3 and the traditional PDO index are most likely due to the fact that the former is based on global SST, and thus includes the SST in the tropical Pacific. As will be shown later, the inclusion of tropical Pacific SST is very important when considering the significance of SST-related atmospheric teleconnections in boreal summer. PC 3 appears to have decadal variability, with interchanging periods of positive and negative values every 20-30 years. PC 3 is slightly negative during the mid 1950s, mostly positive from the late 1950s through the 1960s, very negative during the mid 1970s, and mostly positive from

the late 1970s through mid 1990s (1984 and 1988 are notable exceptions), then negative after about 1998. Irrespective of whether PC 3 is truly the PDO or not, it is physically important because its periodicity appears to match the long term wet and dry periods in the central U.S. For example, McKee et al. (1999) note dry conditions in Colorado in the 1950s and 1970s and wet conditions in the 1960s and the period since the late 1970s. The most recent wet period ended in the late 1990s and a long-term drought ensued, peaking in the summer of 2002 (Hoerling and Kumar 2003; Pielke et al. 2005).

Of course, the physical mechanisms of ENSO are well known (e.g. Philander 1992). Given the apparent importance of the PDO-like mode (REOF 3), is there a physical mechanism for it? While that is not explicitly a subject of this dissertation, and a whole other area of study in itself, some of the proposed atmospheric mechanisms for decadal variation in Pacific SSTs since Castro et al. (2001) are briefly discussed. In a review article, Alexander et al. (2002) explore the atmospheric bridge hypothesis. This asserts that teleconnection patterns originating the tropical Pacific (associated with ENSO) affect the extratropical North Pacific via interannual variation in surface latent and sensible heat exchanges. In a coupled atmosphere-ocean GCM, the atmospheric forcing can reproduce the pattern of North Pacific SST seen in REOF 3. Deser et al. (2003) suggest that the ocean acts to redden the spectrum of atmospheric forcing, so ocean variability on the interannual (five years or less) timescale is related to stochastic atmospheric forcing with a decorrelation time of a week. The ocean may also be acting as an integrator of the (non-random) atmospheric forcing due to ENSO, which is persistent over a longer timescale, to generate decadal variability. REOF 3 also bears a striking resemblance to the Pacific meridional mode in summer, for example as seen in

Chiang and Vimont (2004), their Fig. 11 for JJA using ENSO neutral years. The time series of this mode (their Fig. 2 time series for the Pacific) shows it has decadal variability which is very close to PC 3. They postulate that the driver of the Pacific meridional mode is wintertime atmospheric variability that leaves an anomalous “footprint” on tropical SST. While ENSO does project onto the Pacific meridional mode, its existence does not depend on ENSO. Internal ocean dynamics may also be contributing to decadal variability in the Pacific, discussion of which is omitted here.

REOF 2 appears as a new global SST mode in the 1950-2000 record. Its PC time series does correlate better with the traditional PDO index (0.52) than PC 3. The PC 2 time series is fairly steady to the late 1970s and shows a large jump in the early 1980s, but, unlike PC 3 and the PDO index, does not show a decrease after 1998. While this mode does show long term cooling in the North Pacific of about 0.4 K, its spatial pattern differs from the PDO. There is not a contrast in SST between the eastern North Pacific off the west coast of North America and the central North Pacific. Whereas REOF 1 and REOF 3 vary mainly in the Pacific Ocean, REOF 2 varies throughout the tropical oceans and indicates warming there over the period. The warming trend in SST over the later twentieth century has been documented, for example, by Levitus et al. (2000) and Kumar et al. (2004). Fig. 1 from Kumar et al. (2004) shows that the magnitude of warming in the tropical oceans since the late 1970s is about 0.25-0.5 K, and this may also be inferred from the SST anomaly composite for REOF 2. Barnett et al. (2001; 2005) and Hansen et al. (2005) assert this warming is due to anthropogenic climate change. While the focus of this chapter is the effect of Pacific SST variability on summer climate, this regime shift

mode in SST should not be ignored. As will be shown, it too has an impact on North American summer climate.

Given the conclusion in Castro et al. (2001) that the most coherent summer climate patterns in western North America occur when a combined index of tropical and North Pacific SSTs (P index) is substantially high or low, the ENSO and PDO-like modes from the SST REOF analyses (REOF 1 and REOF 3) are averaged together (Fig. 5.4). Henceforth this mode is referred to as the Pacific SST variability mode, and it will be shown later that it maximizes the explained variance of summer precipitation because of the different teleconnection patterns associated with REOF 1 and REOF 3. This logic is similar to what Gurshunov and Barnett (1998) concluded for the winter season in North America, in terms of constructive interference of ENSO and PDO.

How well do the time series for PC 1, PC 2, PC 3, and the average of PC 1 and PC 3 compare with the summer SST indices used in Castro et al. (2001)? Table 5.1 shows the correlation coefficients for all the indices and PCs. In addition to Niño 3, the Niño 1.2 index is included. As would be expected, the Niño indices are well correlated with PC 1, but have little, if any, correlation with PC 3. The North Pacific (NP) index best explains the variance of PC 3, though the correlation is not particularly strong when compared to the correlation of Niño indices with PC 1. The NP index also has some correlation with PC 1 (0.39) because ENSO has a signature on North Pacific variability. To account for this, Castro et al. (2001) only considered the ENSO neutral years in their North Pacific composites. The average of PC 1 and PC 3 correlates best with the combined P index of tropical and North Pacific SST. The SST pattern and composite anomalies for the Pacific SST variability mode is nearly identical to that of the high and

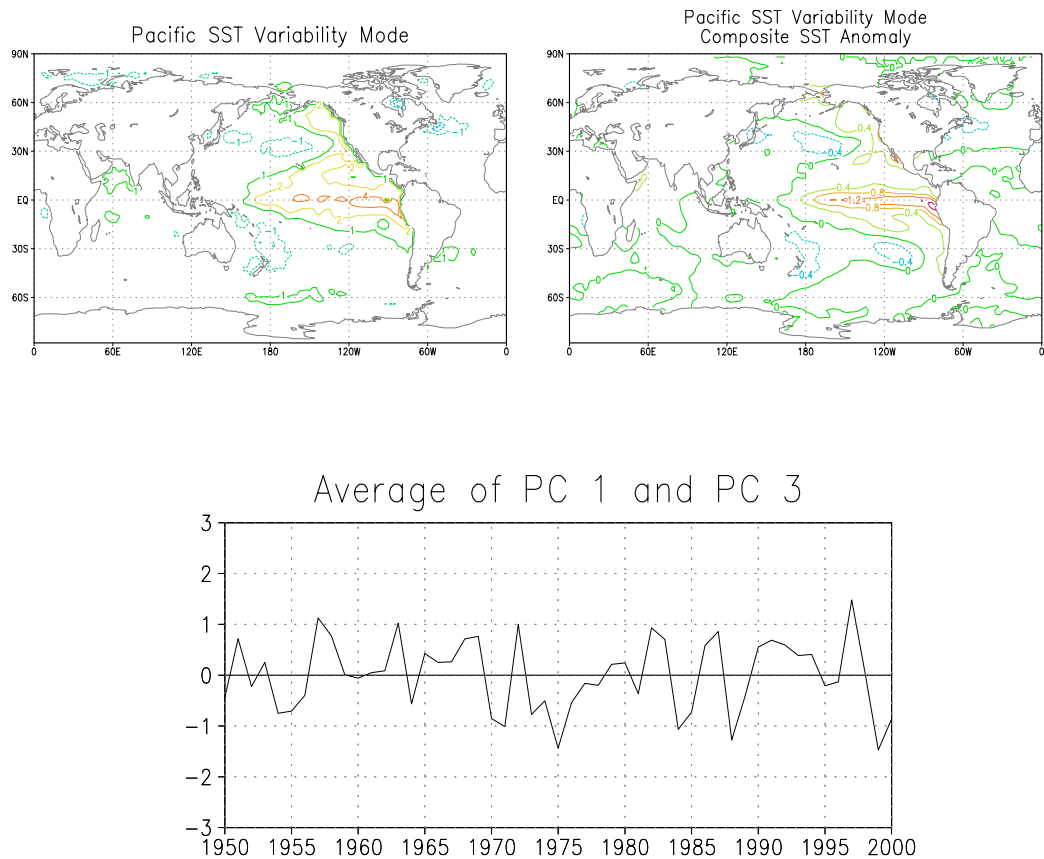


Figure 5.4: The Pacific SST variability mode, computed as the average of ENSO and PDO-like global SST modes for the period 1950-2000. Contouring as in Fig. 5.1.

	PC 1	PC 2	PC 3	PC 1 and PC 3 average
Niño 1.2	0.93	0.17	-0.04	0.64
Niño 3	0.80	0.42	0.19	0.71
NP index	0.39	0.62	0.49	0.62
P index	0.67	0.14	0.43	0.78

Table 5.1: Correlation coefficients between Pacific SST indices in Castro et al. (2001) and PCs of global SST for the period 1950-2000. Highlighted values indicate the highest explained variance of the PC.

low P index summers shown in Castro et al. (2001), their Figs. 12 and 13. PC 2 is best correlated with the NP index (0.62) because of the cooling trend in North Pacific SSTs since the early 1980s or so.

An important question that should be considered is whether these correlation relationships between PCs and SST indices dramatically change within the summer season. Repeating the same analysis for the individual summer months reveals approximately the same correlation as the seasonal average shown, indicating that Pacific SSTs, particularly in the tropics, are fairly constant over the three month period. Any rapid changes in atmospheric teleconnections over the course of the summer are due, then, to changes in the atmosphere as the summer evolves, not SST.

The correlation analysis suggests that simple SST indices, which consider specific areas in the Pacific, capture the behavior of the dominant REOFs of global SST. Therefore there is an a priori expectation that the relationship of North American summer climate to these REOFs should be very close to the indices. Specifically, this means it should be expected that the height anomalies associated with ENSO and PDO-like REOFs should 1) have a time-evolving character such that they appear in early summer then wane and 2) are maximized in specific geographic locations in North America. To show this, for each individual PC and the average of PC 1 and PC 3 (Pacific SST variability mode) a positive and negative composite of years was created (see Tables 5.2, 5.3, 5.4, and 5.5). The positive and negative composites consider years which exceed half a standard deviation of a given PC. As mentioned, the SST anomalies associated with the composites are shown in Figs. 5.1-5.3. This threshold was chosen because it yields a good sample size (greater than ten years) for the composites, which proved to be

<u>PC 1 Negative</u>	<u>PC 1 Positive</u>
1950	1951
1954	1953
1955	1957
1964	1963
1967	1965
1970	1969
1973	1972
1978	1976
1985	1982
1988	1983
1989	1987
1994	1991
1995	1997
1996	1998
1999	
2000	

Table 5.2: Positive and negative composites for PC 1 of global SST for the period 1950-2002.

<u>PC 2 Negative</u>	<u>PC 2 Positive</u>
1950	1982
1951	1983
1952	1984
1953	1985
1954	1986
1955	1987
1956	1988
1957	1989
1960	1990
1962	1991
1963	1992
1964	1993
1965	1994
1966	1995
1967	1996
1968	1997
1971	1998
1975	1999
1977	2000
1978	2001
1981	2002

Table 5.3 Positive and negative composites for PC 2 of global SST for the period 1950-2002.

<u>PC 3 Negative</u>	<u>PC 1 Positive</u>
1955	1957
1956	1958
1971	1961
1973	1963
1974	1966
1975	1967
1976	1968
1983	1969
1984	1978
1988	1980
1998	1982
1999	1986
2000	1987
2001	1990
2002	1991
	1992
	1993
	1994
	1995

Table 5.4: Positive and negative composites for PC 3 of global SST for the period 1950-2002.

<u>PC 1 and PC 3 Average Negative</u>	<u>PC 1 and PC 3 Average Positive</u>
1950	1951
1954	1957
1955	1958
1956	1963
1964	1965
1970	1968
1971	1969
1973	1972
1974	1982
1975	1983
1976	1986
1981	1987
1984	1990
1985	1991
1988	1992
1989	1993
1999	1994
2000	1997
2001	
2002	

Table 5.5: Positive and negative composites for the average of PC1 and PC 3 of global SST (Pacific SST variability mode) for the period 1950-2002.

important in considering precipitation anomalies. The atmospheric circulation anomalies are nearly the same whether a half or a full standard deviation threshold is used. Though the years 2001 and 2002 are not included in the PC analysis, these are considered as PC 3 negative because of the negative sign of the NP index for those years and the aforementioned drought in the central U.S. It is also assumed that the SST trend of PC 2 continues in those years, so the positive composite of PC 2 is just the last twenty-one years of the record. To test the statistical significance of climate patterns in the subsets of years in the proceeding sections, a two-tailed t-test is used which considers the given subset of years against all other years in the record.

5.2 Observed Time-Evolving SST-Associated Teleconnection Patterns

The difference in the 30-day average NCEP Reanalysis 500-mb height field about the date and corresponding statistical significance were calculated for the PC composites in Tables 5.2-5.4. The results for REOF 1 (ENSO mode), REOF 2 (SST regime shift mode), and REOF 3 (PDO-like mode) are shown in Figs. 5.5, 5.6, and 5.7, respectively, for the area which includes the tropical and North Pacific Ocean and North America. Shown in each of the figures is the anomaly of the positive composite minus that of the negative composite divided by two. Statistical significance is shown at the 90% level and above. For convenience and comparison, the same days coincident with Castro et al. (2001) (their Figs. 3 and 4) are used.

Viewing the evolution of height anomalies in this way for the ENSO and PDO-like modes reveals that a JJA summer average misses key details of the nature of boreal summer atmospheric teleconnections. In their ensemble NSIPP GCM simulations using

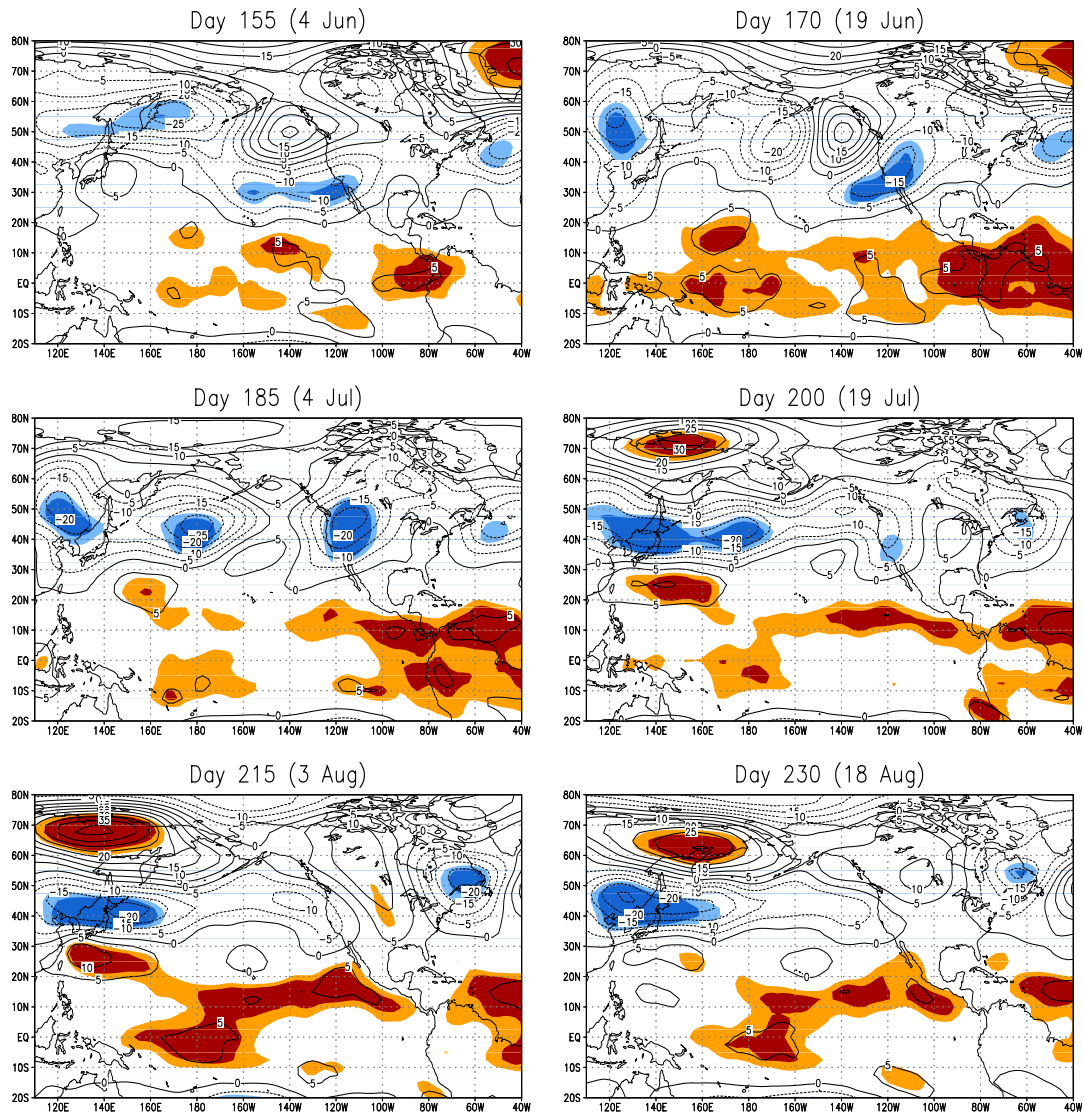


Figure 5.5: Time evolution of 30-day average 500-mb height anomalies (m) through the summer season for the PC 1 composites in Table 5.2. Contour interval is 5 m. Shading indicates statistical significance at the 90 and 95% levels.

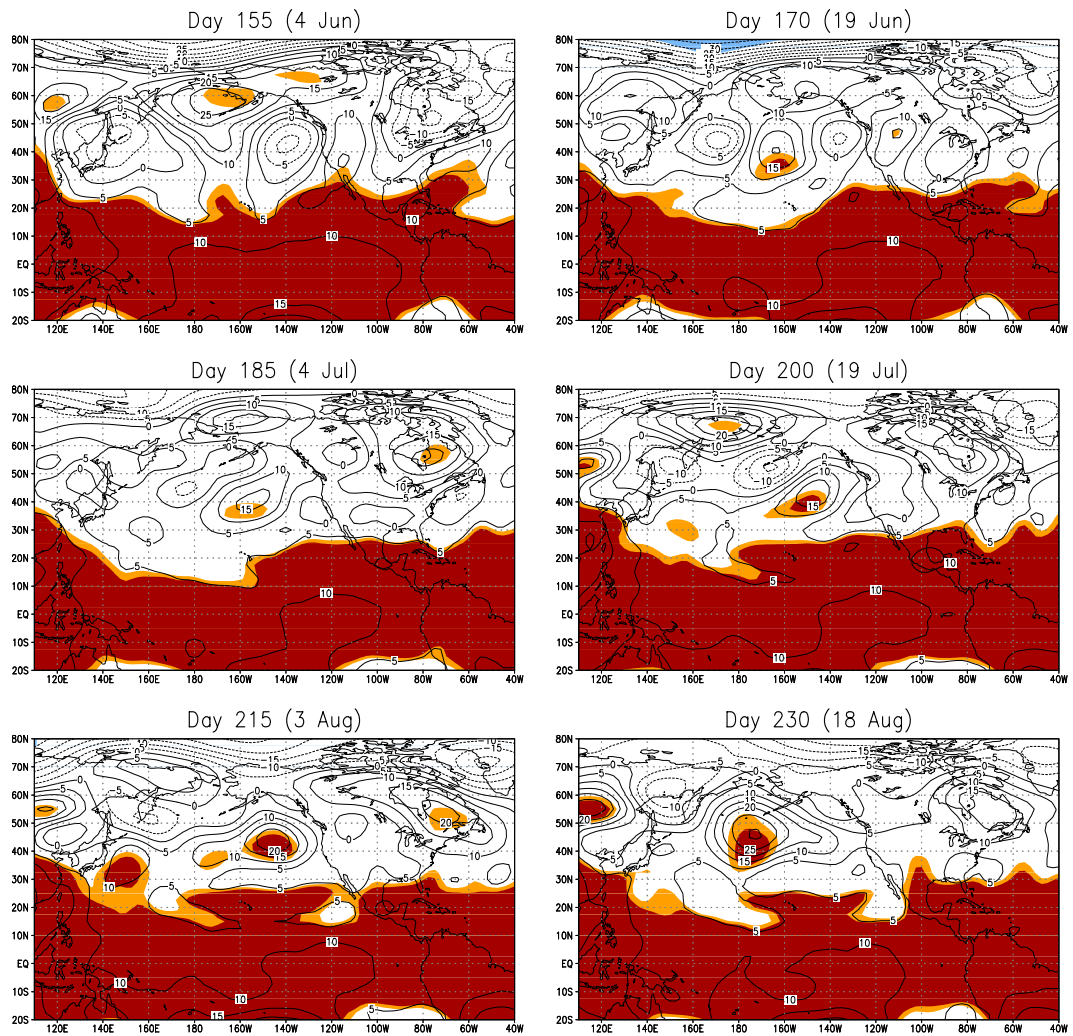


Figure 5.6: Same as Fig. 5.5 for PC 2 composites in Table 5.3.

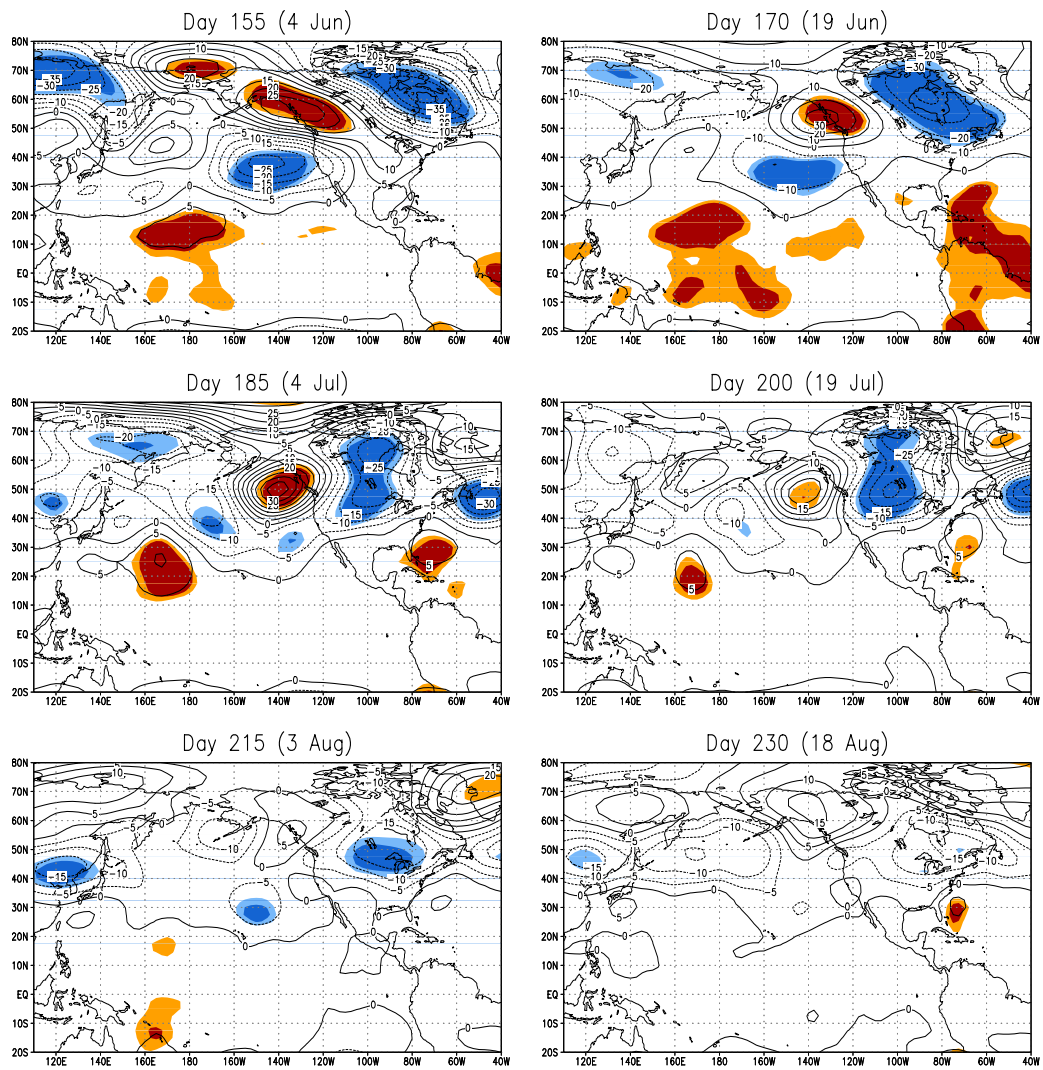


Figure 5.7: Same as Fig. 5.5 for PC 3 composites in Table 5.4.

observed SST forcing, Schubert et al. (2002) found a zonally symmetric response in the 200-mb height field associated with each PC (their Fig. 9) and concluded the same behavior exists in the NCEP Reanalysis (their Fig. 10). However, Figs. 5.5 and 5.7 show the ENSO and PDO-like modes for the 1950-2000 record are associated with wavetrains across the Pacific, consistent with the idealized modeling studies mentioned in Section 1.3 which show quasi-stationary Rossby-wave responses with prescribed tropical atmospheric forcing. As Schubert et al. (2002) would suggest, the weaker teleconnection response is associated with PC 1 (ENSO mode). The ENSO teleconnection has a significant center of action in the northern Rocky Mountains (15-20 m) in early July. The stronger and more significant teleconnection response is associated with PC 3 (PDO-like mode). This teleconnection peaks slightly later (early to mid-July) over the contiguous U.S. than the ENSO teleconnection with a significant center of action over the northern Great Plains (20-25 m). There are also significant centers of action in the North Pacific, especially prior to this time in June. Some of the idealized modeling studies suggest this may be a forcing region for height anomalies over North America (e.g. Liu et al. 1998). The strength of the Bermuda high off the southeast coast of the U.S. is also related to this teleconnection. In both the PC 1 and PC 3 composites, any significant relationships in the 500-mb height field over the contiguous U.S. disappear by August.

If the traditional PDO index is used in lieu of PC 3 to construct the height anomaly composite a very similar relationship to 500-mb height is obtained in the midlatitudes (Fig. 5.8), but PC 3 gives a more statistically significant result. This should not be surprising given the fact that the teleconnections are most likely due to variation in tropical Pacific SST (south of 20° N). To verify that these same teleconnection patterns

appear in the 1980-99 period, the same analysis was performed with PC 1 and PC 2 for that record. A similar pattern of time-dependent height anomalies appears (not shown), though height anomalies in the tropics are more significant for the PC 1 composite in the shorter record.

The time evolution of the teleconnection patterns just described is generally consistent with Castro et al. (2001) in terms of the timing and positioning of the centers of action associated with tropical and North Pacific SSTs and the decay of the teleconnection relationships in late summer. The decay corresponds to a decrease in the strength of the East Asian jet in the western Pacific, shown, for example, in Fig. 5 of Castro et al. (2001). This reduces the effective Rossby wave source in the midlatitudes given a constant heating anomaly in the tropics. At the time of “maximum teleconnectivity” in July the patterns associated with the ENSO and PDO-like modes are distinct. The centers of action over the contiguous U.S. on 4 July, for example, are approximately in quadrature. This physically means that ENSO and PDO-like modes are related to the positioning of the evolving monsoon ridge in two ways. ENSO is associated with north-south deviations of the ridge from its climatological position over the Four Corners region. The PDO-like mode is associated with northeast-southwest deviations of the ridge. This latter response also appears to be persistent over a longer time period in the month of July. It will be investigated whether the NSIPP GCM simulations executed with idealized SST corresponding to these modes can reproduce the observed teleconnection response in Section 5.4.

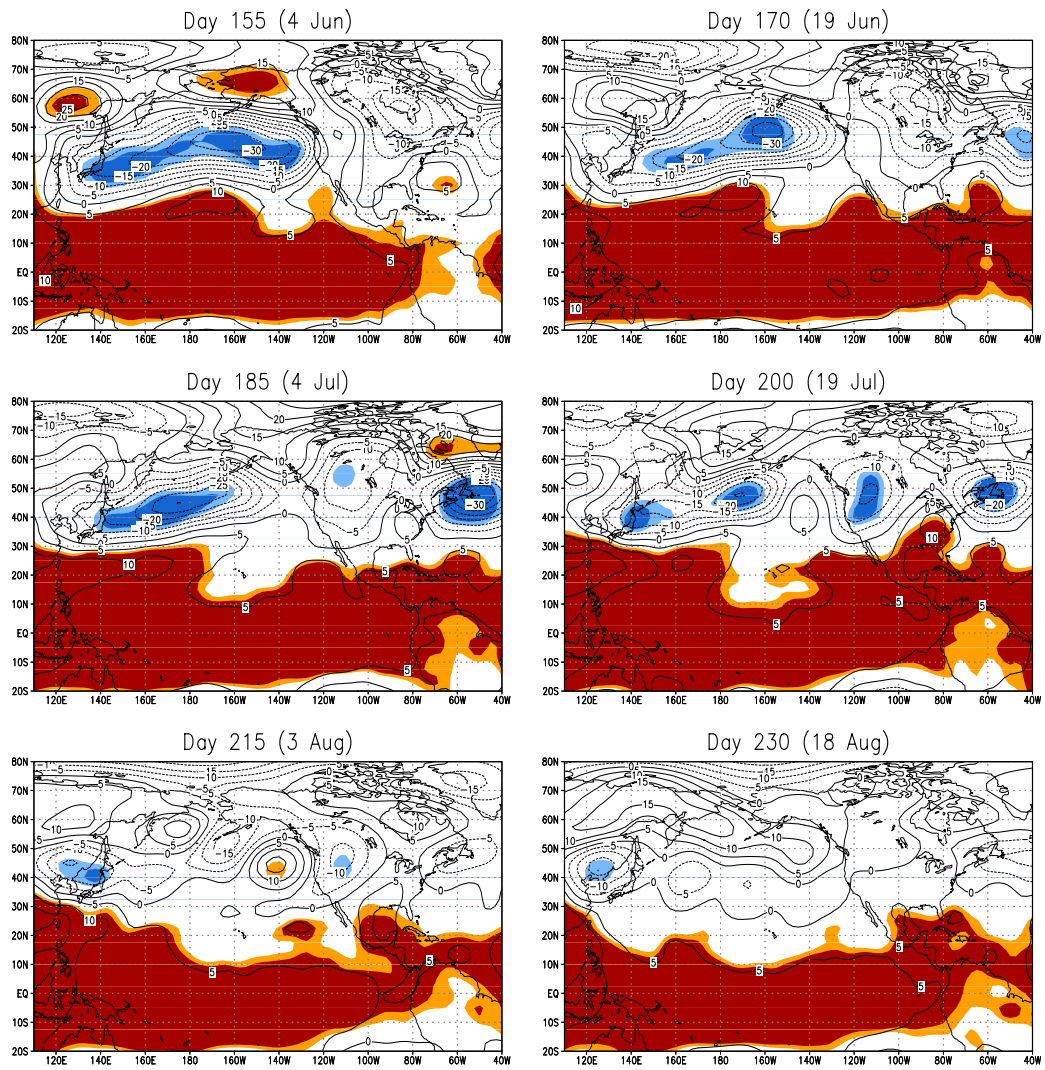


Figure 5.8: Same as Fig. 5.5 for composites constructed with the summer PDO index of Mantua et al. (1997).

The SST regime shift mode (Fig. 5.6) is associated with an increase in 500-mb geopotential height (5-10 m) throughout the tropical atmosphere for the entire summer. The warming of the tropical atmosphere follows from the increase in tropical SST. It should be noted that there is an ongoing debate about whether there has been observed tropospheric warming since the late 1970s, as derived from microwave sounding unit (MSU) temperature data (e.g. Mears et al. 2003). Irrespective of this possible uncertainty in observations, the trend in tropical geopotential height shown here for the NCEP Reanalysis has been replicated in GCM simulations forced with observed SST for the period 1950-2000 (Kumar et al. 2004), strongly suggesting it is real. ENSO also causes a uniform warming of the tropical atmosphere, so the increase in geopotential height due to the SST regime shift mode is likely weakening the statistical significance of height anomalies in Fig. 5.5. Unlike the previous modes discussed, this mode has no significant height anomalies in the midlatitudes during the summer.

5.3 Response of Teleconnections in RCM-Simulated Fields

Next, the RAMS-RCM generated 30-day averaged precipitation differences for the PC composites in Tables 5.2-5.4 are considered in Figs. 5.9, 5.10, and 5.11. As before, statistical significance is plotted at the 90% level and above and the positive minus the negative composite divided by two is shown. It should be noted that a similar pattern of anomalous precipitation and significance appears in the CPC gridded station observations over the contiguous U.S. (not shown). The anomalies are less present for observed precipitation in Mexico, probably owing to a less dense observational network there. No

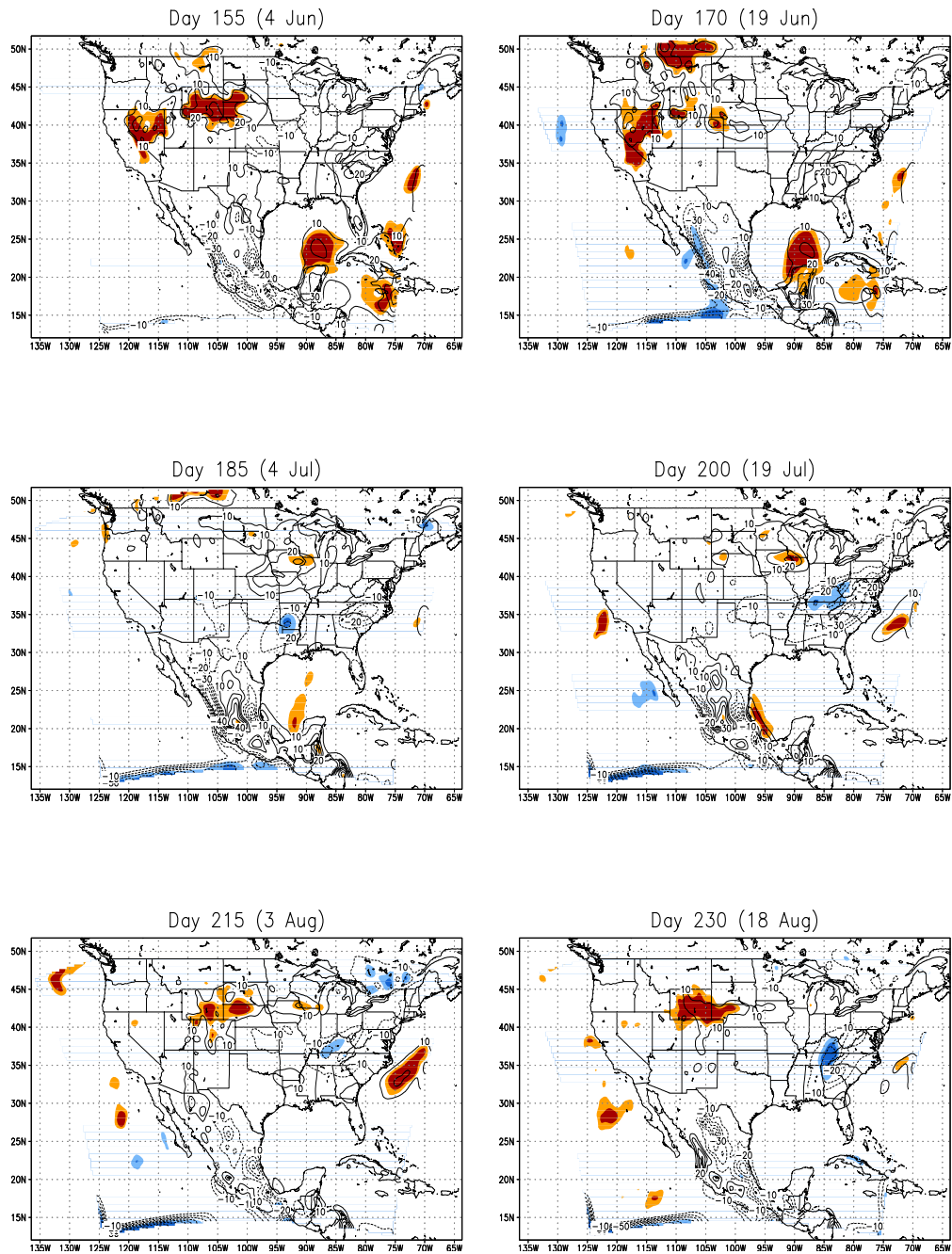


Figure 5.9: Time evolution of 30-day average RAMS precipitation anomalies (mm) through the summer season for PC 1 composite in Table 5.2. Contour interval is 10 mm. Shading indicates statistical significance at the 90 and 95% levels.

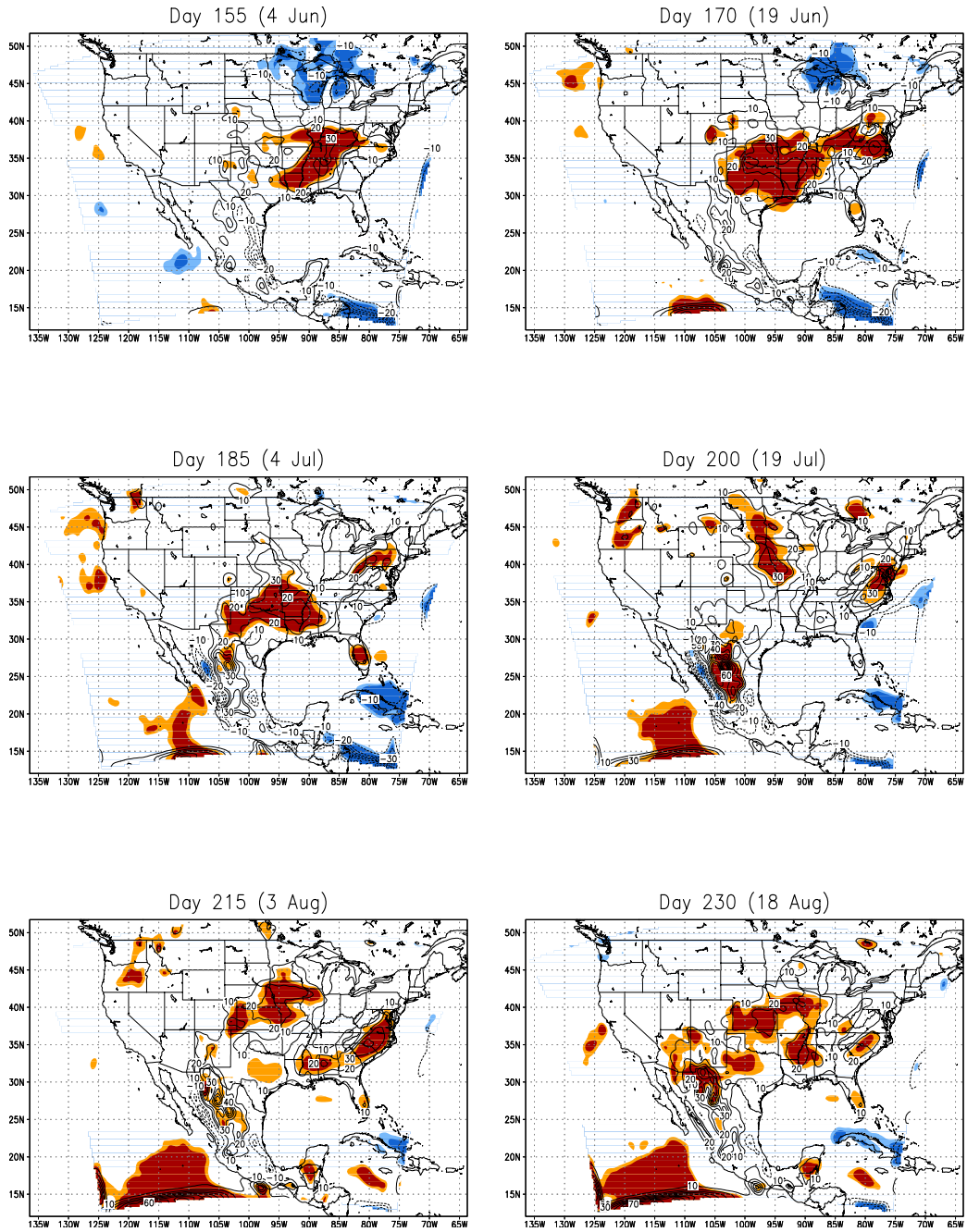


Figure 5.10: Same as Fig. 5.9 for PC 2 composite in Table 5.3.

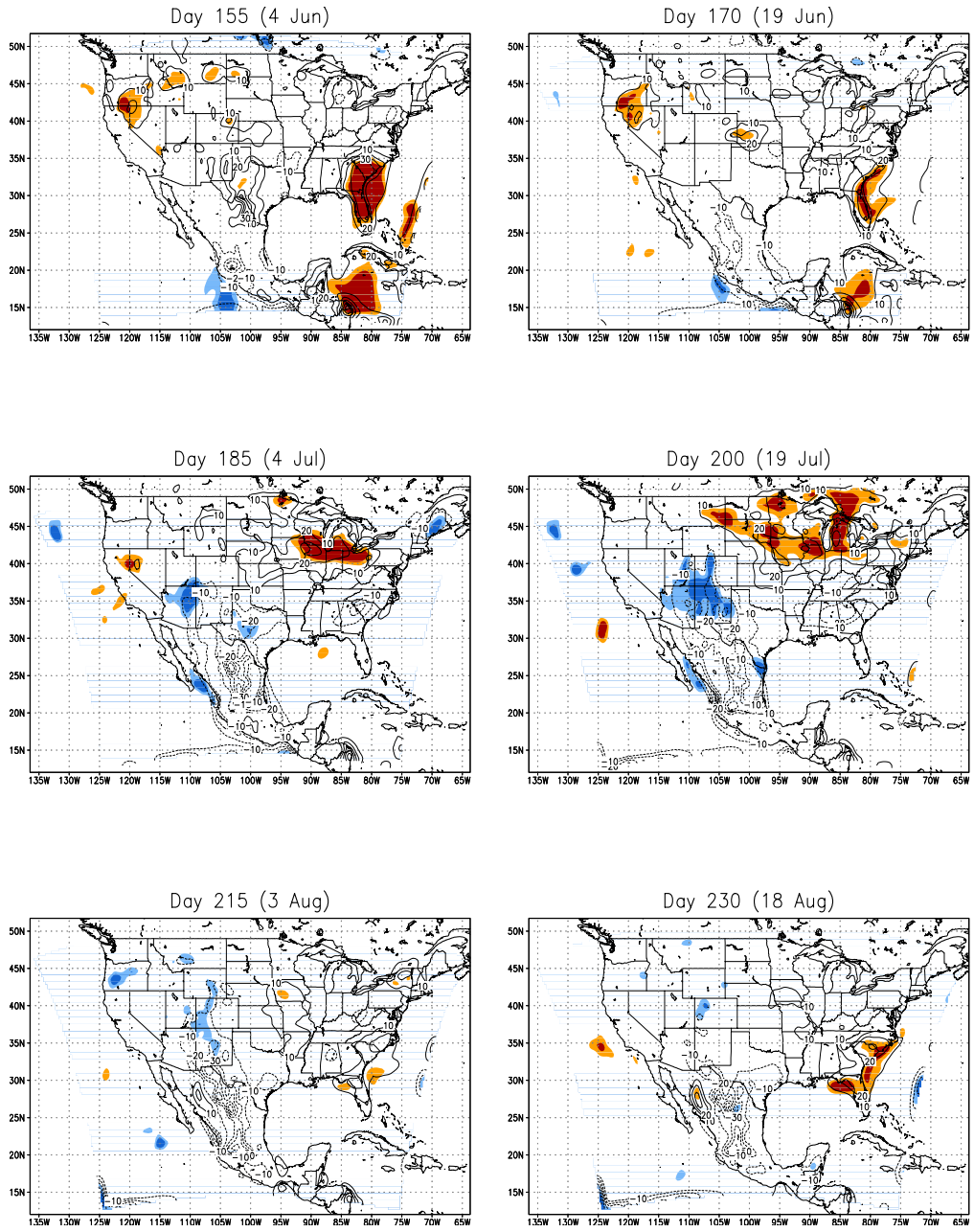


Figure 5.11: Same as Fig. 5.9 for PC 3 composite in Table 5.4.

significant anomalies appear in the NCEP reanalysis precipitation (not shown). The failure of the NCEP Reanalysis to capture the interannual variability in North American precipitation, particularly in the central and Southwest U.S., makes sense given its problems in capturing the climatological transitions in the NAMS (see Chapter 4).

The time evolution of precipitation anomalies for the PC 1 composite (Fig. 5.9) shows the most significant precipitation anomalies occur in late June in two areas. Precipitation is positively related to ENSO over the western and central U.S. and negatively related in western Mexico. By July and August these precipitation anomalies become, for the most part, statistically insignificant. The corresponding evolution for the PC 3 composite (Fig. 5.11) shows a slightly different spatial pattern and later timing of precipitation anomalies in July. At this time, precipitation is positively related to the PDO-like mode in the central and Midwest U.S. and negatively related in the Southwest U.S. Precipitation anomalies for the PC 3 composite are also more statistically significant compared to PC 1. Both the ENSO and PDO-like modes show an opposite relationship in precipitation between the core monsoon region and the central U.S. The timing of the precipitation response in each case is directly linked to the significance of the atmospheric teleconnection previously shown. The precipitation differences are most apparent at the time of maximum teleconnectivity for each mode. As the teleconnections wane, the differences in precipitation become insignificant. The interannual response in precipitation resembles the difference in precipitation between the monsoon peak (late July, early August) minus premonsoon period (late May, early June), as shown for example in Fig 4.4. This indicates the teleconnections are acting to delay or accelerate the climatological evolution of the NAMS. These results are entirely consistent with the

established prior relationships between the Pacific SST indices and reanalysis integrated moisture flux convergence and station precipitation in the Great Plains and Southwest (Castro et al. 2001). The present RAMS model results also show that Mexican precipitation is affected by the evolution of the midlatitude teleconnection patterns and positioning of the ITCZ, primarily in June.

Since ENSO and PDO-like modes are associated with distinct time-dependent responses in summer precipitation, could the Pacific SST variability mode explain more of the interannual variability of precipitation over the summer than either the ENSO or PDO-like modes alone? Mo and Paegle (2000) demonstrated that this is likely the case for the Southwest. Shown in Fig. 5.12 is the evolution of RAMS RCM-generated precipitation anomalies for the Pacific SST variability mode composites in Table 5.5. In this case, precipitation anomalies are, in general, more significant over a longer period (from June through all of July) and over a wider geographic area. Again, the most significant anomalies are located in the core monsoon region and central U.S. at the time of maximum teleconnectivity. It should be noted that the precipitation anomaly in the core monsoon region is larger (20-30 mm) and more statistically significant if the negative composite is considered by itself (not shown). Another interesting feature that becomes clearer in the composite is the reversal in the sign of the precipitation anomaly in the Southwest U.S. through the late spring and early summer, also in agreement with Mo and Paegle (2000). In the central U.S., the sign of the precipitation anomaly remains the same through the late spring and summer periods, with maximum anomalies appearing in early July.

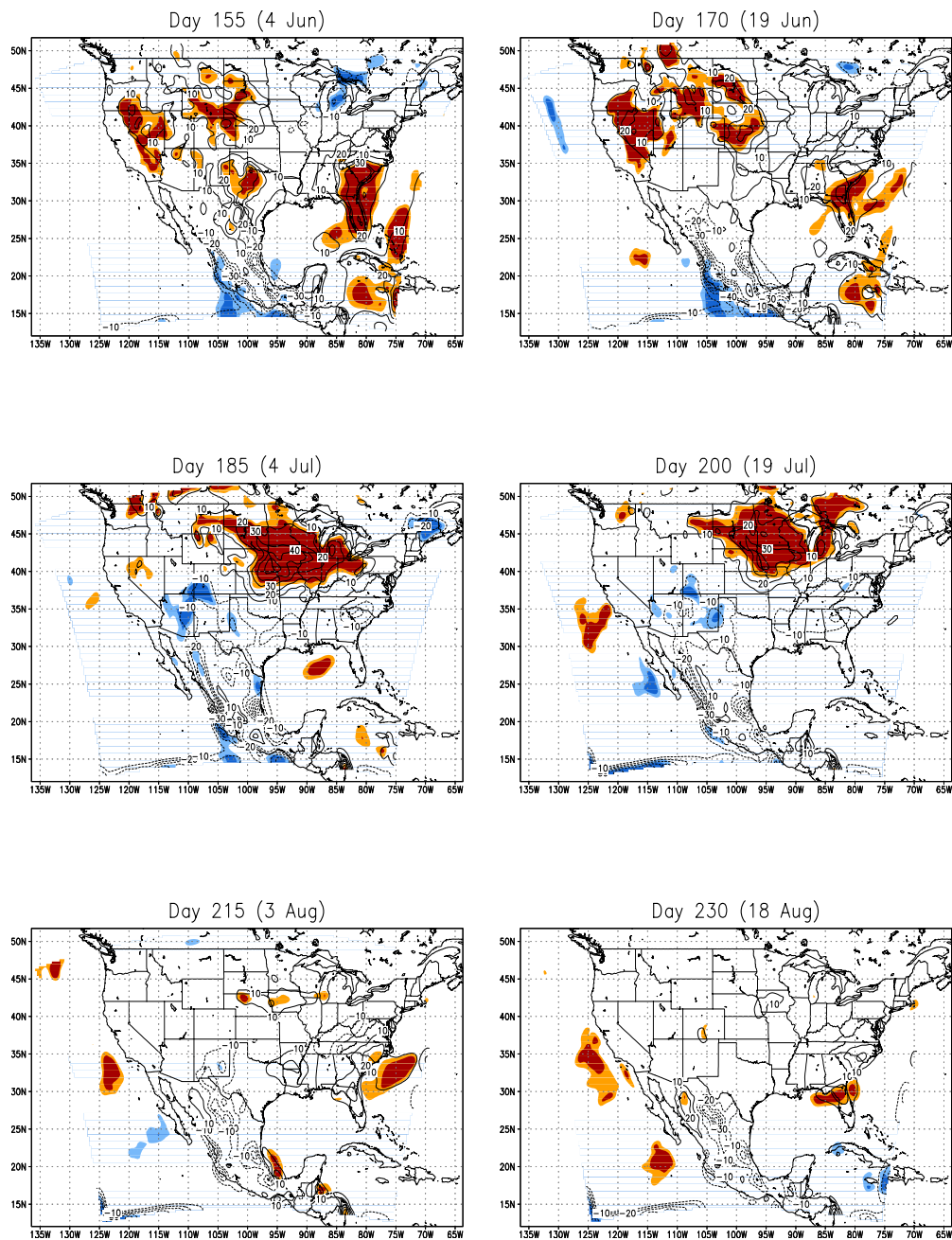


Figure 5.12: Same as Fig. 5.9 for average of PC 1 and PC 3 (Pacific SST variability mode) composite in Table 5.5.

The precipitation anomalies associated with the SST regime shift mode (PC 2) are shown in Fig 5.10. Unlike the Pacific SST variability mode, the SST regime shift mode indicates a general increase in precipitation in the contiguous U.S. east of the continental divide through the entire summer in the last two decades. Where these changes are statistically significant, the increase in precipitation from the RAMS climatology is on the order of 10-20%. The increase in rainfall is due to an increase in moisture, presumably from increased evaporation in the tropics, not changes in the large-scale dynamics caused by a quasi-stationary Rossby wave response as before. Long-term increases in observed atmospheric moisture and precipitation in the contiguous U.S. have been documented over the latter half of the twentieth century (e.g. Karl and Knight 1998; Gaffen and Ross 1999), and the magnitude of these increases is approximately the same as the increase in model-generated precipitation. A very interesting result for precipitation in Mexico occurs during the peak of the monsoon there in July. The RAMS model results show that monsoon precipitation has decreased in the SMO and increased east of the SMO on the Mexican plateau. The decrease is approximately 15% of the model-generated precipitation where it is statistically significant. Given the ability of RAMS to correctly represent NAMS precipitation climatology and interannual variability in the U.S., there is no reason to suggest this long term trend cannot be real, through it is difficult to verify with current long-term observational products. A possible reason for it is the variation of moisture transport in the eastern Pacific off the west coast of Mexico, to be shown later in this section.

Thus far, the variability of the upper-level circulation and RCM-generated precipitation in relation to the dominant modes of summer global SST has been explored.

The variability of RCM-generated surface temperature and moisture flux is now investigated. Since it has already been established that the Pacific SST variability mode maximizes the explained variance of precipitation in terms of time duration and geographical extent of statistical significance, only the behavior of this mode and the long term SST regime shift mode are considered. Instead of showing the entire time series of evolution as before, just the 30-day average about 15 July is shown to illustrate what is happening at the time of maximum teleconnectivity with Pacific SSTs. The positive minus the negative composite divided by two is shown.

The differences in 30-day average RAMS temperature at the first model level, henceforth referred to as surface temperature, are shown at the top of Fig. 5.13 for the date of maximum teleconnectivity. The Pacific SST variability mode composite shows a positive relationship with surface temperature in Mexico and adjacent eastern Pacific Ocean and part of the Southwest U.S. and a negative relationship in the northern Great Plains and Rocky Mountains. These temperature patterns are generally consistent with reanalysis temperature differences between wet and dry periods in the central U.S. found by Mo et al. (1997). Temperature anomalies for the SST trend mode show a slight decrease in surface temperature due to the increase in surface moisture, but the decrease is not very significant. A significant increase in surface temperature occurs off the west coast of Baja California, due to the long-term increase in sea surface temperature there.

For the Pacific SST variability mode, the temperature anomalies in the contiguous U.S. logically follow from the teleconnection responses in the 500-mb height field and rainfall previously shown. The significant temperature response in Mexico is related to a shift in the ITCZ. The changes in temperature observed interannually, like precipitation,

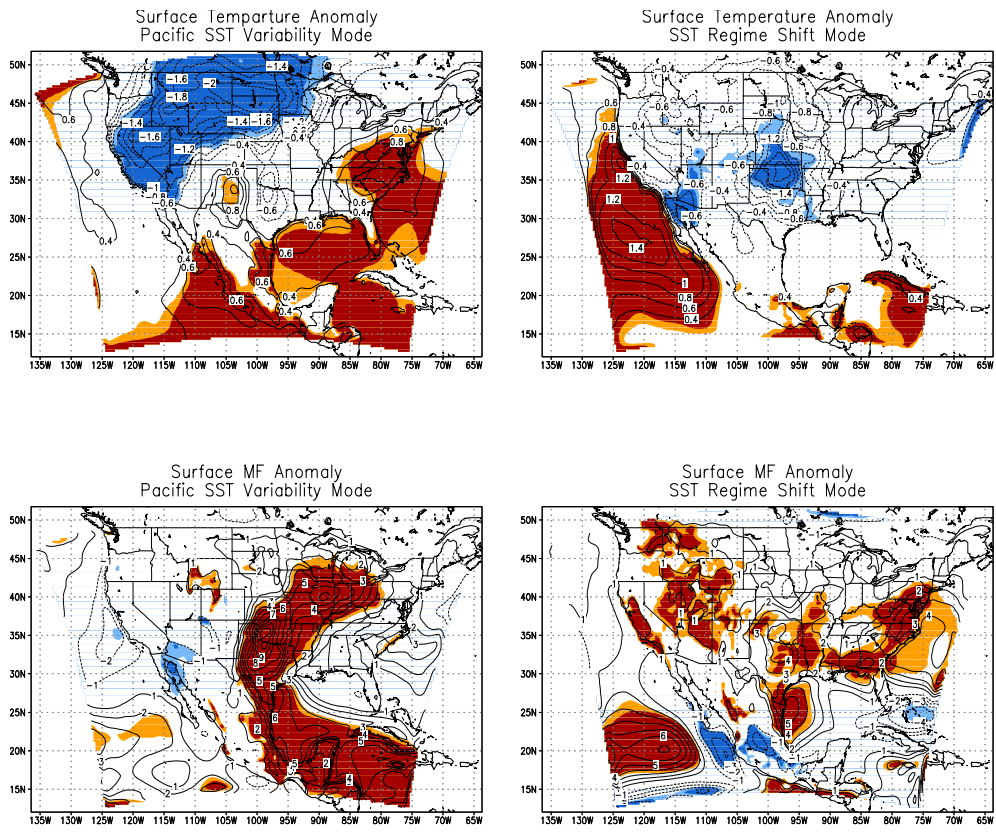


Figure 5.13: 30-day average surface temperature (K) and moisture flux ($\text{m s}^{-1} \text{g kg}^{-1}$) anomalies for Pacific SST variability mode composites and SST regime shift composites at the time of maximum teleconnectivity (see text for details). Shading indicates statistical significance at the 90 and 95% levels. Contour interval for temperature is 0.2 K and contour interval for moisture flux is $1 \text{ m s}^{-1} \text{g kg}^{-1}$.

mirror the changes in climatology from the monsoon peak minus onset period. Not shown are the corresponding changes in the surface sensible and latent heat fluxes. These also reveal the interannual changes in the surface energy budget are similar to the changes in climatology through the summer, and that the greatest differences occur in the south-central U.S. and core monsoon region.

The differences in 30-day average surface moisture flux are shown at the bottom of Fig. 5.13 for the period of maximum teleconnectivity. For the Pacific SST variability mode, the most significant differences occur in areas where low-level jets are present. There is a positive association with the Great Plains LLJ, with significant anomalies extending from the Caribbean and Gulf of Mexico into the central U.S. and Midwest. The largest anomalies occur at the location of the climatological maximum of the Great Plains LLJ, in Texas and Oklahoma ($10 \text{ m s}^{-1} \text{ g kg}^{-1}$). There is a negative association with the Baja LLJ in the northern Gulf of California. An increase in the strength of the Baja LLJ would direct more moisture into the Colorado River valley and Arizona (west of the continental divide). If only the negative composite is considered (not shown), it also shows a significantly enhanced easterly component to the Great Plains LLJ that allows it to transport more moisture westward (east of the continental divide) into New Mexico and Colorado. A very similar result was recently obtained in an evaluation of the Great Plains and Baja LLJs using a 50 km version of the NCEP Regional Spectral Model for the period 1991-2000 (Mo and Berbery 2004). Though the total integrated moisture flux was considered, their LLJ composites based on wet and dry period in the Great Plains (their Fig. 8) and Arizona and New Mexico (their Fig. 9) essentially match the patterns associated with Pacific SST variability seen here.

A change in the mean strength of both LLJs as related to Pacific SST variability should not be surprising given the changes in the atmospheric circulation, surface temperature, and surface energy budget just discussed. The Baja LLJ is fundamentally driven by the temperature gradient across the Gulf of California (e.g. Adams and Comrie 1997) and the mean temperature gradient would be decreased (increased) in years of high (low) phase of the Pacific SST variability mode. The most likely cause for the variation in the strength of the Great Plains LLJ is the interaction of the large-scale atmospheric flow with the topography (Byerle and Paegle 2003; Mo and Berbery 2004). Stronger (weaker) zonal winds upstream of the Rocky Mountains have a lee side response in the form of a stronger (weaker) Great Plains LLJ. This situation would occur with the presence of a trough (ridge) over the western and central U.S. Mo et al. (1997) also discuss a possible mechanism for the intensification of the Great Plains LLJ which would apply to years with a positive phase of the Pacific SST variability mode. Warmer daytime surface temperatures and less surface moisture (a higher Bowen ratio), which occur over New Mexico and the Mexican plateau, coupled with cooler and more moist conditions to the east would intensify the terrain-induced pressure gradient and, hence, the LLJ. This would agree with the idealized modeling study of the Great Plains LLJ by McNider and Pielke (1981). McNider and Pielke (1981) also note cumulus formation to the east of the dryline in the Great Plains would enhance the baroclinicity.

The differences in the Great Plains LLJ noted here between the positive and negative phases of the Pacific SST variability mode is very close to what has been observed in comparing dry and wet period in the central U.S. using NCEP Reanalysis data (e.g. Mo et al. 1997). Similar differences in the reanalysis surface moisture flux in

this region as in the present RAMS data likely exist. Where RAMS adds more value is in the representation of the Baja LLJ in the Gulf of California. The area in the northern Gulf of California where significant anomalies are found can only be resolved by one or two grid points in the NCEP Reanalysis. As with other fields previously discussed, the interannual differences in the LLJs associated with Pacific SSTs mirror the changes which occur climatologically between the monsoon peak minus premonsoon period. It also mirrors the change which is observed during a modeled Gulf surge event in RAMS, with increased winds in the Gulf of California and a more easterly component of the Great Plains LLJ (Saleeby and Cotton 2004). As mentioned in Chapter 4, RAMS tended to underestimate the strength of the Baja LLJ compared to surface observations and satellite-derived winds over the ocean. So it is suspected the actual surface moisture flux anomalies in this area associated with Pacific SST variability are greater in magnitude and extend through most of the length of the Gulf of California. Nonetheless, the difference in moisture transport is sufficient that a significant difference in Arizona rainfall results.

The changes in surface moisture flux associated with the SST regime shift mode are shown in the lower right of Fig. 5.13. Unlike the Pacific SST variability mode, the significant changes in moisture flux over the contiguous U.S. are not due to changes in the LLJs. They are reflective of a general increase in summertime moisture over the latter part of the record. The one area in the domain where there is the largest decrease in moisture flux is off the west coast of Mexico south of Baja California. This decrease in moisture transport (about 5% of the climatological mean) is due to the local decrease in the sea surface temperature gradient in this region, as indicated by the change in surface

temperature. The long term increase in sea surface temperatures in the subtropical eastern Pacific off the west coast of Mexico (0.4 to 0.6 K) since the early 1980s are thus the cause of the significant decrease in model-simulated precipitation in western Mexico. A similar connection of NAMS precipitation to eastern tropical Pacific SSTs was noted by Carleton et al. (1990).

In Chapter 4, a method was presented how to spectrally decompose a given variable into its dominant time-varying modes using a conventional Fourier analysis technique. The weighted spectral power of the given variable as the fraction of spectral power above climatological red noise in a frequency band was considered. Three distinct frequency bands were specified: a synoptic mode (4 – 15 days), a sub-synoptic mode (1.5 – 3 days), and a diurnal mode. Here the interest is in the difference in spectral power, viewed as the difference of the given composite minus the rest of the years divided by the 53-year climatological value of the spectrum. This quantity is multiplied by the weighting factor (W), so only areas where the climatological spectrum exceeds red noise are emphasized. This is referred to as the fractional difference in weighted spectral power.

As before, instead of showing the complete time series of evolution of the fractional difference in weighted spectral power, only a date for the period of maximum teleconnectivity for the Pacific SST variability mode in July is shown. The specific July date is chosen which approximately shows the maximum fractional difference in weighted spectral power. For the diurnal and synoptic bands this date is 15 July and for the sub-synoptic band it is 4 July. Similar patterns of differences were observed from early to mid July. The statistical significance of the fractional difference in weighted

spectral power is not assessed for the composites. This analysis is only intended to show that the spatial patterns of difference in the spectral bands correspond well with the statistically significant differences in precipitation already described.

As mentioned, the integrated moisture flux convergence (MFC) is analyzed because it is a proxy for convective activity. The fractional differences in weighted spectral power for the three bands in the Pacific SST variability mode composites are shown on the left hand side of Fig. 5.14, and these will be discussed first. The positive minus the negative composite divided by two is shown. First, and most important, the diurnal cycle differences are considered. From analysis of the climatology, this mode has the greatest spectral power in the core monsoon region in Mexico. It is also the dominant mechanism for rainfall generation in the Southwest U.S. and Great Plains. The greatest difference in the diurnal cycle occurs between these regions, where its intensity can vary up to 70% in years with differing phases of the Pacific SST variability mode. A high (low) phase of the mode is associated with a more (less) intense diurnal cycle of convection in the Great Plains and less (more) intense diurnal cycle of convection in the Southwest. The demarcation between these two regions with strong interannual variability is quite sharp and is roughly the continental divide. Given the changes already seen in the LLJs, this suggests the continental divide provides a physical barrier separating the moisture coming from each low-level source.

There can be large differences in the interannual variability of diurnal convection over relatively short distances (100s of km). The most striking example is in Colorado,

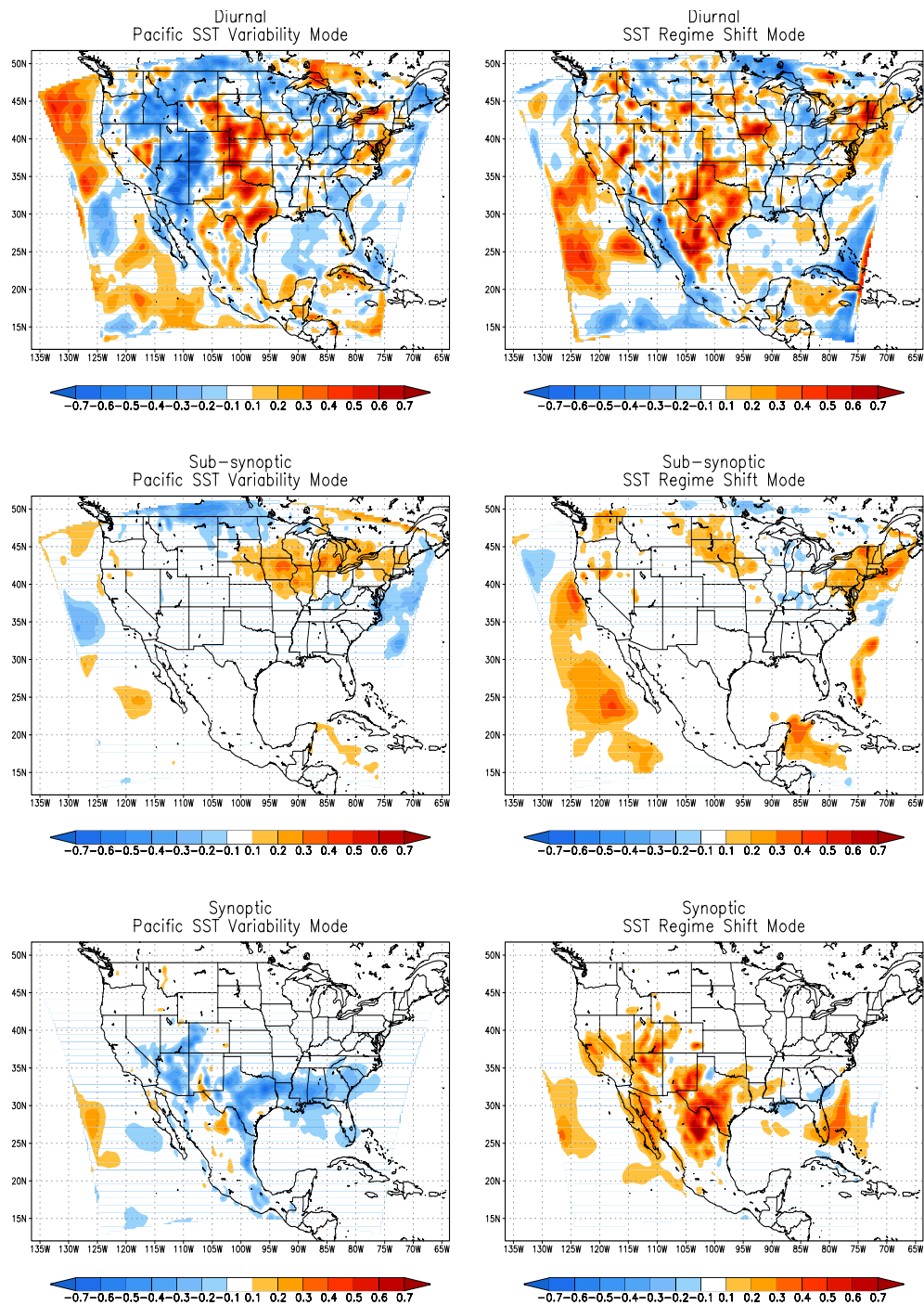


Figure 5.14: Fractional difference in weighted spectral power of integrated moisture flux convergence for Pacific SST variability mode and SST regime shift mode at the time of maximum teleconnectivity (see text for details). Shown are the diurnal (1 day), sub-synoptic (1.5-3 day) and synoptic (4-15 day) bands. Shading indicated by color bars.

where the Eastern Plains and Western Slope regions have completely opposite signals. This would also account for the noted difference in summer precipitation regimes between Arizona and New Mexico (e.g. Mo and Berbery 2004). The interannual changes in the diurnal cycle in relation to decadal variability in Pacific SST support the conclusions of Hu (2003). In that study, an hourly rainfall dataset over the U.S. was used to examine multidecadal variation in the diurnal rainfall pattern. It was found in decades when southerly flow dominated, the diurnal pattern had large rainfall amounts in the late night and morning hours, with a sharp rainfall peak at midnight. In the decades when southerly flow weakened, a different diurnal pattern emerged, with reduced late night/morning hour rainfall. From the present analysis, the pattern during years with a higher nocturnal peak in rainfall would correspond with more intense eastward-propagating mesoscale convective complexes.

While the other modes of MFC have less weighted spectral power, their interannual variability is nonetheless striking and consistent with the large-scale atmospheric teleconnections. As mentioned in Chapter 4, the sub-synoptic component of MFC reflects convection which is occurring beyond the diurnal timescale from fast moving synoptic weather systems or propagating mesoscale convective systems (MCSs) around the northeastern periphery of the monsoon ridge. Since these MCSs typically originate as diurnal convection over the Rocky Mountains, the interannual variation in the MCS signal in the upper Midwest is consistent with the diurnal variation to the west. The weighted spectral power in the sub-synoptic mode due to Pacific SST variability changes on the order of 20-30% in Iowa, northern Illinois, Wisconsin, and Michigan.

This area is approximately the location of largest rainfall anomalies in the contiguous U.S. in Fig 5.12.

The synoptic mode of MFC is related to the passage of eastward propagating disturbances, or tropical easterly waves (TEWs) around the southern periphery of the monsoon ridge. These cause periodic enhancement of the diurnal convection which may propagate westward off the terrain and organize into MCSs in the core monsoon region. As with its climatology, this mode shows the largest changes with Pacific SST variability at lower elevation and it varies as the diurnal cycle in the core monsoon region. There are two possible reasons for the change in spectral power in this mode. First, there may be a change in the strength of TEWs which trigger the convective bursts. Second, the strength of the TEWs does not change, but because of the change in the mean moisture transport from the Gulf of California the TEWs trigger larger and more widespread convective outbreaks in years with a low phase of the Pacific SST variability mode. An analysis of the spectral power of the 500-mb vorticity supports the latter hypothesis. It revealed very small changes (less than 10%) in the synoptic band during the period corresponding to the largest observed differences in the spectral power of MFC. The interannual variability of synoptic MFC in the southeast U.S. is also noteworthy. In Texas, for example, it behaves opposite to that of the diurnal mode, implying the diurnal cycle and synoptic variability of rainfall are not linked there.

The change in the variability of MFC due to the SST regime shift mode, shown in the right hand side of Fig. 5.14, also shows behavior that matches the precipitation anomalies in Fig. 5.10. In this case, the largest and most coherent changes in the diurnal cycle occur in the south-central U.S. and Mexican plateau and western Mexico. As in the

case of the Pacific SST variability mode, the clear dividing point between these regions is the continental divide along the SMO. To the west of the divide, the intensity of the diurnal cycle has decreased over the past twenty years by about 30-50%. The lower frequency modes show increases, owing to the general increase in moisture over the contiguous U.S. The long-term increase in synoptic MFC over the Southwest U.S. is about the same as the magnitude due to Pacific SST variability.

5.4 Dynamical Downscaling of Idealized GCM Experiments

It has been established that time-evolving teleconnections related to Pacific SST variability exist in (reanalysis) observations and that dynamical downscaling with a RCM produces coherent interannual climate signals in North America as a consequence of these teleconnections. This has been done so far in what is referred to as a Type 2 dynamical downscaling mode in Chapter 3, in which the initial atmospheric conditions have been forgotten, but results are dependent on the lateral boundary conditions from a numerical weather prediction GCM or atmospheric reanalysis and on the bottom boundary conditions. Now the question is posed whether similar results can be achieved in a Type 3 dynamical downscaling mode, in which the lateral boundary conditions are provided from a GCM which is forced with specified surface boundary conditions (SST in this case). This will explicitly test the hypothesis that the variations of the ENSO and PDO-like modes of global SST cause the observed regional-scale climate changes that have already been described.

Specifically, the GCM data that will be used for dynamical downscaling is from the NSIPP GCM experiments in Schubert et al. (2002) mentioned in Section 1.3. Four

ensemble experiments for the boreal summer season were performed using (Reynolds) SST forcing corresponding to the first and second rotated EOFs of global SST for the 1980-99 period superimposed on the SST climatology. Recall that REOF 2 in the 1980-99 SST record is the PDO-like mode and corresponds to REOF 3 in the 1950-2000 record. An ensemble consists of ten simulations for a particular sign of the given REOF. The simulations within each ensemble are produced by using ten different 1 May atmospheric and land surface initial conditions (from a longer NSIPP GCM simulation). The maximum imposed SST anomaly is about 1-2° C in the eastern tropical Pacific, about the same as shown in the SST composites in Fig 5.1. In addition to these four ensembles, a fifth ensemble was created using the 1980-99 SST climatology consisting of 40 simulations. All of these 80 GCM simulations were dynamically downscaled with RAMS in exactly the same manner as the NCEP Reanalysis (see Chapter 4), with one important exception. In the NCEP-Reanalysis downscaling, the initial soil moisture is prescribed specific to the year by a NLDAS product. In the NSIPP GCM downscaling, the initial soil moisture is prescribed as the NLDAS soil moisture climatology for the 53-year period for all the simulations, so there is no variation in the initial land state.

A complete description of the results of the variability in REOF 1 (ENSO mode) and REOF 2 (PDO-like mode) ensembles, in terms of their mean summer (JJA) behavior is found in Schubert et al. (2002), and the results pertinent to the present work are summarized. Both SST forced ensembles produce a zonally symmetric response in the geopotential height field, which is stronger in the midlatitudes for REOF 2. The largest shifts in precipitation, as would be expected, occur in the tropical Pacific and Indian oceans since the tropical convection is directly affected by changes in SST. Of particular

importance is the north-south shift of the ITCZ and the east-west shift in convection in the central and western Pacific. Both of these changes provide a potential mechanism for generation of quasi-stationary Rossby waves. The strongest NSIPP GCM generated precipitation anomalies in North America are in the REOF 2 simulations, specifically in northern Mexico and the central U.S., and Schubert et al. (2002) conclude this mode may control the general tendency for wet and dry conditions in these regions. For both REOF cases, the GCM-modeled precipitation patterns compare favorably with global observations gridded approximately to the same scale.

To evaluate whether these RAMS-downscaled NSIPP GCM simulations produce the results similar to the RAMS-downscaled reanalysis, the time evolution of the 500-mb NSIPP GCM height anomalies are first examined and then the behavior of the RAMS-downscaled precipitation, surface temperature, surface moisture flux, and integrated moisture flux convergence are examined in the same manner as done in the previous sections. The anomalies are calculated as the average of the REOF-forced simulation for a given ensemble minus the average of the climatological SST-forced ensemble. The statistical significance is determined by a two-tailed t-test.

The difference in the 30-day average NSIPP GCM 500-mb height field about the date and corresponding statistical significance were calculated for the four REOF 1 and REOF 2 ensembles. The results for REOF 1 are shown in Fig. 5.15 and for REOF 2 in Fig. 5.16. The domain and dates shown is identical to Fig. 5.5. Also, as in Fig. 5.5, the anomaly of the positive ensemble minus the negative ensemble divided by two is shown.

The time-evolution of 500-mb height anomalies for REOF 1 ensembles (Fig. 5.15) shows a strong response in the tropics, but only a weak midlatitude response. As in

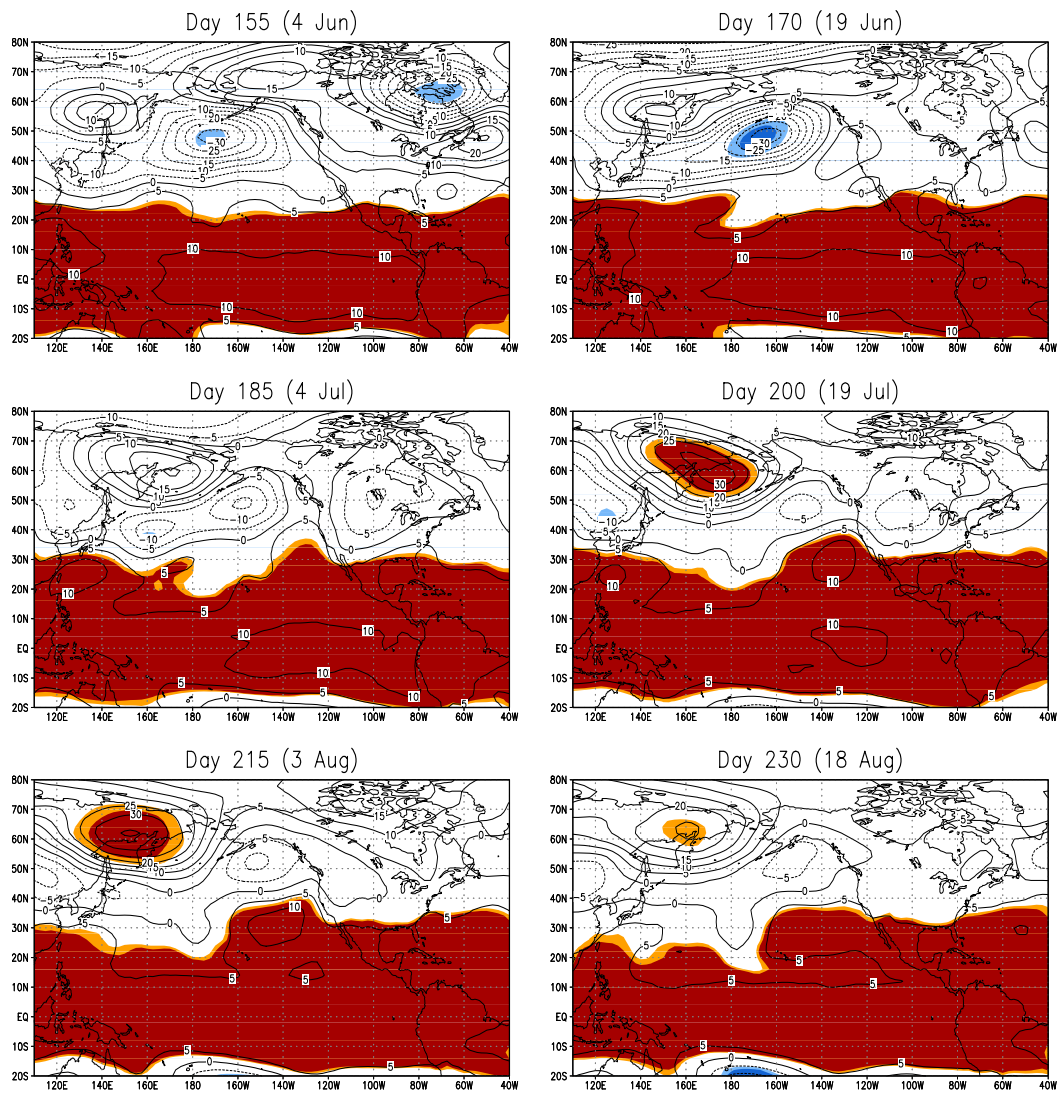


Figure 5.15: Time evolution of 30-day average 500-mb height anomalies (m) for NSIPP SST REOF 1 (ENSO mode) modeled summers. Contour interval is 5 m. Shading indicates statistical significance at the 90 and 95% levels.

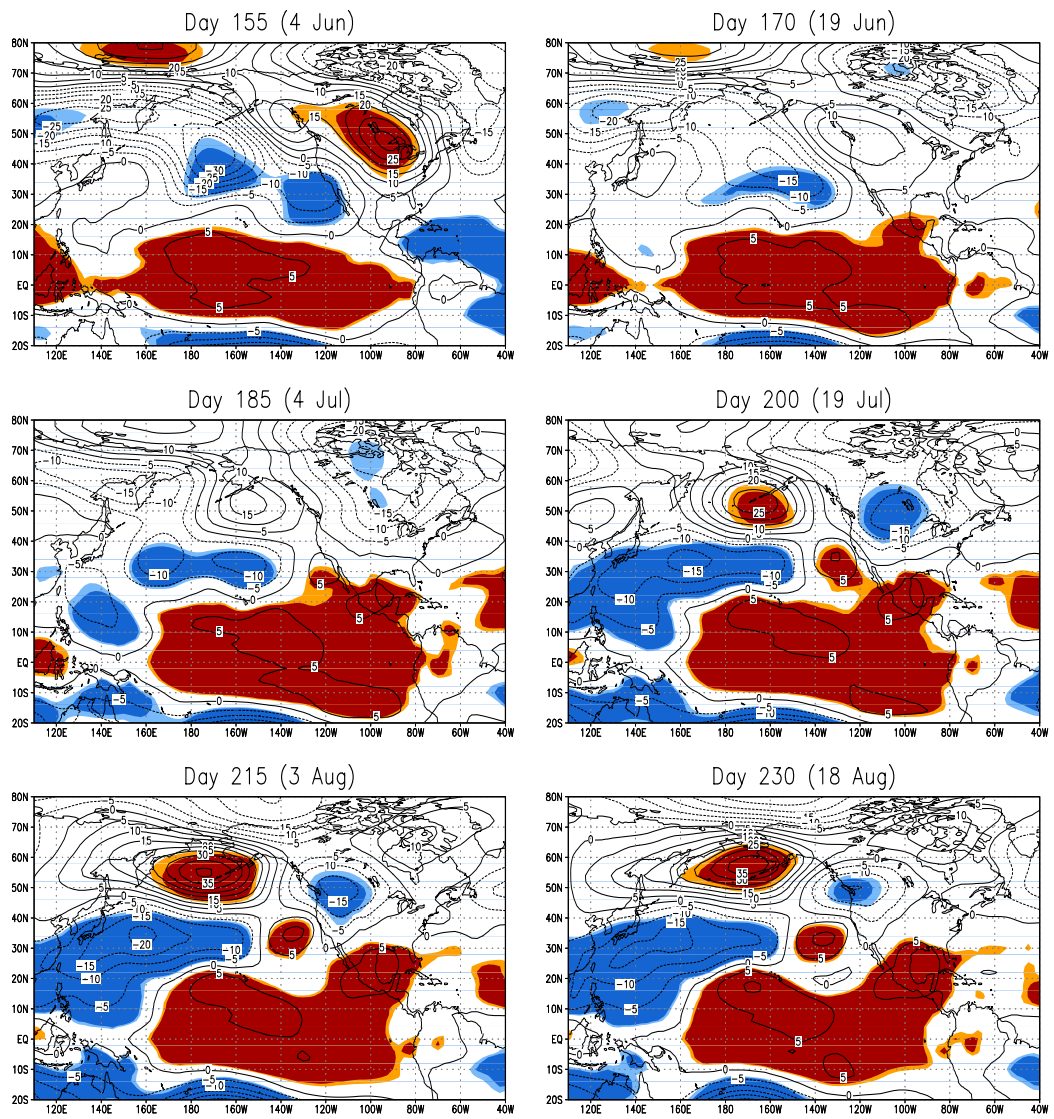


Figure 5.16: Same as Fig. 5.15 for NSIPP SST REOF 2 (PDO-like mode) modeled summers.

observations, the height anomaly over North America peaks on Julian day 185 (4 Jul), but it is not statistically significant when considering the sum of the positive and negative phases of the mode. The specific placement of the anomaly is in the incorrect location in the northern Great Plains instead of the northern Rocky Mountains. Thereafter the height anomalies in the central U.S. dissipate. The height anomalies for the REOF 2 ensembles (Fig. 5.16) are stronger and significant in the midlatitudes. In this case, the height anomaly peaks in late July and early August. It is in the correct location in the northern Great Plains, but peaks slightly later than observations. It is important to note that the height responses between the REOF 2 positive case and the REOF 2 negative case are not completely opposite of each other (not shown). The height anomaly in the northern Great Plains is mainly due to a large response (-30 m) in the positive REOF 2 ensemble. So it should be expected, a priori, that the “best” NSIPP GCM downscaling result with RAMS, in terms of correspondence with reanalysis downscaling already shown, should be for the REOF 2 positive ensemble, since it has the largest height anomaly in North America and most closely matches observations. It should be noted that the NSIPP REOF forced runs have more statistically significant height anomalies in the tropics than the REOF 1 and REOF 3 composites from observations. It is most likely that the SST warming trend in the tropics is masking the signal due to interannual SST variability there. As mentioned, when the shorter 1980-99 record is used there is an increase in the statistical significance of height anomalies in the tropics, particularly for the ENSO mode. The broader point which the NSIPP GCM height anomalies confirm is that the GCM teleconnection response associated with the PDO-like mode, as in observations, evolves in time and significantly affects the atmospheric circulation over North America during a certain

window. Though the height anomaly may be incorrect in terms of its timing, the GCM results demonstrate this fundamental trait of the boreal summer atmosphere.

The results for RAMS-NSIPP dynamical downscaling are shown for the four REOF-SST forced ensembles in Figs. 5.17, 5.18, 5.19, and 5.20. As before, only the time of maximum teleconnectivity corresponding to the NSIPP GCM is shown, chosen as 15 July for REOF 1 and 30 July for REOF 2. The difference shown is that of the REOF-SST forced ensemble minus the 40 year SST climatology ensemble. Statistical significance is computed by a two-tailed t-test.

The precipitation anomalies (Fig. 5.17) reveal, as suspected, that the REOF 2 positive ensemble yields the best GCM downscaling result with RAMS. At the time of maximum teleconnectivity the precipitation anomalies closely resemble those of the Reanalysis downscaled for the same mode of the 1950-2000 record (Fig. 5.11) on 19 July, with positive precipitation anomalies in the central U.S. and negative anomalies in the Southwest U.S. The magnitude of the precipitation anomaly in the central U.S. is about the same as in the reanalysis downscaling. In contrast to the observed years, there are significant precipitation anomalies in central and northern Mexico. These were noted in the precipitation from the NSIPP model as well (Schubert et al. 2002). The other 3 REOF ensembles bear less resemblance to their Reanalysis downscaled counterparts. Though the signal in the Southwest U.S. and northwest Mexico is generally consistent with observations, there is virtually no difference in RCM-simulated precipitation from the 40 year climatology in the central U.S. and a positive precipitation anomaly in the Southeast U.S., where there are no statistically significant differences in the reanalysis downscaled composites. A failure of the NSIPP GCM to correctly represent the

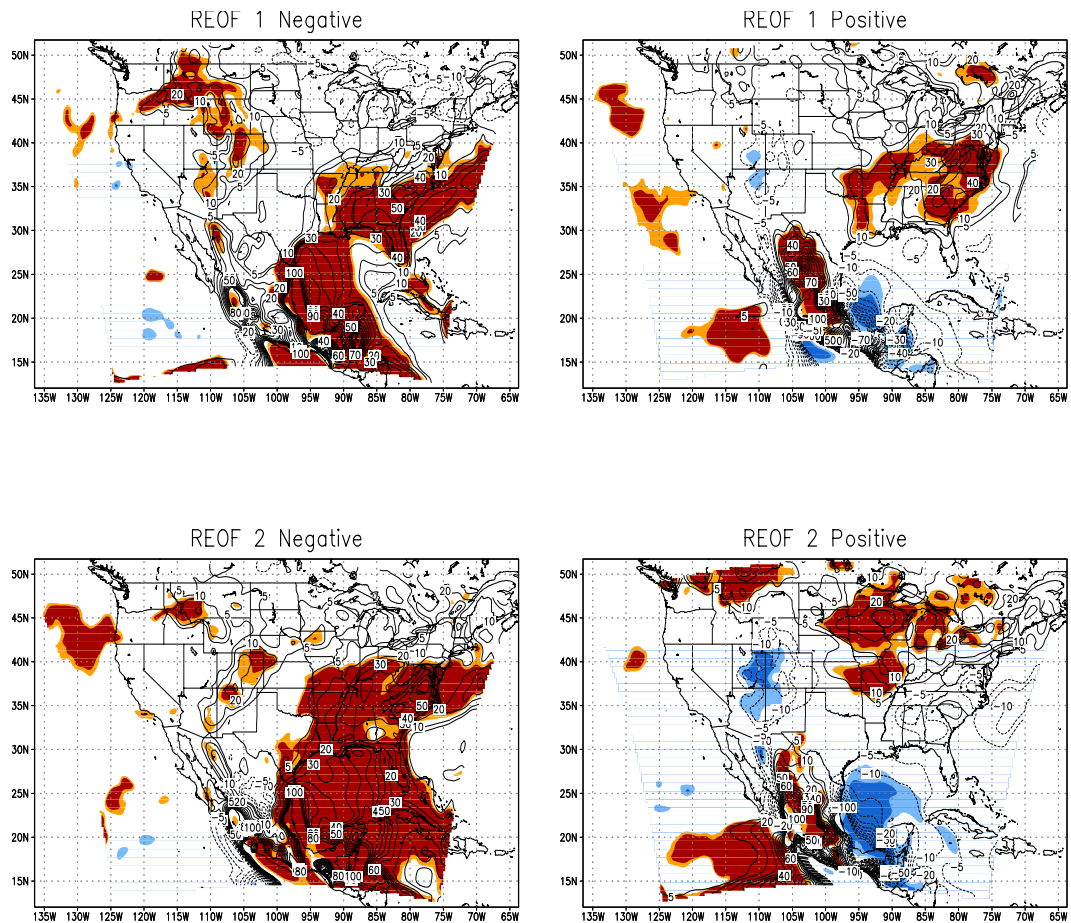


Figure 5.17: 30-day average RAMS precipitation anomalies (mm) of NSIPP REOF 1 and REOF 2 SST forced simulations at the time of maximum teleconnectivity (see text for details). Shading indicates statistical significance at the 90 and 95% levels. Contour interval is 5 mm up to 10 mm and 10 mm thereafter.

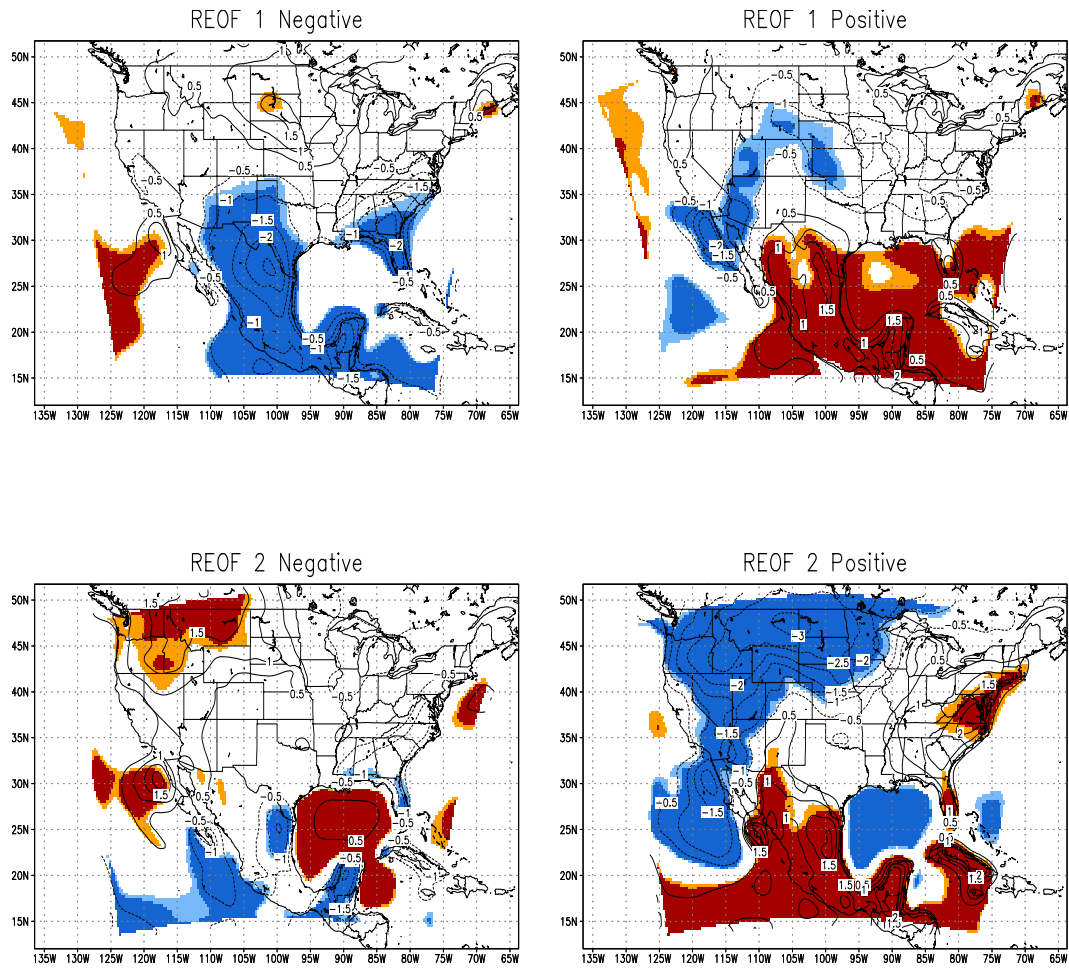


Figure 5.18: Same as Fig. 5.17 for RAMS surface temperature (K). Contour interval is 0.5 K.

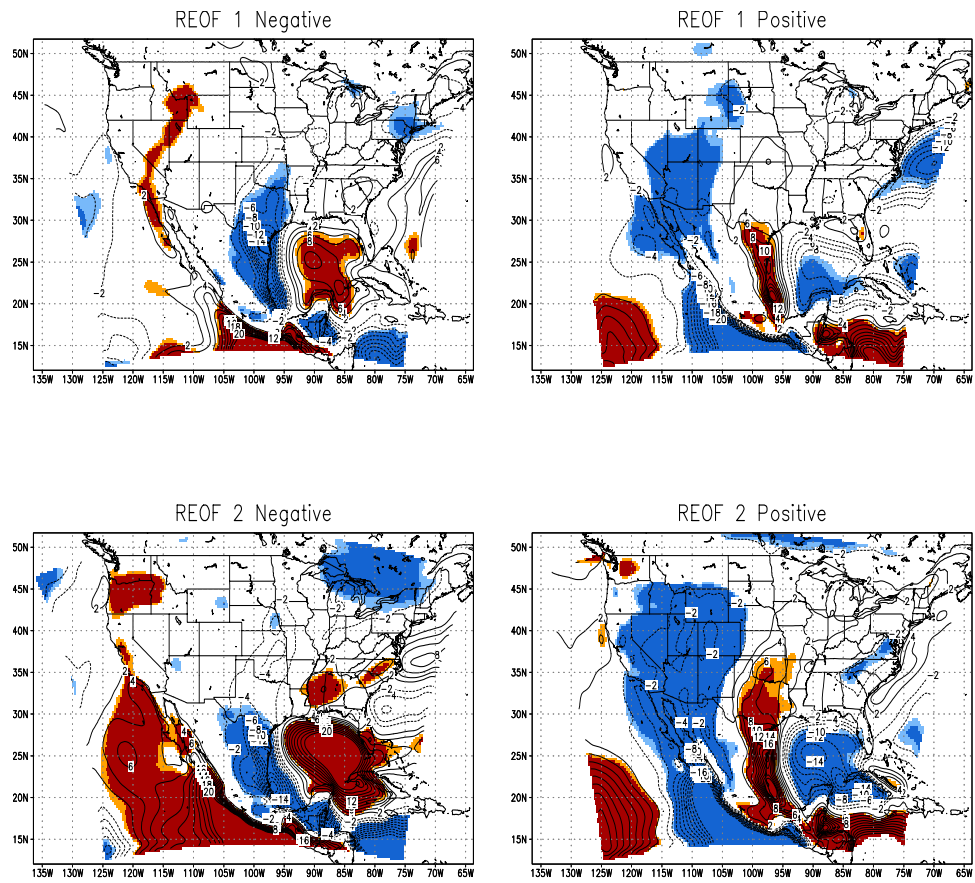


Figure 5.19: Same as Fig. 5.17 for surface moisture flux ($\text{m s}^{-1} \text{g kg}^{-1}$). Contour interval is $2 \text{ m s}^{-1} \text{g kg}^{-1}$.

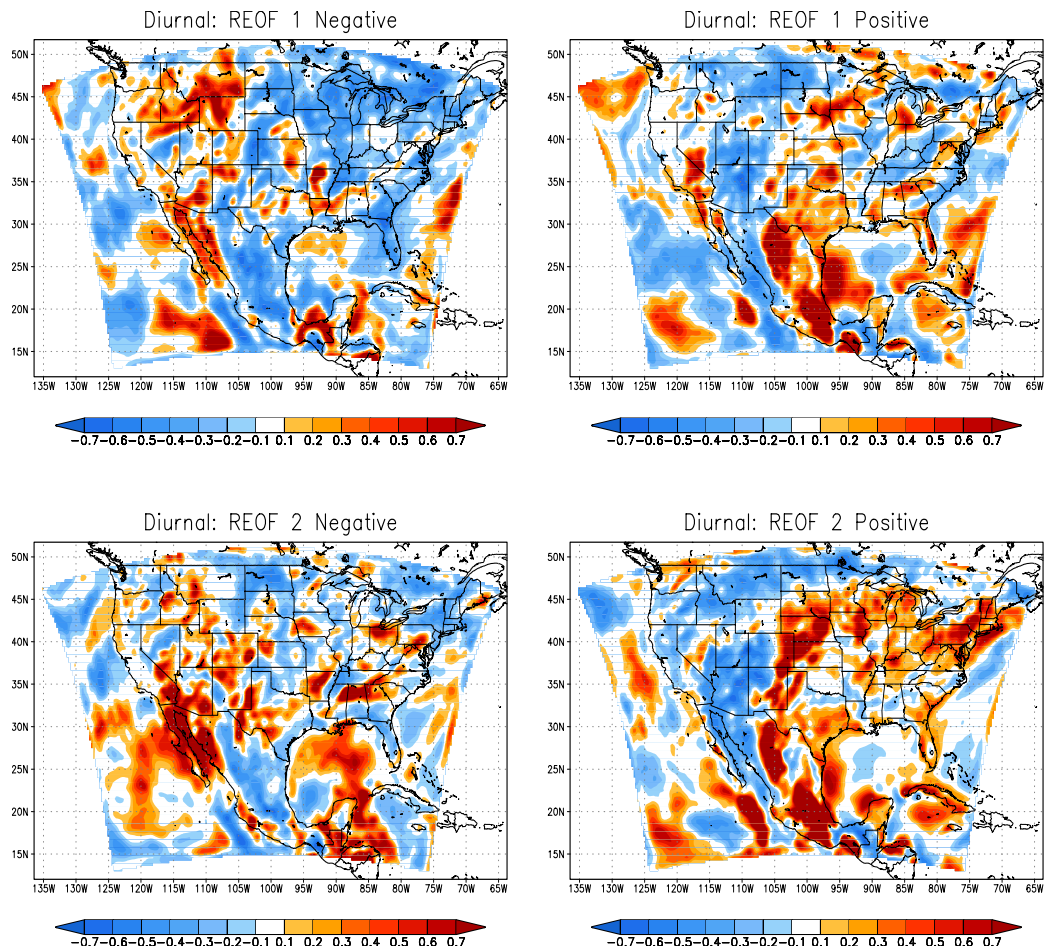


Figure 5.20: Same as Fig. 5.17 for the fractional difference in weighted spectral power of integrated moisture flux convergence. Only the diurnal band shown. Shading indicated by color bars.

atmospheric teleconnection in these cases explains part of the discrepancy. Another part is explained by the biases of the NSIPP GCM itself. Summer temperatures over land are too warm because the turbulent mixing is too weak to allow for adequate heat dissipation (S. Schubert, personal communication). The problem is particularly acute in the central U.S., where surface temperature in the NSIPP GCM is overestimated on the order of 5 K. This causes a large decrease in RAMS-simulated precipitation in this region as the summer progresses because the soil moisture excessively dries and the atmospheric environment is unfavorable for convection.

In spite of the weakness in the precipitation signal, the surface temperature (Fig. 5.17) and surface moisture flux anomalies (Fig. 5.18) are more consistent with reanalysis downscaling. In the REOF 1 ensembles and REOF 2 positive ensembles, the most significant temperature anomalies occur over Mexico, most likely related to the displacement of the ITCZ in the NSIPP GCM simulations. The most significant temperature response in the contiguous U.S. occurs in the REOF 2 positive ensemble because the midlatitude teleconnection is the strongest. The changes in surface moisture flux show the expected changes in the strength of the Great Plains LLJ associated with Pacific SST variability, though the extent of the significant anomalies does not extend as far northward into the central U.S. There are significant surface moisture flux anomalies in the central Gulf of Mexico associated with changes in easterly transport. Surface moisture flux anomalies in the vicinity of the Gulf of California are indicative of a change in the Baja LLJ. The decrease of the Baja LLJ significantly affects the surface moisture transport into the western U.S., mainly west of the continental divide, in the positive cases.

The fractional differences in weighted spectral power of integrated moisture flux convergence are shown for the diurnal band in Fig. 5.20. The other bands corresponding to Fig. 5.13 are not shown because those had much less spectral power than the RAMS-Reanalysis downscaled simulations. As would be expected, the most coherent signal in the interannual variability of the diurnal cycle occurs in the REOF 2 positive ensemble. The approximate dividing line between the central U.S. and Southwest U.S. regimes is the continental divide, and this is consistent with Fig. 5.13. Moreover, in the NSIPP-RAMS downscaled simulations a strong separation in the interannual variability of the diurnal cycle between northwest Mexico and central Mexico also occurs at the continental divide in the SMO, and this accounts for the significant differences in precipitation in that region. This behavior in Mexico resembles that of the SST regime shift mode in observations and there is a significant change in the magnitude of moisture transport from the eastern Pacific. The other REOF downscaled ensembles, with the possible exception of the REOF 2 negative ensemble, show the same demarcation in the interannual variability of the diurnal cycle between the Southwest U.S. and central U.S. Even in spite of the noted deficiencies in the NSIPP GCM, the diurnal cycle in RAMS exhibits a consistent response to the large-scale dynamical forcing imposed by the atmospheric teleconnections.

5.5 Summary and Discussion

In this chapter, results of summer dynamical downscaling simulations with RAMS in North America (1950-2002) were evaluated to investigate connections to global SST modes, with a focus of Pacific SST variability. An additional series of RCM

simulations dynamically downscaled data from the NSIPP GCM, for GCM simulations executed with idealized SST distributions corresponding to the dominant modes of Pacific SST variability, to establish the causal link to remote SST forcing. Time-evolving teleconnections associated with variability in Pacific SSTs modulate the evolution of the summer climate over North America. This occurs via their control of the strength and position of the monsoon ridge over the contiguous U.S. and the latitudinal position of the ITCZ. The teleconnection pattern associated with the PDO-like mode was shown to exist in both reanalysis observations and NSIPP GCM simulations. As in Castro et al. (2001), the teleconnection patterns and timing of each mode is distinct. The height anomalies peak in early summer (late June and July). At this time of maximum teleconnectivity the patterns associated with ENSO and PDO-like modes are in quadrature, at least in reanalysis observations. As noted by Schubert et al. (2002), the PDO-like mode has the stronger and more statistically significant teleconnection relationship in the midlatitudes. A SST regime shift mode is related to a warming of the tropical atmosphere. This mode does not have any significant relationship to height anomalies in the midlatitudes.

The existence of a midlatitude teleconnection response in boreal summer is supported by the idealized modeling studies using baroclinic and barotropic models as discussed in Section 1.3 and Castro et al. (2001). Anomalous diabatic heating patterns in the tropics provide the sources and sinks for quasi-stationary Rossby waves that propagate into the extratropics. The time-dependency arises because of the rapid changes in upper-level winds over the Pacific as the summer proceeds, and hence a change in the Rossby wave forcing in the western Pacific for a constant source of tropical atmospheric

heating. As the westerlies weaken over the Pacific, Newman and Sardeshmukh (1998) suggest the forcing region for the Rossby waves shifts westward with time and the forcing diminishes later in the summer. This would account for the tendency of height anomalies associated with the ENSO mode to peak before those of the PDO-like mode and for the decay of teleconnection relationships in August. Schubert et al. (2004) also emphasize that most of the forcing in their NSIPP GCM simulations comes from the tropics, though the possible forcing from the extratropical North Pacific cannot be discounted.

In a Type 2 dynamical downscaling mode in which the lateral boundary conditions are constrained by an atmospheric reanalysis, the modes associated with variability in Pacific SSTs generate a response in RCM-generated precipitation over North America that occurs approximately simultaneously with the time of maximum teleconnectivity. At these times a positive (negative) phase of the Pacific SST variability mode favors increased (decreased) precipitation in the central U.S. and decreased (increased) precipitation in the core monsoon region. Since the times of maximum teleconnectivity and teleconnection patterns are slightly different for the ENSO and PDO-like modes, the combined index of these modes maximizes the explained variance in precipitation over a longer period and wider geographic area. This is in agreement with the observational analysis of Mo and Paegle (2000). The response of the other variables investigated is consistent with the precipitation response. The teleconnections modulate the strength of the Great Plains and Baja LLJs in opposite ways, affecting the moisture transport into the central U.S. and core monsoon region, respectively. The enhanced (or decreased) moisture amplifies (or diminishes) the diurnal cycle of

convection in these regions, separated approximately by the continental divide. The lower frequency modes of convection (longer than one day), namely MCSs, which occur at a distance from the elevated terrain are similarly affected. The differences can be interpreted as a modulation of the summer climatological cycle in North America because the anomaly patterns mimic the difference between premonsoon and monsoon peak conditions.

There is also important behavior associated with the SST regime shift which occurred in approximately the late 1970s to early 1980s. The important features of this shift include a 0.25-0.5 K warming in tropical SSTs and a 0.4 K cooling in the North Pacific. Tropical 500-mb geopotential height has significantly increased by 5-10 m. A 10-20% increase in model-generated summer precipitation across the contiguous U.S., particularly east of the Rockies, occurred over the past two decades. There is little or no time dependence of the precipitation anomalies as the summer progresses. The increase in RCM-simulated precipitation in the contiguous U.S. is due to an observed increase in atmospheric moisture during the latter part of the record. The region which exhibited a significant precipitation decrease and a decrease in the strength of the diurnal cycle of convection is western Mexico because of reduced moisture transport from the eastern Pacific. The long-term trend in Mexican precipitation as simulated by RAMS merits further investigation, as the NAMS provides the majority of rainfall there.

The NSIPP-RAMS downscaled simulations showed similar patterns of climate variability coincident with the time of maximum teleconnectivity in the NSIPP GCM, particularly for the ensemble with had the closest height anomalies to observations (REOF 2 positive for the 1980-99 SST record). This demonstrates that the RCM still

yields some predictive skill in a Type 3 dynamical downscaling mode in which the lateral boundary conditions are from a GCM with specified SST conditions, but this conclusion is not especially strong. There were two main reasons for deficiencies in the NSIPP-RAMS downscaling simulations. First, and most important, the NSIPP GCM has a high temperature bias in its mean summer climatology, affecting the summer precipitation in the central U.S. Second, the NSIPP GCM was not able to produce the observed teleconnection response in all four ensembles with perturbed SST. The weaker ENSO teleconnection was the more difficult to produce, in terms of its positioning and timing. The difference could be due, among other things, to how the NSIPP GCM represents the upper-level winds across the Pacific as this would affect the Rossby wave forcing and propagation (Newman and Sardeshmukh 1998). It is suggested that the NSIPP GCM experiments of Schubert et al. (2002) be repeated with a variety of GCMs to evaluate the existence of the time-evolving teleconnection response in boreal summer and any systematic model biases that would affect how the GCM would dynamically downscale. Additional GCM ensembles should be performed to evaluate the effect the of the Pacific SST variability mode. Only if the teleconnection responses exist and the model biases in summer climate could be reduced, as compared to the reanalysis, a more robust RCM dynamical downscaling result could probably be achieved.

The present RCM experiments shown, as previous GCM and observational studies have suggested, that large-scale wet and dry summer conditions in the contiguous U.S. and Mexico are highly dependent on remote forcing from Pacific SSTs. A significant relationship to precipitation occurs even when the same initial land surface state is used in the RCM. Though there are significant relationships between North

American summer precipitation and antecedent land surface conditions, such as snow cover (Gutzler and Preston 1997; Gutzler 2000; Lo and Clark 2002), such relationships are unstable over decadal timescales and regionally dependent. There is the possibility that these relationships occur as a consequence of the evolution of Pacific-SST associated teleconnections through an annual cycle (Castro et al. 2001). Whether or not land surface anomalies in North America upscale to affect the large-scale atmospheric circulation is an unsolved issue and merits further investigation. To date, studies with GCMs and RCMs have found conflicting results (e.g. Wang and Kumar 1998; Pal and Eltahir 2003).

Irrespective of this possible upscaling effect, summer land surface anomalies in North America certainly do have local impact due to their modification of the surface energy budget and boundary layer structure. RCM investigations of the 1993 Flood and 1988 Drought conclude there is a positive feedback between soil moisture and rainfall, and the feedback is stronger in drought years (e.g. Hong and Pan 2000; Pal and Eltahir 2001). Additional work on the more recent 1998 drought suggests the same is equally true for other years (Hong and Kalnay 2002). Fewer RCM studies have considered the impact of soil moisture on NAMS rainfall in Mexico or the Southwest U.S., but they have demonstrated local soil moisture variation can also affect rainfall there (e.g. Small 2001; Kanamitsu and Mo 2003).

More unknown is the possible role of vegetation feedback on summer climate. Through transpiration, vegetation and its spatial distribution may be just as important as soil moisture in explaining variability of summer rainfall (e.g. Pielke 2001b). For example, using normalized difference vegetation index (NDVI) derived leaf area index (LAI) instead of model-prescribed LAI in the land surface scheme, Lu and Shuttleworth

(2002) showed RAMS produces a wetter and cooler climate in the summer growing season in the central U.S. Sensitivity studies with other RCMs are just beginning to look at possible vegetation influences in the core NAMS region (Matsui et al. 2005). Future work with the RAMS model will use the present set of simulations as a baseline to evaluate the influence of land surface conditions in different Pacific SST regimes. In particular, do land surface feedbacks enhance the relationship with Pacific SSTs?

Finally, if SST-forced boreal summer teleconnections truly are global in nature, as Schubert et al. (2002) show, then it could be expected that climate variability in other parts of the world besides North America would be impacted, such as East Asia (Lau and Weng 2002) and Europe (Katsafados 2005). Dynamical downscaling of atmospheric reanalyses and GCM data in the same vein as done here for North America may also yield similar significant results for these regions when considering SST-climate relationships.

Chapter 6
GENERAL SUMMARY, CONCLUSIONS, AND
SUGGESTIONS FOR FUTURE WORK

With an appropriate experimental design, RCMs are a valuable tool to enhance understanding of processes on the mesoscale, which is particularly important when considering summer climate in North America. The first part of this research focused on developing that experimental design for RAMS. The Kain-Fritsch cumulus parameterization scheme, which is commonly used in other regional models, with a terrain-adjusted trigger function, was implemented as an alternative in RAMS to the existing Kuo scheme. The value restored and added by dynamical downscaling in a Type 2 mode, with reanalysis lateral boundary forcing, was evaluated by considering the spectral behavior of the RAMS solution in relation to domain size and grid spacing in a series of basic sensitivity experiments. Follow-on experiments investigated the effect of varying the surface forcing and model parameterizations. The model modifications and sensitivity analyses were all necessary steps before proceeding to the main theme of this research, constructing a long-term (1950-2002) RCM climatology of the contiguous U.S. and Mexico by downscaling the NCEP Reanalysis. This climatology was validated against observed surface data and the time-varying modes of convection were examined. The RCM simulations were then evaluated with respect to the dominant modes of global SST, with an emphasis on Pacific SST variability. An additional series of regional

climate model simulations dynamically downscaled data from the NASA Seasonal to Interannual Prediction Project (NSIPP) GCM, for GCM simulations executed with idealized SST distributions corresponding to ENSO and PDO-like modes. These Type 3 simulations sought to establish a causal link of North American summer climate variability to remote sea surface temperature forcing.

The dynamical downscaling sensitivity investigation in Chapter 3 revealed very important, and large, sensitivities to the user-defined specifications of a RCM. At large scales, RAMS underestimated atmospheric variability as determined by the column integrated kinetic energy and integrated moisture flux convergence. As the grid spacing of domain size increased, the underestimation of atmospheric variability at the large scales worsened. The model simulated evolution of the kinetic energy relative to the reanalysis regrided kinetic energy exhibited a decrease with time and was more pronounced with larger grid spacing. The surface boundary forcing was the dominant factor in generating atmospheric variability for small-scale features and it exerted greater control on the regional climate model solution as the influence of lateral boundary conditions diminished. The sensitivity to surface forcing was also influenced by the model parameterizations, as demonstrated by using the Kain-Fritsch convection scheme in lieu of the Kuo convection scheme. Dynamical downscaling in a RCM mode (Type 2 and higher) does not appear to retain value of the large scale of that which exists the larger reanalysis or GCM driving data. The utility of the RCM, or value added, is to resolve the smaller-scale features with have a greater dependence on the surface boundary. This conclusion regarding RAMS is expected to be true for other RCMs as well.

The first part of this research established important necessary conditions for RCM simulations with RAMS, which were applied to the summer climatology in Chapters 4 and 5. First, a domain should be sufficiently constrained in size in order for the lateral boundary forcing to affect the model solution. A continental-scale, or smaller, domain is most appropriate. Second, weak internal nudging (at a one-day timescale, for example) forces the RCM solution to the reanalysis (or GCM) solution at the large-scale, while allowing the surface forcing to act on the small scale. Finally, use of the Kain-Fritsch cumulus parameterization scheme is more appropriate for the warm season because it is more sensitive to the surface forcing and yields a better representation of precipitation, in terms of amount and spatial distribution.

The summer RCM climatology for North America was reasonable, in light of observations and comparison to previous RCM results. The simulations captured the seasonal transitions in precipitation and temperature associated with the development of the North American Monsoon System, particularly the abrupt increase in precipitation in the core monsoon region. As in previous studies, the model generated precipitation was overestimated compared to gauge data and agreed better with satellite-derived estimates. The Baja and Great Plains low-level jets and their evolution through the summer were represented, though the Baja low-level jet and associated gulf surge events were too weak. RAMS also showed the development of a monsoon ridge over western North America and a transition to easterlies south of the ridge. The diurnal cycle was the dominant mode of variability in convection, especially in the core monsoon region and central U.S., and was modulated by the large-scale circulation. The lower frequency

modes of variability in convection, though weaker, were still physically important and accounted for the variability of convection at a remote distance from elevated terrain.

The length of the RCM climatology was sufficient to characterize the variability of North American summer climate with respect to global SST modes. Time-evolving teleconnections associated with ENSO and PDO-like SST modes accelerate or delay NAMS evolution, and these appear in both the NCEP Reanalysis and NSIPP GCM data. The PDO-like mode produced the stronger teleconnection response. The SST regime shift mode in the 1950-2000 record was associated with an increase in tropical SST and tropical tropospheric temperature, but had no relation to significant height anomalies in the midlatitudes. The most significant response in RAMS-generated fields, with respect to Pacific SST variability mode, occurs simultaneously with the time of maximum teleconnectivity (late June and July). At this time, a positive (negative) phase of the Pacific SST variability mode favored increased (decreased) precipitation in the central U.S. and decreased (increased) precipitation in the core monsoon region. The teleconnections affected the strength of the Great Plains and Baja low-level jets, and their respective moisture transport in the continental interior, in opposite ways. The changes in low-level moisture transport affected the magnitude of the diurnal cycle, as well as the lower frequency modes of convection. The SST regime shift mode was associated with a general increase in atmospheric moisture and rainfall across the eastern U.S. and eastern Mexico throughout the summer. Model-generated monsoon rainfall in western Mexico decreased since the early 1980s due to the increase in SST in the eastern tropical Pacific.

Suggestions for future research with respect to the investigation of North American summer climate include:

- *Investigation of the impact of the land surface state.* How do snow cover, vegetation, and soil moisture interact with the climate forcing by Pacific SSTs? Is there a positive feedback? The present set of RCM simulations could be used as a baseline to evaluate the influence of land surface conditions in different Pacific SST regimes.
- *Finer resolution simulations with RCMs.* These simulations should ideally be at the cloud-resolving scale and would provide a better representation of summertime convection and mesoscale circulation features, such as the Baja low-level jet. The recent North American Regional Reanalysis can provide more resolved lateral boundary conditions for model experiments, though this product is only available since the late 1970s.
- *Additional GCM simulations forced with the dominant modes of global SST variability.* A variety of different GCM should be used to confirm the robustness of the time-evolving teleconnection response related to Pacific SSTs and effect of the SST regime shift mode. These simulations could then be dynamically downscaled by a single RCM or suite of RCMs in the same manner as done here.

- *Dynamical downscaling for other parts of the world.* If the boreal summer teleconnection response to Pacific SSTs is truly global in nature, then regional boreal summer climate responses likely exist in areas like East Asia and Europe. Dynamical downscaling in the same vein as done for North America may also yield significant results.

REFERENCES

- Adams, D.K., and A.C. Comrie, 1997: The North American monsoon. *Bull. Amer. Meteor. Soc.*, **78**, 2197-2213.
- Adegoke, J.O., R.A. Pielke Sr., J. Eastman, R. Mahmood, and K.G. Hubbard, 2003: Impact of irrigation on midsummer surface fluxes and temperature under dry synoptic conditions: a regional atmospheric model study of the U.S. High Plains. *Mon. Wea. Rev.*, **131**, 556-564.
- Alexander, M.A., I. Bladé, M. Newman, J.R. Lanzante, N.C. Lau, and J.D. Scott, 2002: The atmospheric bridge: The influence of ENSO teleconnections on air-sea interaction over the global oceans. *J. Climate*, **15**, 2205-2231.
- Anderson, B.T., J.O. Roads, S. Chen, and H.H. Juang, 2000: Regional simulation of the low-level monsoon winds over the Gulf of California and the southwestern United States. *J. Geophys. Res.*, **105**, 24,455-24,467.
- Anderson, B.T., 2002: Regional simulations of intraseasonal variations in the summertime hydrologic cycle over the southwestern United States. *J. Climate*, **15**, 2282-2299.
- Anderson, B.T., H. Kanamaru, and J.O. Roads, 2004: The summertime atmospheric hydrologic cycle over the southwestern United States. *J. Hydrometeor.*, **5**, 679-692.

- Arkin, P.A., 1979: The relationship between the fractional coverage of high cloud and rainfall accumulations during GATE over the B-array. *Mon. Wea. Rev.*, **107**, 1382-1387.
- Barlow, M., S. Nigam, and E.H. Berbery, 1998: Evolution of the North American monsoon system. *J. Climate*, **11**, 2238-2257.
- Barnett, T.P., D.W. Pierce, and R. Schnur, 2001: Detection of anthropogenic climate change in the world's oceans. *Science*, **292**, 270-274.
- Barnett, T.P., D.W. Pierce, K.M. Achuta Rao, P.J. Gleckler, B.D. Santer, J.M. Gregory, and W.M. Washington, 2005: Penetration of human-induced warming into the world's oceans. *Science*, **309**, 284-287.
- Bell, J.D., and J.E. Janowiak, 1995: Atmospheric circulation associated with the Midwest floods of 1993. *Bull. Amer. Meteor. Soc.*, **76**, 681-695.
- Berbery, E.H., 2001: Mesoscale moisture analysis of the North American monsoon. *J. Climate*, **14**, 121-137.
- Berbery, E.H., and M.S. Fox-Rabinovitz, 2003: Multiscale diagnosis of the North American monsoon system using a variable resolution GCM. *J. Climate*, **16**, 1929-1947.
- Black, T.J., 1994: The new NMC mesoscale Eta model: description and forecast examples. *Wea. Forecasting*, **9**, 265-278.
- Brubaker, K.L., P.A. Dirmeyer, A. Sudradiat, B.S. Levey, and F. Bernal, 2001: A 36-yr climatological description of the evaporative sources of warm-season precipitation in the Mississippi River basin. *J. Hydrometeor.*, **2**, 537-557.

- Bryson, R.A., and W.P. Lowry, 1955: The synoptic climatology of the Arizona summer precipitation singularity. *Bull. Amer. Meteor. Soc.*, **36**, 329-339.
- Byerle, L., and J. Paegle, 2003: Modulation of the Great Plains low level jet and moisture transports by orography and large scale circulation. *J. Geophys. Res.*, **108 (D16)**, 8611, doi:10.1029/2002JD003005.
- Carbone, R.E., J.D. Tuttle J.D., D.A. Ahijevych, and S.B. Trier, 2002: Inferences of predictability associated with warm season precipitation episodes. *J. Atmos. Sci.*, **59**, 2033-2056.
- Carleton, A.M., D.A. Carpenter, and P.J. Weser, 1990: Mechanisms of interannual variability of the southwest United States summer rainfall maximum. *J. Climate*, **3**, 999-1015.
- Castro, C.L., T.B. McKee, and R.A. Pielke Sr., 2001: The relationship of the North American monsoon to tropical and north Pacific sea surface temperatures as revealed by observational analyses. *J. Climate*, **14**, 4449-4473.
- Cavazos, T., A.C. Comrie, and D.M. Liverman, 2002: Intraseasonal variability associated with wet monsoons in southeast Arizona. *J. Climate*, **15**, 2477-2490.
- Chen, C. and W.R. Cotton, 1983: A one-dimensional simulation of the stratocumulus-capped mixed layer. *Bound. Layer Meteor.*, **25**, 298-321.
- Chen, C., and W.R. Cotton, 1987: The physics of the marine stratocumulus-capped mixed layer. *J. Atmos. Sci.*, **44**, 2951-2977.
- Chen, Q.-S., and Y.-H. Kuo, 1992: A harmonic-sine series expansion and its application to partitioning and reconstruction problems in a limited area. *Mon. Wea. Rev.*, **120**, 91-112.

- Chiang, J.C.H., and D.J. Vimont, 2004: Analogous Pacific and Atlantic meridional modes of tropical atmosphere-ocean variability. *J. Climate*, **17**, 4143-4158.
- Cotton, W.R., R.L. George, P.J. Wetzel, and R.L. McAnelly, 1983: A long-lived mesoscale convective complex. Part I: the mountain-generated component. *Mon. Wea. Rev.*, **111**, 1893-1918.
- Cotton, W.R., R.A. Pielke Sr., R.L. Walko, G.E. Liston, C. Tremback, H. Jiang, R.L. McAnelly, J.Y. Harrington, M.E. Nicholls, G.G. Carrio, and J.P. McFadden, 2003: RAMS 2001: Current status and future directions. *Meteor. Atmos. Phys.*, **82**, 5-29.
- Davies, H.C., 1976: A lateral boundary formulation for multi-level prediction models. *Quart. J. Roy. Meteor. Soc.*, **102**, 405-418.
- de Elía, R., R. Laprise, and B. Denis, 2002: Forecasting skill limits of nested limited-area models: a perfect-model approach. *Mon. Wea. Rev.*, **130**, 2006-2023.
- Denis, B., J. Côté, and R. Laprise, 2002: Spectral decomposition of two-dimensional atmospheric fields on limited area domains using the discrete cosine transform (DCT). *Mon. Wea. Rev.*, **130**, 1812-1829.
- Denis, B., R. Laprise, J. Côté, and D. Caya, 2002: Downscaling ability of one-way nested regional models: the big-brother experiment. *Climate Dyn.*, **18**, 627-646.
- Deser, C., M.A. Alexander, and M.S. Timlin, 2003: Understanding the persistence of sea surface temperature anomalies in midlatitudes. *J. Climate*, **16**, 57-72.
- Douglas, M.W., R.A. Maddox, and K. Howard, 1993: The Mexican monsoon. *J. Climate*, **6**, 1665-1677.

- Douglas, M.W., 1995: The summertime low-level jet over the Gulf of California. *Mon. Wea. Rev.*, **123**, 2334-2347.
- Eastman, J.L., M.B. Coughenour, and R.A. Pielke, Sr., 2001: The effects of CO₂ and landscape change using a couple plant and meteorological model. *Global Change Biology*, **7**, 797-815.
- Englehart, P.J., and A.V. Douglas, 2002: On some characteristic variations in warm season precipitation over the central United States (1910-2000). *J. Geophys. Res.*, **107 (D16)**, 4286, doi:10.1029/2001JD000972.
- Englehart, P.J., and A.V. Douglas, 2003: Assessing warm season drought episodes in the central United States. *J. Climate*, **16**, 1831-1842.
- Errico, R.M., 1985: Spectra computed from a limited area grid. *Mon. Wea. Rev.*, **113**, 1554-1562.
- Fritsch, J.M., R.J. Kane, and C.R. Chelius, 1986: The contribution of mesoscale convective weather systems to the warm-season precipitation in the United States. *J. Climate Appl. Meteor.*, **25**, 1333-1345.
- Gaffen, D.J., and R.J. Ross, 1999: Climatology and trends of U.S. surface humidity and temperature. *J. Climate*, **12**, 811-828.
- Gilman, D., P. Fuglister, and J.M. Mitchell, 1963: On the power spectrum of red noise. *J. Atmos. Sci.*, **20**, 182-184.
- Gochis, D.J. W.J. Shuttleworth, and Z.L. Yang, 2002: Sensitivity of the modeled North American monsoon regional climate to convective parameterization. *Mon. Wea. Rev.*, **130**, 1282-1298.

- Gochis, D.J., W.J. Shuttleworth, and Z.L. Yang, 2003: Hydrometeorological response of the modeled North American monsoon to convective parameterization. *J. Hydrometeor.*, **4**, 235-250.
- Giorgi, F., M.R. Marinucci, and G.T. Bates, 1993a: Development of a second-generation regional climate model (RegCM2). Part I: Boundary-layer and radiative transfer processes. *Mon. Wea. Rev.*, **121**, 2794-2813.
- Giorgi, F., M.R. Marinucci, and G.T. Bates, 1993b: Development of a second-generation regional climate model (RegCM2). Part II: convective processes and assimilation of lateral boundary conditions. *Mon. Wea. Rev.*, **121**, 2814-2832.
- Grell, G.A., J. Dudhia, and D. Stauffer, 1994: A description of the fifth generation Penn State/NCAR mesoscale modeling system (MM5). NCAR Technical Note, NCAR/TN-397+STR, 117 pp.
- Gurshunov, A., and T.B. Barnett, 1998: Interdecadal modulation of ENSO teleconnections. *Bull. Amer. Meteor. Soc.*, **79**, 2715-2725.
- Gutzler, D.S., and J.W. Preston, 1997: Evidence for a relationship between spring snow cover in North America and rainfall in New Mexico. *Geophys. Res. Lett.*, **24**, 2207-2210.
- Gutzler, D.S., 2000: Covariability of spring snowpack and summer rainfall across the southwest United States. *J. Climate*, **13**, 4018-4027.
- Gutzler, D., and Coauthors, 2004: *The North American Monsoon Model Assessment Project (NAMAP)*. NCEP Climate Prediction Center Atlas 11, 32 pp.
- Hansen, J., L. Nazarenko, R. Ruedy, M. Sato, J. Willis, A. Del Genio, D. Koch, A. Lacis, K. Lo, S. Menon, T. Novakov, J. Perlwitz, G. Russell, G.A. Schmidt, and N.

- Tausenev, 2005: Earth's energy imbalance: confirmation and implications. *Science*, **308**, 1431-1435.
- Higgins, R.W., J.E. Janowiak, and Y. Yao, 1996: *A gridded hourly precipitation data base for the United States (1963-1993)*. NCEP Climate Prediction Center Atlas 1, 47 pp.
- Higgins, R.W., Y. Yao, and X.L. Wang, 1997a: Influence of the North American monsoon system on the U.S. Summer precipitation regime. *J. Climate*, **10**, 2600-2622.
- Higgins, R.W. Y.Yao, E.S. Yarosh, J.E. Janowiak, and K.C. Mo, 1997b: Influence of the Great Plains low-level jet on summertime precipitation and moisture transport over the central United States. *J. Climate*, **10**, 481-507.
- Higgins, R.W., Y. Chen, and A.V. Douglas, 1999: Interannual variability of the North American warm season precipitation regime. *J. Climate*, **12**, 653-680.
- Higgins, R.W., and W. Shi, 2001: Intercomparison of the principal modes of interannual variability of the North American monsoon system. *J. Climate*, **14**, 403-417.
- Hoerling, M., and A. Kumar, 2003: The perfect ocean for drought. *Science*, **299**, 691-694.
- Hong, S.Y., and H.L. Pan, 2000: Impact of soil moisture anomalies on seasonal summertime circulation over North America in a regional climate model. *J. Geophys. Res.*, **105**, D24, 29,625-29,634.
- Hong, S.Y., and E. Kalnay, 2002: The 1998 Oklahoma-Texas drought: mechanistic experiments with NCEP global and regional models. *J. Climate*, **14**, 2469-2480.

- Houghton, J.T., Y. Ding, D.J. Griggs, M. Noguer, P.J. van der Linden and D. Xiaosu (Eds.), 2001: *Climate Change 2001: The Scientific Basis Contribution of Working Group I to the Third Assessment Report of the Intergovernmental Panel on Climate Change (IPCC)*. Cambridge University Press, UK, 944 pp.
- Hu, Q., and S. Feng, 2001: Variations of ENSO and interannual variation in summer rainfall in the Central United States. *J. Climate*, **14**, 2469-2480.
- Hu, Q., and S. Feng, 2002: Interannual variations in the North American summer monsoon region: 1900-98. *J. Climate*, **15**, 1189-1203.
- Hu, Q., 2003. A multidecadal variation in summer season diurnal rainfall in the central United States. *J. Climate*, **16**, 174-178.
- Huang, J., H.M. van den Dool, and K.P. Georgarakos, 1996: Analysis of model-calculated soil moisture over the United States (1931-1993) and application to long-range temperature forecasts. *J. Climate*, **9**, 1350-1362.
- Jacob, D., and R. Podzun, 1997: Sensitivity studies with the regional climate model REMO. *Meteor. Atmos. Phys.*, **63**, 119-129.
- Jones, R.G., J.M. Murphy, and M. Noguer, 1995: Simulation of climate change over Europe using a nested regional-climate model. Part I: assessment of control climate, including sensitivity to location of lateral boundaries. *Quart. J. Roy. Meteor. Soc.*, **121**, 1413-1449.
- Jones, R.G., J.M. Murphy, M. Noguer, and A.B. Keen, 1997: Simulation of climate change over Europe using a nested regional-climate model. Part II: comparison of driving and regional model responses to a doubling of carbon dioxide. *Quart. J. Roy. Meteor. Soc.*, **123**, 265-292.

- Kain, J.S., 2004: The Kain-Fritsch convective parameterization scheme: an update. *J. Appl. Meteor.*, **43**, 170-181.
- Kalnay, E., M. Kanamitsu, R. Kistler, W. Collins, D. Deaven, L. Gandin, M. Iredell, S. Saha, G. White, J. Woollen, Y. Zhu, M. Chelliah, W. Ebisuzaki, W. Higgins, J. Janowiak, K. Mo, C. Ropelewski, J. Wang, A. Leetmaa, R. Reynolds, R. Jenne, and D. Joseph, 1996: The NCEP/NCAR 40-year reanalysis project. *Bull. Amer. Meteor. Soc.*, **77**, 437-471.
- Kanamitsu, M., and K.C. Mo, 2003: Dynamical effect of land surface processes on summer precipitation over the southwestern United States. *J. Climate*, **16**, 496-503.
- Karl, T.R., and R.W. Knight, 1998: Secular trends of precipitation amount, frequency, and intensity in the United States. *Bull. Amer. Meteor. Soc.*, **79**, 231-241.
- Katsafados, P., A. Papadopoulos, and G. Kallos, 2005: Regional atmospheric response to tropical SST perturbations. *Geophys. Res. Lett.*, **32**, L04806, doi:10.1029/2004GL021828.
- Kida, H., T. Koide, H. Sasasaki, and C. Masaru, 1991: A new approach for coupling a limited area model to a GCM for regional climate simulations. *J. Meteor. Soc. Japan*, **69**, 723-728.
- Kumar, A., F. Yang, L. Goddard, and S. Schubert, 2004: Differing trends in the tropical surface temperature and precipitation over land and oceans. *J. Climate*, **17**, 653-664.
- Kuo, H.L., 1974: Further studies of the parameterization of the influence of cumulus convection on large-scale flow. *J. Atmos. Sci.*, **31**, 1232-1240.

- Laprise, R., 2003: Resolved scales and nonlinear interactions in limited-area models. *J. Atmos. Sci.*, **60**, 768-779.
- Lau, K.M., and L. Peng, 1992: Dynamics of atmospheric teleconnections during the northern summer. *J. Climate*, **5**, 140-158.
- Lau, K.M., and H. Weng, 2002: Recurrent teleconnection patterns linking summertime precipitation variability over East Asia and North America. *J. Meteor. Soc. Japan*, **80**, 1309-1324.
- Levitus, S., J.I. Antonov, T.P. Boyer, and C. Stephens, 2000: Warming of the world ocean. *Science*, **287**, 2225-2229.
- Li, J., X. Gao, R.A. Maddox, and S. Sarooshian, 2004: Model study of evolution and diurnal variations of rainfall in the North American Monsoon during June and July 2002. *Mon. Wea. Rev.*, **132**, 2895-2915.
- Liang, X-Z., L. Li, K.E. Kunkel, M. Ting, and J.X.L. Wang, 2004: Regional climate model simulation of U.S. precipitation during 1982-2002. Part I: Annual Cycle. *J. Climate*, **17**, 3510-3529.
- Liston, G.E., and R.A. Pielke, Sr., 2001: A climate version of the Regional Atmospheric Modeling System. *Theor. Appl. Climatology*, **68**, 155-173.
- Lo, F., and M.P. Clark, 2002: Relationships between spring snow mass and summer precipitation in the southwestern United States associated with the North American Monsoon system. *J. Climate*, **15**, 1378-1385.
- Lu, L., and W.J. Shuttleworth, 2002: Incorporating NDVI-derived LAI in to the climate version of RAMS and its impact on regional climate. *J. Hydrometeor.*, **3**, 347-362.

- Mahrer, Y., and R.A. Pielke Sr., 1977: A numerical study of the airflow over irregular terrain. *Beitrage zur Physik der Atmosphere*, **50**, 98-113.
- Mantua, N.J., S.R. Hare, U. Zhang, J.M. Wallace, and R.C. Francis, 1997. A Pacific interdecadal climate oscillation with impacts on salmon production. *Bull. Amer. Meteor. Soc.*, **78**, 1069-1079.
- Matsui, T., V. Lakshmi, and E.E. Small, 2005: The effects of satellite-derived vegetation cover variability on simulated land-atmosphere interactions in the NAMS. *J. Climate*, **18**, 21-40.
- Maurer, E.P., A.W. Wood, J.C. Adam, D.P. Lettenmaier, and B. Nijssen, 2002: A long-term hydrologically based dataset of land surface fluxes and states for the conterminous United States. *J. Climate*, **15**, 3237-3251.
- McKee, T.B., N.J. Doesken, and J. Kleist, 1999: Historical dry and wet periods in Colorado. *Climatology Report 99-1, Part A: Technical Report*, Department of Atmospheric Science, Colorado State University, 121 pp.
- McNider, R.T., and R.A. Pielke, Sr., 1981: Diurnal boundary-layer development over sloping terrain. *J. Atmos. Sci.*, **38**, 2198-2212.
- Mears, C.A., M.C. Schabel, and F.J. Wentz, 2003: A reanalysis of the MSU channel 2 tropospheric temperature record. *J. Climate*, **16**, 3650-3664.
- Mellor, G.L, and T. Yamada, 1974: A hierarchy of turbulence closure models for planetary boundary layers. *J. Atmos. Sci.*, **31**, 1791-1806.
- Mesinger, F., T.L. Black, and M.E. Baldwin, 1997: Impact of resolution and of the Eta coordinate on-skill of the Eta model precipitation forecasts. *Numerical Methods*

- in Atmospheric and Oceanic Modeling*. C. Lin, R. Laprise, and H. Ritchie, Eds.,
The Andre J. Robert Memorial Monograph Soc., NRC Research Press, 399-423.
- Mesinger, F., and Coauthors, 2004: North American regional reanalysis. *Bull. Amer. Meteor. Soc.*, submitted.
- Miguez-Macho, G., G.L. Stenchikov, and A. Robock, 2005: Regional climate simulations over North America: interaction of local processes with improved large-scale flow. *J. Climate*, **18**, 1227–1246.
- Mo, K.C., J.N. Paegle, and R.W. Higgins, 1997: Atmospheric processes associated with summer floods and droughts in the Central United States. *J. Climate*, **10**, 3028-3046.
- Mo, K.C., and J.N. Paegle, 2000: Influence of sea surface temperature anomalies on the precipitation regimes over the southwest United States. *J. Climate*, **13**, 3588-3598.
- Mo, K.C., and E.H. Berbery, 2004: Low-level jets and summer precipitation regimes over North America. *J. Geophys. Res.*, **109**, D06117, doi:10.1029/2003JD004106.
- Molinari, J., 1985: A general form of Kuo's cumulus parameterization. *Mon. Wea. Rev.*, **113**, 1411-1416.
- Newman, M., and P.D. Sardeshmukh, 1998: The impact on the North Pacific/North American response to remote low-frequency forcing. *J. Atmos. Sci.*, **55**, 1336-1353.
- Pal, J.S., and E.A.B. Eltahir, 2001: Pathways relating soil moisture conditions to future summer rainfall with a model of the land-atmosphere system. *J. Climate*, **14**, 1227-1242.

- Pal, J.S., and E.A.B. Eltahir, 2003: A feedback mechanism between soil moisture distribution and storm tracks. *Quart. J. Roy. Meteor. Soc.*, **129**, 2279-2297.
- Philander, S.G., 1990: *El Niño, La Niña, and the Southern Oscillation*. Academic Press, 291 pp.
- Pielke Sr., R.A., W.R. Cotton, R.L. Walko, C.J. Tremback, W.A. Lyons, L.D. Grasso, M.E. Nicholls, M.D. Moran, D.A. Wesley, T.J. Lee, and J.H. Copeland, 1992: A comprehensive meteorological modeling system—RAMS. *Meteor. Atmos. Phys.*, **49**, 69-91.
- Pielke Sr., R.A., 2001a: Earth system modeling -- An integrated assessment tool for environmental studies, In: *Present and Future of Modeling Global Environmental Change: Toward Integrated Modeling*, T. Matsuno and H. Kida, Eds., Terra Scientific Publishing Company, Tokyo, Japan, 311-337.
- Pielke Sr., R.A., 2001b: Influence of the Spatial Distribution of Vegetation and Soils on the Prediction of Cumulus Convective Rainfall. *Rev. Geophys.*, **39**, 151-177.
- Pielke Sr., R.A., 2002: *Mesoscale Meteorological Modeling*, Second Edition, Academic Press, 676 pp.
- Pielke, R.A. Sr., N. Doesken, O. Bliss, T. Green, C. Chaffin, J.D. Salas, C. Woodhouse, J.L. Lukas, and K. Wolter, 2005: Drought 2002 in Colorado - An unprecedented drought or a routine drought? *Pure Appl. Geophys.*, **162**, 1455-1479, doi:10.1007/200024-005-2679-6.
- Reynolds, R.W., and T.M. Smith, 1994: Improved global sea surface temperature analyses using optimal interpolation. *J. Climate*, **7**, 929-948.

- Richman, M.B., 1986: Review article: rotation of principal components. *J. Climatol.*, **6**, 293-335.
- Saleeby, S.M., and W.R. Cotton, 2004: Simulations of the North American monsoon system. Part I: model analysis of the 1993 monsoon season. *J. Climate*, **17**, 1997-2018.
- Sardeshmukh, P.D., and B.J. Hoskins, 1988: The generation of global rotational flow by steady idealized tropical divergence. *J. Atmos. Sci.*, **45**, 1228-1251.
- Sasaki, H., K. Hedji, T. Koide, and C. Masaru, 1995: The performance of the long-term integrations of a limited area model with the spectral coupling method. *J. Meteor. Soc. Japan*, **73**, 165-181.
- Schmitz, J.T., and S. Mullen, 1996: Water vapor transport associated with the summertime North American monsoon as depicted by ECMWF analyses. *J. Climate*, **9**, 1621-1634.
- Schubert, S.D., M.J. Suarez, P.J. Pegion, and M.A. Kistler, 2002: Predictability of zonal means during boreal summer. *J. Climate*, **15**, 420-434.
- Schubert, S.D., M.J. Suarez, P.J. Pegion, R.D. Koster, and J.T. Bacmeister, 2004: Causes of long term drought in the U.S. Great Plains. *J. Climate*, **17**, 485-503.
- Seth, A., and F. Giorgi, 1998: The effects of domain choice on summer precipitation simulation and sensitivity in a regional climate model. *J. Climate*, **11**, 2698-2712.
- Smagorinsky, J., 1963: General circulation experiments with the primitive equations. Part I, the basic experiment. *Mon. Wea. Rev.*, **91**, 99-164.
- Small, E.E., 2001: The influence of soil moisture anomalies on variability of the North American monsoon system. *Geophys. Res. Lett.*, **28**, 139-142.

- Stensrud, D.J., R. Gall, and M. Nordquist, 1997: Surges over the Gulf of California during the Mexican monsoon. *Mon. Wea. Rev.*, **125**, 417-437.
- Takle, E.S., W.J. Gutowski, Jr., R.W. Arritt, Z. Pan, C.J. Anderson, R. Ramos da Silva, D. Caya, S.-C. Chen, F. Giorgi, J.H. Christensen, S.-Y. Hong, H.-M. Juang, J. Katzfey, W.M. Lapenta, R. Laprise, G.E. Liston, P. Lopez, J. McGregor, R.A. Pielke, Sr., and J.O. Roads, 1999: Project to Intercompare Regional Climate Simulations (PIRCS): description and initial results. *J. Geophys. Res.*, **104**, 19443-19461.
- Tatsumi, Y., 1986: A spectral limited-area model with time dependent lateral boundary conditions and its application to a multi-level primitive equation model. *J. Meteor. Soc. Japan*, **64**, 637-663.
- Ting, M., and H. Wang, 1997: Summertime U.S. precipitation variability and its relation to Pacific sea surface temperature. *J. Climate*, **10**, 1853-1873.
- Trenberth, K.E., and G.W. Branstator, 1992: Issues in establishing causes of the 1988 drought over North America. *J. Climate*, **5**, 159-172.
- Tripoli, G.J., and W.R. Cotton, 1980: A numerical investigation of the several factors contributing to the observed variable intensity of deep convection over south Florida. *J. Appl. Meteor.*, **19**, 1037-1063.
- Tripoli, G.J., and W.R. Cotton, 1989: Numerical study of an observed orogenic mesoscale convective system. Part 1: simulated genesis and comparison with observations. *Mon. Wea. Rev.*, **117**, 273-304.
- von Storch, H., and F.W. Zwiers, 1999: *Statistical Analysis in Climate Research*. Cambridge University Press, 484 pp.

- von Storch, H., H. Langenberg, and F. Feser, 2000: A spectral nudging technique for dynamical downscaling purposes. *Mon. Wea. Rev.*, **128**, 3664-3673.
- Walko, R.L., and Coauthors, 2000: Coupled atmosphere-biology-hydrology models for environmental modeling. *J. Appl. Meteor.*, **39**, 931-944.
- Wang, W., and A. Kumar, 1998: A GCM assessment of atmospheric seasonal predictability associated with soil moisture anomalies over North America. *J. Geophys. Res.*, **103**, 28,637-28,646.
- Weaver, C.P., S.B. Roy, and R. Avissar, 2002: Sensitivity of simulated mesoscale atmospheric circulations resulting from heterogeneity to aspects of model configuration. *J. Geophys. Res.*, **107(D20)**, 10.1029/2001JD000376.
- Wetzel, P.J., W.R. Cotton, and R.L. McAnelly, 1983: A long-lived mesoscale convective complex. Part II: evolution and structure of the mature complex. *Mon. Wea. Rev.*, **111**, 1919-1937.
- Xu, J., and E. Small, 2002: Simulating summertime rainfall variability in the North American monsoon region: The influence of convection and radiation parameterizations. *J. Geophys. Res.*, **107**, 4727, doi: 10.1029/2001JD00247.
- Xu, J., X. Gao, J. Shuttleworth, S. Sarooshian, and E. Small, 2004: Model climatology of the North American monsoon onset period during 1980-2001. *J. Climate*, **17**, 3892-3906.
- Xue, M., K.K. Droegemeier, and V. Wong, 2000: The Advanced Regional Prediction System (ARPS) – A multi-scale nonhydrostatic atmospheric simulation and prediction model. Part I: model dynamics and verification. *Meteor. Atmos. Phys.*, **75**, 161-193.

- Xue, M., K.K. Droegemeier, V. Wong, A. Shapiro, K. Brewster, F. Carr, D. Weber, Y. Liu, and D. Wang, 2001: The Advanced Regional Prediction System (ARPS) – A multi-scale nonhydrostatic atmospheric simulation and prediction tool. Part II: model physics and applications. *Meteor. Atmos. Phys.*, **76**, 143-146.
- Zhang, Y., J.M. Wallace, and D.S. Battisti, 1997: ENSO-like interdecadal variability: 1900-93. *J. Climate*, **10**, 1004-1020.